Technical Report Documentation Page

1. Report No. 1395-3	2. Government Accession No.	3. Recipient's Catalog No.
4. Title and Subtitle FIELD AND COMPUTATIONAL STUDIES OF STEEL TRAPEZOIDAL BOX GIRDER BRIDGES		5. Report Date August 20, 2000
7. Author(s) Todd A. Helwig and Zhanfei Fan		6. Performing Organization Code 8. Performing Organization Report No. Research Report 1395-3
9. Performing Organization Name and Address University of Houston 4800 Calhoun, Bldg. D, Rm. N107 Houston, Texas 77204-4791		10. Work Unit No. (TRAIS) 11. Contract or Grant No. Research Study 0-1395
12. Sponsoring Agency Name and Address Texas Department of Transportation Research and Technology Transfer Section/Construction Division P.O. Box 5080 Austin, TX 78763-5080		13. Type of Report and Period Covered Interim 14. Sponsoring Agency Code

15. Supplementary Notes
Project conducted in cooperation with the Federal Highway Administration.
Research Study Title: Trapezoidal Box Girder Systems

16. Abstract

Trapezoidal steel box girders are seeing increased use in the state of Texas as well as throughout the United States. In addition to a number of serviceability and aesthetic advantages for trapezoidal box girders, the large torsional stiffness of the closed box section is also a major structural advantage, particularly for curved girders. Curved bridges are essential components of the highway system, particularly for efficient transfer of traffic between highway interchanges in urban environments. Although the composite box in the completed bridge has a large torsional stiffness, the open steel section requires a number of internal and external bracing systems during transport, erection, and casting of the concrete deck.

This report documents results from field and computational studies on trapezoidal box girders. Field studies were conducted on a three-span continuous curved box girder bridge. More than eighty strain gages were applied to the girder cross-section and the top flange lateral truss prior to girder erection. Stresses in the girder and bracing members were monitored during erection, construction, and subsequent live loading. The construction of the box girder bridge was simulated with a three-dimensional FEA model of the quasi-closed steel section. Results from the field studies were used to study the girder behavior during construction and also the interaction of adjacent girders during live loading.

Finite element analyses were used to verify the results from the field tests. The FEA model was used also to conduct a number of parametric studies on the top flange lateral truss and the internal bracing systems for box girders. The results indicate that current design methods often predict unconservative brace forces and girder stresses in box girders. Based on equilibrium and compatibility criteria, design equations were developed to evaluate the bending-induced brace forces in the horizontal trusses and the lateral bending stresses of the top flange. Design equations were also developed to calculate brace forces in internal K-frames in quasi-closed box girders during construction. FEA analysis of live loading on the completed bridge from the field studies was also conducted to investigate live load distribution.

17. Key Words	18. Distribution Statement
curved girder, box girder, steel bridge, field studies, bracing	No restrictions. This document is available to the public through the National Technical Information Service, Springfield, Virginia 22161.

19. Security Classif. (of report)	20. Security Classif. (of this page)	21. No. of pages	22. Price
Unclassified	Unclassified	238	

Form DOT F 1700.7 (8-72) Reproduction of completed page authorized

FIELD AND COMPUTATIONAL STUDIES OF STEEL TRAPEZOIDAL BOX GIRDER BRIDGES

by

Todd Helwig and Zhanfei Fan

Research Report Number 1395-3

Research Project 0-1395
Trapezoidal Box Girder Systems

Conducted for the

TEXAS DEPARTMENT OF TRANSPORTATION

in cooperation with the

U.S. DEPARATMENT OF TRANSPORTATION
Federal Highway Administration
by the

UNIVERSITY OF HOUSTON

AUGUST 2000

DISCLAIMERS

The contents of this report reflect the views of the authors, who are responsible for the facts and the accuracy of the data presented herein. The contents do not necessarily reflect the official views or policies of the Federal Highway Administration or the Texas Department of Transportation. This report does not constitute a standard, specification, or regulation.

There was no invention or discovery conceived or first actually reduced to practice in the course of or under this contract, including any art, method, process, machine, manufacture, design or composition of matter, or any new and useful improvement thereof, or any variety of plant, which is or may be patentable under the patent laws of the United States of America or any foreign country.

NOT INTENDED FOR CONSTRUCTION,
BIDDING, OR PERMIT PURPOSES

Todd A. Helwig
Research Supervisor

ACKNOWLEDGMENTS

The authors would like to thank the project director, Arnie Cohen and the monitoring committee that consisted of John Vogel, Mike Smith, and Tamar Ahmed for input during this project. Arnie Cohen and John Vogel were particularly helpful during the field studies for the research investigation. The authors would also like to thank David McDonald, J. C. Liu, and John Holt for comments and recommendations during the research investigation.

Research performed in cooperation with the Texas Department of Transportation and the U.S. Department of Transportation, Federal Highway Administration.

SUMMARY

Trapezoidal steel box girders are seeing increased use in the state of Texas as well as throughout the United States. In addition to a number of serviceability and aesthetic advantages to using trapezoidal box girders, the large torsional stiffness of the closed box section is also a major structural advantage, particularly for curved girder applications. Curved bridges are essential components of the highway system, particularly for efficient transfer of traffic between highway interchanges in urban environments. Although the composite box section in the completed bridge has a large torsional stiffness, the open steel section requires a number of internal and external bracing systems during transport, erection, and casting of the concrete deck.

This report documents results from field and computational studies on trapezoidal box girders. Field studies were conducted on a three-span continuous curved box girder bridge. More than eighty strain gages were applied to the girder cross-section and the top flange lateral truss prior to girder erection. Stresses in the girder and bracing members were monitored during erection, construction, and subsequent live loading. The construction of the box girder bridge was simulated with a three-dimensional FEA model of the quasi-closed steel section. Results from the field studies were used to study the girder behavior during construction and also the interaction of adjacent girders during live loading.

Finite element analyses were used to verify the results from the field tests. The FEA model was used also to conduct a number of parametric studies on the top flange lateral truss and the internal bracing systems for box girders. The results indicate that current design methods often predict unconservative brace forces and girder stresses in box girders. Based on equilibrium and compatibility criteria, design equations were developed to evaluate the bending-induced brace forces in the horizontal trusses and the lateral bending stresses of the top flange. Design equations were also developed to calculate brace forces in internal K-frames in quasi-closed box girders during construction. FEA analysis of live loading on the completed bridge from the field studies was also conducted to investigate live load distribution.

TABLE OF CONTENTS

LIST OF FIGURES

LIST OF TABLES

CHAPTER 1 INTRODUCTION

1.1 General

Horizontally curved bridges are widely used in urban areas for highway interchanges and access ramps, as well as large viaduct systems. Curved bridges are essential components for the efficient transfer of traffic flows between roadways. The main difference between curved and straight bridges is the superstructures (the slab and girder systems). Due to the large torsional moment that results from the curved alignment, the behavior of curved bridges is generally more complex than for straight bridges. Curved bridges can therefore be particularly challenging to design engineers.

Most curved bridge superstructures make use of composite action between the steel girders and concrete deck. In early practice, curved bridges were usually built by a series of simply supported straight I-girders aligned along the chords of the curved roadway. Many of these bridges are still in service. In addition to the poor bridge aesthetics, there are a number of structural disadvantages with the chord layouts. One of the main drawbacks with the chord layouts is the difficulty of employing continuous girders, which results in inefficient use of the steel sections and the requirement of additional substructure elements.

Technological advances in the steel fabrication industry make the use of curved girders economically feasible in modern curved bridges. There are generally two types of steel cross-sections used in curved girders — I-shaped girders and box girders. The behavior of I-girder systems is relatively well understood, particularly when compared to box girder systems. The design criteria for I-girder systems are therefore relatively well established. This better understanding of I-girder behavior has led to wide-spread use of I-girder systems in curved bridges compared to box girders.

Although I-girder systems have been used more frequently, it has been well established that the torsional behavior of box girders is superior to I-shaped systems. The closed cross-sections of box girders results in values of the torsional stiffness that often range from 100 to 1000 times larger than comparable I-shaped sections (Heins and Hall 1981). Unfortunately, the structural behavior of curved box girder bridges is not as well understood as for I-girder systems. The lack of practical design methodologies and aids is one of the main factors limiting the widespread use of curved box girders.

In addition to the large torsional stiffness, there are a number of other structural, maintenance and aesthetic advantages that make box girders attractive for use in both curved and straight bridges (Hall 1997). Box girder bridges usually do not require external diaphragms between the girders except at the supports, thus reducing erection time in the field. The smooth contour of the box girders provides a number of attractive serviceability features. Corrosion problems in steel bridges typically occur in regions of the girders where water and debris can collect. Box girder bridges have fewer areas where these corrosion agents can collect, which reduces potential in-service problems during the life of the bridge.

The smooth shape of the boxes also leads to better bridge aesthetics, an increasingly important factor in modern bridge design.

1.2 Design and Construction of Box Girder Bridges

Composite box girder bridges usually consist of one or more steel girders of U-shaped trapezoidal cross-section with two top flanges and a concrete slab as shown in Fig. 1.1. The concrete slab is usually cast in-place on the steel sections that are erected earlier. Therefore, during the construction the steel girders are subjected to the gravity load of the slab as well as other construction loads without the composite action from a hardened concrete deck.

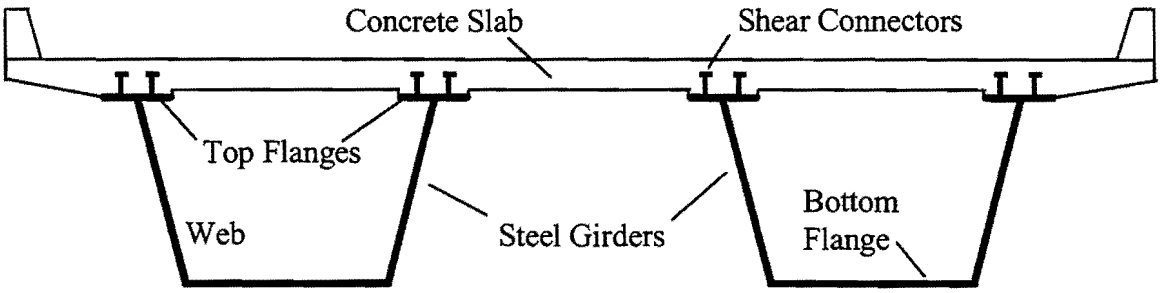

Figure 1.1. Cross-Section of Box Girder Bridge

Although the torsional stiffness of a composite box girder is very large in the completed bridge, during transport, erection and construction the girder consists of an open section with a relatively low torsional stiffness. This poses a major problem during the early stages of bridge construction when the girders may be subjected to relatively large torques. Bracing systems such as those shown in Fig. 1.2 are therefore employed in box girders to increase the torsional stiffness of the steel section. Internal cross-frames (Fig. 1.2a) or diaphragms are used to control distortion of the cross-section from the applied torsion. Although external diaphragms between adjacent girders can be used to increase the torsional stiffness of the bridge, they are mainly used only at supports due to aesthetic and fatigue concerns. A horizontal truss fastened to the box near the top flanges is commonly used to increase the torsional stiffness of the steel section. The girder with the horizontal truss as shown in Figs. 1.2b and 1.2c is often referred as a quasi-closed box girder.

The purpose of the horizontal top truss is to increase the torsional stiffness of the box girder during construction. Once the concrete slab develops its full strength, the cross-section of a box girder is fully closed and therefore a high torsional stiffness is achieved. Although individual box girders are used in bridges with small widths, most box girder bridges consist of more than one steel box. The behavior of a multiple box bridge under service loading is usually better than an I-girder bridge, because traffic loads are more efficiently distributed to girders in the lateral direction due to the large torsional stiffness of the individual boxes.

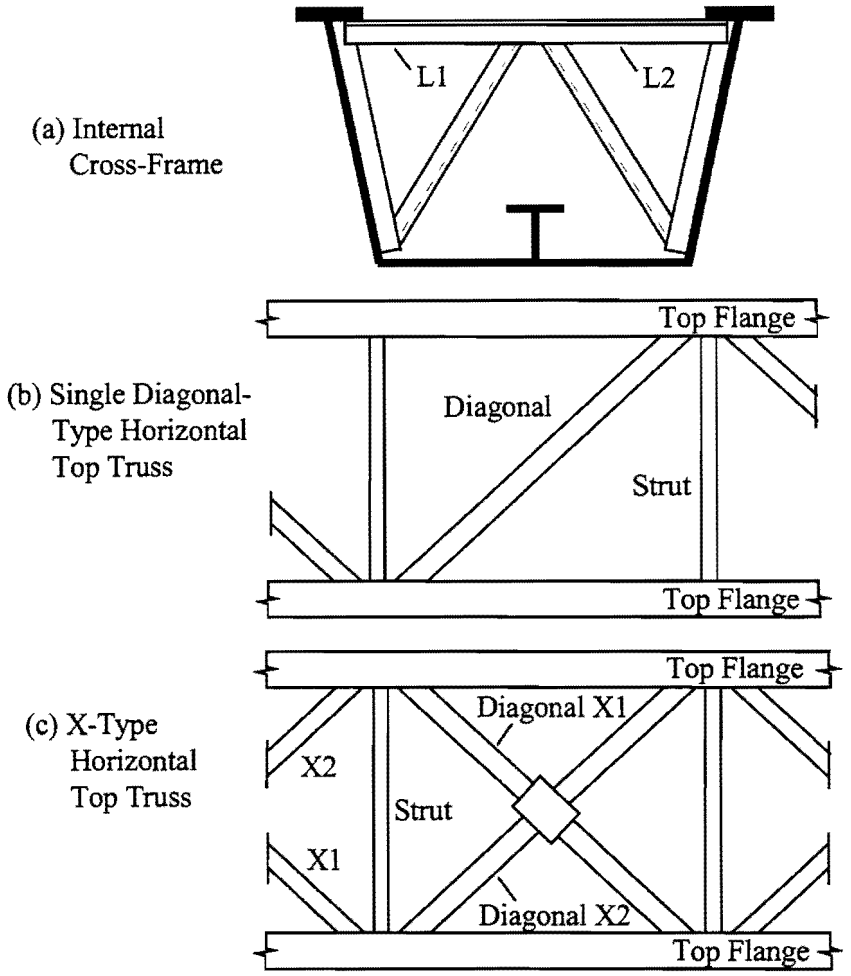

Figure 1.2 Bracing Systems for Box Girders

The design of box girder bridges typically consists of two major phases that need to be considered: the quasi-closed box girders during construction, and the composite box girders with live loading. Special techniques must be employed in dealing with the quasi-closed sections as well as multi-box bridges. Although research investigations have been carried out to develop design methods for the box girders during critical stages, most of these research efforts were conducted more than 20 years ago. Design methods for box girder bridges are inadequate in many areas.

1.3 Research Efforts on Steel Curved Bridges

There are a number of isolated investigations on curved bridges in the U.S. that date back to the early 20th century (McManus et al 1969). The majority of the research efforts, however, were conducted in the 1960's and 1970's (Task 1978).

The major structural member forces in curved bridges are the bending and torsional moments. The bending and torsional theory of straight box girders was established based on

traditional structural analysis theory. The horizontally curved beam theory that couples bending and torsion was established by Vlasov (1961) and Dabrowski (1968). Although these theoretical studies are difficult to apply directly in practice, they provide the foundation that many design methods for curved bridges are based upon. In addition to the theoretical investigations, many research studies have focused on the design and construction of box girder bridges. The main purpose of these investigations was to improve the understanding of the behavior of the bridges. This was accomplished by developing effective analytical methods for engineers, as well as design criteria resulting from the strength and stiffness requirements of the bridges.

In the 1960s the highway administrations and related organizations in the U.S. began sponsoring systematic research investigations on curved bridges. In the area of structural analysis of curved bridges, a milestone is the publication of the U.S. Steel special reports (Richardson 1963, United 1984) that proposed the V-Load method. The V-load method is an approximate method for the analysis of curved I-girder bridges and is still widely used today. In the early 1970's, numerical methods based on the stiffness methods of structural analysis as well as the folded plate theory were studied by several researchers. A number of computer programs were developed for the analysis of curved bridges based upon these analytical methods (Till et al 1976). During the same period of time, Tung and Fountain (1970) proposed the M/R method, which is an approximate method for the torsional analysis of curved box girder bridges.

The largest research activity for the development of design methods for steel curved bridges in the United States thus far was the Consortium of University Research Teams (CURT) project in the late 1960s and early 1970s (Till et al 1976, Task 1978). The study was a pool-funded investigation sponsored by 25 state highway departments and directed by the Federal Highway Administration (FHWA). The purpose of CURT was to conduct a comprehensive analytical and experimental research program on the behavior of horizontally curved highway bridges. CURT was comprised of four teams from Syracuse University, Carnegie-Mellon University, the University of Rhode Island, and the University of Pennsylvania. In addition, investigations were also carried out at the University of Maryland, the University of California at Berkeley, the University of Illinois, and the University of Washington. These research efforts led to the publication of the first edition of the Guide Specification for Horizontally Curved Bridges by the American Association of State Highway and Transportation Officials (AASHTO) in 1980 (Guide 1993).

Although numerous curved bridges have been constructed in the last thirty years, there has been little research work on curved bridges conducted since the early 1970s. There are a number of deficiencies in the current design methods, which are primarily based on the studies carried out more than 20 years ago. As indicated by National Cooperative Highway Research Program (NCHRP 1998), many provisions in the Guide Specification are overly conservative, and many may be difficult to implement. Other provisions lend themselves to misinterpretation, which may lead to uneconomical designs or designs with a lower factor of

safety than intended. Design guides provide little or no guidance for some aspects of the design. In addition, some of the previous research lacked experimental validation, or employed over-simplified models due to limited computer resources. For many aspects of the design, engineers have no guidance.

After relatively little research for more than a decade, a number of highway administrations and organizations have organized and sponsored research projects in an effort to improve design methods for curved highway bridges in recent years. For example, a National Cooperative Highway Research Program (NCHRP) project is designated to update the current curved girder specifications and to develop a Load and Resistance Factor Design (LRFD) specification. Another project sponsored by the Federal Highway Administration (FHWA) is pool-funded similar to the CURT projects and is intended to extend the knowledge of the behavior of curved steel bridges. The scope of the FHWA project originally included box girders, however boxes have been dropped from the scope of the study due to time constraints. In addition, the Minnesota Department of Transportation has sponsored a research project to conduct field and computational studies on stresses in curved I-shaped steel girder bridges (Galambos et al 1996).

This report presents results from TxDOT research study 0-1395, which was a joint study between the University of Houston and the University of Texas at Austin. The objective of the project is to develop a comprehensive design method for curved trapezoidal box girder systems. The scope of the study includes several areas that are not well addressed by current design specifications. These areas include the recommendations for bracing of the top flanges during transportation and erection, the behavior and design of internal and external diaphragms, the behavior and design criteria for twin box girders, and the design of the compression region over continuous supports including the bearings. The research includes field measurements, computational studies, and laboratory testing. This report will focus on the field measurements and the computational studies.

1.4 Aims, Scope and Organization of the Report

The objective of this report is to study the static behavior of curved trapezoidal box girder systems under various loading conditions and to improve the design methods. The degree of curvature of a curved bridge can be measured by the subtended angle per 100 feet of bridge length. However, the effect of curvature on the structural behavior of curved bridges is governed by the subtended angle between consecutive bridge supports. Design guides often provide a lower limit on bridge curvature, below which the girder may be designed as a straight girder. The effect of curvature can be neglected in design if the subtended angle in each span of a bridge is less than the values specified in Table 1.1 (Guide 1993).

However, the specification (Guide 1993) does not provide the upper limit for the bridge curvature. If a bridge is severely curved, nonlinear stress distributions on the girder cross-section may occur, and the system cannot be modeled by beam theory on which the current

Table 1.1. Limiting Central Angle for Neglecting Curvature

Number of Girders	Angle for 1 Span	Angle for 2 or More Spans
2	2°	3°
3 or 4	3°	4°
5 or more	4°	5°

specifications are based. Few studies have been conducted to determine this upper limit of bridge curvature, which varies for different structural types. Tung and Fountain (1970) showed that approximations using beam theory can be successfully applied to a single box girder with a subtended angle per span being as much as 40°. This benchmark for box girder is larger than the curvatures of most highway bridges.

The curvatures of the bridges considered in this report are in the *small to medium* range, i.e., the subtended angle between consecutive supports along the girder length is larger than the lower limit specified in Table 1.1 so that the effect of curvature should be considered. However, the bridge curvatures are not so severe as to cause nonlinear stress distributions on the girder cross-section induced due to curvature. The main effect of curvature is the inducement of torsional moments even when the loads are acting on the shear center of a bridge. The majority of curved bridges in the state of Texas fall into the category of small to medium curvature.

Following the introduction in Chapter 1, Chapter 2 provides a general review of the basic mechanics of box girder bridges as well as the current design methods. Bending, torsion and distortion of box girders will be discussed, along with approximate and numerical methods for the analysis of curved bridges. The current design methods for both quasi-closed boxes and complete bridges will be briefly summarized.

Chapter 3 will focus on field measurements of a curved steel box girder during construction. The three-dimensional Finite Element Analysis (FEA) for box girder bridges is discussed in Chapters 4 through 7. The FEA model was compared with field measurements and also used in parametrical studies on box girder behavior. Chapter 4 presents the comparison between the FEA solutions and the field measurements during construction. In Chapter 5, the FEA model is used to study the effect of box girder bending on the top flange lateral truss system. FEA analyses are presented in Chapter 6 that focus on the distortional behavior of quasi-closed box girders.

The behavior of the completed box girder bridges will be studied in Chapter 7. Results from live load testing of the instrumented bridge are presented. The test results were processed to obtain the influence lines of the girder stresses. Numerical studies are also presented that include the development of both a line element model for a single girder, as well as a three dimensional FEA model for a completed box girder bridge with a composite slab. The results from the FEA models were compared with the test results for verification. The FEA models are also used to study the stress distributions on the critical cross-sections

of the bridge. Behavior of the live load distribution of the box girder bridge is discussed. Finally, Chapter 8 summarizes the findings in this report and discusses the future research needs for box girder bridges.

CHAPTER 2 BACKGROUND ON THE ANALYSIS OF BOX GIRDER BRIDGES

2.1 Basic Mechanics of Box Girders

Steel bridges usually fit into the classification of thin-walled beams. The members are classified as thin-walled because the thickness of the elements are small compared to the width and height of the cross-section, and these cross-sectional dimensions are small compared to the length of the bridge. Timoshenko (1961) as well as Vlasov (1961) made major contributions to the development of the mechanical understanding of the behavior of thin-walled structural members.

This section provides a summary of the thin-walled beam theory necessary to understand the behavior of the individual plates in thin-walled structures such as box girders. The deformations in thin-walled members depend on the loading conditions that the member is subjected to. Figure 2.1 shows plate elements subjected to axial load, bending, and pure shear. If the external forces act within the plane of the plate and cause a state of plane stress, the plate will experience in-plane membrane deformation. Thin-walled members are usually designed to carry external loads by using the in-plane stiffness of the plates. Under certain circumstances, however, a plate may also bend in the out-of-plate direction as shown in Fig. 2.2. In this case, bending moments and shears in the through-thickness direction of the plates are developed. These forces are usually relatively small in most loading cases due to the small stiffness of the plate in the through-thickness direction. In box girders, however, this stiffness may be relatively large and play a significant role in the behavior of the girders (Dabrowski 1968).

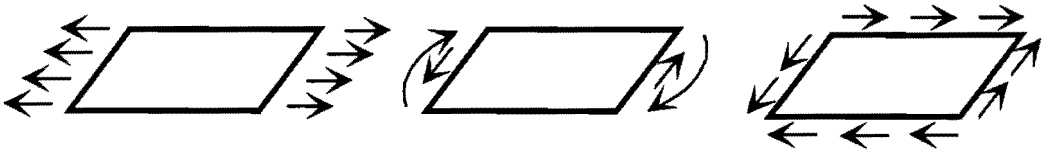

(a) Axial Load (b) Bending (c) Pure Shear

Figure 2.1. In-Plane Forces in Plates

Figure 2.2. Out-of-Plane Deformations of Plates

2.1.1 Bending

Economical box girders often have span-to-depth ratios of 25 or more for single-span girders and ratios of 35 or more for continuous girders. Because of these large span/depth

ratios, bending causes significant stresses in the girders. Bending of box girders can usually be analyzed using traditional beam theory. For example, the longitudinal stress, f, is calculated by

$$f = \frac{Mz}{I}, \qquad (2.1)$$

in which M is the bending moment, z is the distance from the neutral axis to the point being studied, and I is the moment of inertia of the cross-section. For composite bridges, the moment of inertia in the completed bridge is substantially larger than that of the steel section alone. However, during construction the steel section must support the weight of the concrete and other construction loads.

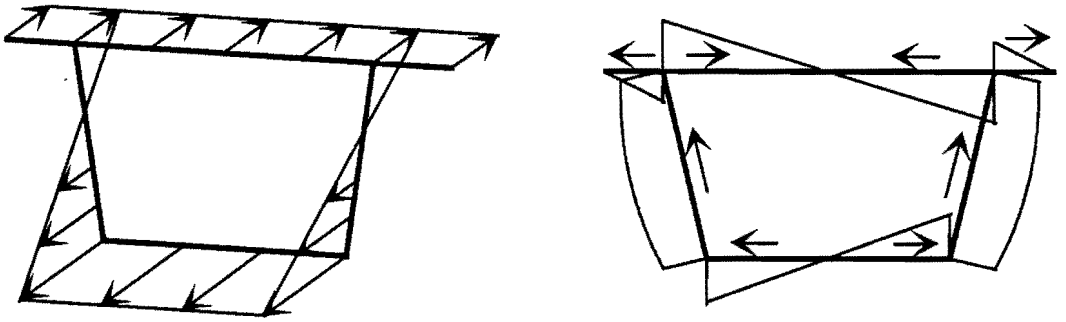

(a) Normal Stress (b) Shear Stress

Figure 2.3. Distribution of Bending Stresses in Box Girders

A typical distribution of bending stresses on the cross-section of a box girder is demonstrated in Fig. 2.3. The top and bottom plates are subjected to in-plane tensile and compressive stresses from bending moments, as well as in-plane shear stress if a bending moment is not uniform along the length. Box girders that are relatively wide compared to the depth are prone to shear lag. Shear lag is a phenomenon that weakens the bending capacity because it causes the longitudinal bending stress to vary across the width of the member (Nakai and Yoo 1988). For example, if the bottom flange is relatively wide, the longitudinal bending stress in the middle of the flange will be less than the stress near the webs due to shear lag. The effect of shear lag can be minimized by using a width close to the girder depth. The box girders considered in this project have relatively "square" cross-sections and therefore shear lag will not be discussed in this report.

2.1.2 Torsion

Torsional moments are resisted by the shear stresses on the girder cross-section. Torsion in thin-walled structures is usually categorized as either Saint-Venant torsion or warping

torsion. Saint-Venant torsion is the result of pure shear deformation in the plane of the plates that make up the thin-walled member. Warping torsion is associated with the bending deformation in the plane of the individual plates. In general, both Saint-Venant torsion and warping torsion are developed when thin-walled members are twisted. A rigorous theory for warping torsion was established by Vlasov (1961). Significant warping torsion may develop in girders with an open cross-section such as I-shaped girders. Box girders are usually dominated by Saint-Venant torsion due to the closed cross-section. The longitudinal normal stresses due to warping torsion are usually negligible (Kollbrunner and Basler 1969).

The large Saint-Venant stiffness of a box girder provides a torsional stiffness that may be 100~1000 times that of a comparable I-section. The torsional stiffness of a thin-walled box section is a function of the shear modulus of the material, G, and the torsional constant, K_T, which is related to the geometric profile of the cross-section. The torsional stiffness transforms the torsional deformation to torsional moments by the expression (Kollbrunner and Basler 1969)

$$M_T = GK_T \frac{d\phi}{dx} , \tag{2.2}$$

where M_T is the torque on the cross-section of the member, G is the shear modulus, ϕ is the rotation of the cross-section, and x denotes the longitudinal axis of the member. The torsional constant for single cell box girders is given by

$$K_T = \frac{4A_0^{\,2}}{\sum_i b_i / t_i} , \tag{2.3}$$

where A_0 is the enclosed area of the cross-section of the box girder, b_i and t_i in the summation are the respective width and thickness of the *i*th plate in the box.

The shear stress due to Saint-Venant torsion can be solved using Prandtl's membrane analogy (Kollbrunner and Basler 1969). For example, for girders with a single cell cross-section, a uniform shear flow, q, develops along the perimeter of the box and can be determined using the Bredt's equation

$$q = \tau t = \frac{M_T}{2A_0} , \tag{2.4}$$

in which t is the thickness o f the plate, and τ is the shear stress, which is essentially uniform through the thickness of the plates. The distribution of torsional shear stress is demonstrated in Fig. 2.4.

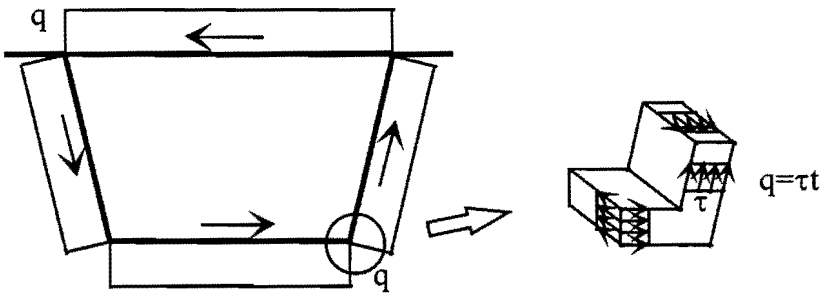

Figure 2.4. Shear Flow in Box Girder Due to Saint-Venant Torsion

The torsional warping stresses in the box girder are usually negligible. However, significant warping stresses due to the cross-sectional distortion of box girders may develop, as will be discussed in the following sub-section.

2.1.3 Distortion

The torsional analysis outlined in the previous sub-section is based on the assumption that the cross-section of the box girder maintains the original shape. Torsional loads on box girders usually result from either eccentric loads or the bridge geometry. Although the torsional moment can be applied so as not to distort the cross-section, under general torsional loads, the cross-sections of box girders will distort from the original profile. Box girder distortion results in additional longitudinal warping stresses as well as out-of-plane bending stresses in the individual plates of the box girder sections (Dabrowski 1968). The distortional stresses in the box girder are a function of the box girder geometry and the magnitude of the distortional load.

Cross-sectional distortion is induced by torsional loads that do not result in a uniform Saint-Venant shear flow. General torsional loading can therefore be modeled as a uniform torsional component superimposed on a distortional component. The magnitude and direction of the distortional load depends on the geometry of the box and how the torsional load is applied to the girder. For example, consider the box girder shown in Fig. 2.5a. The thin-walled box has a depth and width of h and b, respectively. Torsion is applied to the girder by vertical forces that form a couple and generate a torsional moment, m_T. This couple can be modeled by the uniform torsional component given in Fig. 2.5b superimposed on the distortional component given in Fig. 2.5c. If, on the other hand, the torsional load is a result of two horizontal forces as shown in Fig. 2.6a, the couple can be modeled by the torsional loads given in Figs. 2.6b and 2.6c. The two loading conditions above result in the same uniform torsional component on the cross-section, however, the distortional component is in the opposite direction and the distribution of the stresses can be significantly different.

Since the cross-sectional distortion discussed here is induced by the torsional loads that do not result in a uniform Saint-Venent shear flow, it is often referred as torsional

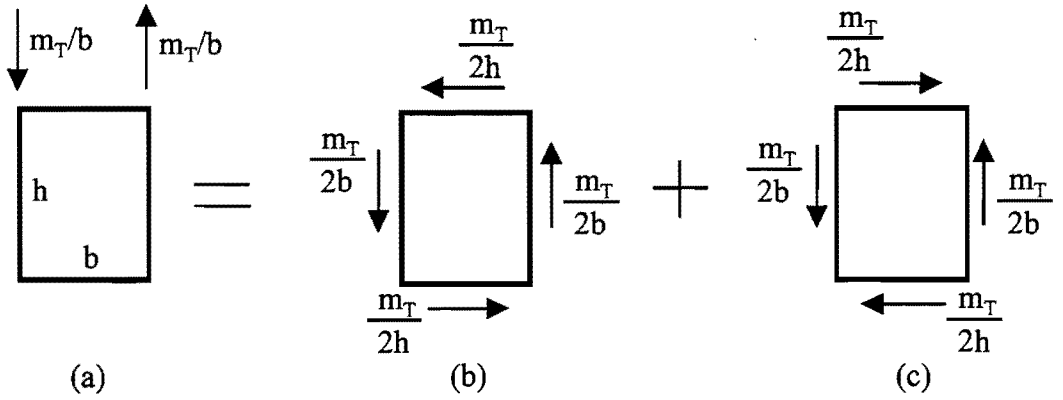

Figure 2.5. Torsion and Distortion by Vertical Loads

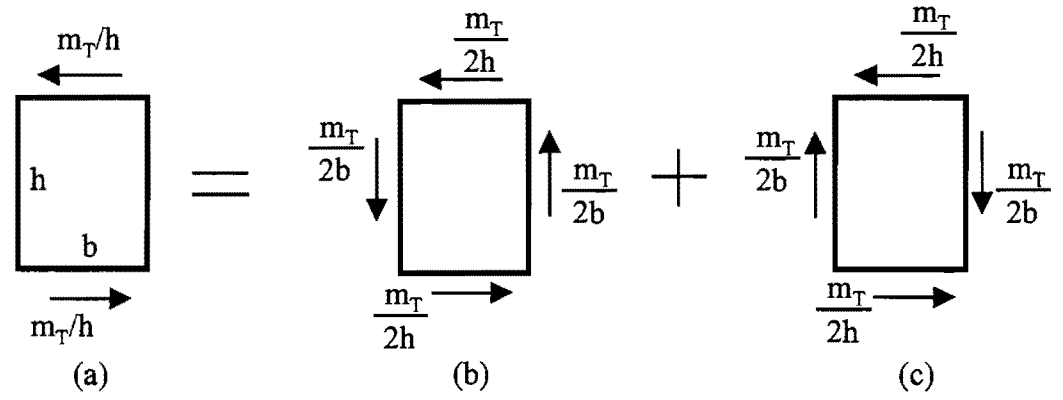

Figure 2.6. Torsion and Distortion by Horizontal Loads

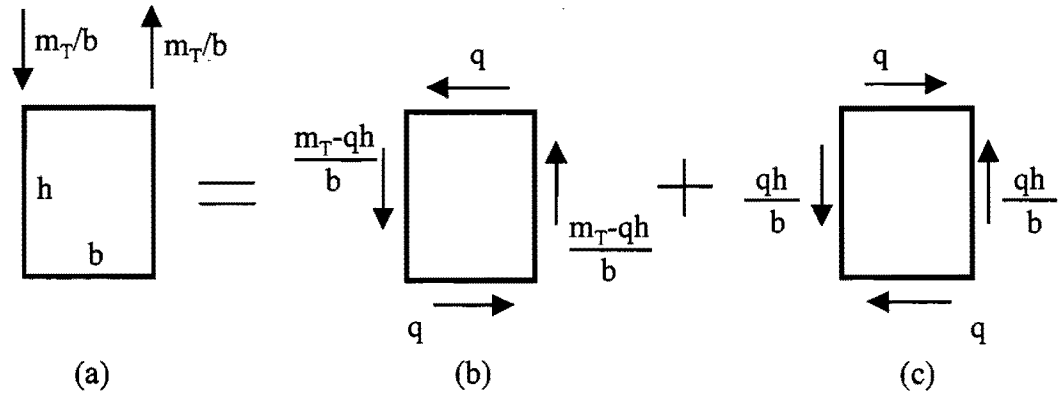

Figure 2.7. A General Decomposition for Torsional and Distortional Loads

distortion. Other forces such as bending loads may lead to distortion of the cross-section near the load locations. These kinds of distortion will generate additional stresses in the localized regions and generally don't effect the overall behavior of the box girder. Only torsional distortion will be studied in this report.

A fundamental question for the distortional analysis of box girders is the determination of the distortional loads. A distortional load consists of four force components on the plates of the box, as shown in Figs. 2.5c and 2.6c. These four components cause the cross-section to distort, however they do not induce torsion on the girder. Traditional box girder theory (Dabrowski 1968) does not provide a rational method to determine the magnitude and direction of the distortional loads. The loads as shown in Fig. 2.5a can also be divided into the components as shown in Figs. 2.7b and 2.7c, in which q is an arbitrary value, resulting in an indeterminate distortional load in Fig. 2.7c. Therefore, additional criteria must be established in order to determine the magnitude of the distortional loads. The principle used for this purpose is that, in the decomposition as shown in Fig. 2.7, q must be determined such that the torsional load as shown in Fig. 2.7b is purely torsional (without distortion). The distortional components are fully eliminated from the external torsional load and are only represented by the loading shown in Fig. 2.7c. Chapter 6 and Appendix D discuss the determination of this pure torsional load as well as the distortional load on box girders. It is found that the state of pure torsion (without distortion) in box girders can only be achieved if the components of a torsional load are distributed along the circumference of the cross-section in proportion to the Saint-Venent shear flow. The torsional loads shown in Figs. 2.5b and 2.6b for rectangular box girders satisfy this requirement and are therefore purely torsional. The distortional loads for box girders with trapezoidal cross-sections can also be determined using these criteria.

The stresses caused by the cross-sectional distortion can be significantly reduced by providing internal diaphragms or cross-frames along the box girder length. Solid diaphragms are usually used only at the supports, while intermediate internal cross-frames as shown previously in Fig. 1.2a are spaced along the length of the girder. A major objective for the distortional analysis of box girders is to determine the spacing and stiffness of the internal cross-frames in order to control the distortional stresses. It is also important to determine the brace forces developed in the cross-frames in order to provide adequate strength for the cross-frame members. Chapter 6 will focus on the distortional behavior of box girders. An approximate method to calculate the axial forces in internal K-frames for quasi-closed box girders is also presented in Chapter 6.

2.2 Analysis of Curved Box Girder Bridges

For curved bridges with small to medium curvature (defined in Chapter 1), the cross-sectional stress distributions caused by bending and torsional loads are similar to those in straight girders. Therefore, a major assumption made in the analysis of curved bridges, is that the bridge curvature does not affect the bending or torsional stress distribution on the girder.

The cross-sectional properties for curved girders are therefore evaluated by the same method as for straight girders. The main issue for the analysis of curved girders is the solution of the structural forces, given the curved bridge geometry and supporting conditions.

The curved thin-walled beam theory, which includes the governing differential equations for combined bending, torsion and distortion, was developed by Vlasov (1961) and Dabrowski (1968). Direct solutions of these equations were pursued. For example, Dabrowski (1968) has provided a number of closed-form solutions for curved beams with different span and loading arrangements. However, these analytical solutions are difficult to apply directly in design. The majority of the research investigations were therefore devoted to the development of approximate methods and numerical models.

2.2.1 Approximate Methods

A major difficulty in the analysis of horizontally curved bridges is the combination of bending and torsion under general applied loads. Naturally, it is expected that an approximate method would focus on solving the bending and torsional solutions separately and then combining the solutions using the principle of superposition.

The most popular approximate method for curved box girder bridges is the M/R method developed by Tung and Fountain (1970). This method is based upon the assumption made for bridges with small to medium curvature. However, it was found that the method is effective for a wide range of curved highway bridges. For example, bridges with as much as 40° subtended angle between two torsionally-fixed supports can be analyzed using the M/R method (Tung and Fountain 1970). Since the radius is relatively large, it is assumed that the effect of curvature on the bending behavior of a curved girder is negligible. The bending moment of the girder can be determined by neglecting the curvature and using the traditional beam theory for straight girders. Therefore, bending moments are determined in the first step of M/R method by assuming the girder is straight with the spans equal to the developed lengths of the curves.

Torsional moments in curved girders can be induced by the curvature of girder alignment even without direct torsional load on the girders. This effect can be represented by an equivalent distributed torsional load, M/R, for which the method is named. Consider a horizontally curved box girder subjected to vertical loads as shown in Fig. 2.8. The force in the top flange can be approximated as M/h where M is the bending moment and h is the girder depth. These forces act on the curved segment as shown in Fig. 2.9a. Due to the curvature of the segment, a lateral component of $(M/h)d\theta$ is developed on the flange. If this lateral force is divided by the length of the segment, ds, a distributed lateral load equal to M/(Rh) is derived. The effect of the curvature can thus be approximated by a straight model in which the flange segment is subjected to the longitudinal force of M/h and an external distributed load of M/(Rh) in the lateral direction as demonstrated in Fig. 2.9b. The bottom flange is also subjected to the same amount of the lateral load but in the opposite direction.

As a result, these two horizontal components form a distributed torsional load equal to M/R acting on the girder (Fig. 2.10). Therefore, the torsional moments due to the curvature of the girder are approximately equal to the torsional moments in a straight beam due to the distributed torsional load of M/R.

In addition, there may exist other direct torsional loads such as those due to vertical loads eccentric to the shear center of the girder. The torsional analysis due to M/R as well as other torsional loads can be approximated by neglecting the curvature of the girder. Therefore, the M/R method does not require a curved beam model for both the bending and torsional analysis. If twist is prevented at all supports, the torsional analysis can be performed by considering only one span at a time since torsional warping is usually very small in box girders and thus the torsional deformation in one span does not significantly affect adjacent spans.

The assumption used in the M/R method is also the basis of the V-Load method for curved I-girder bridges. Instead of the shear flow developed on cross-sections of the girders, the equivalent torque M/R is resisted by the warping-type non-uniform bending of different girders in the I-girder system (Richardson 1963).

2.2.2 Numerical Methods

A number of different numerical methods can be used in bridge analysis, such as the Finite Difference Method or the Finite Strip Method. However, the most widely used method is the Finite Element Method based upon the stiffness method of structural analysis (Zienkiewicz 1977). Advances in the Finite Element Method over the last three decades have improved choices in element types and modeling techniques. There are a wide variety of commercial programs available for structural modeling. The computational tools available today have significantly improved compared to those used in earlier investigations on curved bridges in the CURT projects.

The numerical analysis of curved bridges can be performed at different levels of accuracy. Although the analysis can be quite costly in terms of time of computer resources, a high accuracy can be achieved by modeling the spatial geometry of the curved structure. Individual plates that comprise the girders may be idealized by shell elements in a FEA model. This model allows the width and depth of the cross-sections, along with the dimensions in the longitudinal direction to be precisely modeled. The models are therefore three dimensional, resulting in direct stress solutions instead of the member forces such as moments and shears. The method is directly based upon elasticity as well as plate and shell theory without relying on the assumptions made on thin-walled structures. This refined modeling, however, often results in a large number of degrees of freedom that may require extensive computer resources and special modeling techniques. Therefore, this method currently has limited applications in bridge design and is mainly used in research.

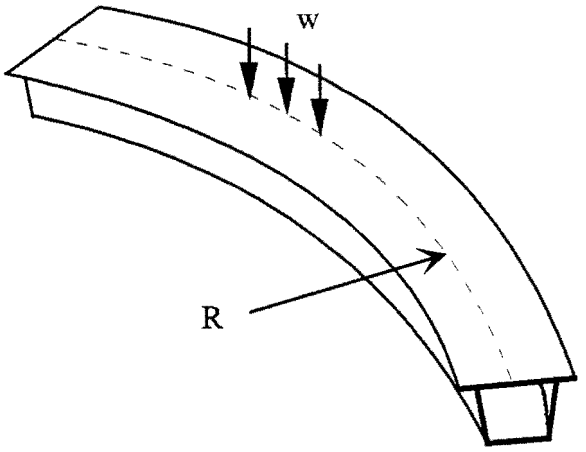

Figure 2.8. Curved Box Girder Under Vertical Loads

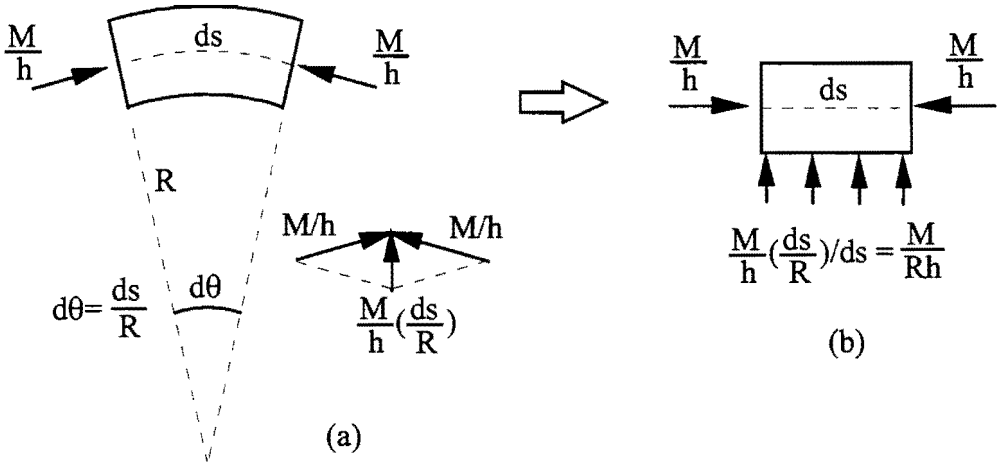

Figure 2.9. Approximation of the Effect of Curvature on Box Girder Flanges

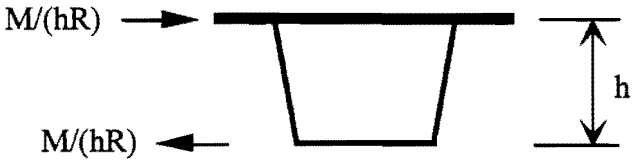

Figure 2.10. Equivalent Torsional Loads on Curved Box Girder

Analyses with a lower level of accuracy are usually performed with the application of line elements to model steel girders. This approach is widely used in practice, and most programs for bridge design, such as DESCUS (1996), make use of the line element analysis. The line element models are based upon the bending and torsional theories of thin-walled members, thus requiring the input of cross-sectional properties for bending and torsion, such as the moment of inertia and torsional constant. Since multiple girders are encountered in most bridges, most programs make use of the grid analysis as shown in Fig. 2.11. The line elements in a grid analysis include the degrees of freedom corresponding to the rotations in the longitudinal and transverse directions, as well as the displacement in the vertical direction. In recent years, new line elements have been developed to account for the torsional warping and cross-sectional distortion (Razaqpur and Li 1991, Zhang and Lyons 1984). However, grid analysis programs are unable to account for the effect the concrete slab has on live load analysis unless additional shell elements are included in the model. Therefore, the loads on each girder have to be determined with the application of pre-assumed live load lateral distribution factors that will be discussed later in this chapter.

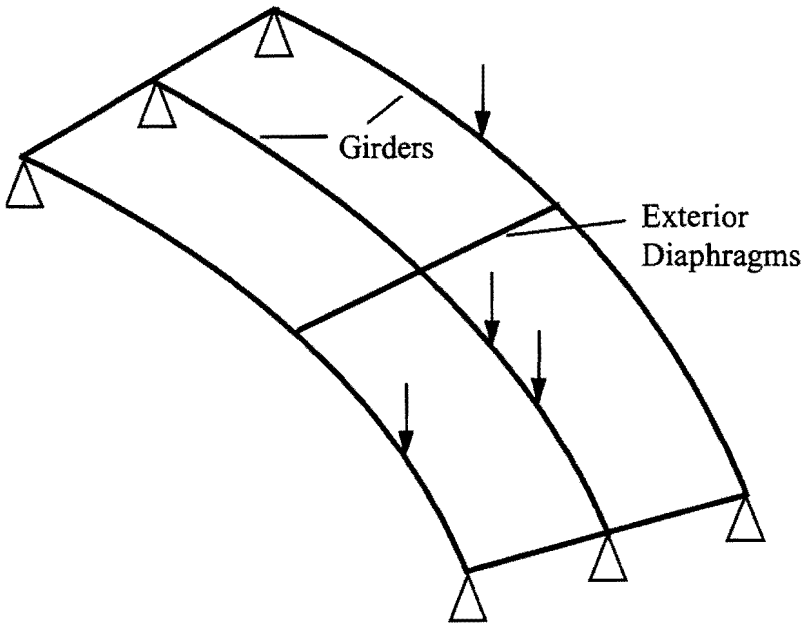

Figure 2.11. Grid Analysis of Curved Girder System

Both the refined 3D FEA models and line element models are used in this investigation. The 3D model is used extensively to study both the quasi-closed box girders during construction and the completed bridge under live loads. The development of the 3D model will be discussed in Chapter 4 for the construction phase and in Chapter 7 for additional features to account for the concrete slab. The line element model, which will be discussed in Chapter 7, was used to simulate the behavior of a single box girder during the live load tests. The purpose of the line element analysis is to examine the effectiveness of simple models in predicting the response of the bridge. Curvature and grid analysis are thus not included in the model.

2.3 Analysis of Quasi-Closed Box Girders

As indicated earlier in Chapter 1, without the concrete slab, box girders do not have a closed cross-section during construction. A lateral truss system is installed at the top flange level to form a quasi-closed cross-section to increase the torsional stiffness of the girder.

The torsional analysis of a quasi-closed box girder is usually performed using the Equivalent Plate Method (EPM) developed by Kollbrunner and Basler (1969). Two types of truss systems that are usually considered consist of a Single Diagonal (SD-type) or an X-system (X-type) as shown previously in Figs. 1.2b and 1.2c. According to the EPM, the top lateral truss system is treated as a fictitious plate so that the torsional properties of the box can be approximated during the structural analysis. The thickness of the fictitious plate must be determined to use Eq. 2.3 to calculate the torsional constant of the box girder. The equivalent thickness of the fictitious plate was developed by Kollbrunner and Baslar (1969) for various truss systems using energy methods. The resulting torsional properties are used in structural analysis to determine the torsional moments in the girders. Once the distribution of torsional moment is known, the shear flow, q, can be determined using Eq. 2.4 and treating the girder as a fully closed cross-section as shown in Fig. 2.12a. The shear flow acting on the fictitious plate is then transformed to diagonal member forces in the lateral truss as demonstrated in Fig. 2.12b and 2.12c. The diagonals are designed to carry the resulting axial member forces from the torsional analysis. Many design guides (Guide 1993, Highway 1982, and Heins 1975) recommend the EPM for the design of the diagonals of the horizontal truss.

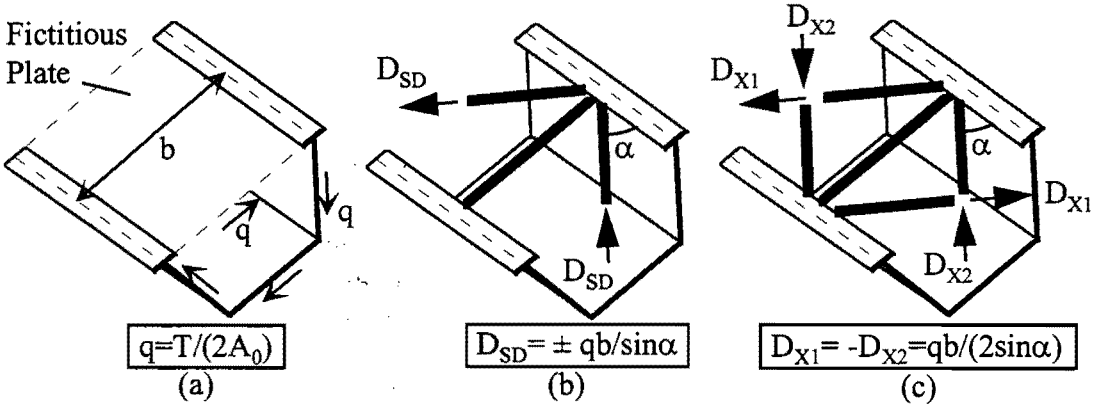

Figure 2.12. Diagonal Brace Forces Due to Torsion According to EPM

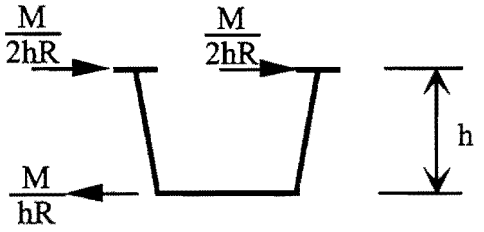

Figure 2.13. Lateral Load Components on Quasi-Closed Box Girder Due to Curvature

Another problem in box girders with a top lateral truss system is the lateral bending of the top flanges. The torsional and bending loads on box girders may include lateral load components acting on the top flange, causing it to bend in the lateral direction. For example, the torsion induced by the curvature of the girder can be modeled as two horizontal forces acting on the top and bottom flanges of a box girder, as demonstrated previously in Fig. 2.10. A similar loading condition exists for quasi-closed girders as shown in Fig. 2.13, and the lateral components on the top flanges, M/(2Rh), will induce the lateral bending stresses in the top flanges. Lateral bending stresses are derived from the lateral bending moments in the top flanges that are often approximated using the following expression (Highway 1982),

$$M_{LC} = \frac{M_1 d^2}{10Rh}, \qquad (2.5)$$

in which M_{LC} is the lateral bending moment due to curvature, M_1 is the vertical bending moment due to the self-weight of the steel girder, the concrete slab weight and construction loads, d is the distance between diaphragms and internal cross-frames, R is the radius of the curved girder, and h is the depth of the girder.

The sloping webs of the trapezoidal girders also induce a lateral load component on the top flange. This lateral load component causes additional lateral bending stress as well as axial forces in the lateral struts of the top flange truss. The struts for the top flange truss are typically designed to carry the horizontal component due to the sloping webs. Figure 2.14 demonstrates the transformation of the vertical load into a web shear and a horizontal component, p. Design guides (Highway 1982, and Four 1997) provide recommendations for the design of the struts for the lateral load component as well as accounting for lateral bending of the flanges between the struts. One of the assumptions in these recommendations for evaluating the required forces in the struts and the lateral bending stresses in the top flange, is that the top and bottom flanges each carry half of the horizontal web components of the applied load. Based on this assumption, the half acting on the bottom flange does not generate any top flange lateral bending stress or forces in the struts. For a truss panel length of s, the recommended design tensile force for the struts is therefore equal to ps/2. The maximum lateral bending moment in the top flanges due to the horizontal component is

therefore equal to $(0.5ps^2)/12$, assuming the flange behaves like a continuous beam supported at the strut locations.

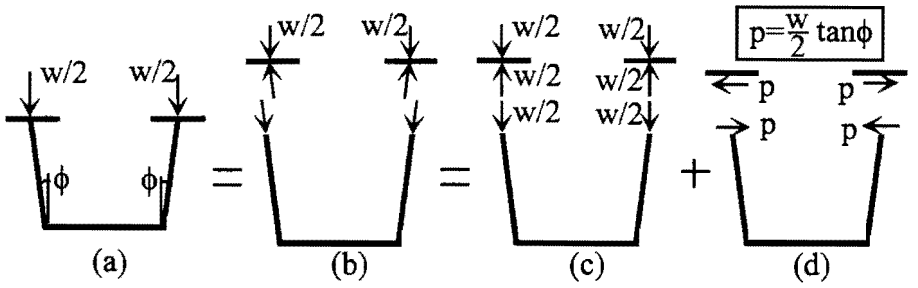

Figure 2.14. Horizontal Component of Applied Loads on the Top Flanges

Current design guidelines (Guide 1993, Highway 1982) do not consider the effects of the vertical bending of box girders on the behavior of the top flange lateral truss. Results will be presented in Chapter 5 that show large forces can be induced due to vertical bending of the box girder. Expressions are developed that can estimate truss forces and top flange lateral bending stresses due to vertical bending.

Additional bracing members in box girders are the internal cross-frames spaced along the girder length. The cross-frames are provided to resist the distortion of the cross-section of the girder. Although the distortional behavior of closed box girders has been studied previously, no research results were focused on the distortional behavior of quasi-closed box girders. As a result, there is no effective design method for the selection of the stiffness and spacing of cross-frames in quasi-closed box girders. In Chapter 6, an approximate formula is proposed to evaluate the brace forces in internal K-frames due to the distortion of the quasi-closed box girders.

2.4 Analysis of Complete Box Girder Bridges Under Live Loads

The behavior of composite box girder bridges under live loads is quite different from quasi-closed box girders during construction. The concrete slab fully closes the box sections and significantly increases the torsional and flexural stiffness of the girder. A complete bridge should be treated as a 3D structure to correctly model the interaction between girders. This approach, however, is unrealistic for design due to the complexity of the analysis and the large size of the problem. Simple models, such as line element models for individual girders are usually employed.

If a bridge has only one box girder, the application of the beam model is relatively straight forward. AASHTO specifies that the governing load effect should be the largest result from one standard truck (the HS20 truck) or a uniformly distributed load over the entire bridge in

each of the traffic lanes (AASHTO 1994). Therefore, if the bending moment of the composite box girder in a single-box bridge due to the one truck (or one distributed load) is solved using beam theory, the multiplication of this moment to the number of traffic lanes results in the largest bending moment that could possibly be encountered due to the live loads.

This concept is extended to the analysis of general bridges with multiple girders by the use of Distribution Factors (DF) that represent the lateral distribution of live load between girders. In this approach, an individual girder is analyzed so that the moment due to the standard truckload is obtained. The design moment of the girder is equal to this standard moment multiplied by the DF. The DF is a parameter reflecting the maximum amount of traffic loads that would be transmitted to a girder in the lateral direction, i.e.,

$$DF = \frac{M_{Max}}{M_0}, \tag{2.6}$$

in which M_{max} is the maximum bending moment developed in a girder in the bridge, and M_0 is the bending moment in the individual girder due to a standard AASHTO load.

The DF approach is widely used in design for the analysis of highway bridges. The value of the DF depends on a number of factors, such as the type of structure, as well as the number and spacing of girders. As an example of the use of the DF in design, consider the simply-supported bridge shown in Fig. 2.15. The bridge has 5 I-girders spaced at 7.5 ft in the lateral direction.

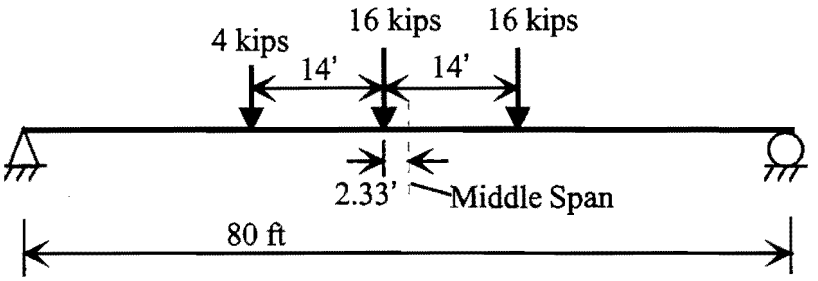

(a) Single Girder under HS-20 Truck Wheel Loads

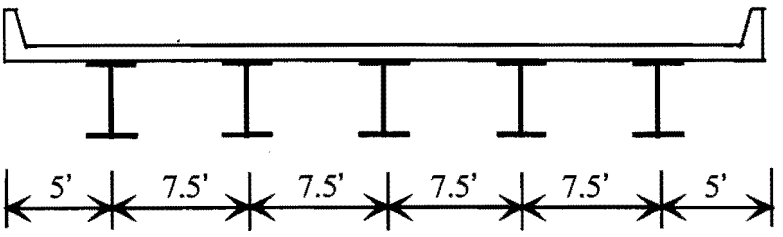

(b) Cross-section of the Bridge

Figure 2.15. A Simply Supported Bridge with I-shaped Girders

An individual girder is subjected to the wheel loads of an HS-20 truck (Fig. 2.15a). The largest bending moment in the girder due to the HS-20 wheel loads is 582 k-ft, when the truck is located at the position shown in the figure. AASHTO (1994) specifies that the DF for the interior girders in an I-girder bridge is S/5.5, which results in a DF=7.5/5.5=1.36. Therefore, the design moment due to live load for each of the three interior girders in the bridge is 1.36(582)=792 kip-ft. For exterior girders the DF is found by treating the slab as simply supported between girders and using statics.

The determination of the DF for different bridges has been a research topic for a number of studies. In general, the DF must be determined based on the largest stresses developed in a girder, and different DFs may have to be applied in calculating stresses due to bending moments, shears and torsional moments. AASHTO (1994) provides formulas for the calculation of the DFs for many different bridges.

The DF for composite box girder bridges specified in AASHTO is based upon work conducted by Mattock (1971) on simply supported straight bridges. Tests were conducted on a one-quarter scale model to simulate a two-lane, three girder prototype bridge with an 80 ft. span and HS20 truck loading. The tests were also simulated numerically using a computer program based upon folded-plate theory. The program was then used to study the behavior of a series of thirty-one composite box girder bridges with a wide range of spans. The study also considered the number of traffic lanes and the number of girders. Based on the investigation, the following equation was proposed to calculate the wheel distribution factor for straight box girder bridges

$$DF = 0.1 + 1.7\frac{N_L}{N_G} + \frac{0.85}{N_L}, \qquad (2.7)$$

in which,
DF = wheel load distribution factor,
$N_L = W_C/12$, reduced to the nearest whole number,
W_C = roadway width, ft, between curbs,
N_G = number of box girders, and $0.5 \le \frac{N_L}{N_G} \le 1.5$.

Equation 2.7 is derived based on investigations carried out on simply supported straight bridges. Analytical studies as well as experimental investigations on prestressed concrete bridges (Mattock and Kaar 1961, Mattock 1971) show that the lateral distribution of load in the negative moment region in a continuous bridge is the same as that occurring at the midspan. It was assumed that similar behavior exist for continuous box girder bridges, making Eq. 2.7 applicable for both the maximum positive and negative bending moments in box girder bridges. However, there is no experimental validation on the issue. Investigations on the behavior of continuous box girder bridges are therefore warranted. Results from field

and computational studies for the twin-box bridges with truck loading are presented in Chapter 7.

For curved bridges, Heins (1978) proposed an adjustment such that the wheel load distribution factor for bending moments in curved girders, DF_C, is calculated by

$$DF_C = (1440X^2 + 4.8X + 1)DF_S \ , \qquad (2.8)$$

where

DF_S = wheel load distribution factor for straight girders calculated by Eq. 2.7,
X = 1/R, R is the radius of the centerline of the bridge, ft.

This modification is usually small for most curved highway bridges. For example, the curved bridge studied in this project (Chapter 3) has a radius of approximately 900 ft. Equation 2.8 results in DF_c =1.007 DF_S , a 0.7% increase over the DF based on straight bridges due to the curvature. No other study was reported on the behavior of the lateral distribution of live loads in curved box girder bridges.

CHAPTER 3 FIELD MONITORING OF A CURVED BOX GIRDER BRIDGE DURING THE CONSTRUCTION

3.1 Introduction

This chapter presents the procedures and results of the field studies conducted during the construction of a curved steel box girder bridge. The objective of the field study was to measure the girder stresses and brace forces developed during construction. Results from the live load tests on the bridge will be discussed in Chapter 7. Results presented in this chapter will be further used and discussed in Chapter 4 for the computational study of the construction stage.

3.2 The Bridge and the Instrumentation

The bridge used for the field studies is a three-span-continuous unit of the interchange connecting the east bound lanes of North Beltway 8 to the north bound lanes of Interstate 45 in Houston, Texas as shown in Fig. 3.1. The bridge consists of two trapezoidal box girders with a composite concrete deck. The cross-section of the completed bridge is illustrated in Fig. 3.2. The spans and the radius along the centerline of the bridge are shown in Fig. 3.3. The spans of the individual girders (Girders I and E, I — Interior, E — Exterior) vary slightly from Fig. 3.3 due to the bridge curvature.

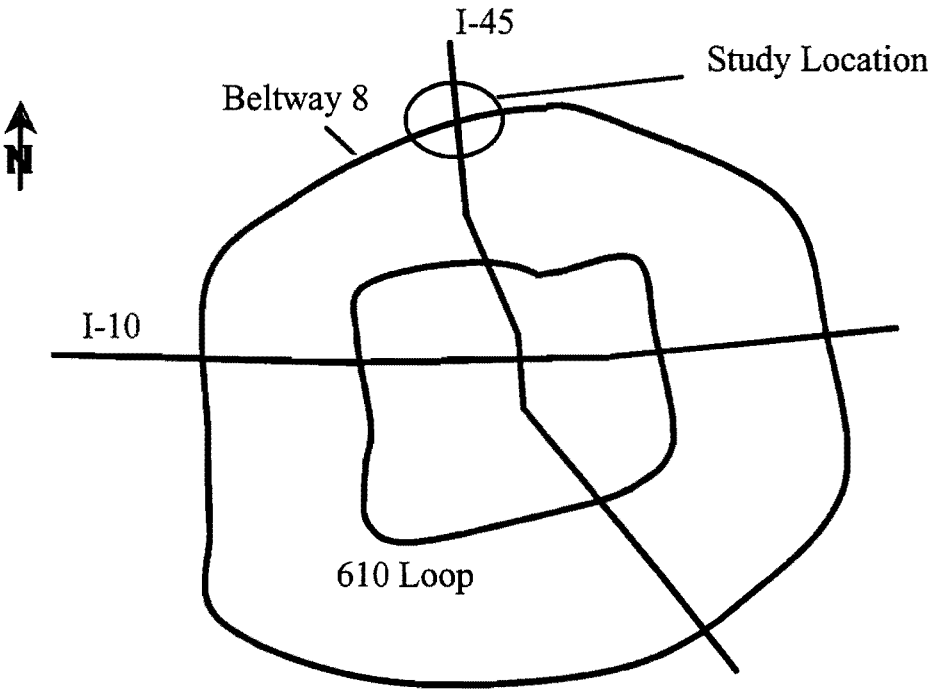

Figure 3.1. Location of the Field Studies

The steel trapezoidal girders are comprised of two top flanges, one bottom flange, and two inclined webs. The depth and box width of the U-shaped "tub" is usually uniform along the length of the bridge, as is illustrated in Fig. 3.2. However, the plate thickness and the top flange widths vary along the length. A top flange lateral truss as shown in Fig. 3.3 was provided along the length for both girders at approximately 11 inches below the top flanges. The large offset (11 inches) between the top flange and the lateral truss was due to the orientation of the WT-shape diagonals that had the stem on the top. If the stem is oriented on the bottom of the truss (downward), the connection to the girder can be placed closer to the top flanges. Solid diaphragms were provided at the supports, while internal cross-frames were spaced at approximately 20 ft. External diaphragms or cross-frames were provided at the supports.

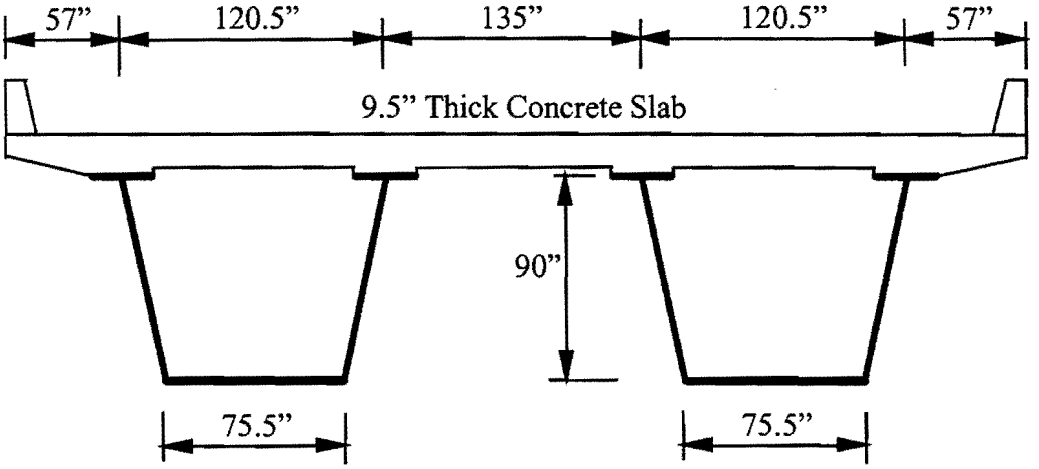

Figure 3.2. Cross-Section of the Box Girder Bridge

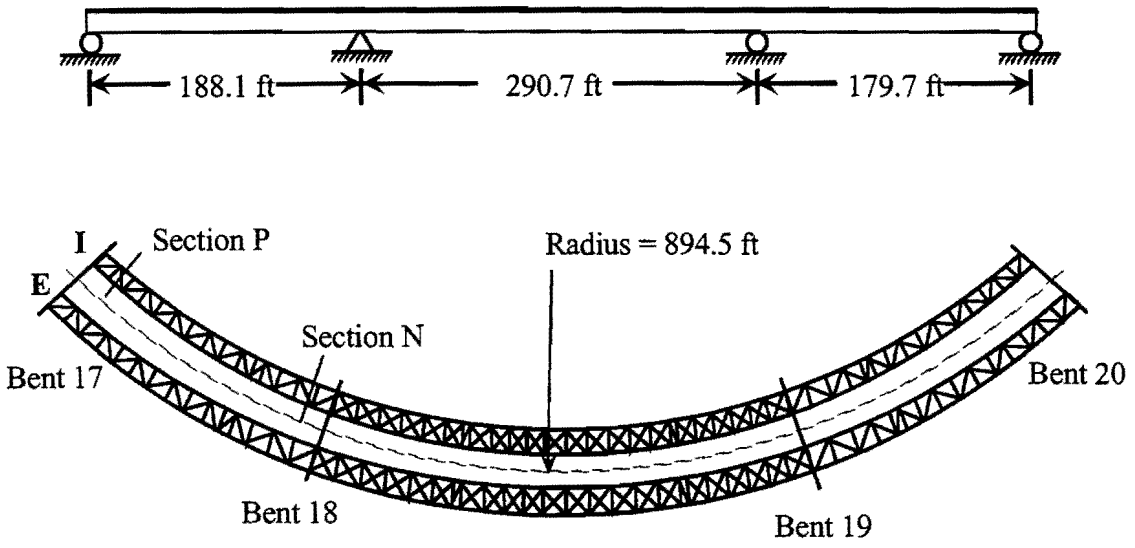

Figure 3.3. Spans and Radius of the Project Bridge

The individual box girders were fabricated in seven segments for transportation and erection purposes. The erection and splicing of the segments during the construction will be discussed later. The individual segments are numbered from 901 to 914. The lengths and self-weights of the segments are presented in Table 3.1.

Table 3.1. Length and Weight of the Girder Segments

Interior Girder (Girder I)			Exterior Girder (Girder E)		
Segment	Length (ft)	Weight (kips)	Segment	Length (ft)	Weight (kips)
901	111.85	88	902	114.61	90
903	117.48	188.6	904	120.23	192.6
905	48.79	51.8	906	49.68	52.8
907	106.23	135.8	908	109.12	138.6
909	46.00	49.4	910	47.08	50.2
911	117.52	188	912	120.25	192
913	104.50	86.4	914	106.74	88.2
Total	652.37	788	Total	667.71	804.4

The interior girder (Girder I in Fig. 3.3) was instrumented at two locations that were labeled Section P and Section N in the figure, representing the positive and negative moment regions and located in Segment 901 and 903, respectively. The location of the two cross-sections are shown in Fig. 3.4, and the top flange width and the plate thickness of the sections are given in Table 3.2. The instrumentation was installed in December of 1995 when the girders were on the ground approximately one mile from the bridge location. A lateral strut and diagonal bracing member in the top lateral truss system was also instrumented for each of the sections. The member size for the struts and diagonals are given in Table 3.2. Strain gages were installed at the middle of the length of these bracing members to minimize localized stress effects near the ends (Fig. 3.4).

The strain gages were monitored with a data acquisition system contained within the box girder. Fig. 3.5 illustrates the components of the data acquisition system as well as their connectivity. Data were recorded and stored in a Campbell Scientific 21X Data Logger. The 21X has 8 channels for data recording, however, the number of channels was expanded to 80 with the use of five multiplexors to which the gages were wired. A total of 16 gages were wired to each multiplexor. Each channel corresponds to a foil gage, and was labeled by a letter (representing the multiplexor the gage was wired to) and a number between 1 and 16 (representing the channel for the gage in the multiplexor). A modem with a cellular phone link was incorporated to allow remote data retrieval. The frequency of channel scanning was programmed and the data was downloaded on a remote computer. A 12 Volt automobile/marine battery that was recharged by two solar panels powered the data acquisition system.

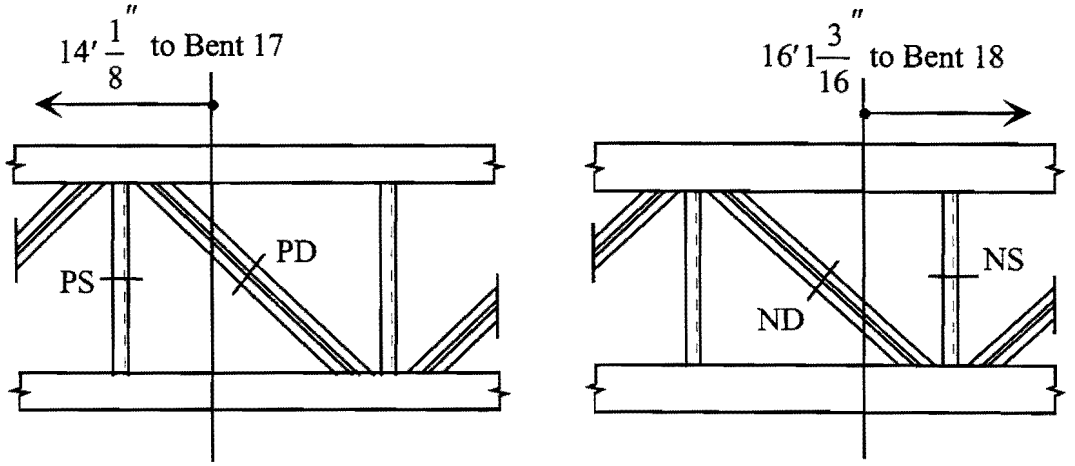

Figure 3.4. Location of the Instrumented Cross-Sections

Table 3.2. Dimension of the Instrumented Cross-Sections

	Section P	Section N
Top Flange Width	12″	30″
Top Flange Thickness	0.75″	2.875″
Web Thickness	0.625″	0.875″
Bottom Flange Thickness	0.75″	2.75″
Longitudinal Stiffener	none	ST 10×48
Instrumented Diagonal	WT 7×34	WT 7×34
Instrumented Lateral Strut	L 5×5×3/8	L 5×5×3/8

Three different types of strain gages were used in the study: foil gages, one-sided gages, and 45° foil rosettes. Two channels were required for each one-sided gage and three for a rosette. Enough gages were installed on the girder, longitudinal stiffener, and the top flange lateral truss to give a good measurement of the stress distribution during erection, construction, and subsequent live loading. Problems were encountered with the one-sided gages since they were not temperature compensated. These gages were replaced with foil gages following the girder erection. The locations and channels of the strain gages will be presented later along with the corresponding results.

Since the instrumentation would be exposed to the elements for a long period of time, weather protection was an important aspect of the instrumentation. A two-part protection system was used for the gages. A microcrystalline wax was melted and applied to the gages, followed by a silicon coating. During installation of the instrumentation 1 to 2 inches of water was encountered in the bottom of the box. Although the water was removed, there was concern that the gages on the bottom flange might be submerged and compromise the wax and silicone moisture bearer. Therefore, gages on the bottom flange were also protected with PVC pipe caps and a silicone seal.

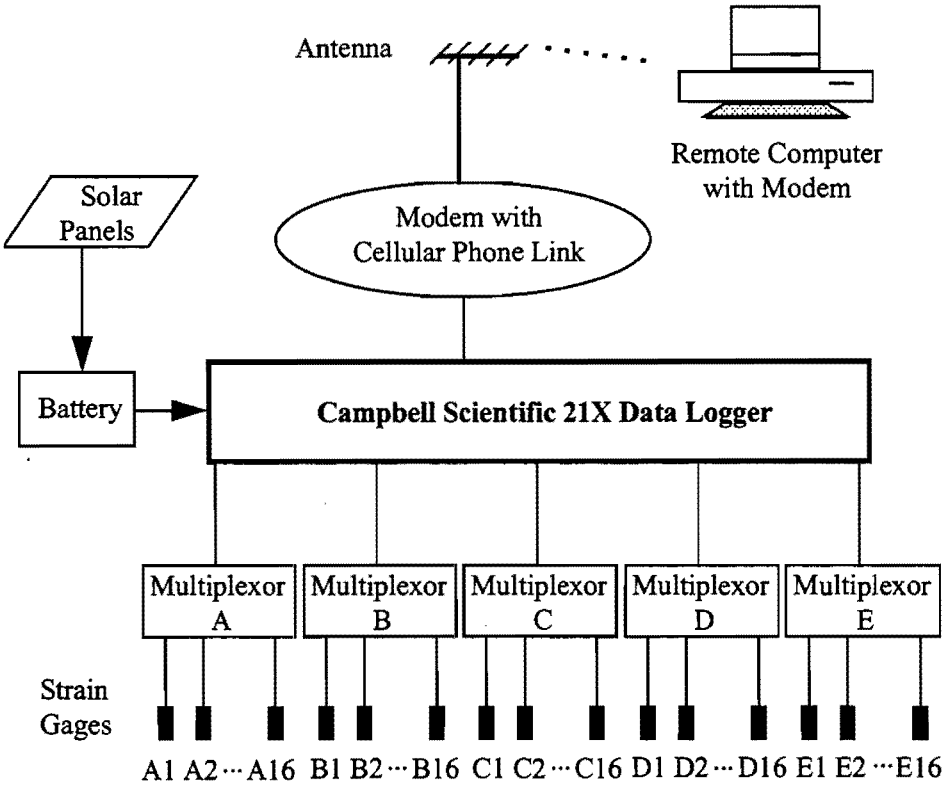

Figure 3.5. The Data Acquisition System

The instrumentation was installed in December of 1995 and was kept in place until October of 1997. Although data were routinely collected throughout this time, the following key dates were milestones in the field measurements.

December 1995 — Instrumentation installed at location remote from the bridge site.
Mid-January 1996 — Girders moved to bridge site.
Mid-January - February 1996 — Girder erection.
August 1996 — Installation of metal deck forms and rebar for concrete deck.
September 1996 — Construction of the concrete bridge deck.
April 1997 — Live load testing of the bridge.
June 1997 — Bridge open to traffic.
October 21, 1997 — Instrumentation removed.

3.3 Field Study During Bridge Construction

3.3.1 Construction of the Bridge Superstructure

The construction of the bridge superstructure (the girders and the slab system) was conducted after the concrete piers were completed and bearings were placed on the pier caps. During the erection of the steel girders and the construction of the concrete slab, the roadway

underneath the bridge (I-45) was closed to traffic for safety reasons. To minimize traffic delays, girder erection and slab construction were typically performed between the hours of 10 pm and 5 am.

Erection of many of the girder segments required two cranes due to load restrictions and lifting stability. Once the girders were lifted into place, bolted splices were performed in the air while the cranes held the girders. The erection started from the external spans and ended in the middle with segment 907 and 908 the last segments being connected for the interior and exterior girders, respectively. Figure 3.6 demonstrates the erection sequence for the interior girder I. The first step was the erection and splicing of segment 901 and 903, as well as segment 913 and 911 (Fig. 3.6a). These segments formed two simply supported beams that cantilevered into the middle span. Segment 905 and 909 were then added to the cantilevers in Step 2 (Fig. 3.6b). Segment 907 was a drop-in segment to complete the continuous girder (Fig. 3.6c). The erection sequence for the exterior girder was similar to the interior girder. As introduced earlier, the instrumentation for the field measurement was installed on Segment 901 and 903.

The weight of the concrete slab was the largest load that the girders were subjected to during the construction of the bridge. There were a number of problems that occurred during girder erection that raised concerns by TxDOT engineers and the bridge contractor. Researchers on the project as well as outside consultants were asked to check the safety of the bridge during slab construction. The girder stress levels and brace forces during the slab construction were examined using the refined FEA models, which were developed in this project and will be discussed in the next chapter. As a result of the review of the slab construction, the initial plan of concrete casting was modified and the external cross-frames between the girders at supports were retrofitted.

The slab construction was delayed more than six months after the girders were erected due to the review and modification on the initial construction plan. During this period the metal deck forms were placed on the box girders, as well as the reinforcing steel. Construction of the concrete bridge deck was divided into three stages, as shown in Fig. 3.7, all conducted in September of 1996. Concrete was delivered by trucks and pumped to the deck forms, and was spread and flattened by a screed which moved along temporary rails installed outside the edges of the deck. The parapets were added in April of 1997. Live load testing was conducted on April 24, 1997, before the bridge was opened to traffic in June of 1997.

3.3.2 Field Measurement and Data Processing

The stress readings for all major construction activities were recorded. Section N in Segment 903 was monitored during erection while strain gages on Section P in 901 had to be disconnected. However, the initial support conditions of Segment 903 when it was laid on the ground is unclear, which makes the loading condition difficult to define. Therefore, for the

girder erection phase, only the data corresponding to the connection of Segment 905 and 907 (Fig. 3.6b and 3.6c) will be presented in next section. For the slab construction phase, data for all three stages shown in Fig. 3.7 will be processed and presented in Section 3.4.

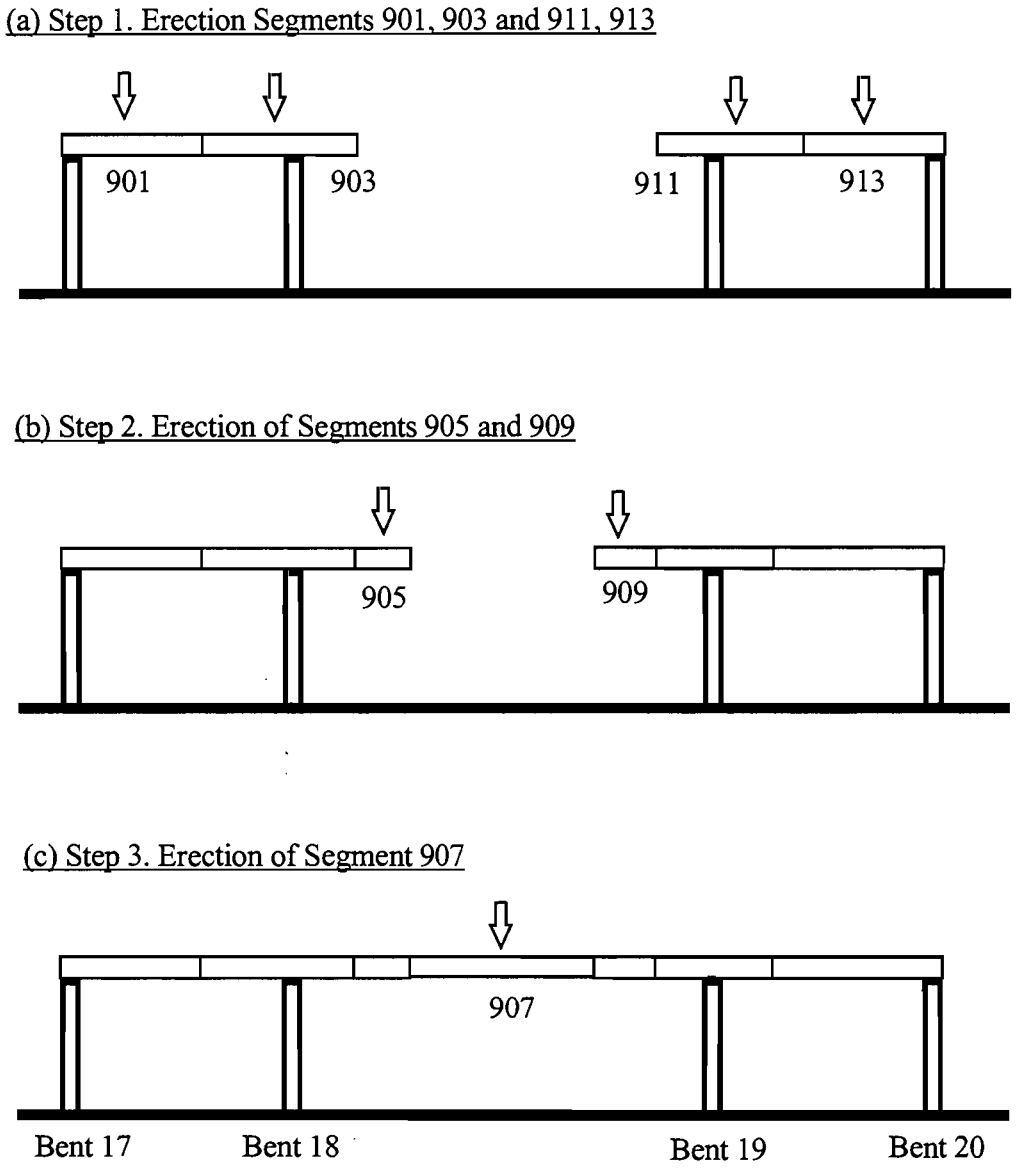

Figure 3.6. Erection Sequence of the Interior Girder

The entire construction procedure was closely monitored, and the times for all major construction activities were manually recorded. The 21X system was programmed to take a reading every hour during most of the construction process. To find the stress changes due to construction activity, the data for a 24-hour period during which the work was performed was closed analyzed. The readings were converted to stresses using the gage parameters and

the stress increases were graphed as a function of time (all curves start at zero). If evidential and abrupt stress changes were observed from the plotted curves at the construction time, the stress differences before and after the construction were considered to be the stress due to the applied loads. These 24-hour stress development graphs will be presented and discussed in the following sections.

(a) Stage 1: 9/14/96, Saturday, started at ~ 18:00

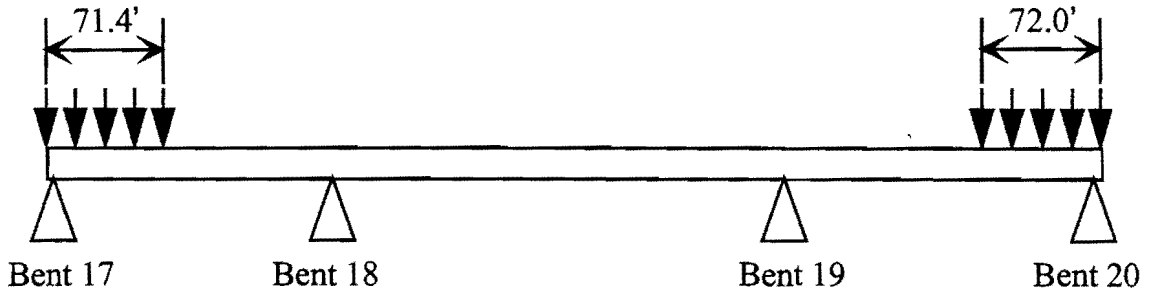

(b) Stage 2: 9/17/96, Tuesday, started at ~ 22:00

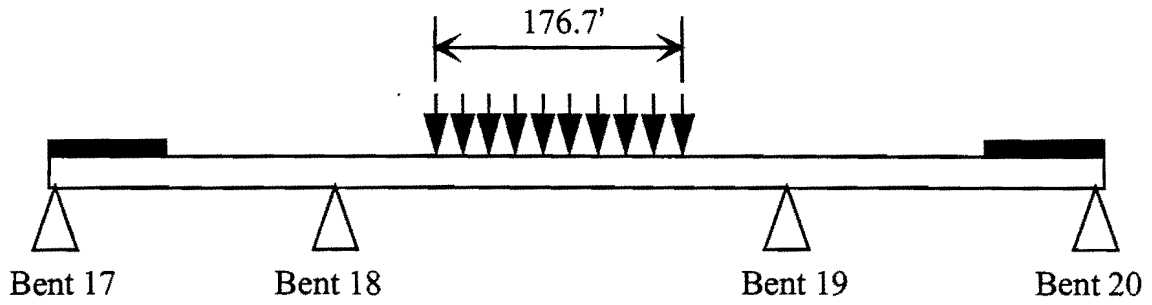

(c) Stage 3: 9/21/96, Saturday, started at ~ 22:00

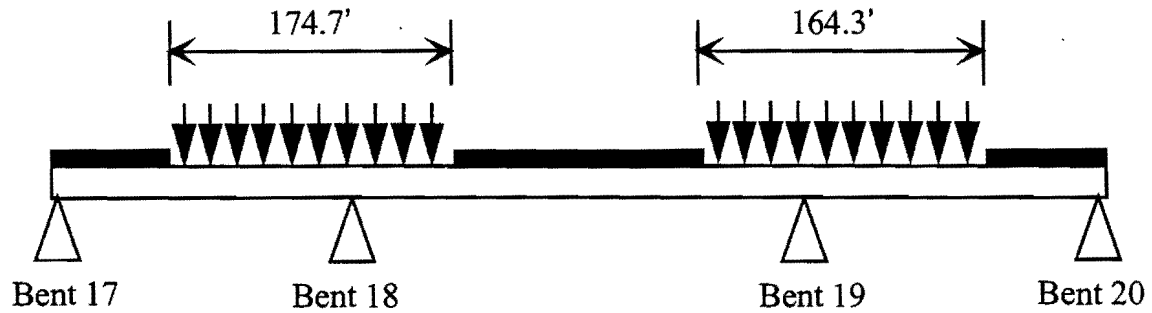

Figure 3.7. Construction Sequence of the Concrete Slab

Although the foil gages that were used were compensated for temperature, three-dimensional thermal gradients and indeterminate restraints of the plates in the cross-section caused daily strain gage fluctuations due to temperature changes. The effect of temperature is not the focus of this report and has discussed by Lopez (1999). However, the stress changes caused by applied loads had to be separated from the recorded data, which included combined results due to both the temperature change and the applied loads. In addition to the strain gages, two thermal couples were also installed inside the instrumentation box to record the temperature changes during the construction. The elimination of the temperature effect was accomplished by analyzing both the stress and temperature data in the days leading up to the construction activity. Once the time interval was determined for a construction activity, the difference of the data in the same time interval on the previous two days were used to approximate the temperature effect during the construction using linear interpolation or extrapolation. Although this approach worked for many of the gages, in some instances changes in gage readings due to the applied loads were too small to be distinguished from the temperature effects. The determination of the time interval corresponding to each construction activity will be discussed in the following sections of this chapter, while the elimination of the temperature effects are presented in Appendix A. All readings of the strain gages have been transferred into stresses in the units of kips/in^2 (ksi).

The results presented in this section include longitudinal stresses in the girder flanges and webs, the longitudinal stiffener, and the bracing members. For bracing members, however, the stress results at the strain gage locations should be converted to the stress resultants, mainly the internal axial forces. An algorithm based on a three-dimensional linear regression method was developed for this purpose. The procedure is presented in Appendix B. In the next two sections, both the stress and the axial force results are presented for bracing members during the construction, along with the stresses in the girder flanges and webs.

3.4 Stress Changes During Girder Erection

As mentioned earlier, one-sided gages were initially installed on the bottom flanges and the webs of the girder. The one-sided gages are ideal for plates, since the gages provide a measure of the axial strains and out-of-plane bending in the member that they are installed upon. Although the gages are not compensated for temperature, researchers on the investigation felt that the gages would still provide meaningful data for the short time interval during a construction procedure. Data during girder erection, however, indicated that the gages were unstable for even small temperature changes. Therefore, all one-sided gages were replaced with foil gages prior to construction of the concrete slab. The results presented in this section only include stress changes due to the erection of Segment 905 and 907 in the top flanges, longitudinal stiffener and bracing members, all of which were installed with foil gages from the beginning of the instrumentation. Figure 3.8 shows the location of the strain gages from which the readings are presented and discussed in this section.

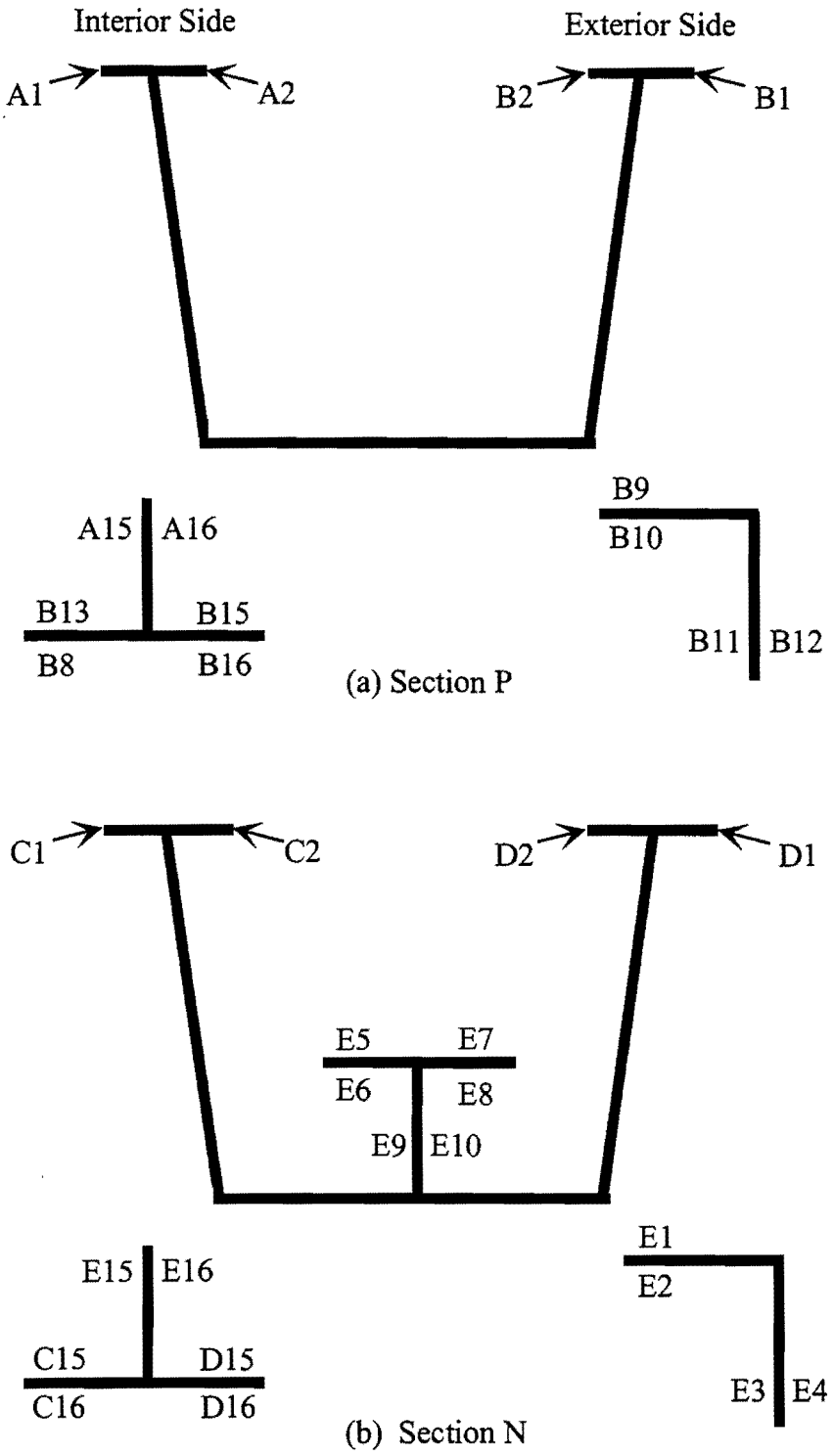

Figure 3.8. Strain Gages Used in Monitoring Girder Erection

3.4.1 Erection of Segment 905

Segment 901 and 903 were lifted onto piers in the first step of the girder erection and formed a statically determinant simple beam with an overhang. The erection of Segment 905 extended the overhang and added the gravity load of the segment to the cantilever (Fig. 3.6b).

The erection and splicing of Segment 905 was conducted between 22:00 and 23:00 on January 9, 1996. Figure 3.9 is a graph of the stress changes in the 24-hour period starting from 17:00 for the gages on the top flanges of Section P. The stress readings have an obvious increase between 22:00 and 23:00, during which the splicing was completed and the segment was released from the cranes. Similar increases can be observed in the same period of time in the top flanges at Section N (Fig. 3.10).

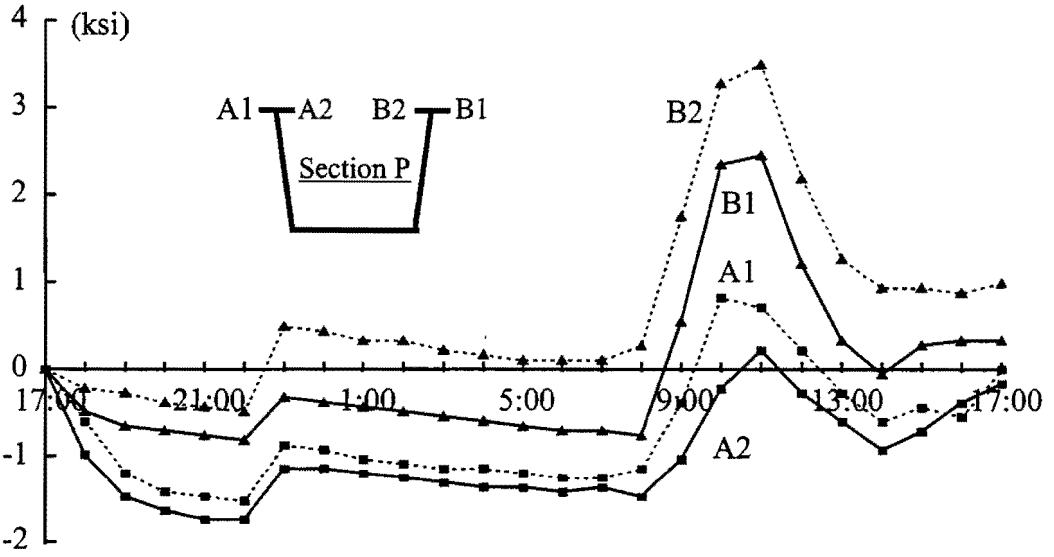

Figure 3.9. Stress Development in the Erection of Segment 905 (Section P, Top Flanges)

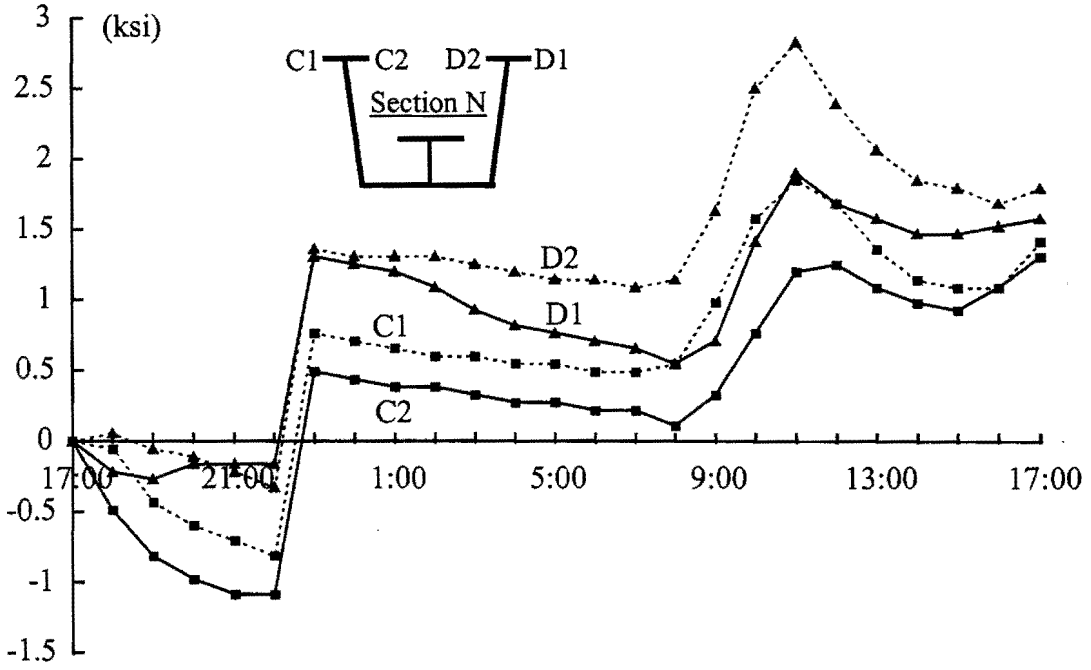

Figure 3.10. Stress Development in the Erection of Segment 905 (Section N, Top Flanges)

Figure 3.11 is a graph of the stress results for strain gages on the longitudinal stiffener at Section N. The abrupt stress change between 22:00 and 23:00 is consistent with what was observed for top flanges, however since the stiffener is below the neutral axis, the stress change is negative. The behavior of Gage E7 is the graph is difficult to explain. After Segment 905 was released at 23:00, the gage continued to experience a stress change until the following morning, and then gradually returned to a level consistent with the other gages. Data on the days prior to the erection of Segment 905 were checked and a similar behavior was observed for Gage E7. This behavior is similar to that observed in the one-sided gages that were affected by temperature. This might be the case because the wires of a gage could have been hooked up to a wrong channel. In order to avoid this possibility later in studying the slab construction, all gages were double checked later to guarantee that the correct records be made for the channel numbers and the corresponding gages. Nonetheless, the amount of increase between 22:00 to 23:00 was close to those in other gages on the longitudinal stiffener.

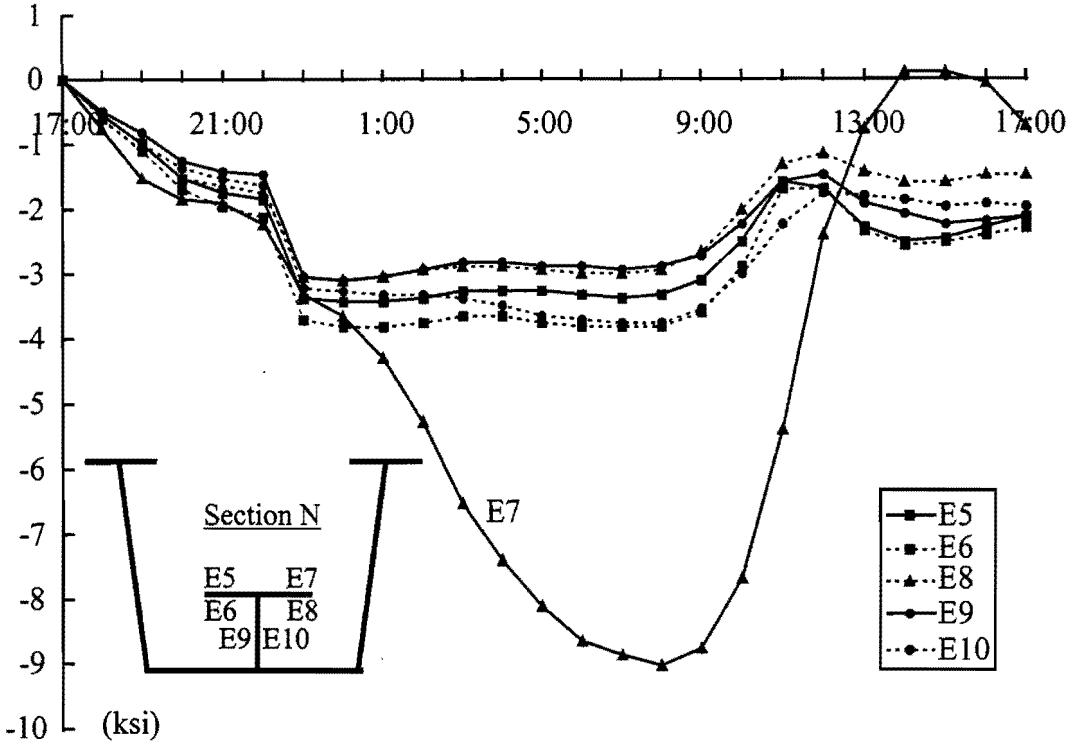

Figure 3.11. Stress Development in the Erection of Segment 905 (Section N, Longitudinal Stiffener)

Stresses in the bracing members at Section P due to the weight of Segment 905 were too small to be identified from the graphs in Figs. 3.12 and 3.13. There is no obvious change before and after the segment was released. However, at Section N the bracing members experienced significant increase between 22:00 and 23:00 (Figs. 3.14 and 3.15), with the maximum incremental stress as high as 5 ksi. A behavior similar to Gage E7 was observed for Gage D15 as shown Fig. 3.14. Channel D15 may have been wired to a one-sided gage and the connectivity was not correctly recorded. The results from Channel D15 were therefore not used in deriving the brace forces during the girder erection.

The graphs shown in Figs. 3.9 to 3.15 reasonably reflect the construction activity. With the exception of the bracing members at Section P, most of the graphs demonstrate distinct changes in stresses at times consistent with the release of the added segment. The differences between the stresses at 22:00 and at 23:00 are then considered as the stresses caused by the addition of Segment 905 to the girder. The temperature effect was accounted for by using the data in the previous two days, which is presented in Appendix A. As a result, the stress increases due to the applied loads for individual gages are presented at the corresponding locations in Fig. 3.16. The axial forces in the diagonals and struts were determined as outlined in Appendix B. At Section N, the forces in the diagonal was 38.8 kips while the strut force was -2.55 kips (compression).

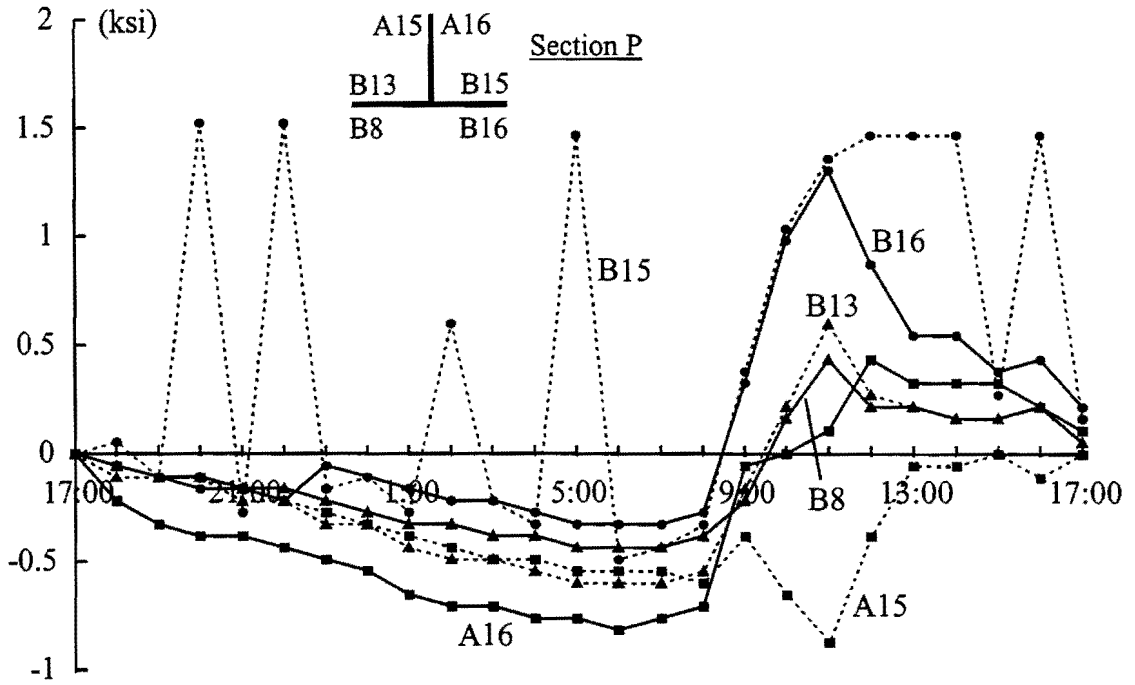

Figure 3.12. Stress Development in the Erection of Segment 905 (Section P, the Diagonal)

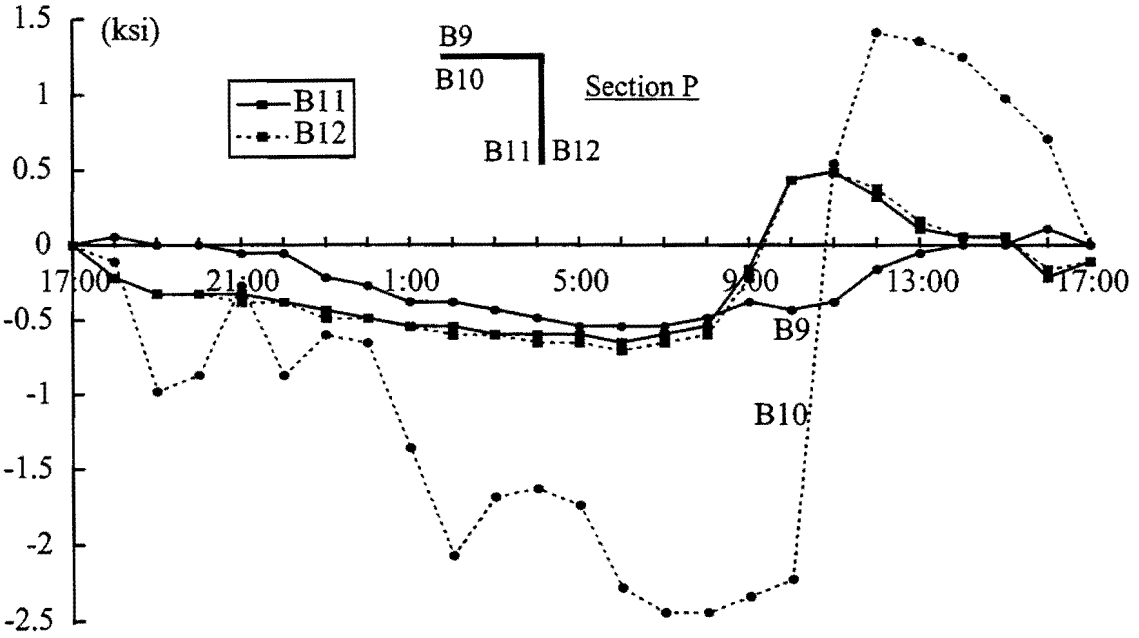

Figure 3.13. Stress Development in the Erection of Segment 905 (Section P, the Strut)

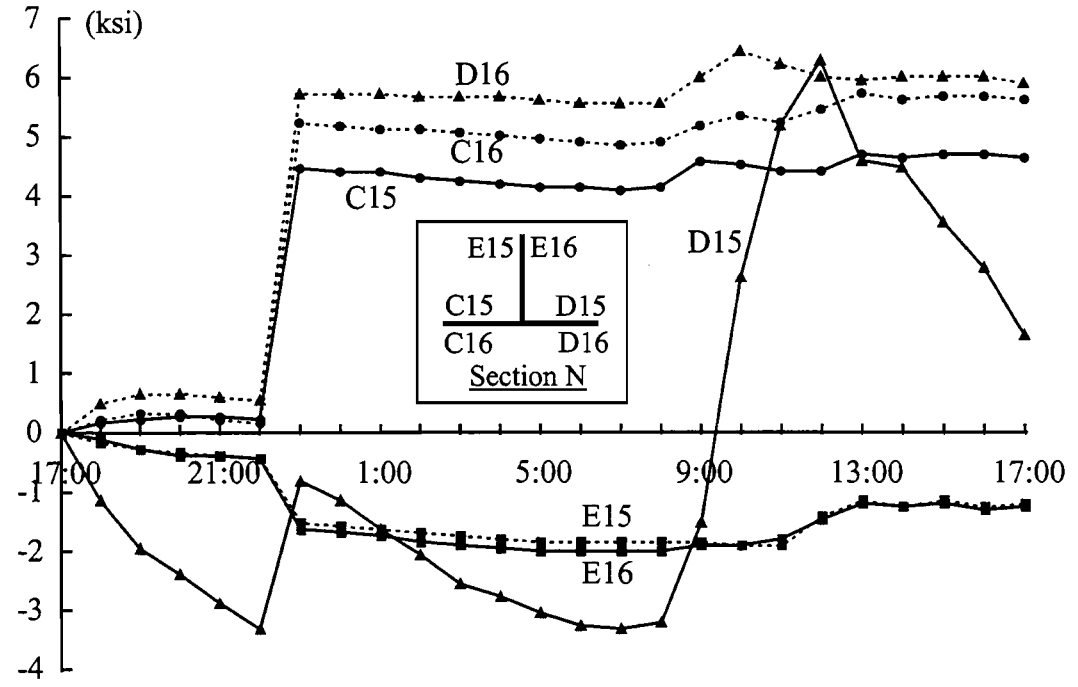

Figure 3.14. Stress Development in the Erection of Segment 905 (Section N, the Diagonal)

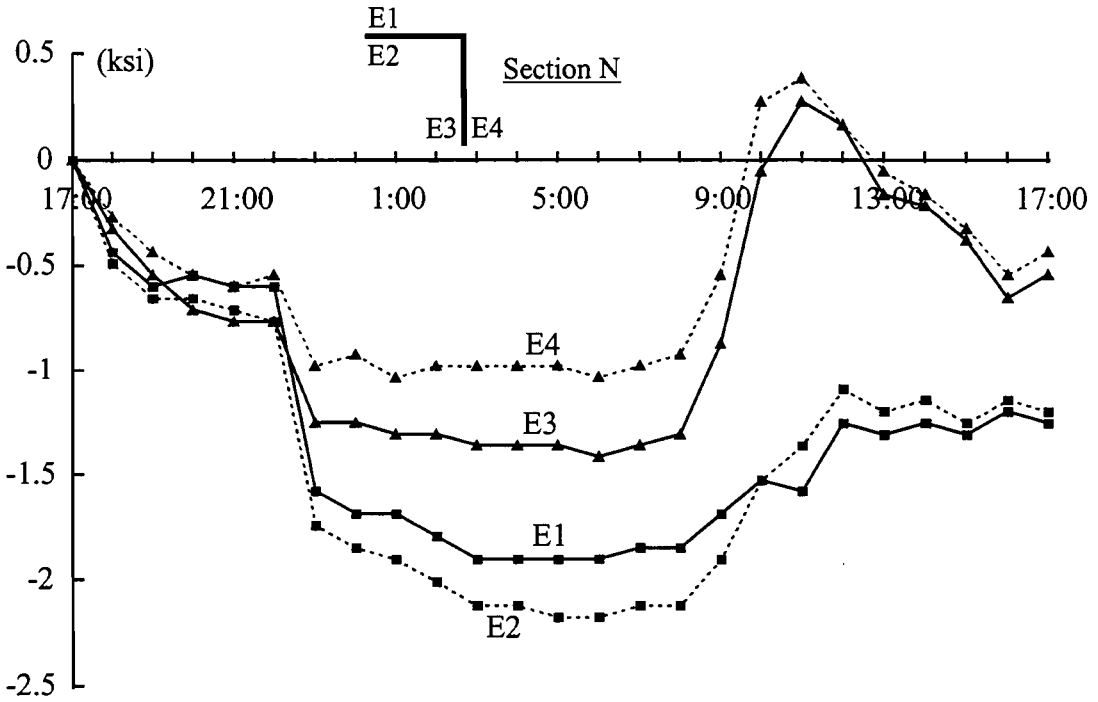

Figure 3.15. Stress Development in the Erection of Segment 905 (Section N, the Strut)

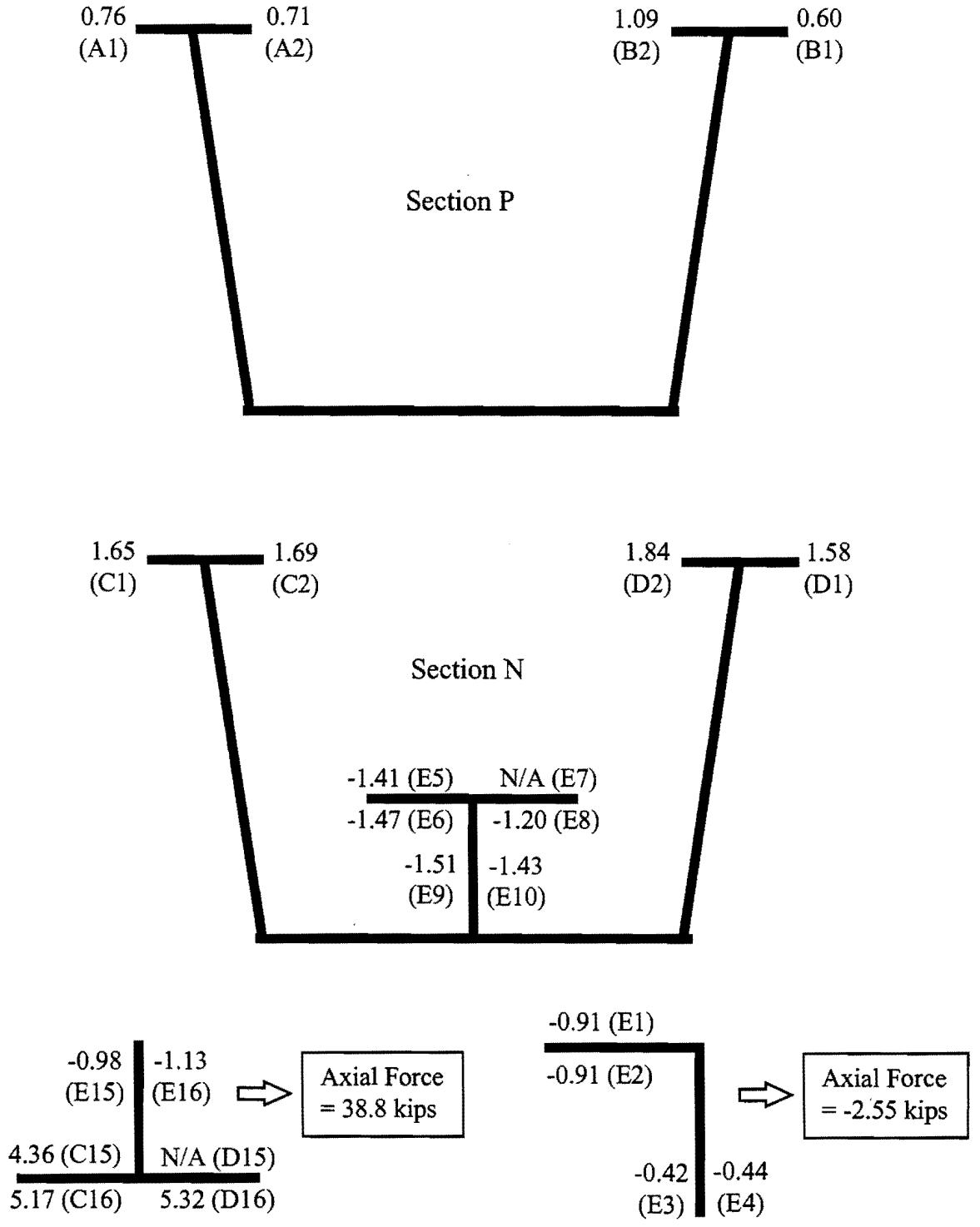

Figure 3.16. Stress Changes Measured During the Erection of Segment 905 (between 22:00, 1/9/96 and 23:00, 1/9/96)

3.4.2 Erection of Segment 907

Segment 907 completed the continuity of the interior girder, as shown previously in Fig. 3.6c. The erection and splicing of Segment 907 were conducted between 22:00, February 11 and 03:00, February 12, 1996. However, it was not until midnight of February 16 that the segment was fully released from the cranes. Therefore, although the girder was subjected to a portion of the loads during splicing, the majority of the gravity load of the segment was applied on February 16.

Figure 3.17 is the stress development in the interior top flange of Section N between February 9 and February 20, 1996. In addition to the oscillation of stress readings caused by temperature changes, significant stress increases can be observed at the earlier morning of February 12, when the Segment 907 was connected, and the midnight of February 15, when the crane support was removed. Similar to the discussion for Segment 905, the stress increases under the gravity load of Segment 907 were calculated as the differences of the stress readings before and after the segment was connected to the girder. Attempts were made to keep the temperature effects as small as possible. Times that the stresses were compared were carefully selected to account for temperature effect. Because of the addition of new structural components, the restraint conditions may change during the construction, resulting in different temperature effects for different construction activities. Therefore, temperature effect for each of the construction activities was accounted for using the data in the days leading up to the corresponding activity.

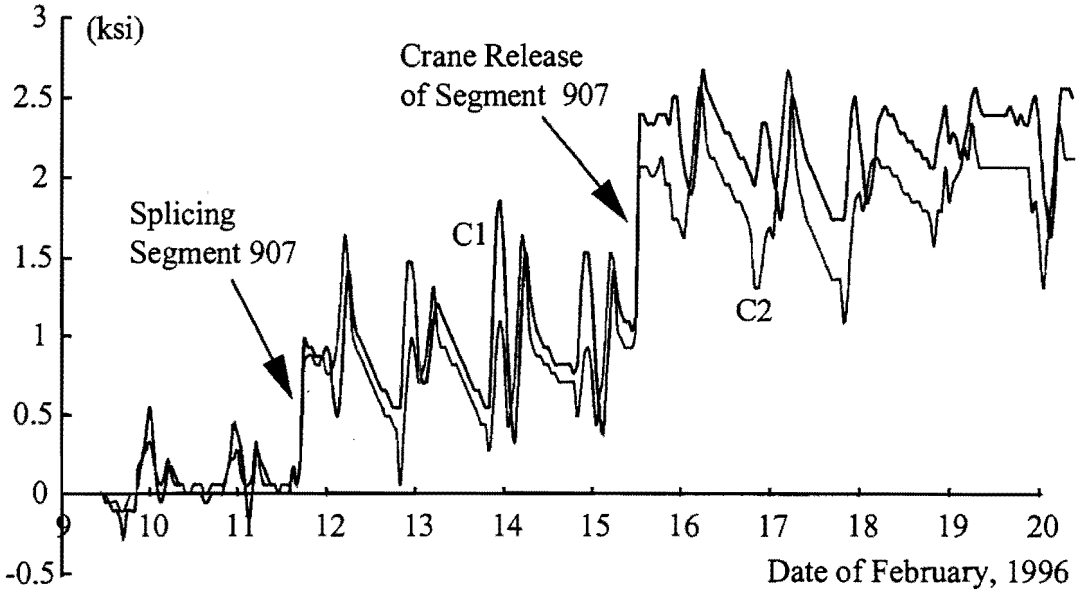

Figure 3.17. Stress Development in the Interior Top Flange of Section N

To minimize the effect of temperature, a two-step scheme was applied to the data in determining the stresses induced by the weight of Segment 907. First, the difference of the readings before and after the activities in the late nights of both February 11 and February 15 were calculated independently. These two differences were then added together as the desired stress results. Temperature effects was eliminated in each of the two steps using the data in the days leading up to each step, which is discussed in Appendix A.

The stress developments in the 24-hour periods that include the nighttime of both February 11 and 15 are plotted in Figs. 3.18 to 3.24. Most curves clearly show some abrupt stress changes corresponding to the construction activities. Gages E7 and D15 again responded to temperature changes poorly as shown in Figs. 3.21 and 3.22, however, stress changes due to the applied loads were exhibited for both gages. During splicing, the exterior top flanges at both Sections P and N experienced the largest increases and then returned to the same levels of the interior top flanges (Figs. 3.18a and 3.21a). This phenomenon was not observed from the stress development in the same time interval on the days before the splicing and may have been caused by forces applied on the girder during the construction.

Based on the consistency between the construction times and the distinct stresses changes in curves presented in Figs. 3.18 to 3.24, it is determined that for the date of February 12, the time interval used to evaluate the stress differences is 03:00 to 07:00, and for February 16, 00:00 to 01:00. Temperature effects were accounted for using the additional data on February 10, 11 and 14, 15, as presented in Appendix A. The total stresses caused by the weight of Segment 907 are considered to be the sum of these two increments. The results are presented at the gage locations in Fig. 3.25.

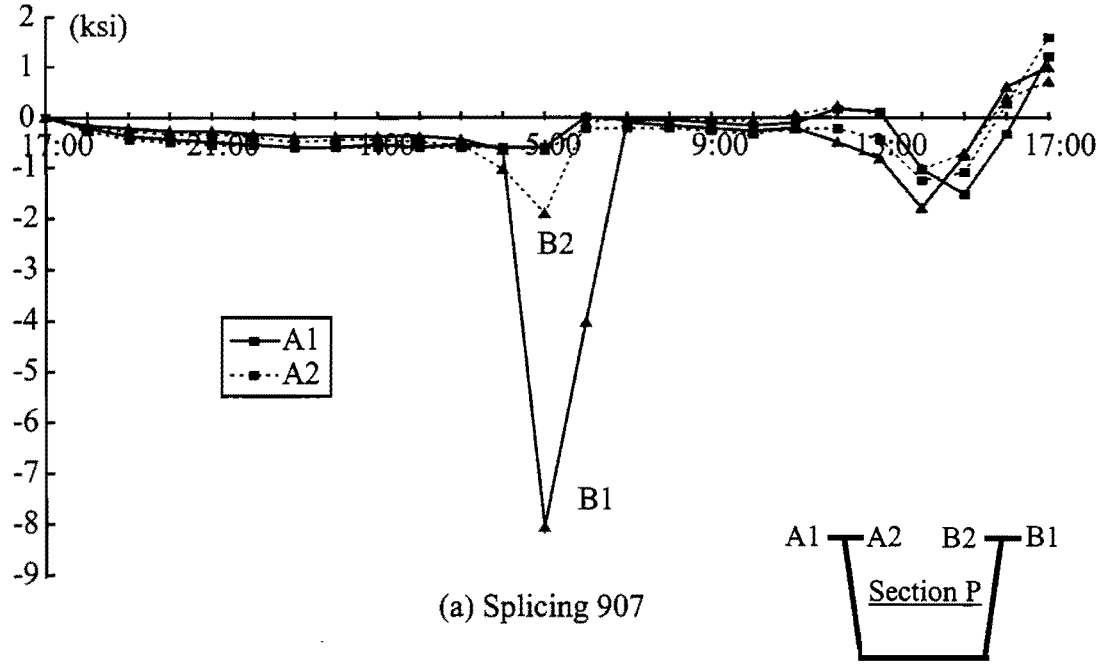

(a) Splicing 907

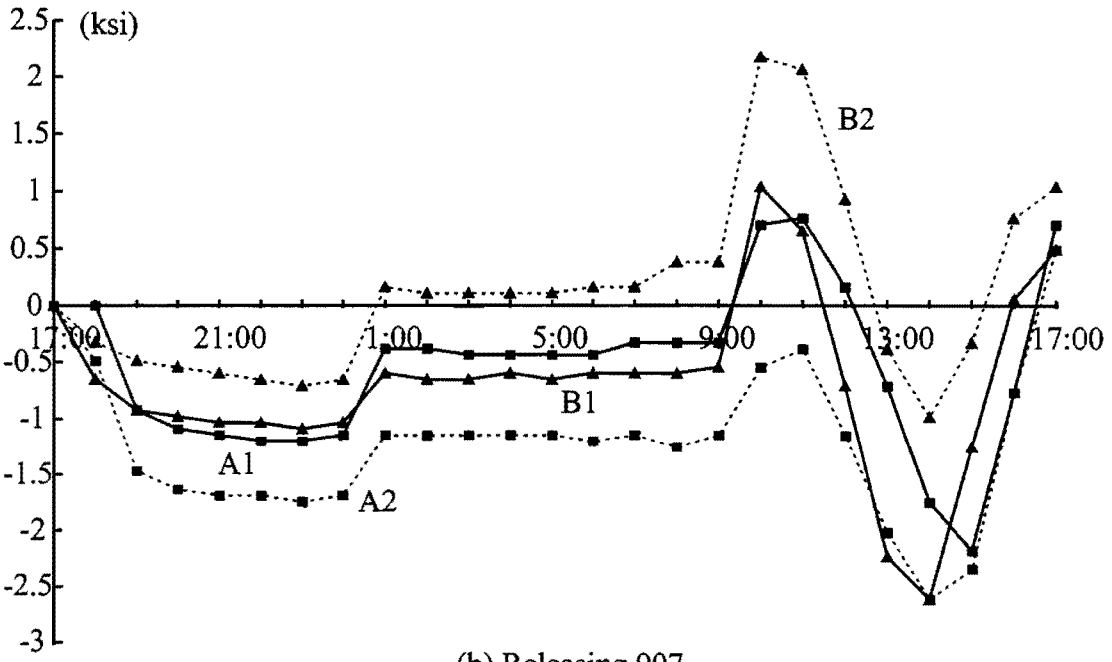

(b) Releasing 907

Figure 3.18. Stress Development in the Erection of Segment 907 (Section P, Top Flanges)

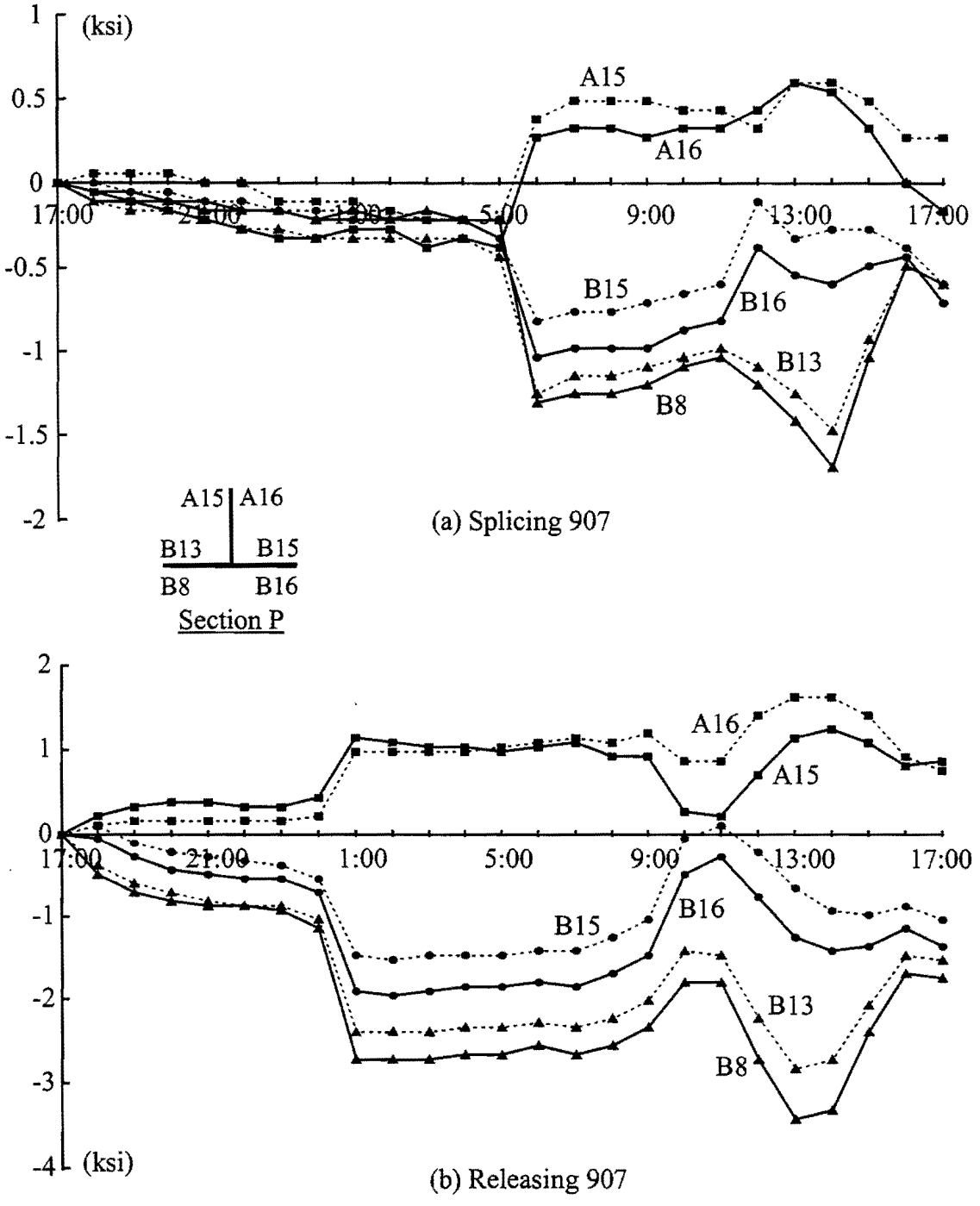

Figure 3.19. Stress Development in the Erection of Segment 907 (Section P, the Diagonal)

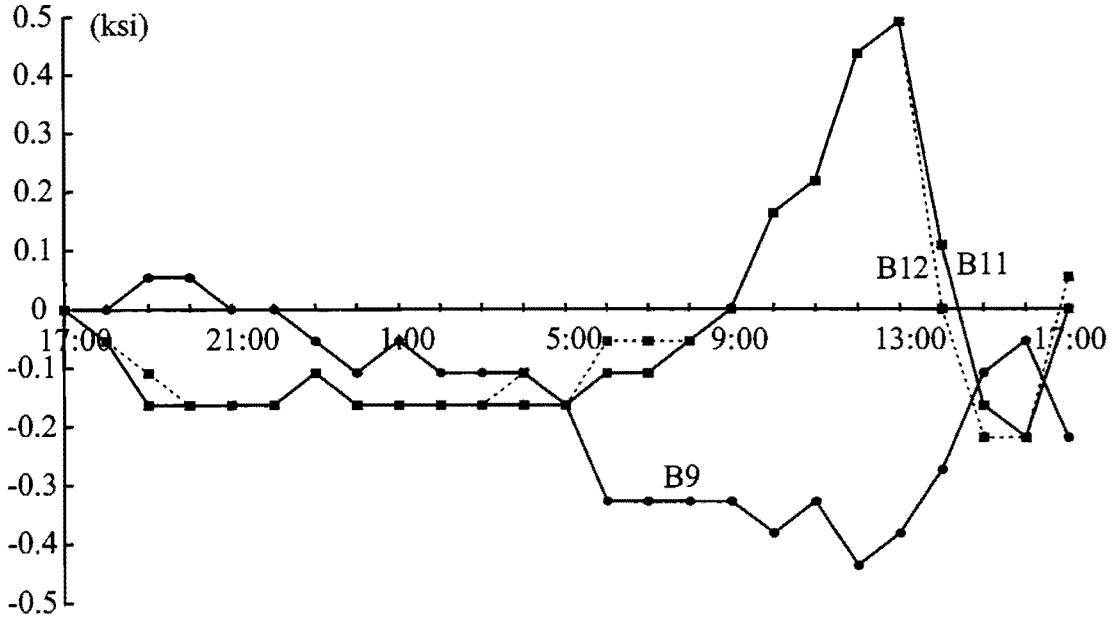

(a) Splicing 907

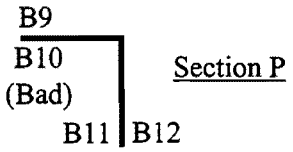

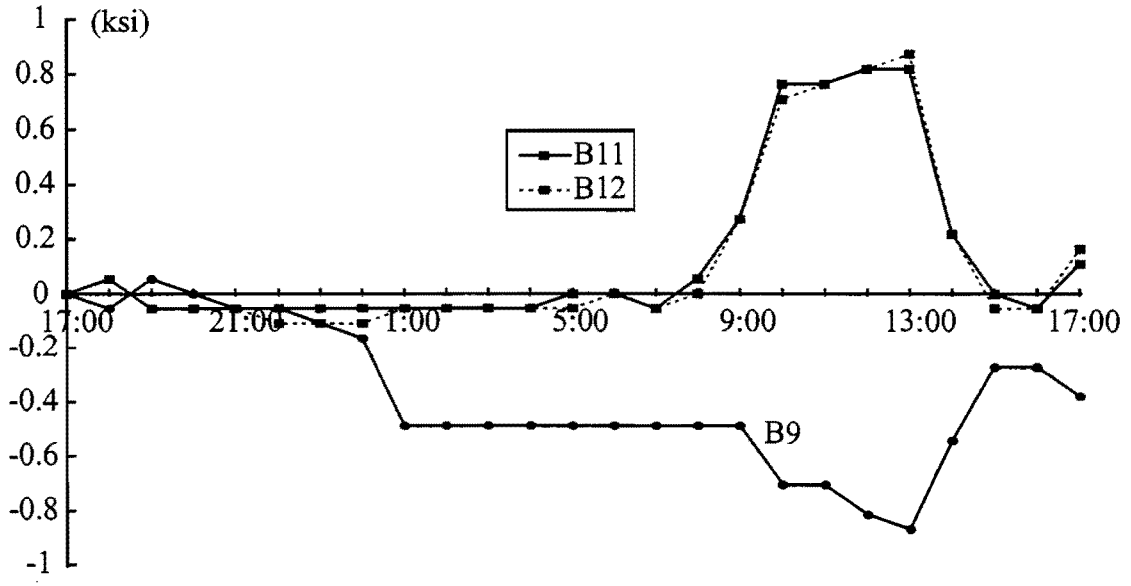

(b) Releasing 907

Figure 3.20. Stress Development in the Erection of Segment 907 (Section P, the Strut)

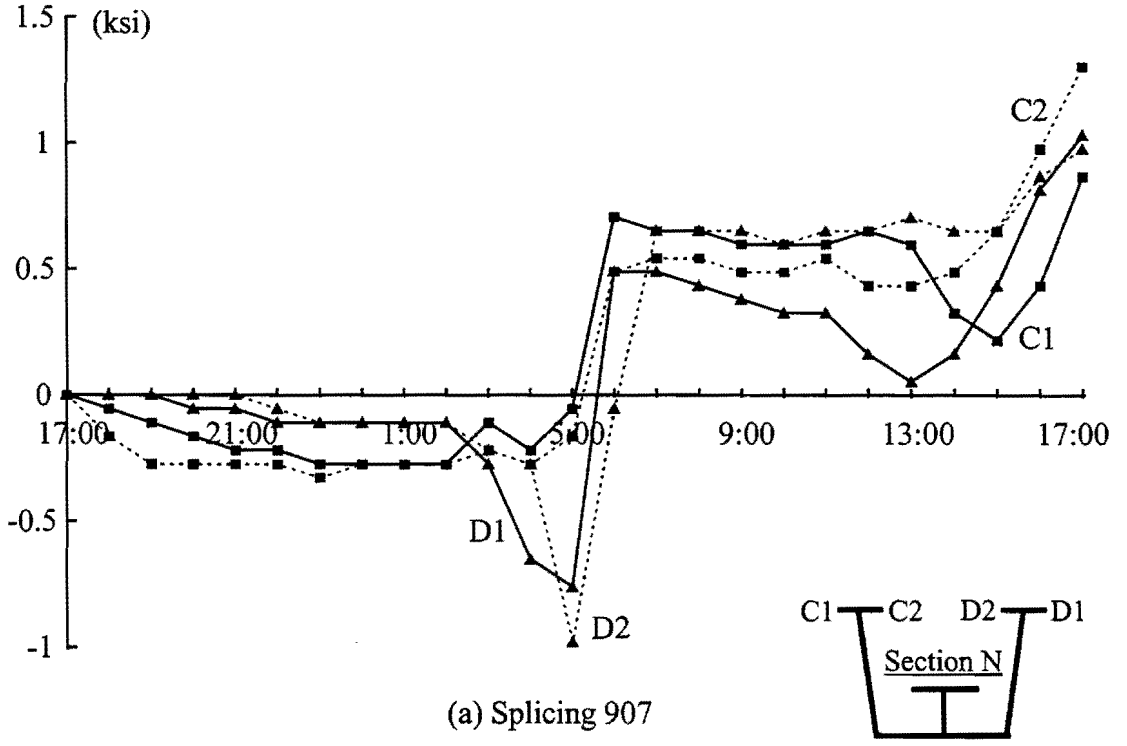

(a) Splicing 907

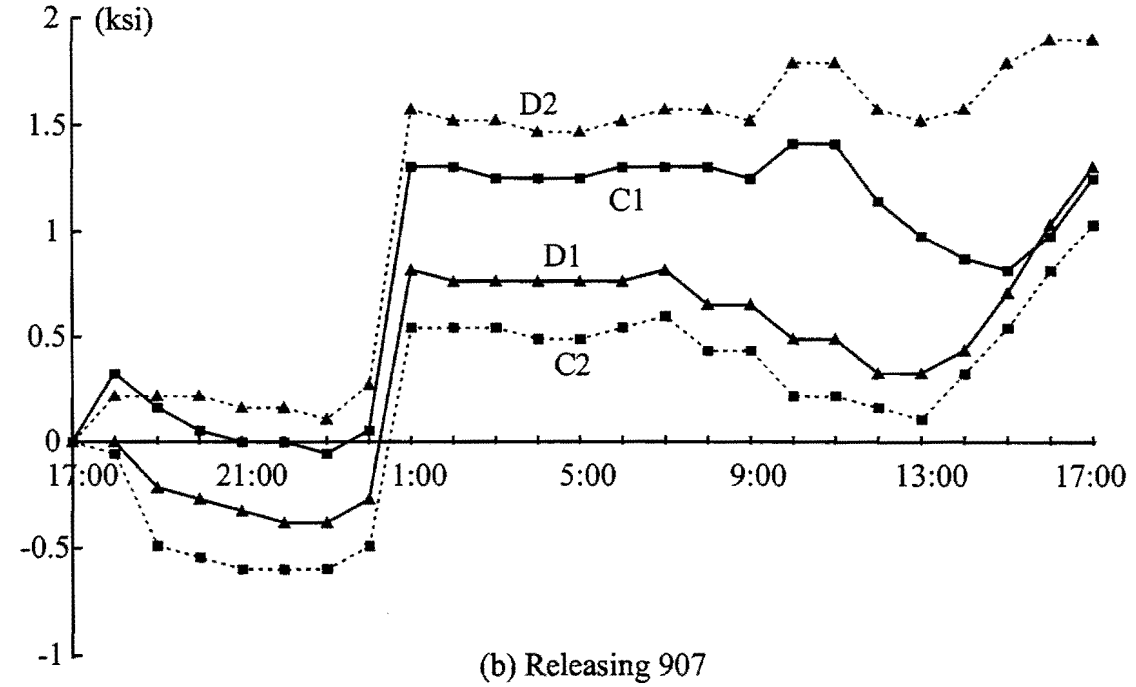

(b) Releasing 907

Figure 3.21. Stress Development in the Erection of Segment 907 (Section N, Top Flanges)

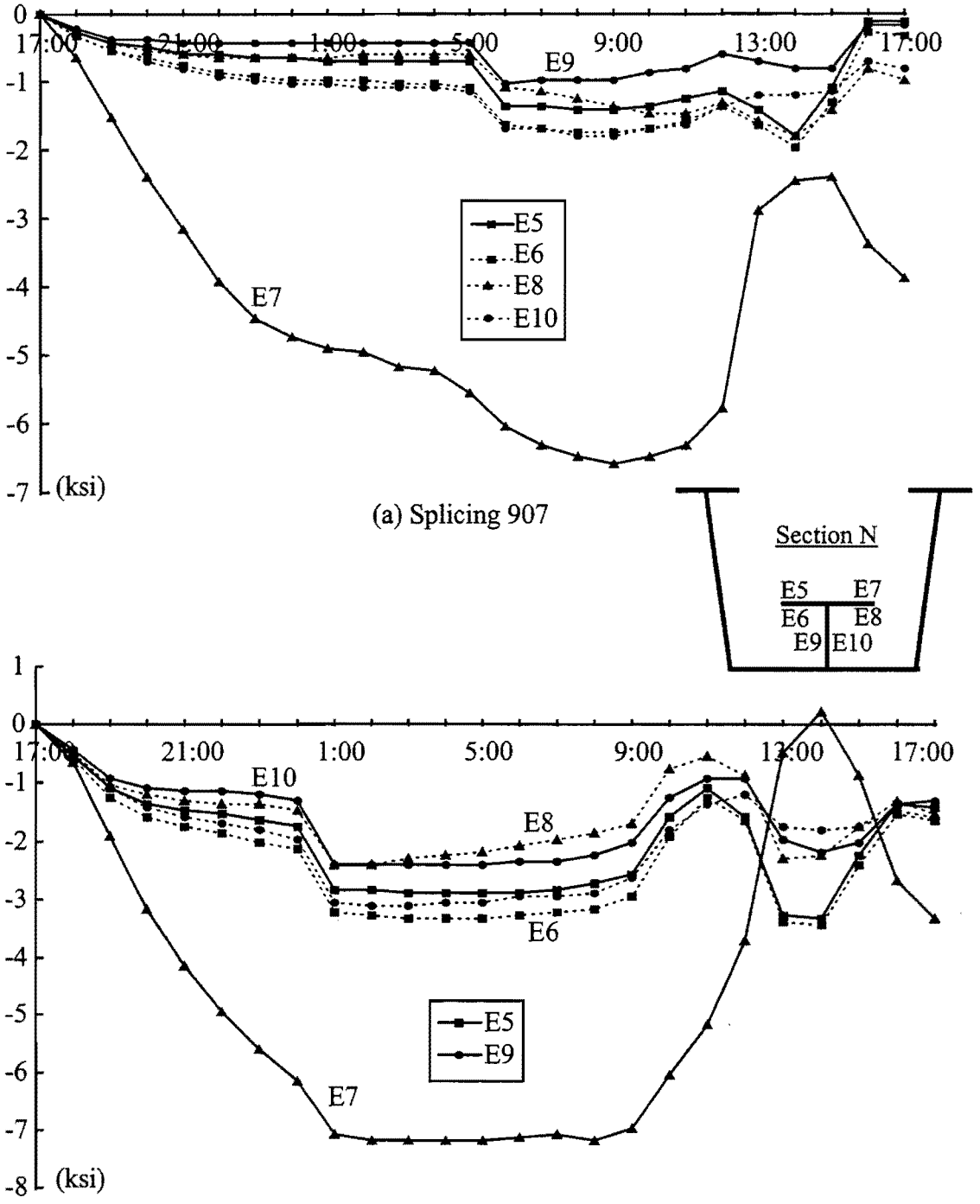

(a) Splicing 907

(b) Releasing 907

Figure 3.22. Stress Development in the Erection of Segment 907 (Section N, Longitudinal Stiffener)

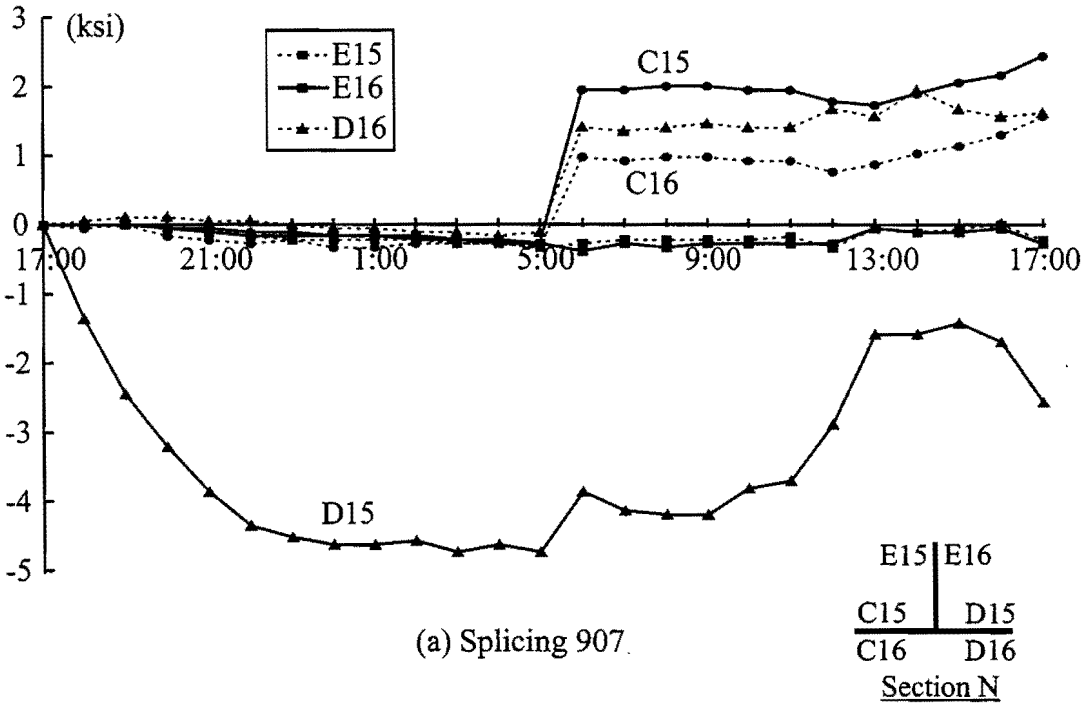

(a) Splicing 907

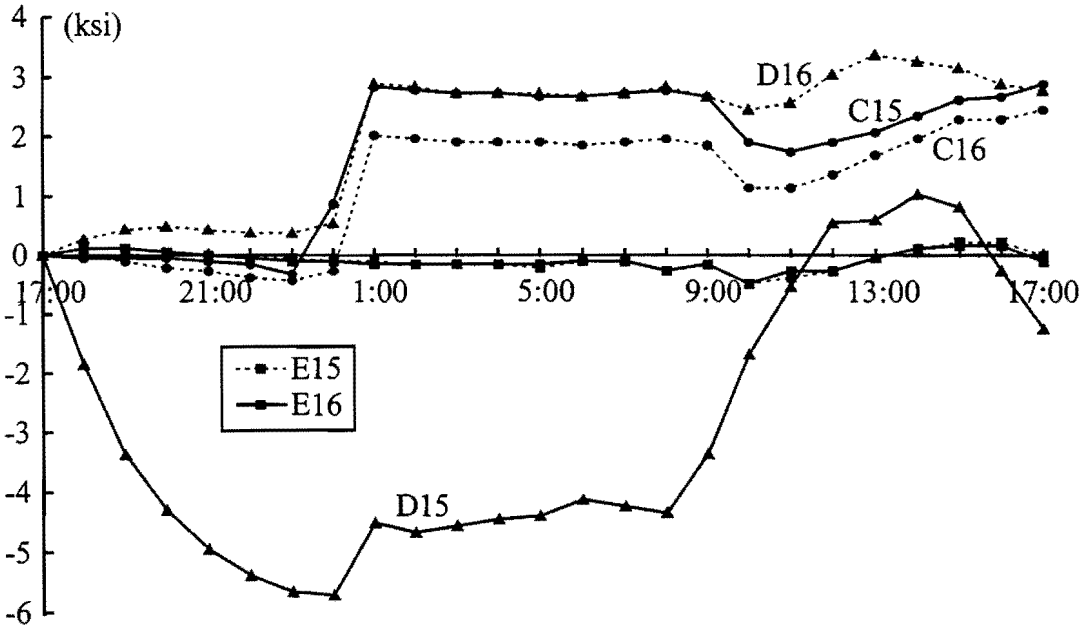

(b) Releasing 907

Figure 3.23. Stress Development in the Erection of Segment 907 (Section N, the Diagonal)

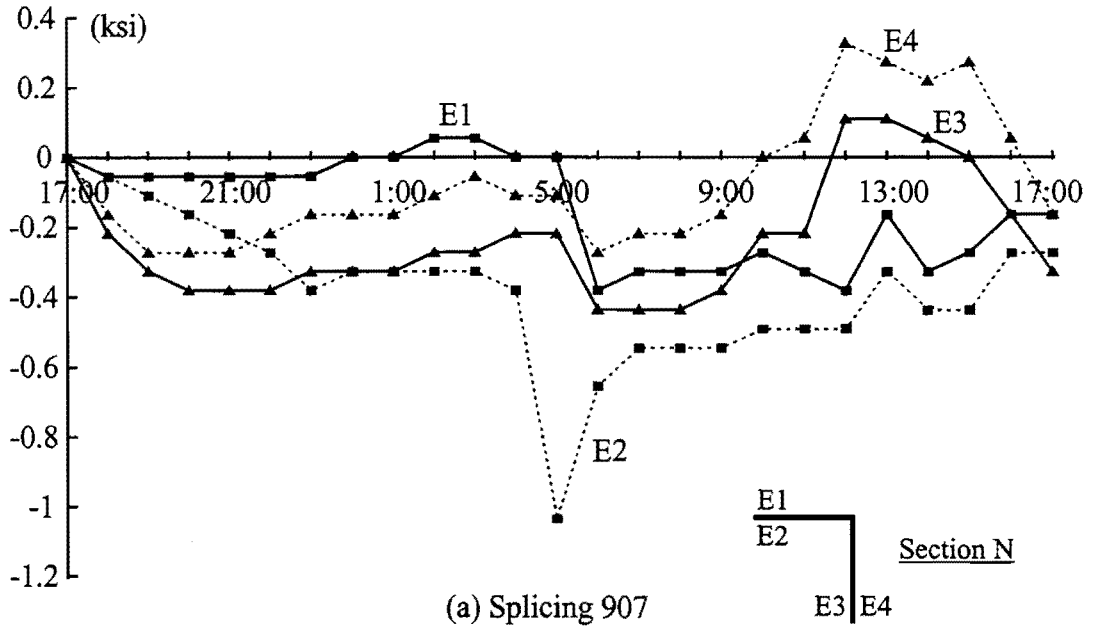

(a) Splicing 907

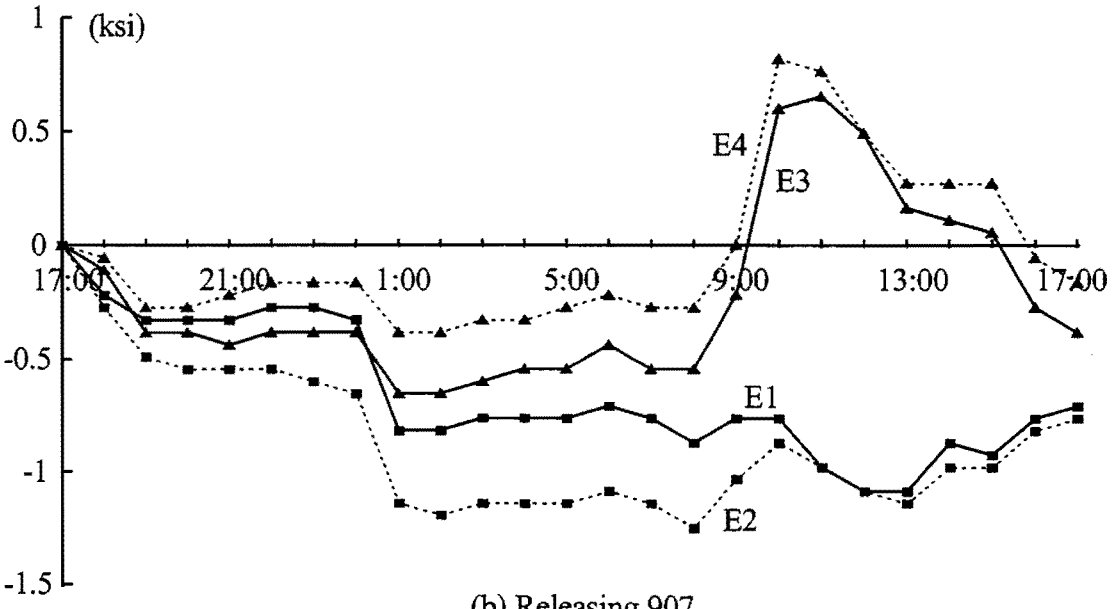

(b) Releasing 907

Figure 3.24. Stress Development in the Erection of Segment 907 (Section N, the Strut)

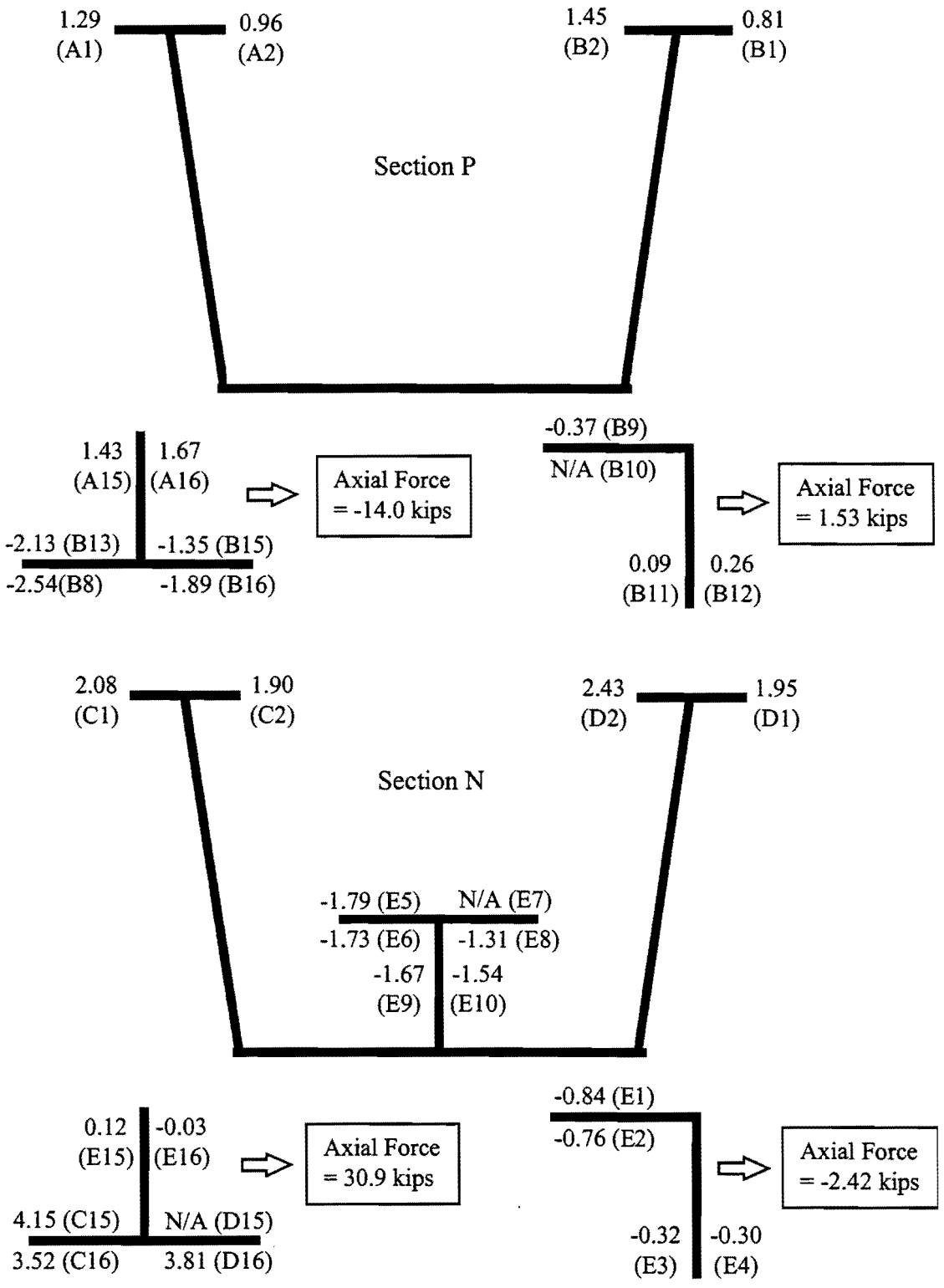

Figure 3.25. Stress Changes Measured During the Erection of Segment 907

3.5 Stress Changes During Slab Construction

The monitoring of the bridge behavior during slab construction is an important part of the field study. The measurement and data processing before the slab construction provided an opportunity to examine whether the data acquisition system was functioning properly, and to correct any problems that were found. For example, the one-sided gages were replaced by foil gages due to the poor behavior outlined earlier. Since the connections to some of the gages were altered, the corresponding channel numbering also changed relative to the erection stage. The location of the strain gages during slab construction are illustrated in Fig. 3.26, and the corresponding stress development in the 24-hour periods that covered each of the three slab construction stages that were shown previously in Fig. 3.7 are presented in this section.

3.5.1 Stress Changes During Stage 1 Slab Construction

The concrete slab constructed during Stage 1 consisted of two parts, one in the north span between Bents 19 and 20 and the other in the south span between Bents 17 and 18, respectively (Fig. 3.7a). The construction started in the north span near Bent 20 at about 18:00 on September 14, 1996, and then moved to the south span near Bent 17 at about 22:00. The stage finished at approximately 01:00 of September 15. The stress changes in the 24-hour period during which Stage 1 slab construction were completed are graphed in Figs. 3.27 to 3.35.

Figures 3.27 and 3.28 show the girder stresses on Section P. The stress changes from 17:00 ~ 19:00 are mainly due to the thermal effects. The weight of the concrete on the north span did not cause significant stresses in the girder at the instrumented section. The majority of the stress increase was caused by the concrete on the south span, right above Section P. Figures 3.29 and 3.30 are the stresses in the instrumented bracing members at the section. The significant change in stresses between 23:00 and 01:00 is due to the addition of the wet concrete slab on the south span of the bridge.

Stress changes at Section N due to the gravity load of concrete can be observed in the graphs shown in Figs. 3.31 and 3.32. Similar to the gages at Section P, abrupt stress changes occurred between 23:00 and 01:00. However, the most significant change occurred on the day after Stage 1 construction, starting at approximately 11:00. It is believed that these changes were due to the temperature of the girders, which were exposed to the direct sunlight at that time. Similar changes were exhibited in the same period of time in the days prior to Stage 1 construction; however, the magnitudes of changes were generally smaller. Some of the gages experienced larger changes than others, which implies a non-uniform response of the girder due to the temperature gradient. This dramatic stress change can also be observed in the longitudinal stiffener (Fig. 3.33) and in the diagonal bracing member (Fig. 3.34). The diagonal of the top lateral truss experienced very little stress increase in Stage 1 compared with the temperature stresses (Fig. 3.35).

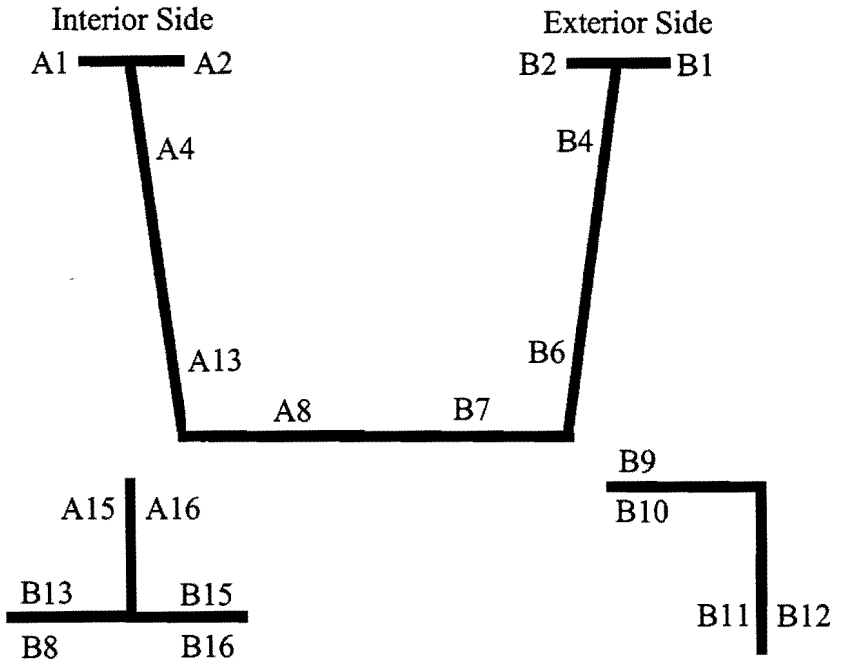

(a) Section P

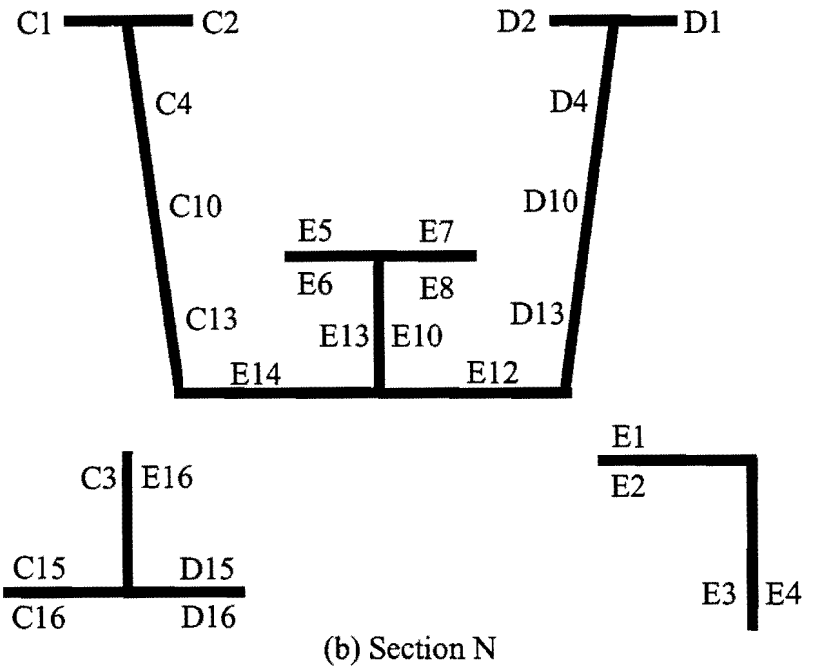

(b) Section N

Figure 3.26. Strain Gages Used in Monitoring Slab Construction

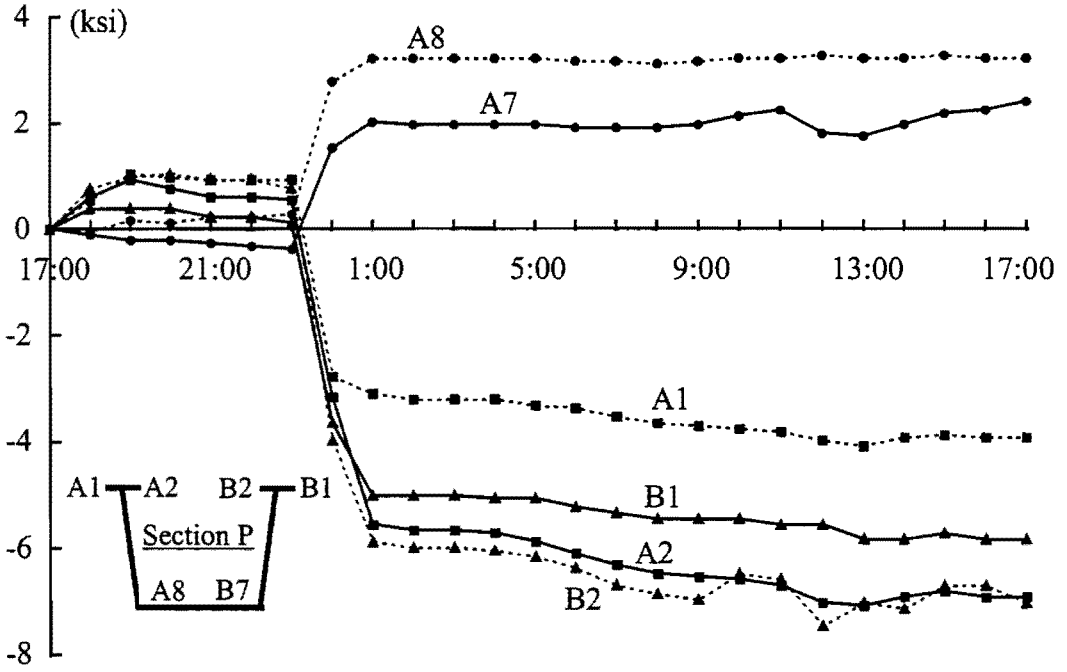

Figure 3.27. Stress Development in Stage 1 Slab Construction (Section P, Top and Bottom Flanges)

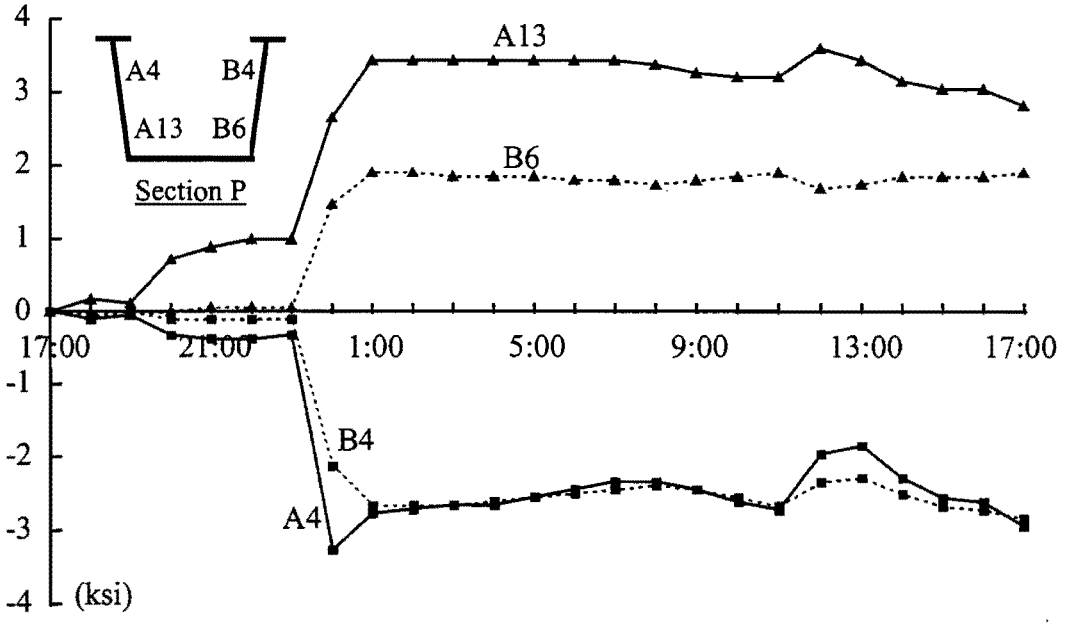

Figure 3.28. Stress Development in Stage 1 Slab Construction (Section P, Webs)

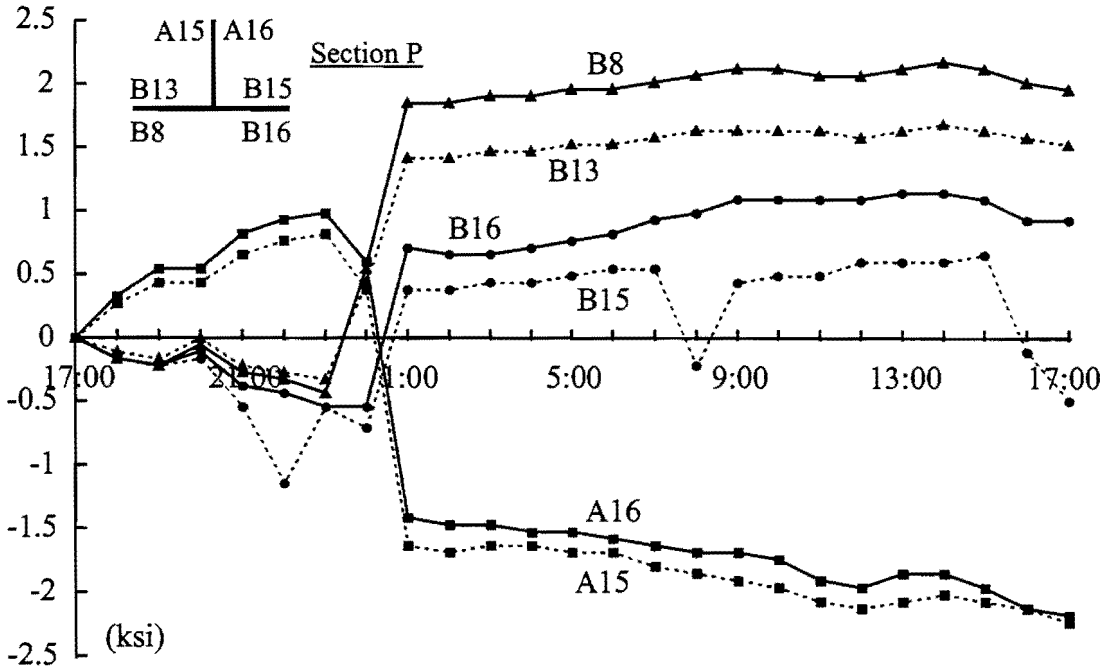

Figure 3.29. Stress Development in Stage 1 Slab Construction (Section P, the Diagonal)

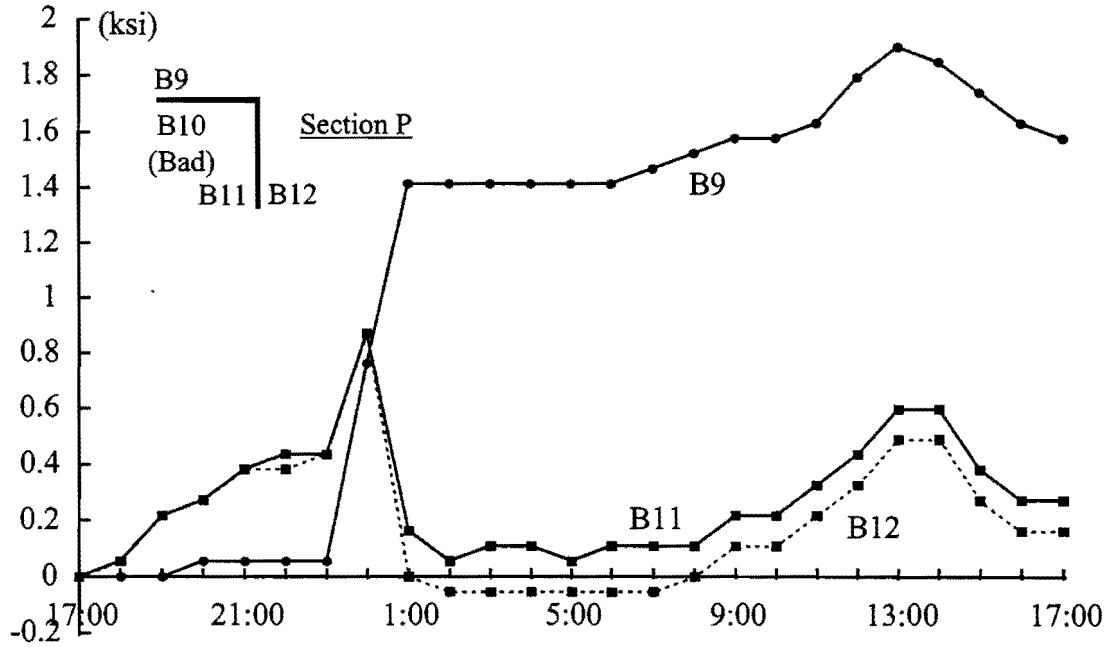

Figure 3.30. Stress Development in Stage 1 Slab Construction (Section P, the Strut)

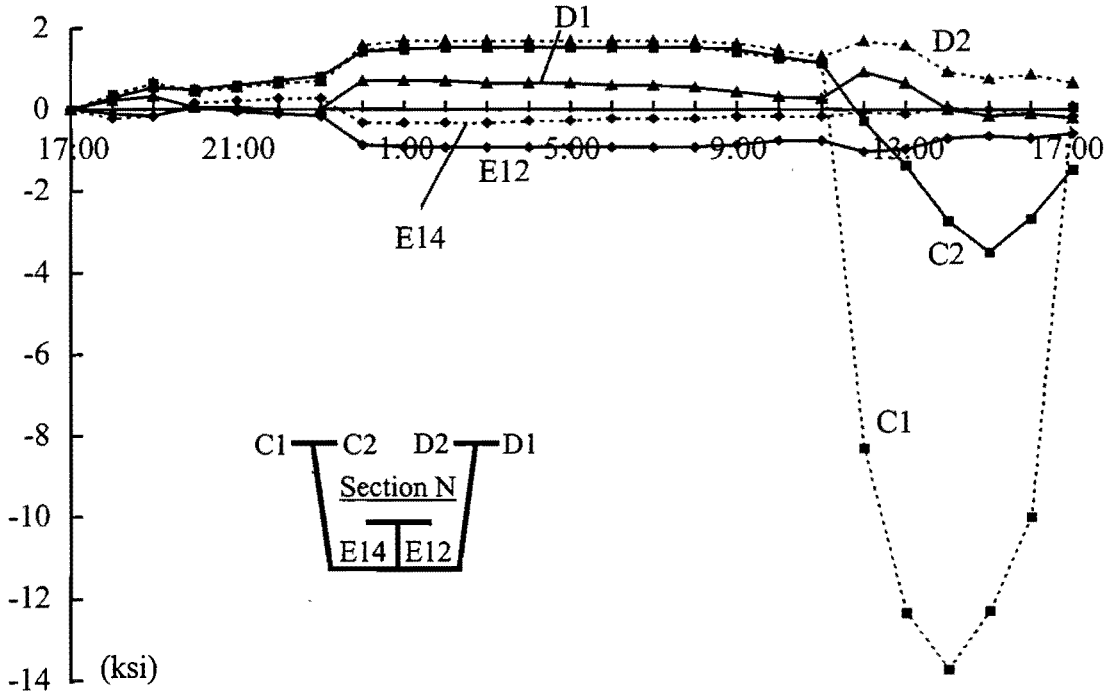

Figure 3.31. Stress Development in Stage 1 Slab Construction (Section N, Top and Bottom Flanges)

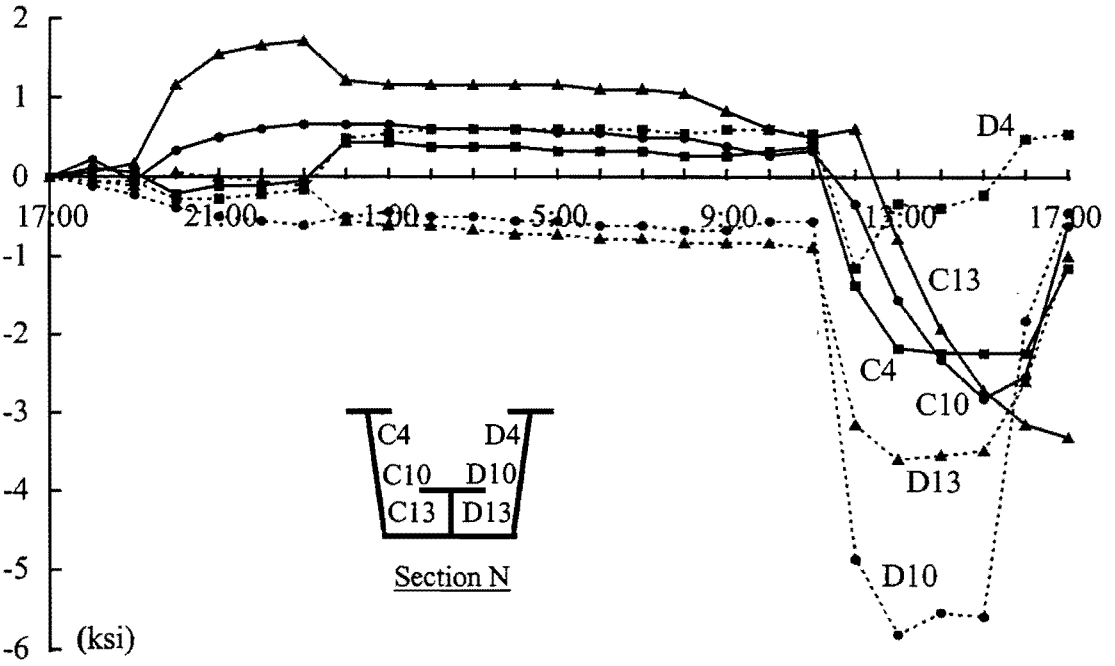

Figure 3.32. Stress Development in Stage 1 Slab Construction (Section N, Webs)

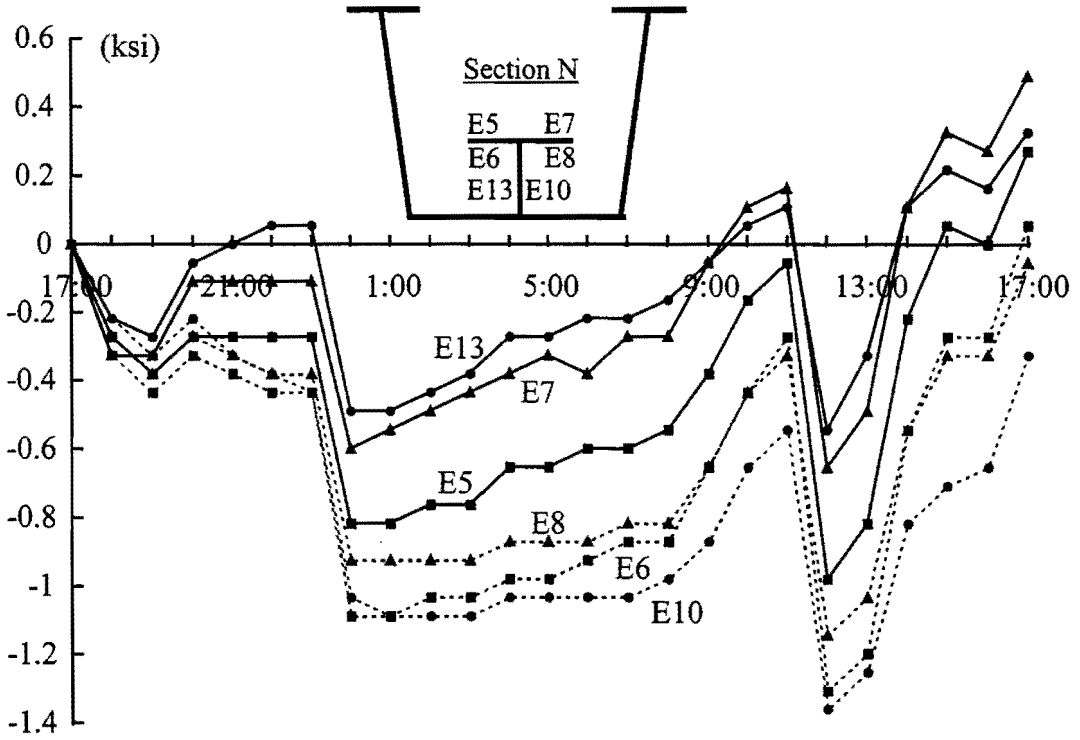

Figure 3.33. Stress Development in Stage 1 Slab Construction (Section N, Longitudinal Stiffener)

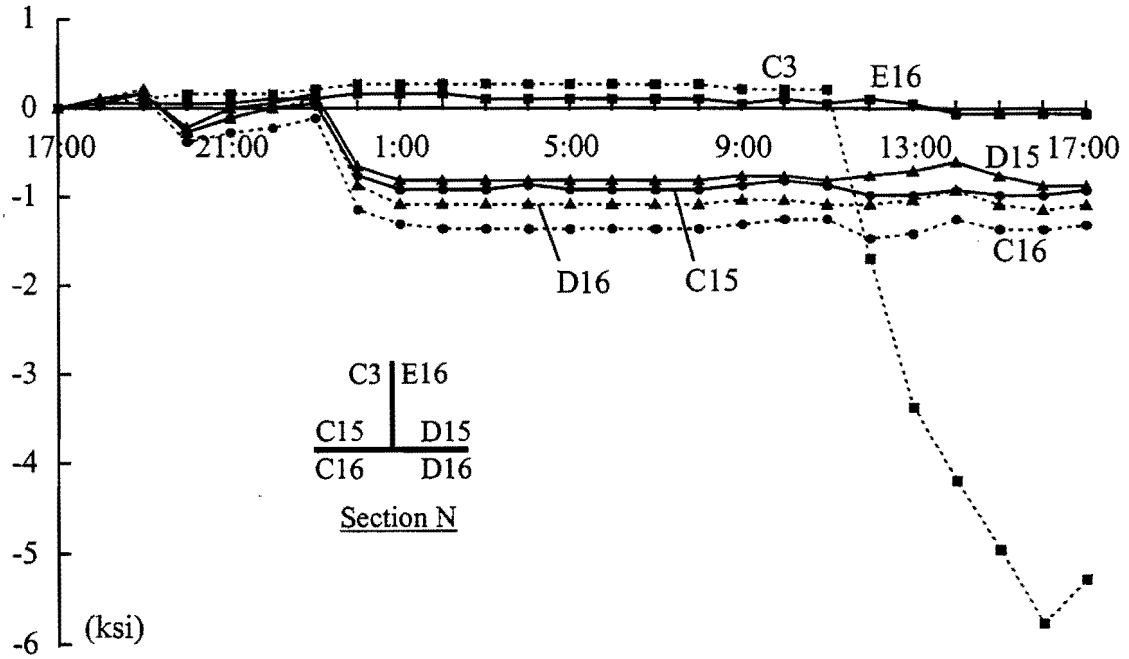

Figure 3.34. Stress Development in Stage 1 Slab Construction (Section N, the Diagonal)

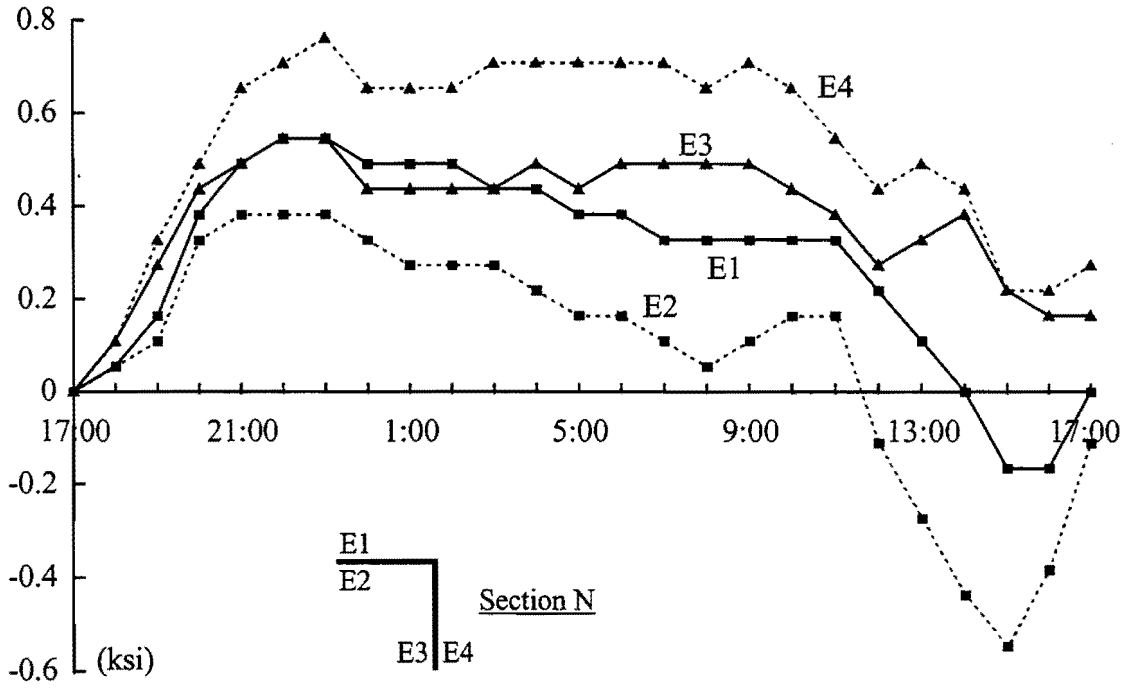

Figure 3.35. Stress Development in Stage 1 Slab Construction (Section N, the Strut)

Based on the above observations on Figs. 3.27 to 3.35, the stress caused by the weight of the second part of the slab constructed in Stage 1, i.e., the slab between Bent 17 and Bent 18, are extracted for investigation of the girder behavior under gravity loads. The stress difference between 23:00 and 1:00, during which the southern portion of concrete was cast, are retrieved. Temperature effects were eliminated as discussed in Appendix A, and the resulting stresses and forces due to the concrete are illustrated in Fig. 3.36.

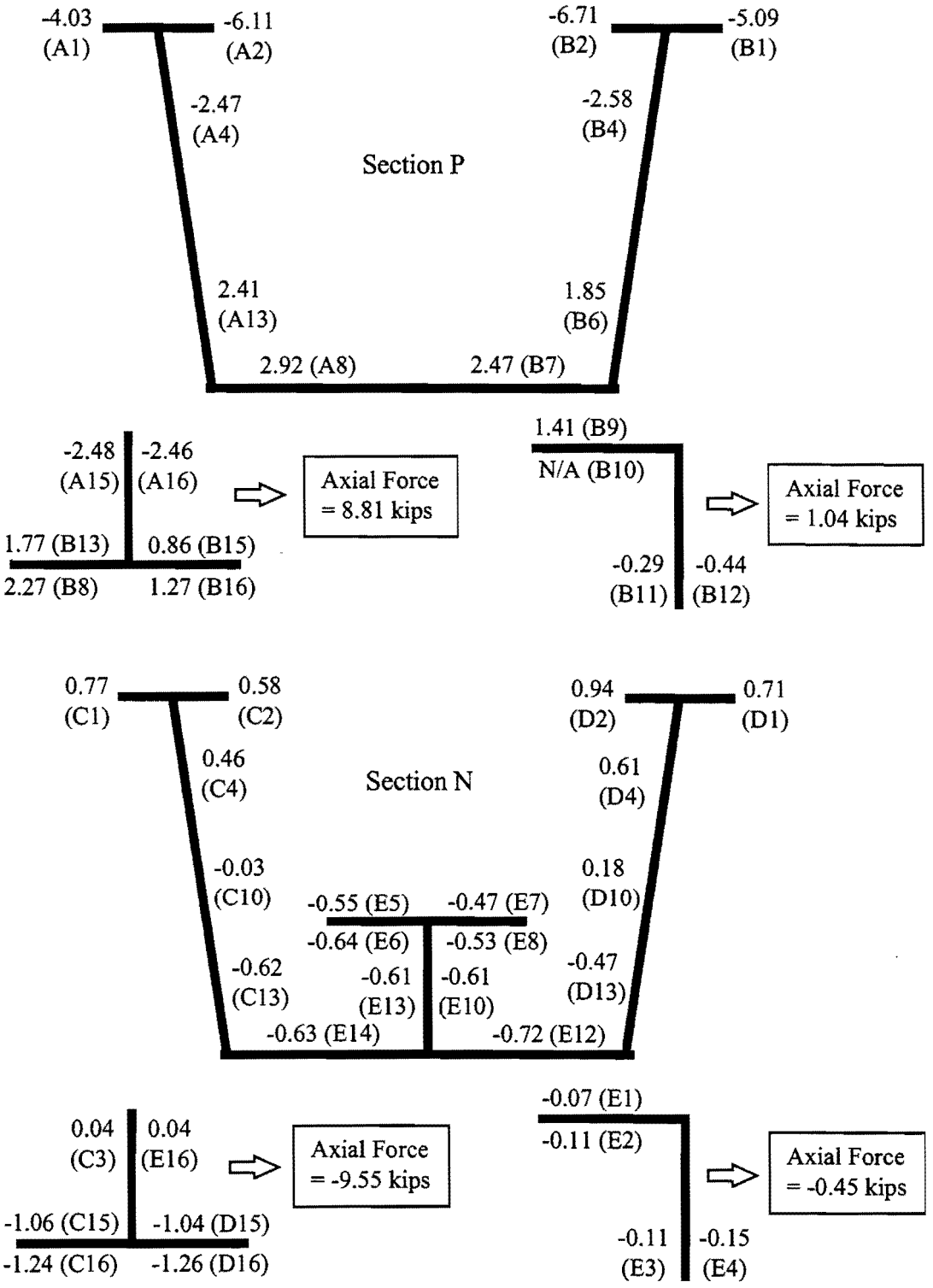

Figure 3.36. Stress Changes Measured During Stage 1 Slab Construction (between 23:00, 9/14/96 and 01:00, 9/15/96)

3.5.2 Stress Changes During Stage 2 Slab Construction

Stage 2 slab construction started at approximately 22:00 of September 17 and finished around 04:00 the next morning. Nearly 180 feet of the slab were constructed in the middle of the internal span between Bent 18 and 19 (Fig. 3.7b) during this period. The stress results in the 24-hour period after 17:00 of September 17 are graphed in Figs. 3.38 to 3.46.

Figures 3.37 to 3.38 are the results of the girder stresses at Section P. Since Stage 1 was completed nearly 48 hours before Stage 2, the concrete on top of Section P had gained some strength, and therefore some composite action in the region near Section P was expected. As a result, the stress increases at Section P during Stage 2 were relatively small (Figs. 3.37 and 3.38). Similarly, only slight stress changes that corresponded to the addition of Stage 2 concrete in the diagonal (Fig. 3.39) were observed. The downward development in stress readings in the strut (Fig. 3.40), starting at 22:00, were believed to be the results of the gravity loads from Stage 2 concrete, since no similar behavior was found during the same time period in early nights.

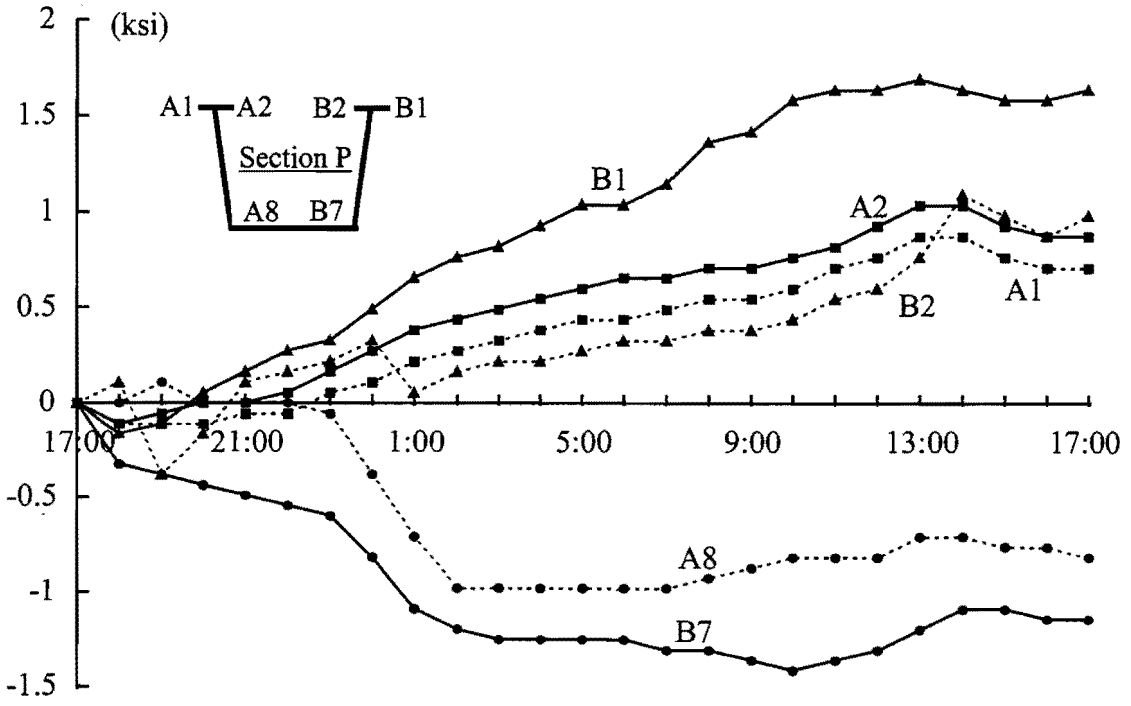

Figure 3.37. Stress Development in Stage 2 Slab Construction (Section P, Top and Bottom Flanges)

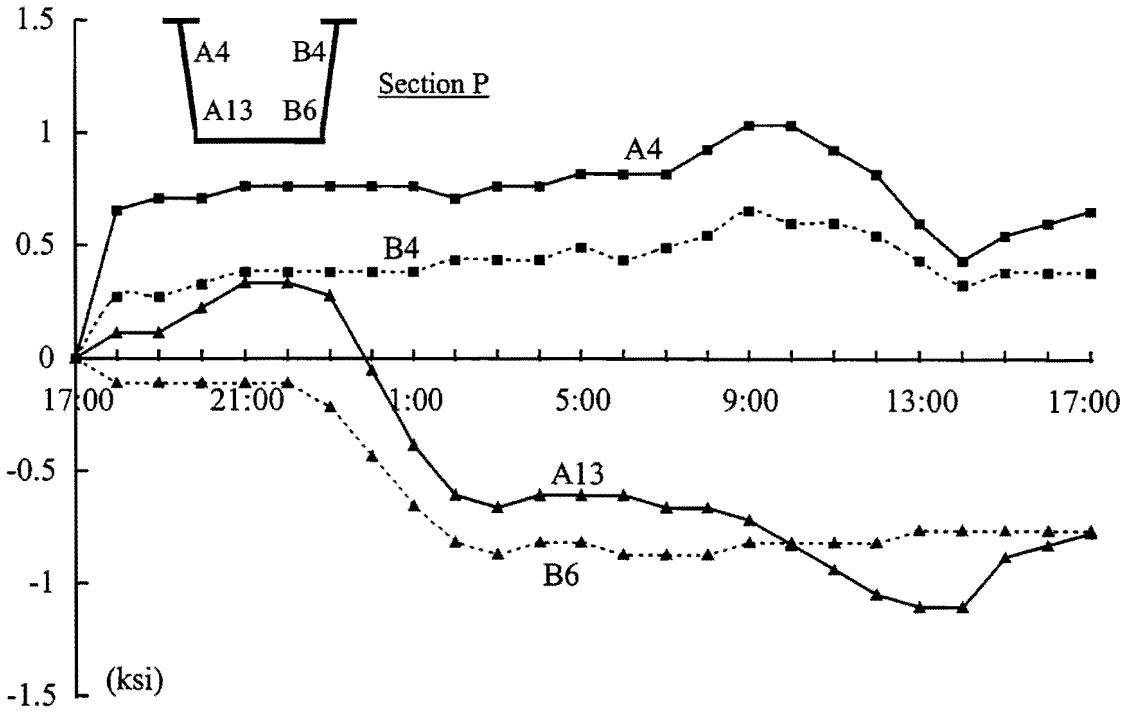

Figure 3.38. Stress Development in Stage 2 Slab Construction (Section P, Webs)

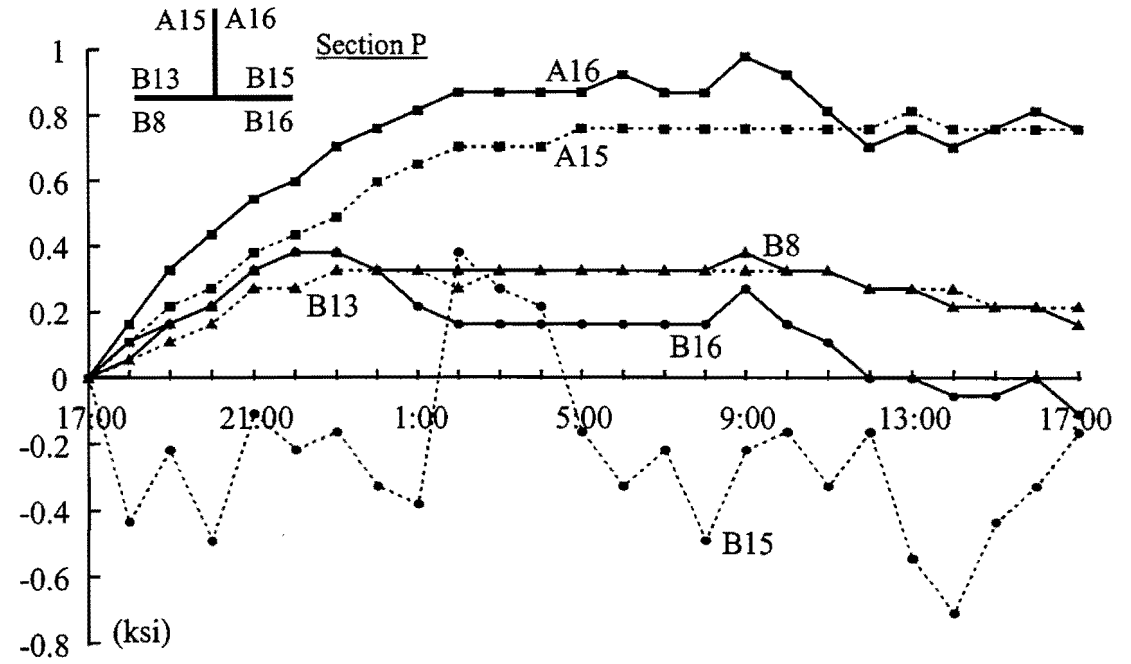

Figure 3.39. Stress Development in Stage 2 Slab Construction (Section P, the Diagonal)

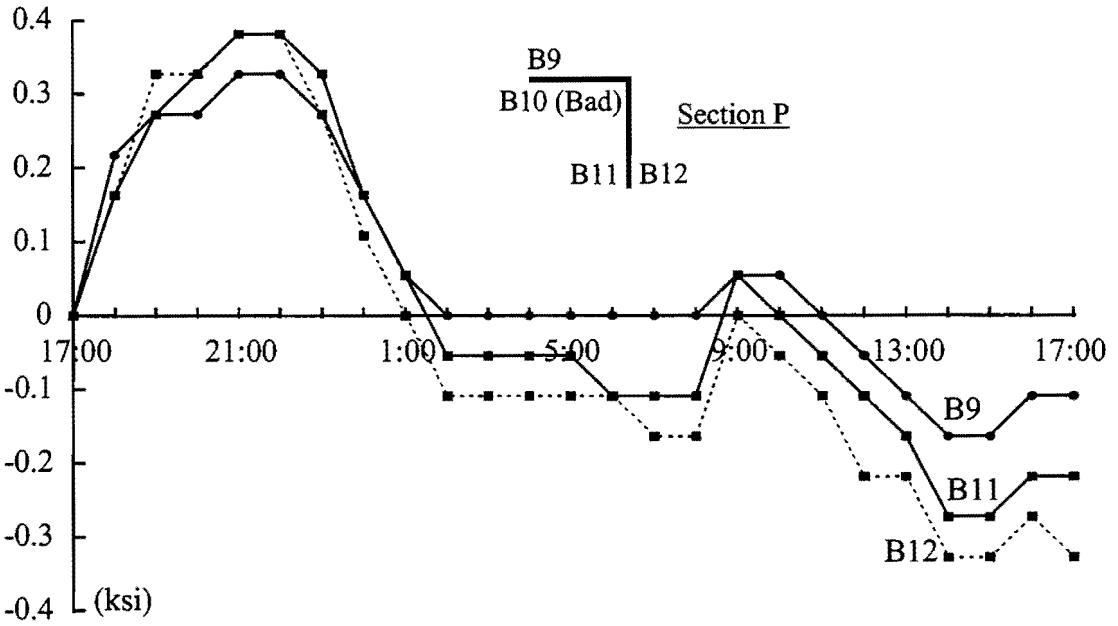

Figure 3.40. Stress Development in Stage 2 Slab Construction (Section P, the Strut)

Figures 3.41 and 3.42 clearly indicate the stress increases for the girder flanges and webs on Section N due to the Stage 2 concrete weight. The majority of the increases were achieved between 23:00 to 02:00. As much as 8 ksi stress was added in the interior edges of the top flanges (Gages C1 and D1). The girder started to respond to the temperature increase at 08:00 the following day. Interestingly, the interior top flange experienced the maximum thermal deformation while the exterior top flange and the bottom flange were essentially unaffected (Fig. 3.41). All gages on the webs show some degree of temperature effect (Fig. 3.42). The longitudinal stiffener also experienced a significant and almost uniform stress change under the Stage 2 concrete loading (Fig. 3.43). Both bracing members started to gain stresses at 22:00 (Figs. 3.44 and 3.45), which is consistent to the behavior of the girder flanges and webs.

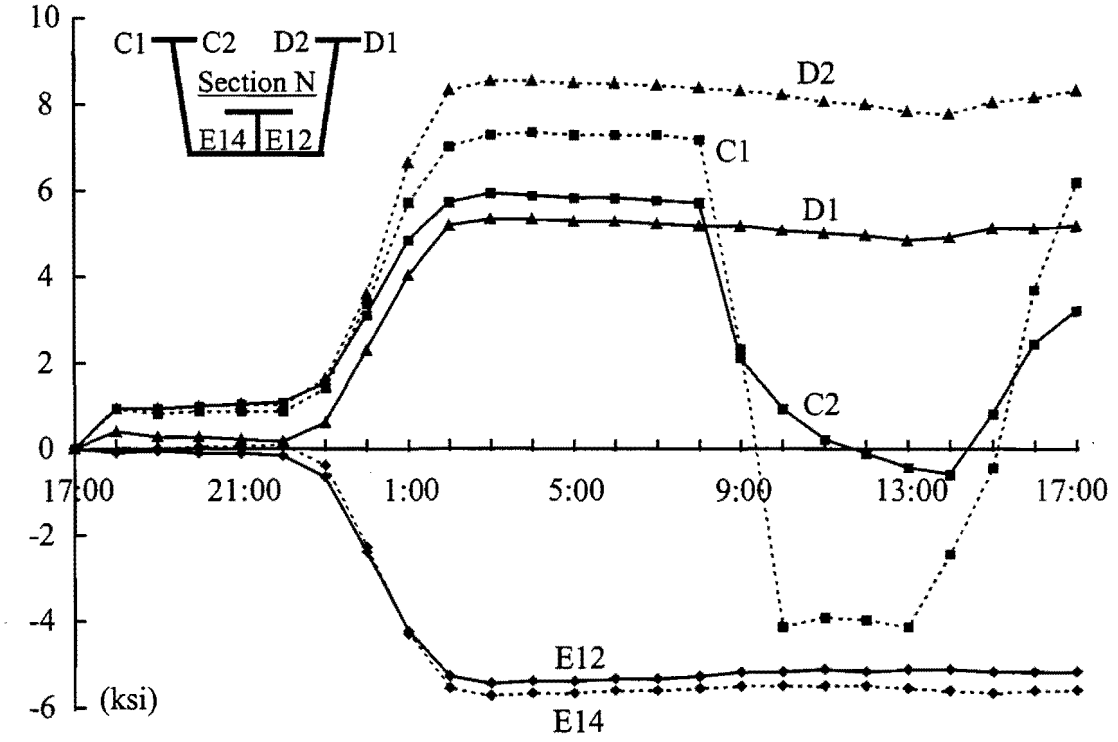

Figure 3.41. Stress Development in Stage 2 Slab Construction (Section N, Top and Bottom Flanges)

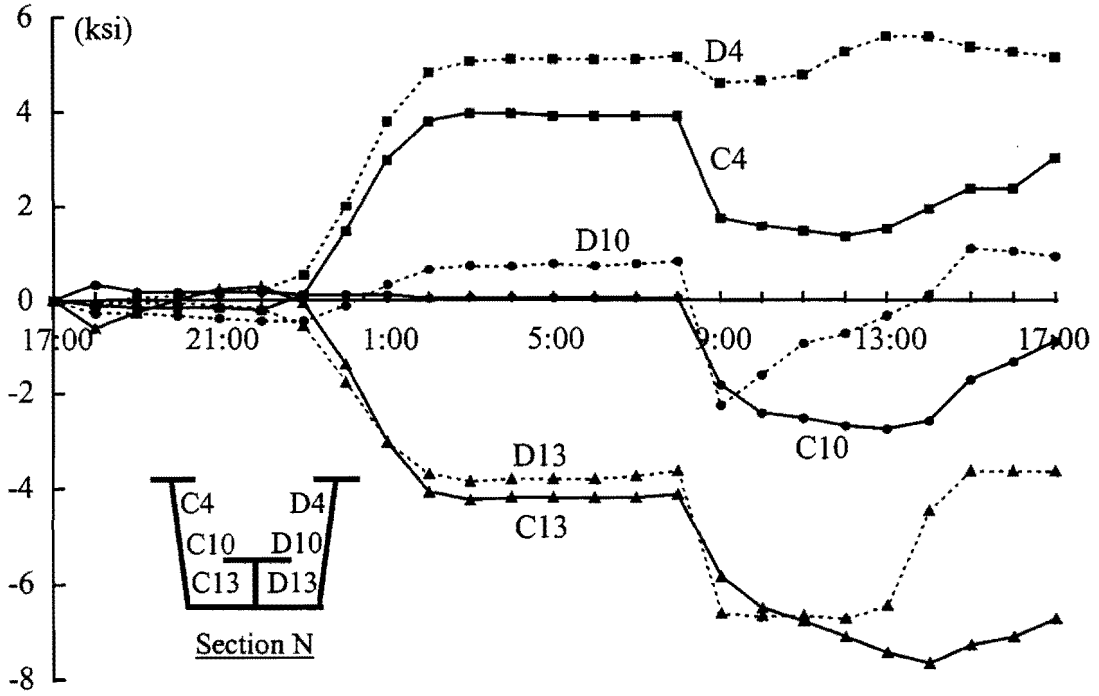

Figure 3.42. Stress Development in Stage 2 Slab Construction (Section N, Webs)

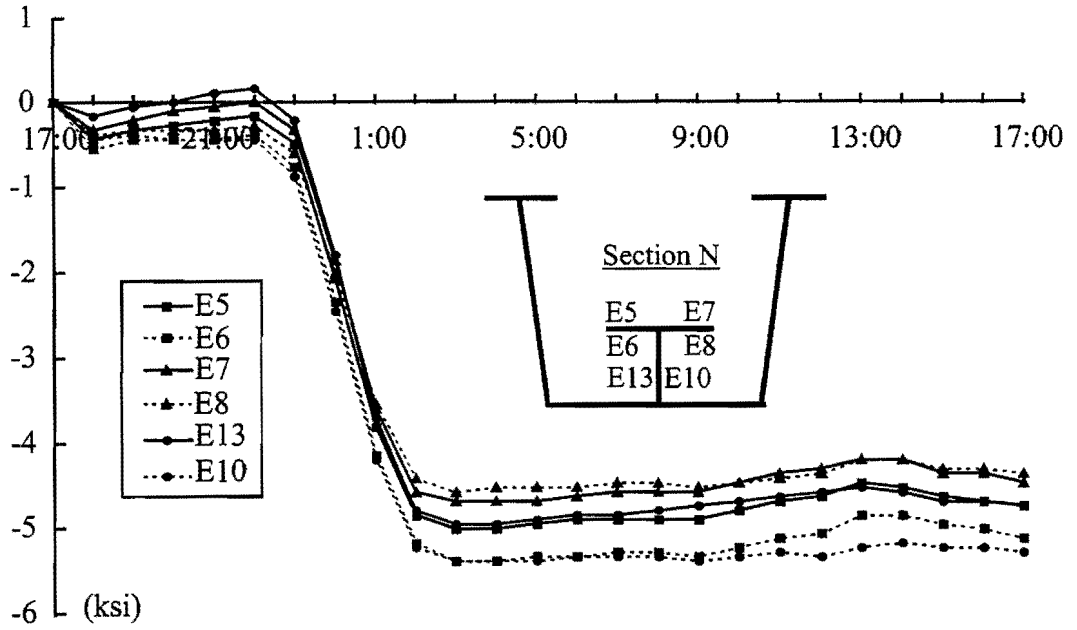

Figure 3.43. Stress Development in Stage 2 Slab Construction (Section N, Longitudinal Stiffener)

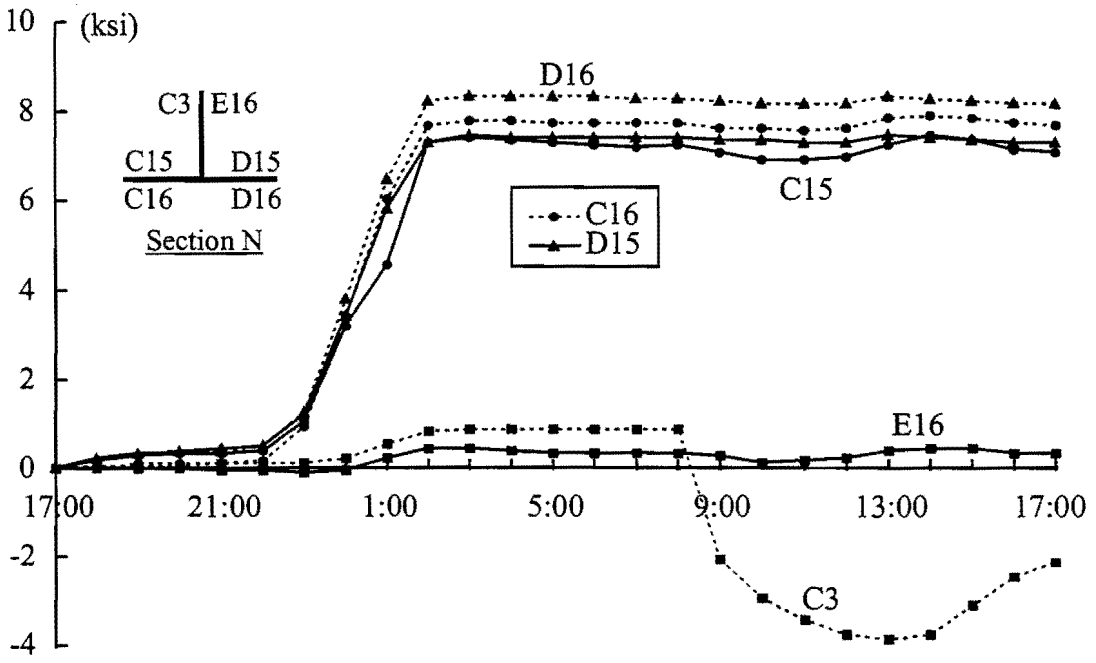

Figure 3.44. Stress Development in Stage 2 Slab Construction (Section N, the Diagonal)

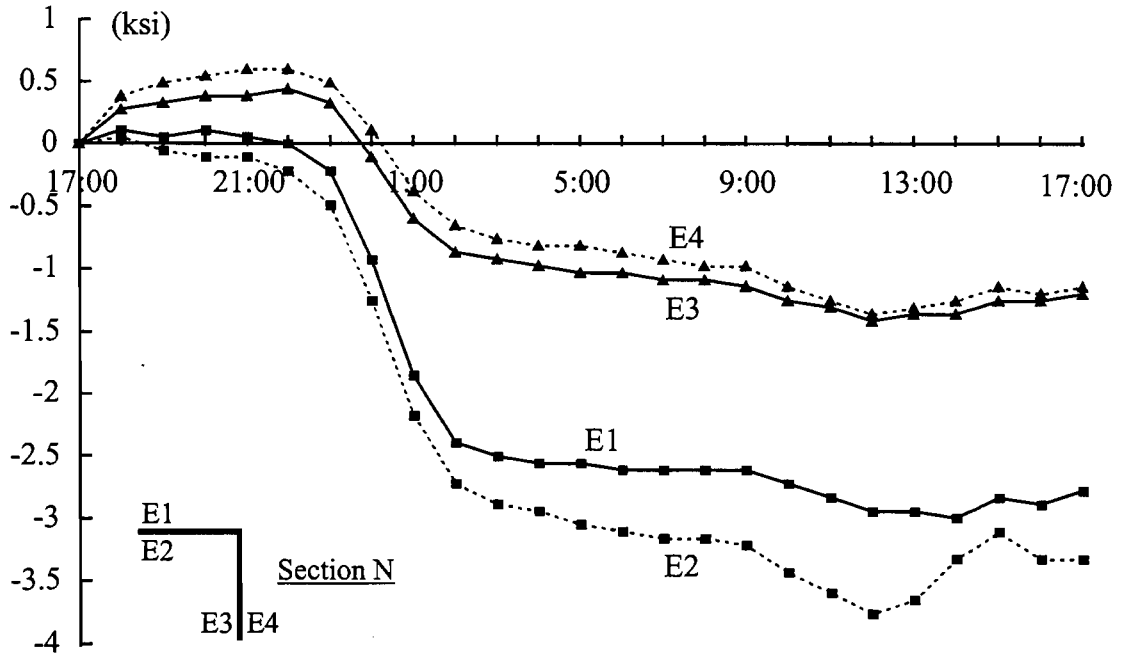

Figure 3.45. Stress Development in Stage 2 Slab Construction (Section N, the Strut)

Based on the above observations on Figs. 3.37 to 3.45, the stress difference between 22:00 and 03:00 are considered as the direct result of the gravity load from the Stage 2 concrete slab. The temperature effect in this time interval was eliminated using the data of previous two days, as presented in Appendix A. The results are presented in Fig. 3.46 where stress changes are shown at the corresponding gage locations.

3.5.3 Stress Changes During Stage 3 Slab Construction

Stage 3 of the slab construction consisted of two regions, the north pour above Bent 19 and the south pour above Bent 18 (Fig. 3.7c). The construction began at the north side at 22:00 on September 21 and finished at the south end at approximately 06:00 the following morning. Stress readings in the 24-hour period starting at 17:00, September 21 are graphed in Figs. 3.47 to 3.55.

Similar to Stage 2, very small stress increases were observed at Section P (Figs. 3.47 and 3.48), mainly due to the composite action from the Stage 1 concrete that had cured for approximately 7 days. In addition to the composite action at Section P, the Stage 3 slab construction included regions on either side of the interior support, which minimizes the moment at Section P. At Section P, concrete cast in the exterior span causes positive moment while concrete cast in the interior span causes negative moment. The stress readings of the gages on the bracing members of Section P (Figs. 3.49 and 3.50) were the combined results of the temperature change and concrete loading. The change in stress was relatively small.

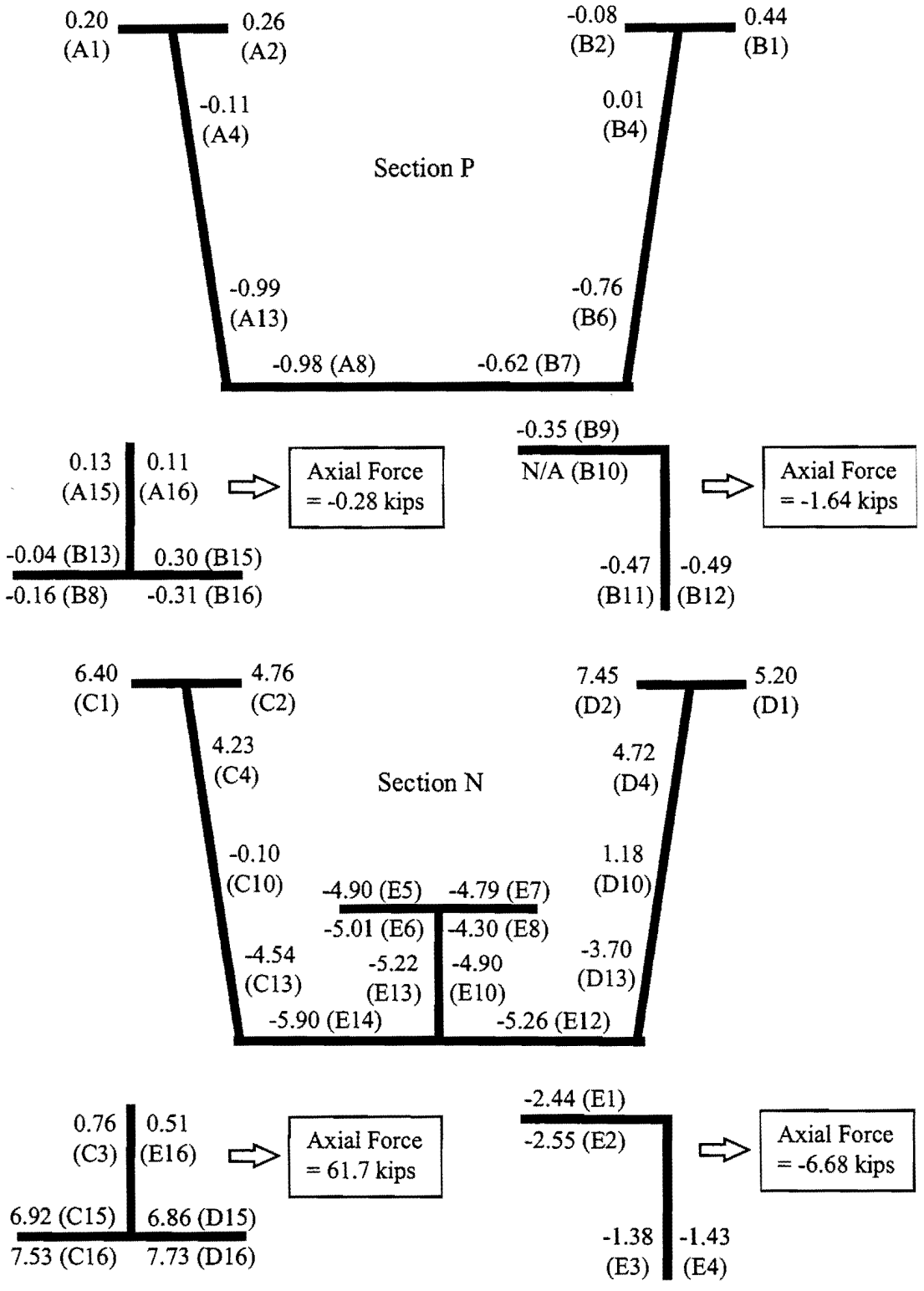

Figure 3.46. Stress Changes Measured During Stage 2 Slab Construction (between 22:00, 9/16/96 and 03:00, 9/17/96)

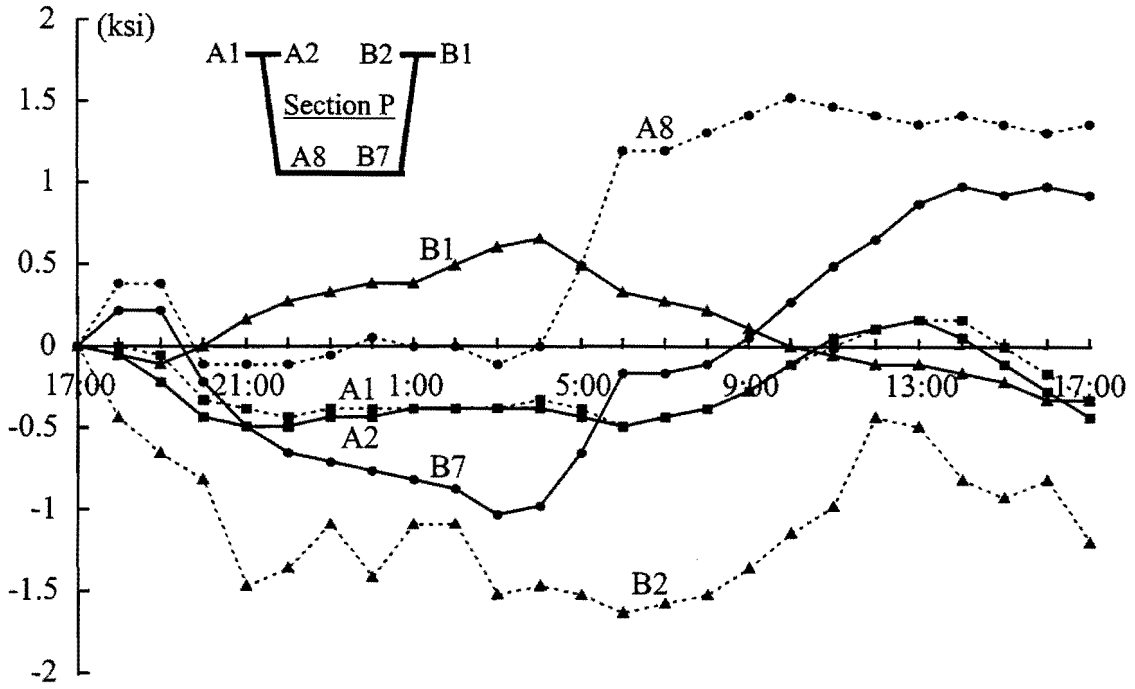

Figure 3.47. Stress Development in Stage 3 Slab Construction (Section P, the Top and Bottom Flanges)

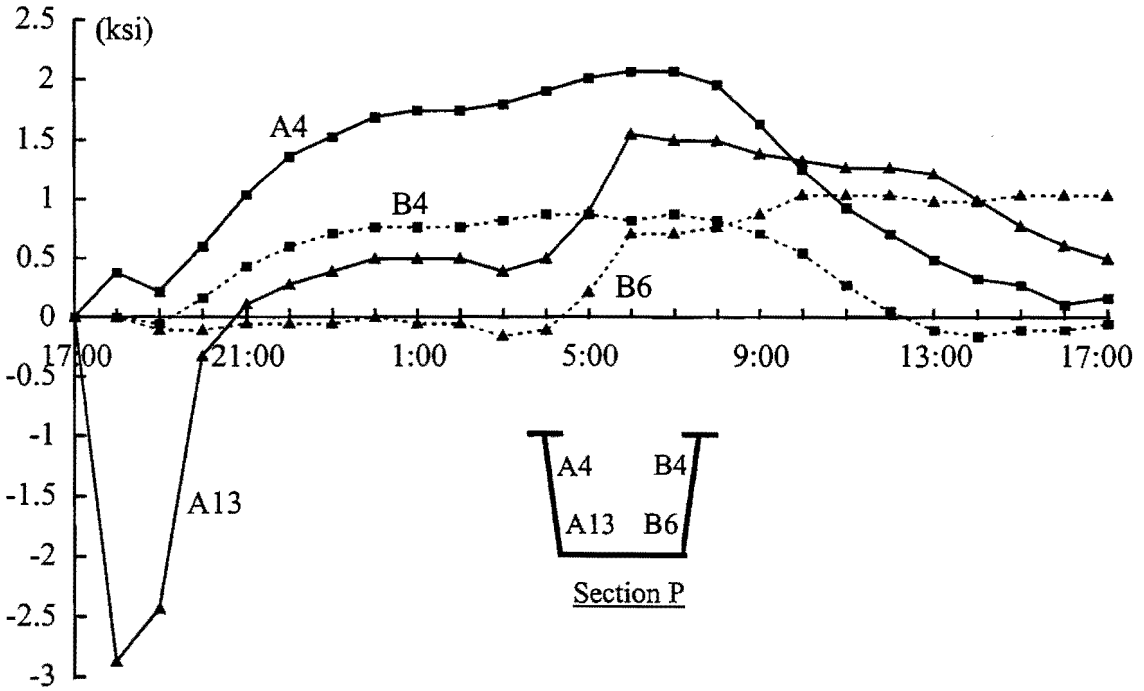

Figure 3.48. Stress Development in Stage 3 Slab Construction (Section P, Webs)

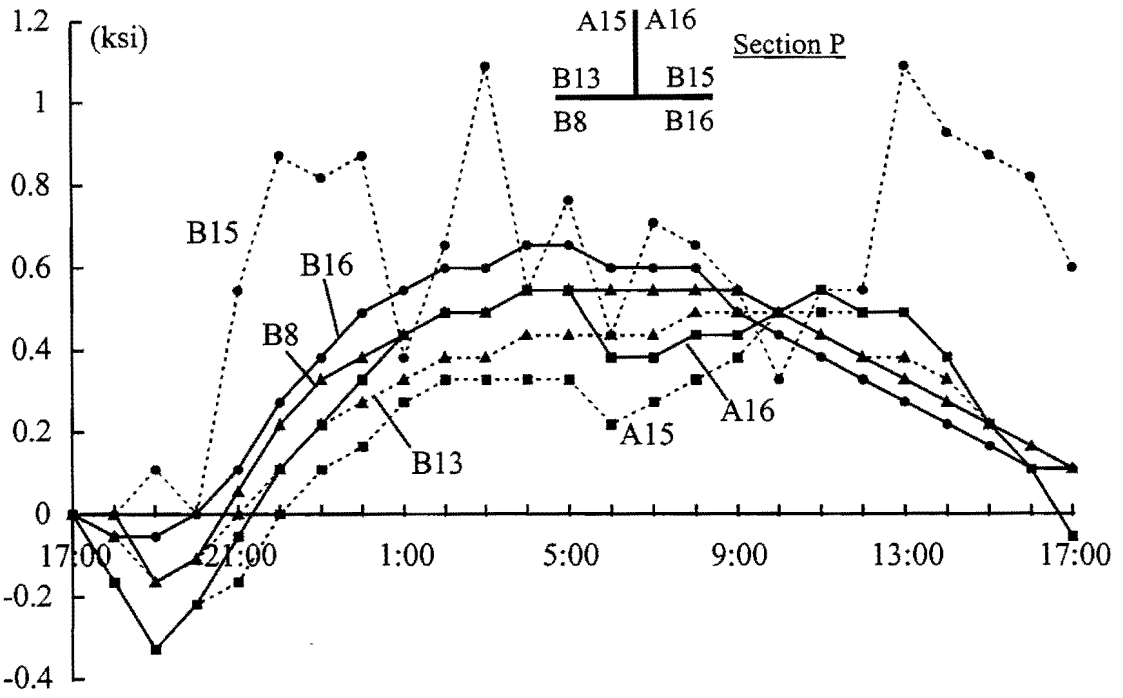

Figure 3.49. Stress Development in Stage 3 Slab Construction (Section P, the Diagonal)

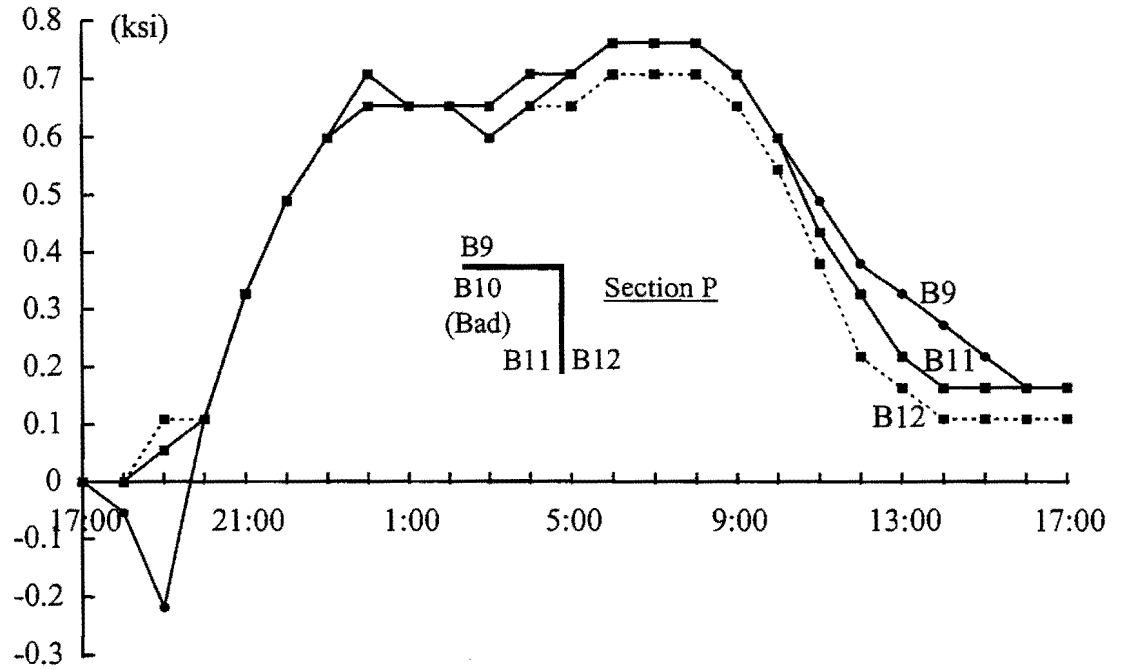

Figure 3.50. Stress Development in Stage 3 Slab Construction (Section P, the Strut)

There was still no hardened concrete slab above Section N in Stage 3, and thus no composite action existed at the section. Therefore, significant stress changes occurred in flanges and webs at Section N (Figs. 3.51 and 3.52). This larger change in stress relative to Section P is also due to a much larger bending moment at Section N. Readings from Gages C4 and C10 show dramatic changes beginning at approximately 04:00 (Fig. 3.52). These two gages are located at the middle and top of the interior web. Large readings were recorded at 04:00, and then the stresses gradually went back to the stress level of other nearby gages a few hours later. One explanation is that the gages were temporarily malfunctioning. However this theory would not be very convincing in explaining the phenomenon of the gradual return of the readings. A more probable explanation to the dramatic change in stress is due to the weight of the wet concrete and screed that were supported by struts that rested on the web of the box. Figure 3.56 shows the support struts for the formwork and screed. The slab construction above Section N took place around 03:00, which is consistent with the stress change. This was also the last portion of the concrete poured on the bridge, and the screed might have been left at the location until the next day. Aside from these two gages, all other gages including those on the longitudinal stiffeners and bracing members seem normal and properly reflected the construction process of the stage (Figs. 3.53 to 3.55).

The stress increases between 22:00, September 21 and 06:00, September 22 are taken as the stresses caused by the slab constructed in Stage 3. As discussed in Appendix A, temperature effects were larger in Stage 3 slab construction than those in other construction stages. The stress and brace force results due to the applied load in Stage 3 are shown in Fig. 3.57. Note that for both Stages 2 and 3, the stresses on Section N were more reliable because of their higher change in stress. The stresses in Section P were relatively small, and thus their accuracy was more likely to be affected by the temperature effects and other local irregularities.

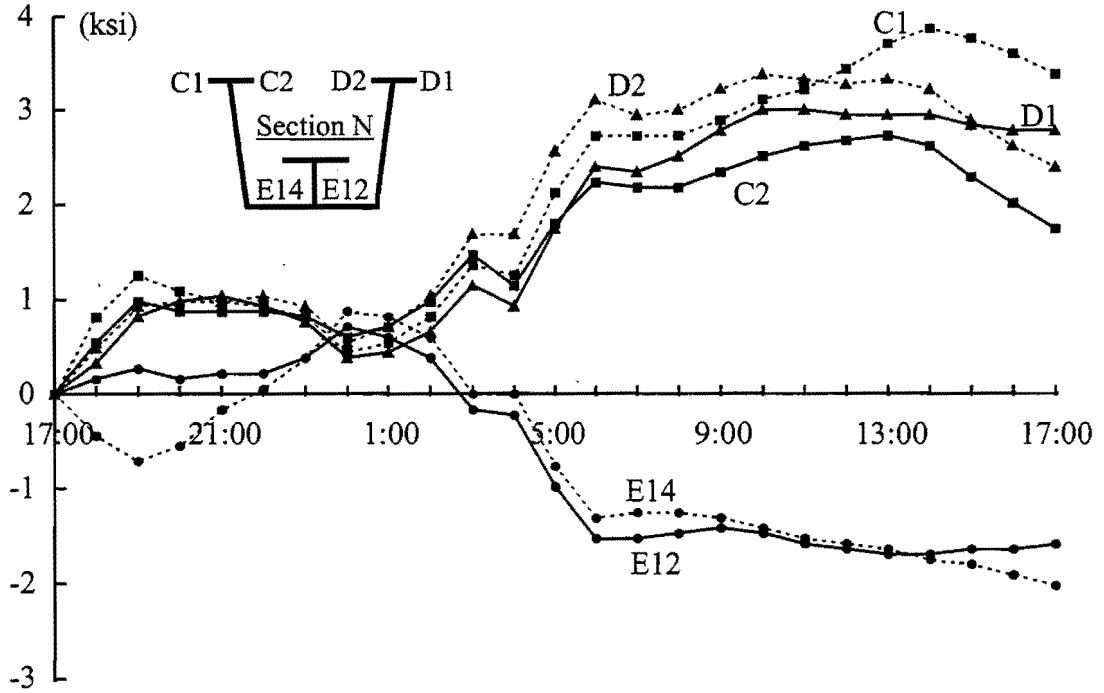

Figure 3.51. Stress Development in Stage 3 Slab Construction (Section N, Top and Bottom Flanges)

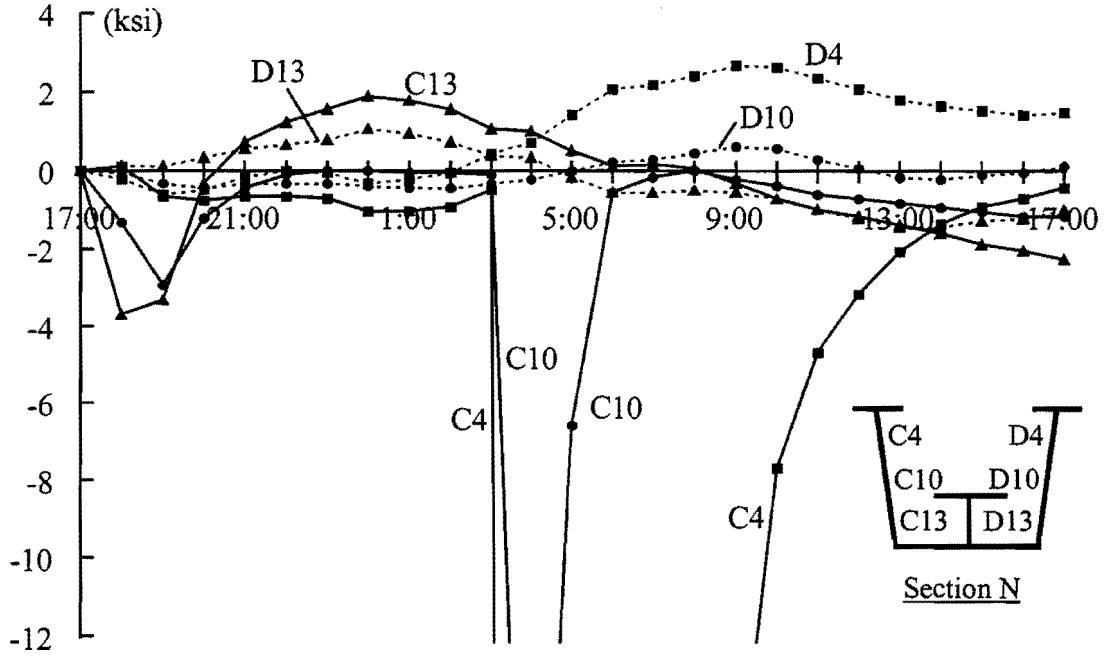

Figure 3.52. Stress Development in Stage 3 Slab Construction (Section N, Webs)

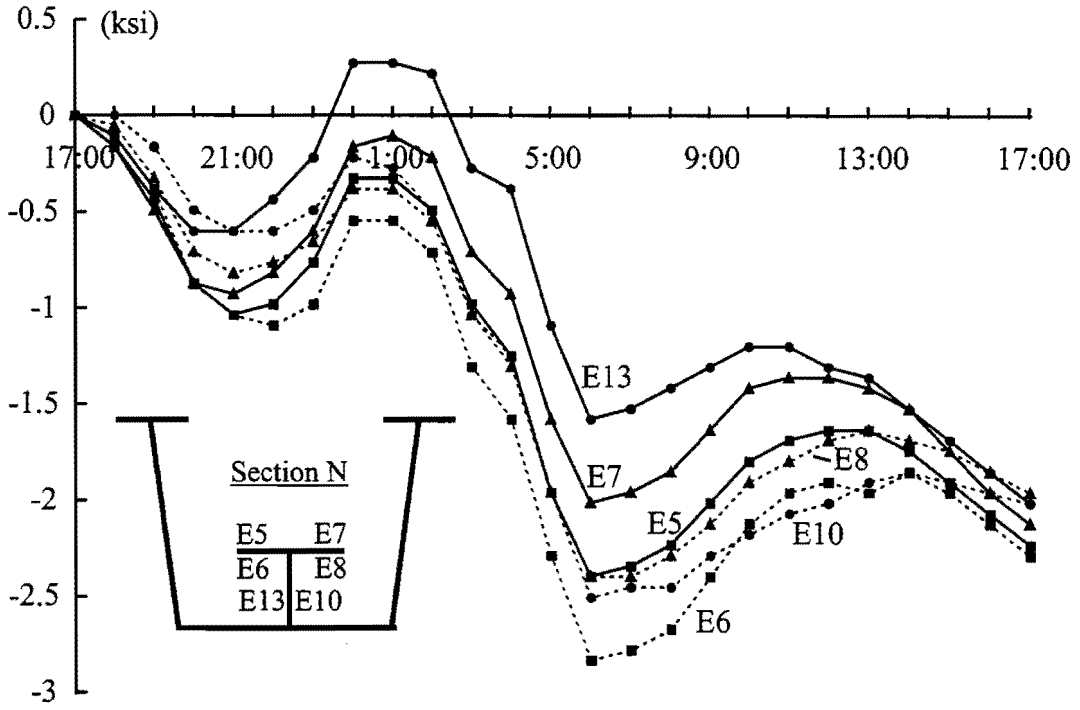

Figure 3.53. Stress Development in Stage 3 Slab Construction (Section N, Longitudinal Stiffener)

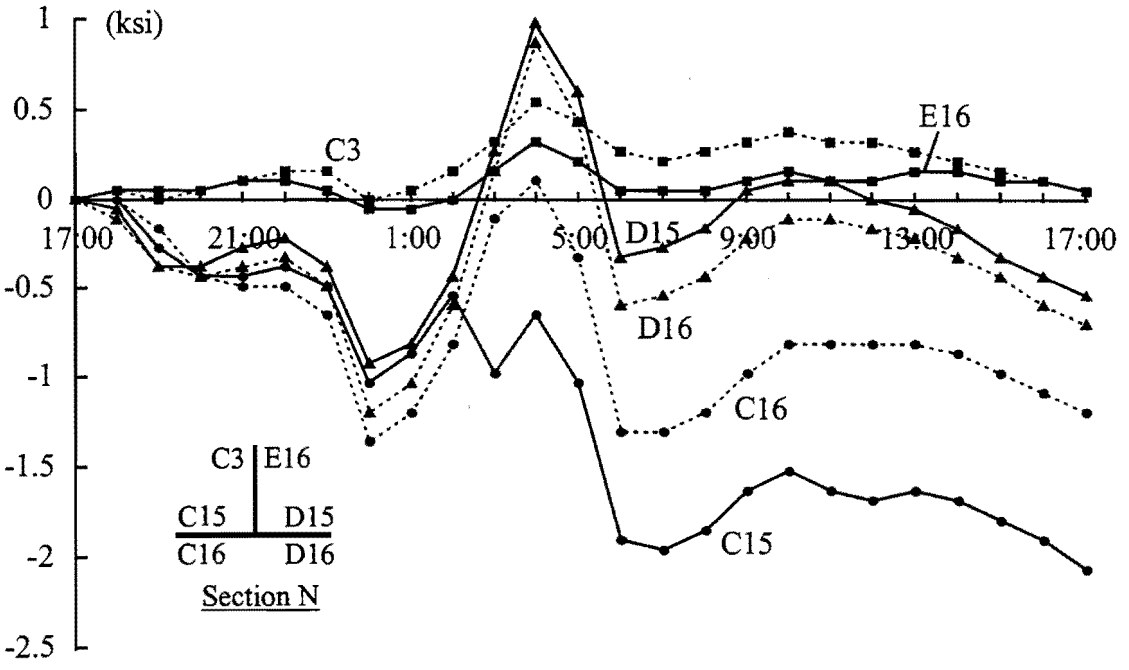

Figure 3.54. Stress Development in Stage 3 Slab Construction (Section N, the Diagonal)

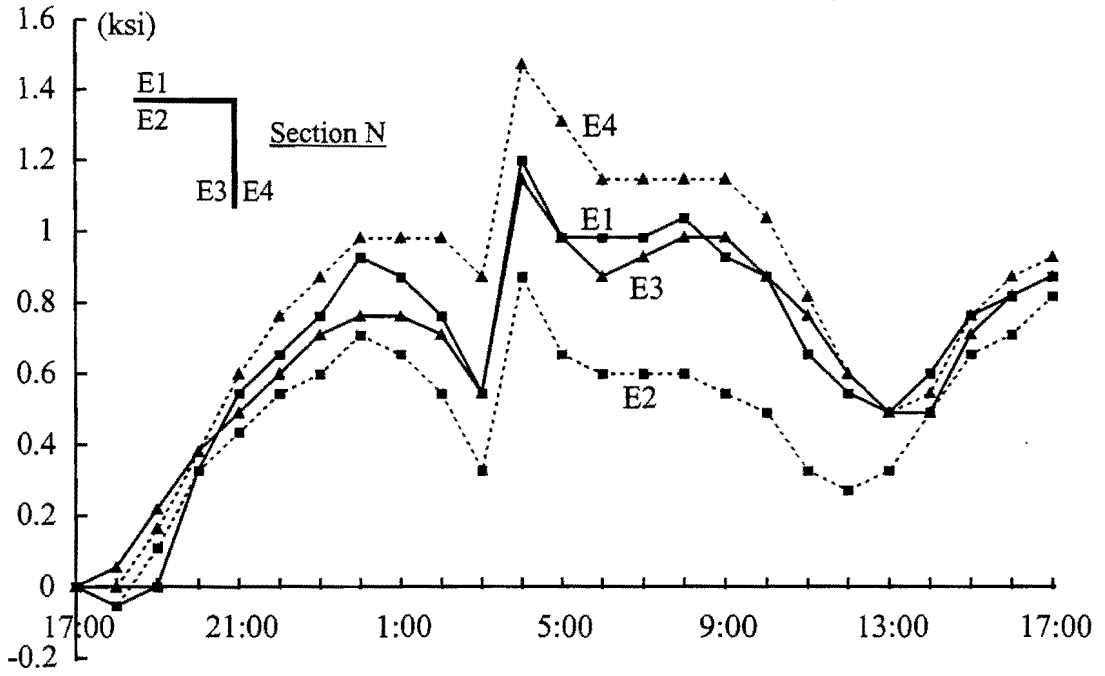

Figure 3.55. Stress Development in Stage 3 Slab Construction (Section N, the Strut)

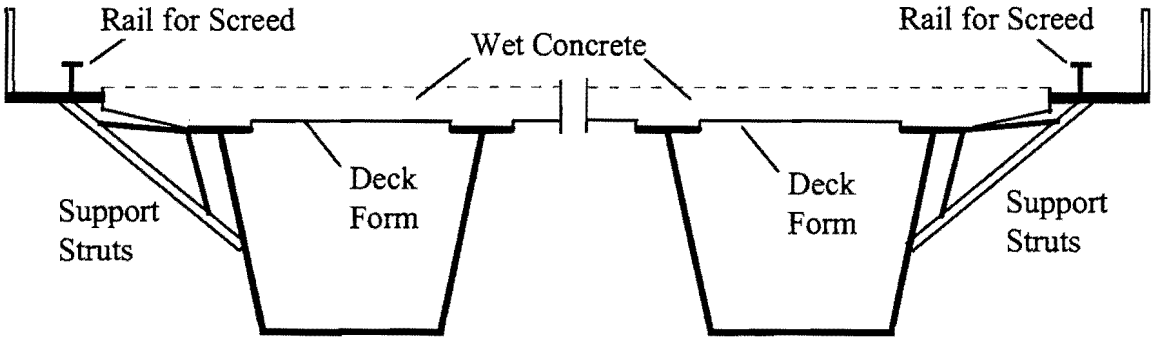

Figure 3.56. Support Struts on the Webs of Box Girders

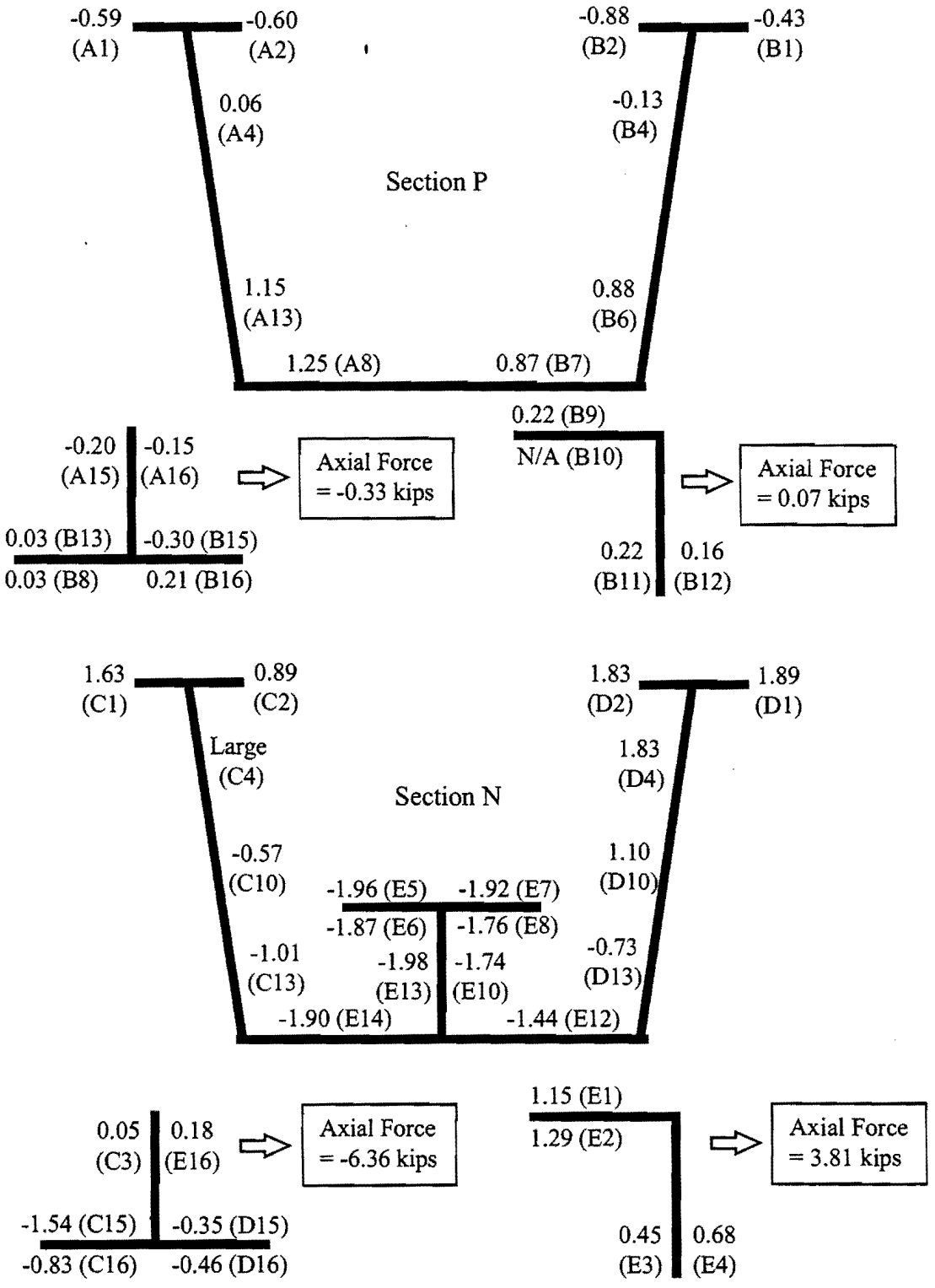

Figure 3.57. Stress Changes Measured During Stage 3 Slab Construction (between 22:00, 9/21/96 and 06:00, 9/22/96)

CHAPTER 4 FINITE ELEMENT ANALYSIS OF BOX GIRDER BRIDGE DURING CONSTRUCTION

4.1 Introduction

This chapter presents the results from a three-dimensional finite element analysis for quasi-closed box girder bridges. The approaches and assumptions used in the numerical studies are discussed. The model was used to study the construction phase of the bridge from the field studies. Comparisons are made between the computational solutions and the measured results presented in Chapter 3.

4.2 Modeling Box Girder Bridges by ANSYS

Results will be presented in this chapter from a three-dimensional Finite Element Analysis using the program ANSYS (ANSYS 1996) and performed on a Silicon Graphics Indy workstation. Three-dimensional FEA models were developed in this research investigation to study box girder bridges under various loading conditions. Both curved and straight girders were studied. The models discussed in this chapter simulate the construction process of the bridges from the field studies. Therefore, only the FEA results for quasi-closed box girders are presented. These models will also be used in Chapter 5 and 6 for the behavior study of quasi-closed box girders. Additional features to account for the concrete slab in the FEA models will be discussed and presented in Chapter 7.

The structural components of the quasi-closed box girders were modeled with shell elements, beam elements, and truss elements. A brief introduction of these elements is provided in this chapter. In addition, a brick element was used to model the haunches between the girder top flanges and the slab, which will be discussed in Chapter 7.

The shell element that was used is an 8-node quadrilateral shell element (Fig. 4.1), which can model both the out-of-plane bending and in-plane membrane deformations. Each node has six degrees of freedom: three linear translations, and three rotations. Stress results are available at the four corner nodes, while displacements are provided at all eight nodes. One of the advantages to using the 8-node shell element in this study is the high-order shape functions that permits modeling the geometry of curved structural components. The element was used to model the webs, the bottom flange and two top flanges of box girders, as well as stiffeners and solid diaphragms. Required input for the shell elements consist of the thickness and material properties. Most of the shell elements used were rectangular, however trapezoidal elements were used in solid diaphragms as well as in the flange transitions when a width change occurred in a small segment in the longitudinal direction.

Three-dimensional truss elements were also used to model some of the structural components. The element has two nodes that each have three degrees of freedom, the translations in the three directions. The element cannot model bending and torsional

deformations, and the cross-sectional area and material properties are the required input for the element. Truss elements were primarily used to model bracing members in the box girder bridges. Since the elements are pin-jointed at the nodes, geometrical instability must be avoided in bracing systems with multiple truss members that intersect at a single joint. Only one truss element can be used for each bracing member. If an X-type truss was modeled with the element, no joint was used at the intersection of the two members.

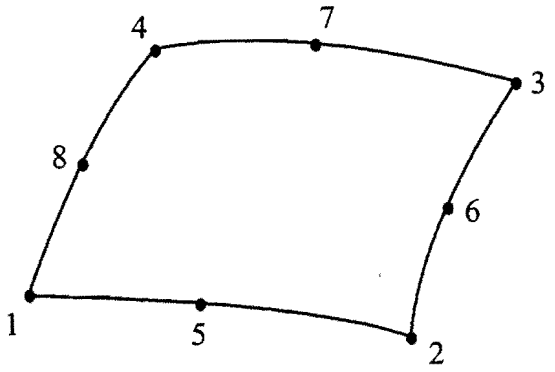

Figure 4.1. 8-Node Shell Element Used in FEA Models

The beam elements that were used were 2-node uniaxial elements with tension, compression, torsion, and bending capabilities. The elements have six degrees of freedom at each node: three translations and three rotations. Since the element is used to model the general beam behavior in 3D space, cross-sectional properties such as moments of inertia, cross-sectional area, and torsional properties are required. The element is unable to account for the warping effect in thin-walled beams. A third node, which must not be collinear with the first two nodes, was sometimes used to define a local coordinate system on the element. The element was used to model some of the bracing members in the box girder bridge. The beam element was required to ensure geometric stability of some of the cross-frames (K-frames) that had multiple truss elements intersecting at a single joint.

The mesh density that was used was fine enough to model the overall girder behavior. The girder cross-sections were modeled with four shell elements for the bottom flange and two elements for each of the top flanges, while five elements were employed for the webs (Fig. 4.2). The mesh density along the longitudinal direction was typically selected by controlling the element length-width ratio to be less than a factor of 3, however more elements were used when transition of plate thickness or top flange width occurs within a bracing panel.

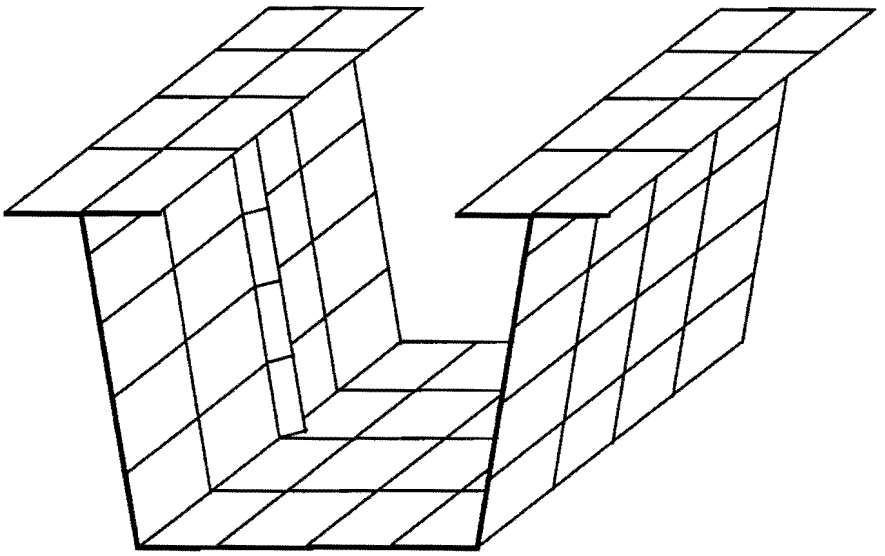

Figure 4.2. Typical FEA Mesh for Trapezoidal Quasi-Closed Box Girders

The fine mesh resulted in a relatively large FEA problem with a large number of nodes. The maximum node number allowed in each analysis in the version of ANSYS used was 16,000, which was less than the number of nodes needed to model the entire twin-girder bridge. The concept and procedure of substructures was therefore used to accommodate the analysis. The development of a substructure element begins by first defining the nodes and elements similar to ordinary FEA models. After the nodes and elements are defined, the substructure element is formed by defining master nodes that connect the substructure to other elements followed by a static condensation to obtain the stiffness information for the substructure. The various substructures are then assembled and solved to derive the displacement results at the master nodes of each substructure. The displacement and stress results inside each substructure are then expanded from the master node results.

4.3 Assumptions and Considerations in FEA Model

The construction process of the project bridge was modeled by ANSYS using the element and techniques described above. The following are some of the details about the assumptions, procedures and considerations that were used in modeling the structure.

4.3.1 Geometry and Configuration

The geometry of the FEA model was obtained from the shop drawings of the bridge. The drawing provided the sizes of all plates that were used in the girder flanges, webs, transverse stiffeners, and solid diaphragms, and also specified the sizes of the bracing members and the longitudinal stiffeners. Before the girders were erected, dimensions of the boxes at several locations were measured for verification of the shop drawings. The measured dimensions of the plates and the bracing members were very close to the specified values in the shop drawings.

The spans, radii, and cross-sectional dimensions of the bridge were given in Figs. 3.2 and 3.3. The bridge had 7.9% super-elevation in the lateral direction. In addition, the downward slope between Bents 17 and 20 was approximately 3°.

As mentioned earlier, the sizes of all plates in the girders were constant except the plate thickness and the width of the top flanges. The plate thickness was input as the real constant of the corresponding shell elements. The change of the top flange width was modeled by trapezoidal elements as illustrated in Fig. 4.3.

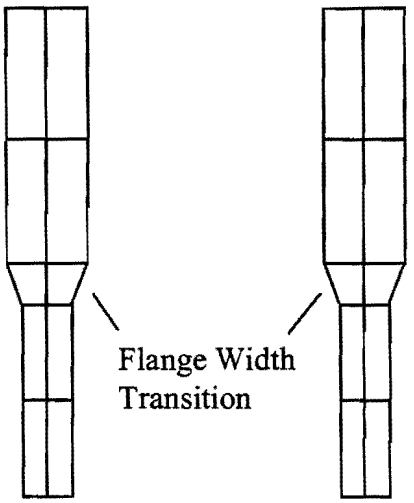

Figure 4.3. Modeling Top Flanges with Shell Elements

All major components of the girders were modeled with the exception of the transverse stiffeners on the solid diaphragms (at the supports) and a few transverse stiffeners on the bottom flanges in the negative moment regions. These structural elements are provided to control local buckling of the individual elements, but were not expected to significantly affect the static analytical results.

The horizontal truss system was located approximately 11 inches below the bottom of top flanges. Members in the truss system were modeled with either beam or truss elements, and were connected directly to the webs. Transverse stiffeners were provided on the webs at the joint to bracing members. For internal K-frames, each diagonal connected to the joint between the web and the bottom flange, and framed to the middle of the lateral strut at the other end. It was found in several trial analyses that the girder stresses, as well as the axial brace forces were essentially the same regardless of whether truss or beam elements were used. This implies that the axial stiffness of the bracing members governs the behavior of the girders. The bending and torsional stiffness of bracing members have little effect on the response of the girder and bracing system to external loads.

4.3.2 Supports and Number of Girders

The box girders were supported by pot bearings on the top of the pier caps. Each girder was supported by a bearing at the middle width of the bottom flange on each support. At Bent 18 both girders were prevented from longitudinal movement. Therefore, in the FEA model roller supports were assumed at Bent 17, 19 and 20 while pin supports were used at Bent 18. These support conditions were applied to the nodes at the middle width of the bottom flange on supports. Radial movement was prevented at all supported nodes.

For curved bridges, the roller supports are usually aligned along the chord direction from the pin support such that the girders are allowed to move radially from the pin support when experiencing thermal deformation. However, field inspection indicated that the chord layout was not adequately realized due to misalignment of the bearings below the girders. The radial supports as discussed above better modeled the condition in the bridge used in the field studies.

The initial model consisted of the twin girders connected to each other by solid diaphragms at Bents 18 and 19 and external cross-frames at Bents 17 and 20. This model gave solutions for the girder stresses and also the stress and axial force results in the external diaphragms and cross-frames. These results were used before slab construction to review the initial design. As a result, it was found the cross-frames proposed in the original design were inadequate for the slab construction and therefore the external cross-frames were retrofitted by doubling the size of the diagonals in each of the K-frame systems. Based on the stress results of the twin-girder FEA model, the slab construction plan was also modified.

The twin-girder model consisted of more than 40,000 nodes and required large computer resources to support the analysis. Trial analyses indicated that the two-girder model was unnecessary in estimating the stresses and brace forces on an individual girder. According to the FEA results, the rotation of the girder cross-section at the support was relatively small due to the stiff diaphragms. Therefore, the single girder model of the interior girder on which the field studies were carried out replaced the twin-girder model. The support conditions shown in Fig. 4.4 were applied to the girder at all supports. The restraint from the external cross-frames and diaphragms was simulated by the rigid lateral restraints at two points on the girder web. Figure 4.4 also shows the FEA mesh for the internal solid diaphragms provided at the supports. An additional longitudinal restraint was also applied on the bottom flange at Bent 18. The FEA results presented in this chapter are from this single girder model.

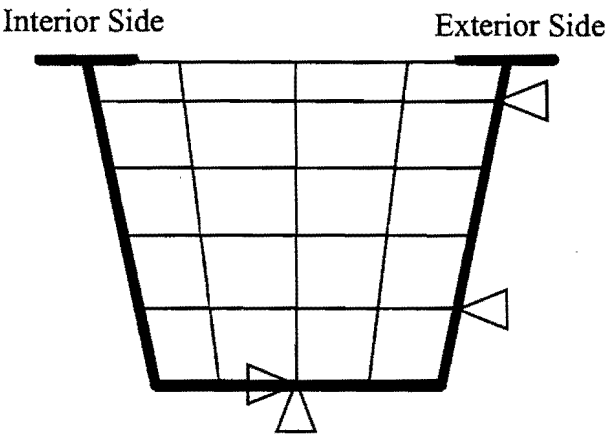

Figure 4.4. Restraints Applied to the Supports of the Single Interior Girder Model

4.3.3 Loads

During construction, the loads on the box girders consisted of the self-weight of the girder segments and the gravity load of the concrete slab. Permanent metal deck forms were connected to the top flanges of the box girder to support the wet concrete. In the FEA model, the gravity load of the concrete and other miscellaneous construction loads were applied to the girders in the form of distributed linear loads (kips/ft) applied at the middle of the top flanges. The weight of the reinforced concrete was assumed to be 0.15 kips/ft^3. An additional 20 lb/ft^2 deck load was added to simulate loading from the construction workers and equipment. The resulting distributed load was estimated to be 2.88 kips/ft on each girder. This load was proportioned between the top flanges based on the layout of the bridge deck. The thickness and length of the overhang was less than half the spacing between adjacent girders as shown previously in Fig. 3.2. As a result, the interior flange had a smaller load than the exterior flanges as shown in Fig. 4.5.

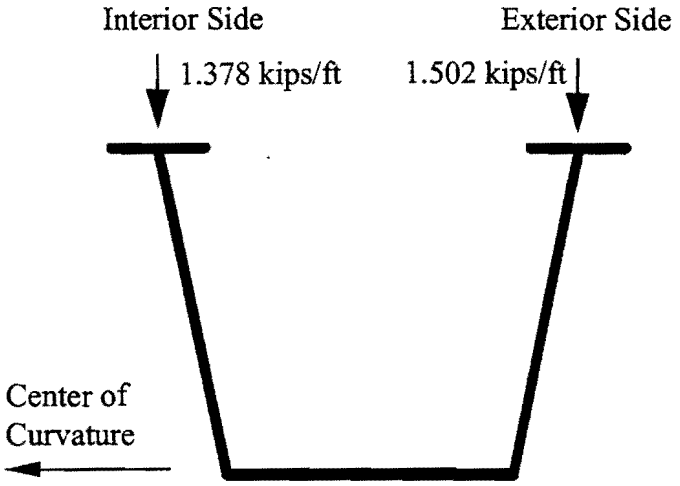

Figure 4.5. Distributed Loads Used to Simulate the Weight of Concrete Slab

The largest equipment in the slab construction was the screed that was used to evenly distribute and finish the concrete. The total weight of the screed was approximately 8.4 kips, which was supported by a rail on the outside of the slab overhang. The weight of the screed was represented by exerting additional concentrated forces (lateral and vertical) and moments at the top flanges. However, it was found that the stress increase due to the screed load was essentially negligible. Therefore, these concentrated loads from the screed were later removed from the FEA model. The gravity load of the construction equipment was assumed to be included in the 20 lb/ft^2 surface construction load.

To simulate the erection of Segment 905 and 907, the self-weight of the girders was approximated using the weights of the segments provided by the shop drawings as presented previously in Table 2.1. Gravity loads were represented by linear distributed loads on the top flanges. The total weights of segments 905 and 907 were divided by the length of the corresponding segments, and the resulting distributed loads were applied evenly to the top flanges.

4.3.4 Composite Section

As outlined in the last chapter, the concrete had time to cure between stages. Therefore in Stages 2 and 3 of the slab construction bridge segments with concrete curing from earlier stages had some composite action between the girders and the slab. The instrumented cross-section in the positive moment region, Section P, was in a region that was partially composite in Stage 2 and 3 slab construction. Composite action between the slab and the girders significantly stiffens the structure. In addition, the neutral axis shifts towards the top flanges, which significantly reduces the forces in the bracing members of the top flange truss system. As a result, girder and brace stresses in these areas were relatively small.

Modeling the composite action of box girders in FEA analyses requires additional techniques. A three dimensional FEA model that can analyze the slab and box girder system were developed in this project. The FEA model for the slab and girder system will be discussed in Chapter 7 along with the results from the live load tests on the bridges.

During the slab construction, however, the concrete had not reached full strength and therefore the elastic modulus was unknown during Stages 2 and 3 of slab construction. In practice, the partially hardened slab is usually not considered, resulting in a conservative estimation of girder stresses. Therefore, in studying the slab construction process, the concrete that was cast in the earlier stages was not included in the FEA model. As a result, the FEA stress and brace force results at Section P that will be presented for Stages 2 and 3 will generally be larger than the measured results. Although neglecting composite action during Stages 2 and 3 may have a small effect on the stresses at Section N, the effect should be relatively small.

4.3.5 Effect of Metal Deck Forms

Metal deck forms were placed on the top flanges prior to the construction of reinforced concrete slab (Fig. 4.6). The deck forms increase the stiffness of the box girder system and improve the stability during the construction. The bracing effect of the metal deck forms is generally neglected in current design methods, which often results in conservative designs of bracing systems for construction loads.

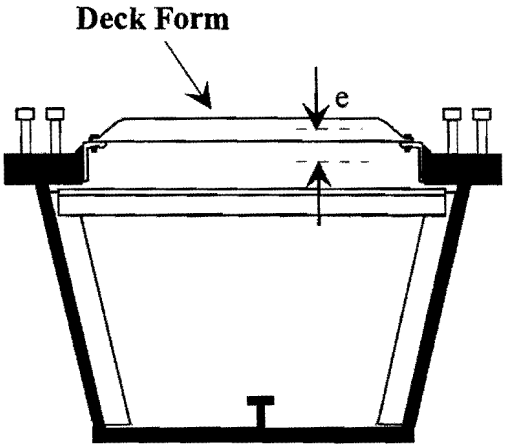

Figure 4.6. Metal Deck Form on Box Girder

The in-plane tensile stiffness of the deck in the longitudinal direction of the girders is relatively small due to the corrugation in the forms. The deck forms will therefore have a negligible effect on the bending stiffness of the box girders, particularly compared to the large bending stiffness of the U-shaped girders. The in-plane shear stiffness of the metal forms can be quite substantial and may significantly increase the torsional stiffness of the girders. Helwig (1994) studied the effect of the metal deck forms in I-girder steel bridges, and found that the contribution of deck forms to the stiffness of the girder system depends heavily on the type of connection used between the deck forms and the girder flanges.

As shown in Fig. 4.6, metal deck forms are often supported on cold-formed angles that allow the form elevation to be adjusted to account for differential camber between adjacent girders. Although the support angle helps maintain a uniform slab thickness, the flexible angle can significantly reduce the in-plane shear stiffness of the deck forms. This is particularly true for large eccentricities (e in Fig. 4.6) between the top flange and the metal deck form.

The eccentricity of the metal deck form to the top flanges was measured approximately every 10 ft. along the girder length in the interior girder between Bents 17 and 18 where the instrumented sections were located. The deck eccentricity was found to vary along the length of the girder. With the exception of a few spots, the offsets between the planes of the deck forms and the girder top flanges in most regions fall into the range of ±1 inch. The

eccentricities at both instrumented sections were found to be close to zero. Therefore, the girder may possess larger torsional stiffness than estimated because of the existence of the metal deck forms.

Another factor that may affect the contribution of the metal deck forms to the girder stiffness is the support condition for the deck forms. Figure 4.6 illustrates the support detail of the deck forms used in the positive moment regions of the bridge, where the support angles were connected to the top flanges of the box girders by intermittent fillet welds. Due to the fatigue concern, however, welding in the field is not allowed on the top flanges in the negative moment regions. Figure 4.7 illustrates the detail used in the negative moment regions of the bridge. The support angle was welded directly to the "strap", a flat plate that spans the top flange of the girder. Welding in the negative moment region in the field was thus eliminated. Since the deck form system was not directly connected to the top flanges, the support detail shown in Fig. 4.7 was generally more flexible than the one shown in Fig. 4.6. It is possible that there were gaps between the support angles and the top flanges. However, as the construction progresses these gaps might be closed due to the deflection of the girder under the applied loads. As a result, the bracing effect of the deck forms may increase during construction because the support angles may come into contact with the girders.

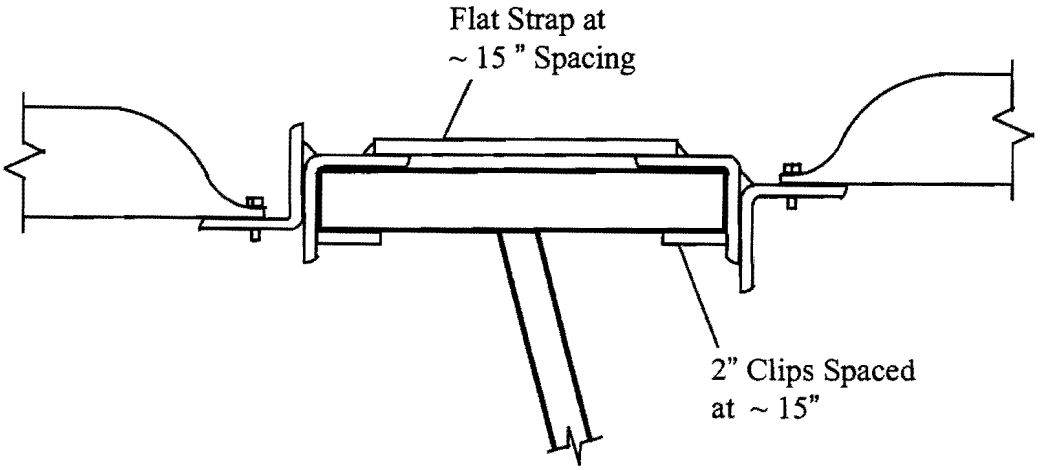

Figure 4.7. Support Detail for Metal Deck Forms in Negative Moment Regions

The stiffness of the deck forms on the bridge was therefore difficult to define, due to the irregular eccentricities to the top flanges and the indeterminate condition in the connection to the box girder. Therefore, the deck forms were not considered in the FEA model in studying the construction. This would only affect the FEA results for the slab construction phase since the forms were placed after the girders were erected.

4.4 Measured and FEA Results for Bridge Construction

The construction processes that were monitored and discussed in the last chapter were simulated using the FEA model discussed in the last two sections. The girder stresses from the FEA solutions will be presented at the corner nodes of the shell elements. The FEA output for the bracing members was the axial forces, which will be compared with the field results. The axial forces from the field results were converted from the stress readings from gages on bracing members using the algorithm discussed in Appendix B. Material behavior in all the analyses was assumed to be linear-elastic.

4.4.1 Results for Girder Erection

The FEA model for the erection of Segment 905 only included Segments 901, 903 and 905 as shown in Fig. 4.8a. The self-weight of Segment 905 was modeled by distributed loads applied on the top flanges. The erection of Segment 907 was represented by the entire interior girder subjected to the distributed load above Segment 907 (Fig. 4.8b). The distributed loads were equal to the total self-weights divided by the lengths of the respective segments. Due to the poor behavior of the one-sided gages, stress readings on the webs and the bottom flanges were unavailable during the erection of the girders, as indicated in the last chapter.

Figures 4.9 to 4.12 are the measured and FEA results for the erection of Segment 905, which generated negative bending moments in the span between Bents 17 and 18. The moment on Section P was relatively small, and the only discernible stress changes on Section P were in the top flanges. The measured and FEA results for the top flanges are presented in Fig. 4.9. Stresses from the FEA model are larger than the field results. Similar behavior can be observed for top flange and longitudinal stiffener stresses on Section N (Fig. 4.10), however the agreement between measured and FEA stresses are generally better than those on Section P. Significant axial force developed in the diagonal member near Section N in the horizontal truss. The FEA model predicted 29.3 kips tensile force, which is 24.5% less than the measured value of 38.8 kips. The measured and FEA model gave respective strut forces of -2.55 kips and -2.19 kips. The negative value indicates compression.

Larger stresses developed during the erection of 907. Reasonable agreement was achieved between the test and FEA results on Section P (Fig. 4.11) for both the top flange stresses and the brace forces. Approximately 14 kips of compressive axial force developed in the diagonal, as reported from both the test and the FEA model. For the lateral strut, a tensile axial force of 1.53 kips was measured during the test. FEA results also predicted a tensile force, however the force was nearly zero (0.2 kips).

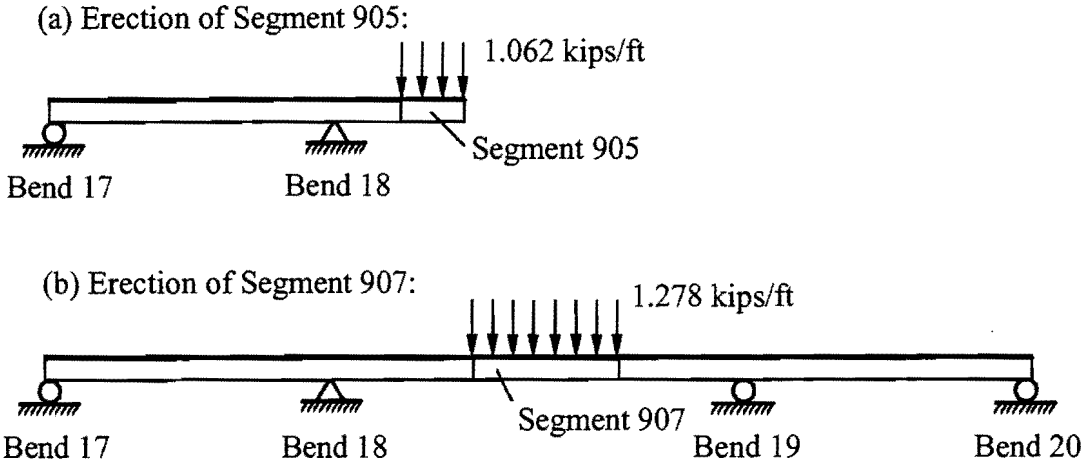

Figure 4.8. Models Used to Simulate the Erection of Segments 905 and 907

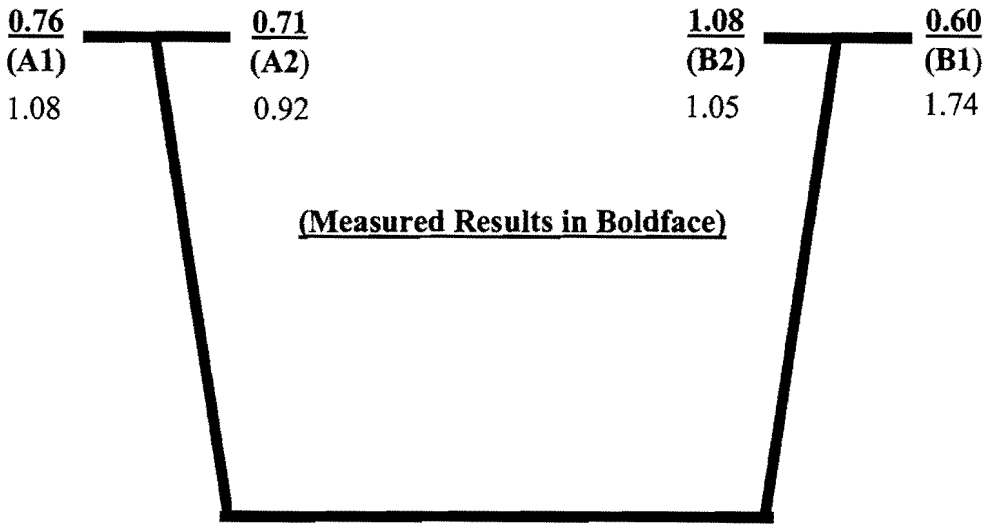

Figure 4.9. Field and FEA Results for the Erection of Segment 905, Section P

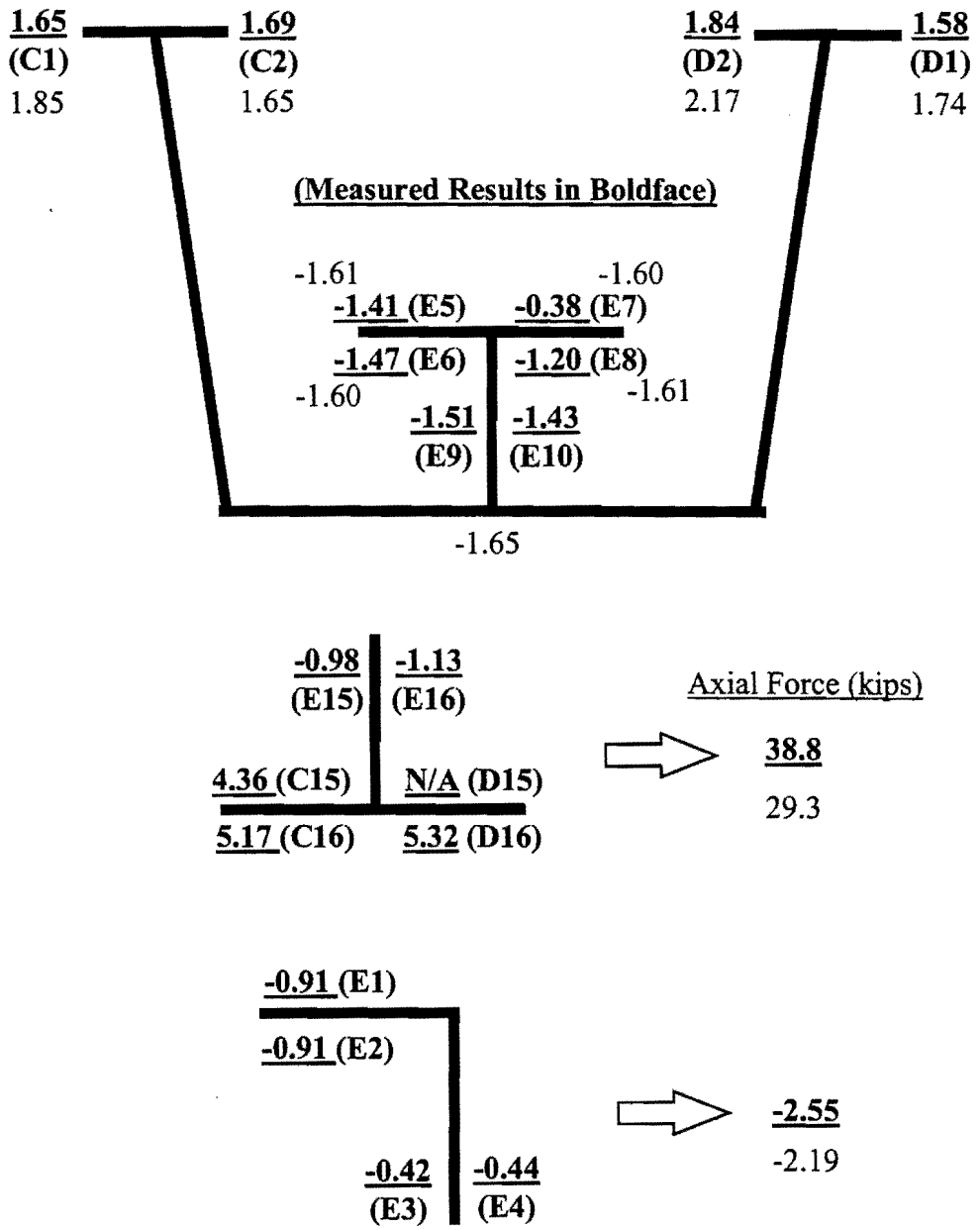

Figure 4.10. Field and FEA Results for the Erection of Segment 905, Section N

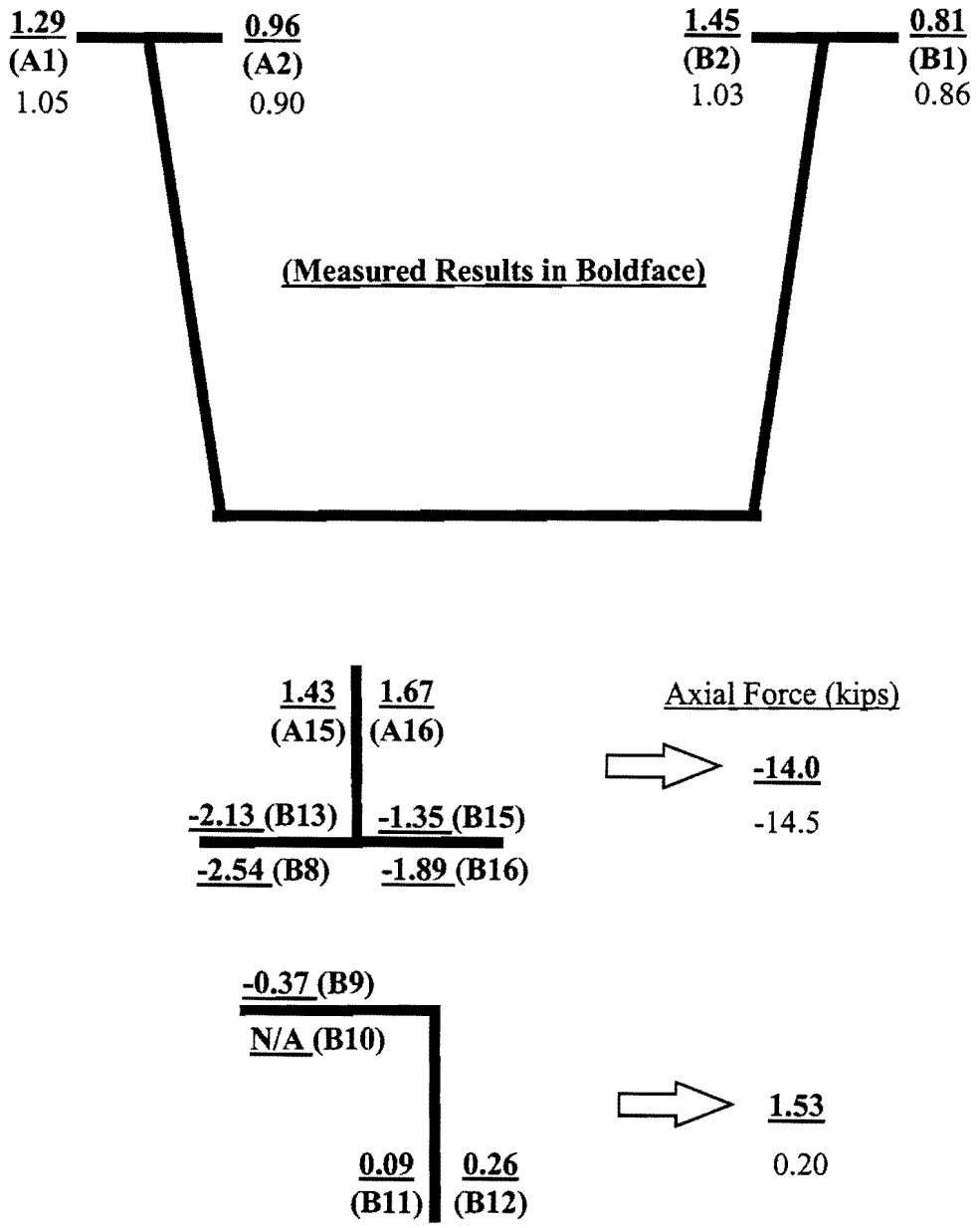

Figure 4.11. Field and FEA Results for the Erection of Segment 907, Section P

Measured and FEA results on Section N during the erection of Segment 907 also matched relatively well, as shown in Fig. 4.12. The stresses in the top flanges and in the longitudinal stiffener were still relatively small, as was the brace force in the strut. The measured force in the diagonal was 30.9 kips, which has a good agreement with the 29.7 kip force from the FEA model. The results for the strut force for both the measured and FEA solution were in compression, however the measured value was approximately 34% larger than the FEA value.

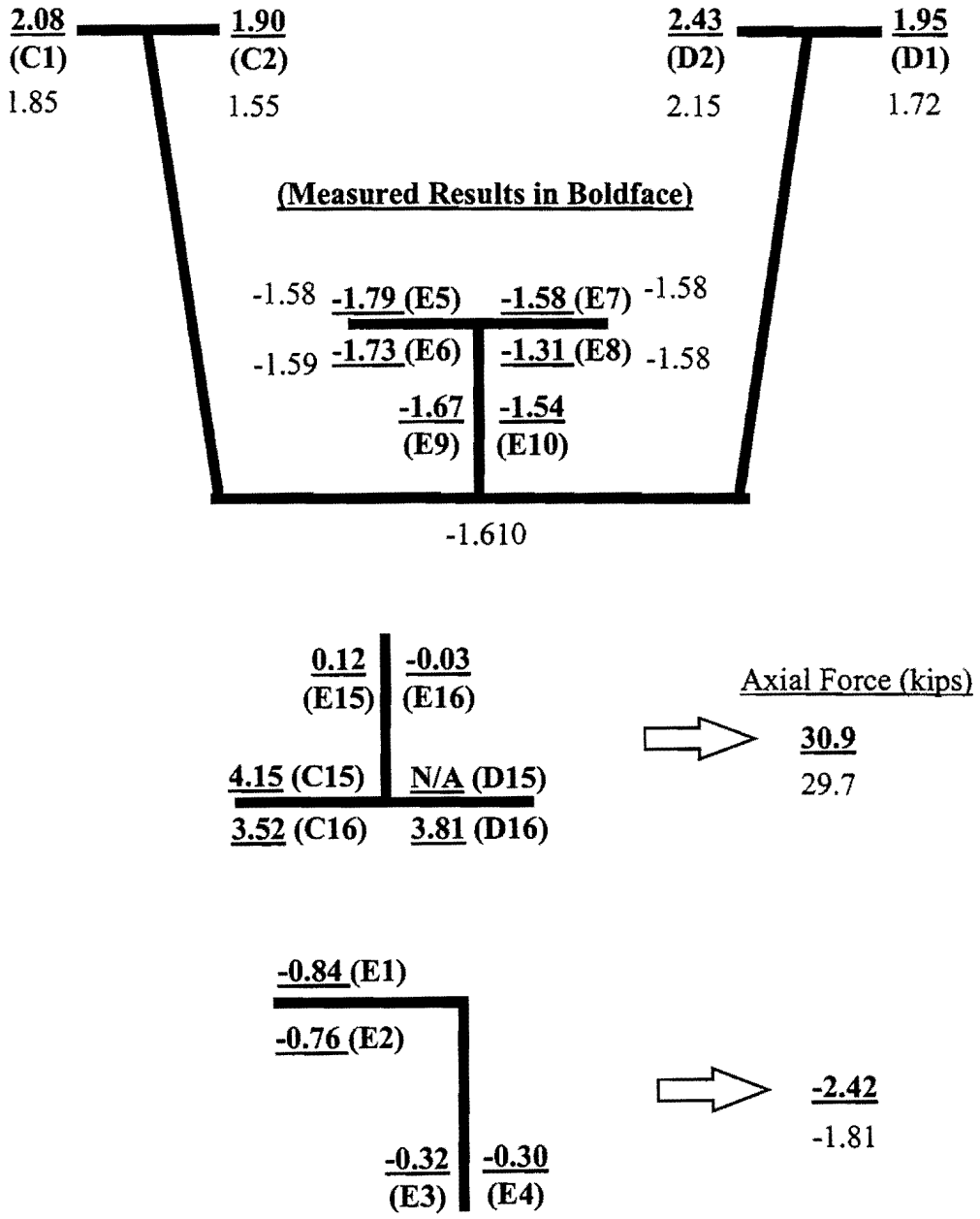

Figure 4.12. Field and FEA Results for the Erection of Segment 907, Section N

4.4.2 Results for Slab Construction

The FEA models for slab construction consisted of the entire interior girder without considering the composite action. The loading conditions were previously illustrated in Fig. 3.7. The one-sided gages were replaced on the web and the bottom flange so that stresses could be measured throughout the cross-section.

Figure 4.13 presents measured and FEA results at Section P due to the concrete cast on the south side (near Bent 17) during Stage 1 slab construction. The top flange gages had better agreement with the FEA results than the bottom flange gages. Stresses on Section N were relatively small during Stage 1 slab construction, as shown in Fig. 4.14. Although the top flange brace forces had good agreement at Section N, very poor agreement was observed at Section P. The FEA solution significantly overestimated the brace forces, probably due to bracing provided at the permanent metal deck forms as outlined earlier. Although agreement between the FEA and measured results for the brace forces varied between Sections P and N, the FEA model predicted the girder stresses that match the field results reasonably well for the first stage of slab construction.

The concrete cast in Stage 1 developed some strength when Stages 2 and 3 slab construction took place. Therefore, composite action was expected in regions with concrete curing from earlier stages. Composite action was not considered in the FEA model in studying Stages 2 and 3. As a result, the measured girder stresses and brace forces are considerably smaller than the FEA stress results at Section P, as shown in Figs. 4.15 and 4.17. Most stress readings were less than 1 ksi. Without the concrete, the FEA model predicted the girder stresses and brace forces that were several times larger than the test results.

Section N is located in a region in which the slab was constructed in Stage 3. Therefore, no direct composite action occurred on Section N throughout the entire slab construction. The FEA stress results had reasonable agreement at Section N for both Stages 2 and 3, as shown in Figs. 4.16 and 4.18. The girder experienced the largest stress increase in Stage 2, with more than 7 ksi tensile stresses added in some areas of the top flanges. The FEA model not only predicted the stress levels relatively well, but also showed the lateral bending of the top flanges in the same direction as observed from the field results. Therefore, although the cross-sectional properties of the girder was not precisely modeled in the FEA analysis in some regions along the girder length due to neglecting the partial composite action, the girder stresses in other regions can still be effectively evaluated.

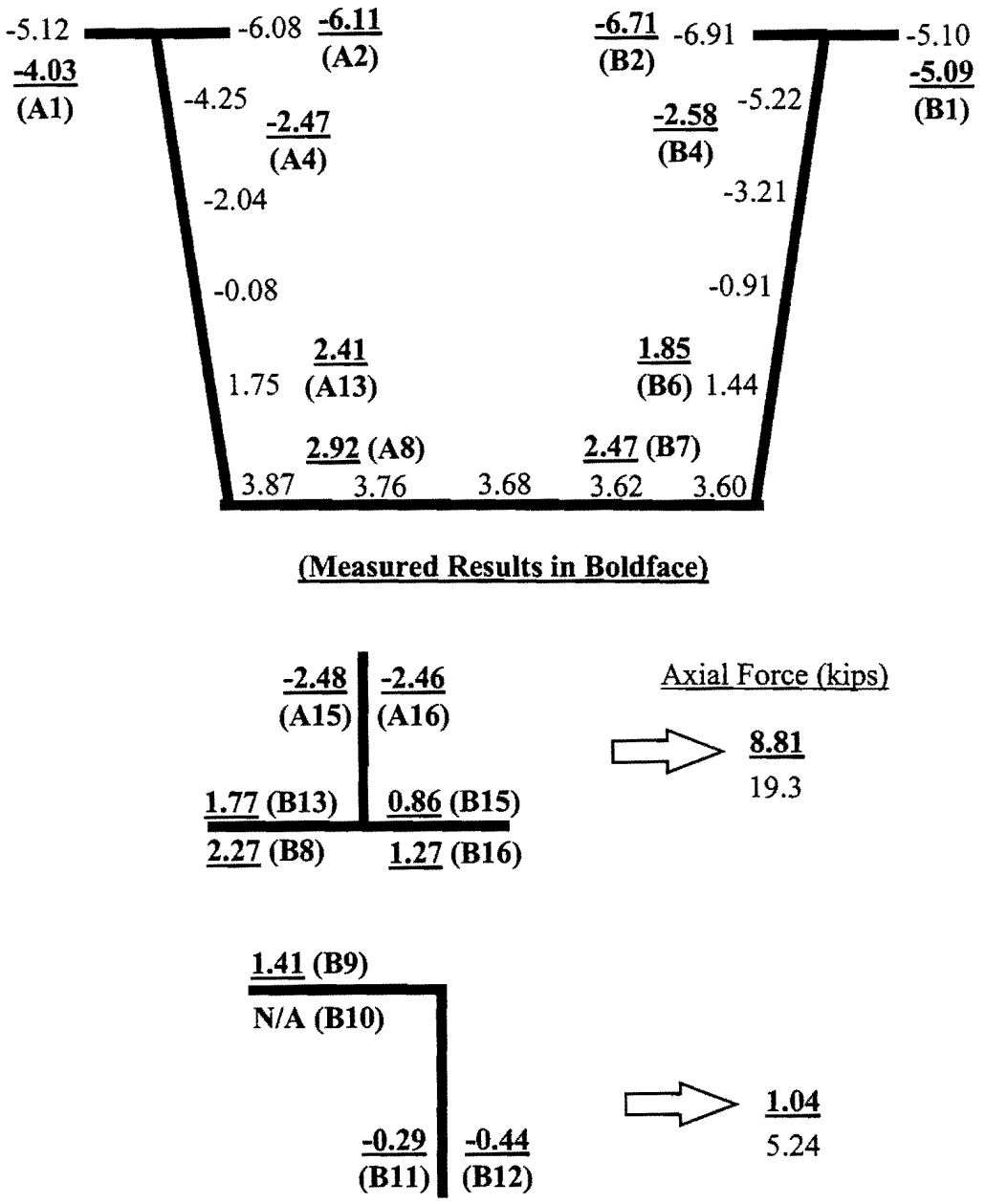

Figure 4.13. Field and FEA Results for Stage 1 Slab Construction, Section P

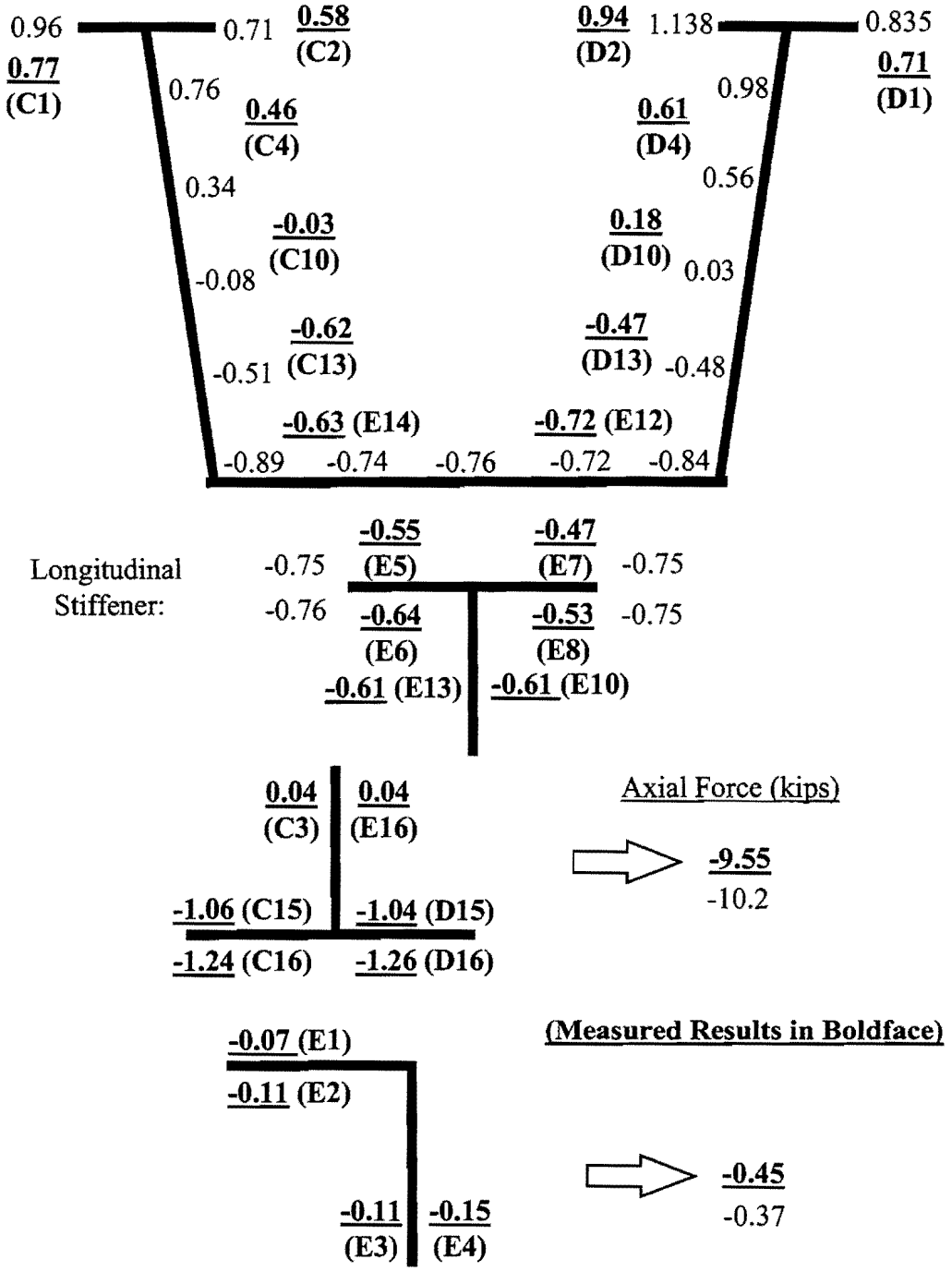

Figure 4.14. Field and FEA Results for Stage 1 Slab Construction, Section N

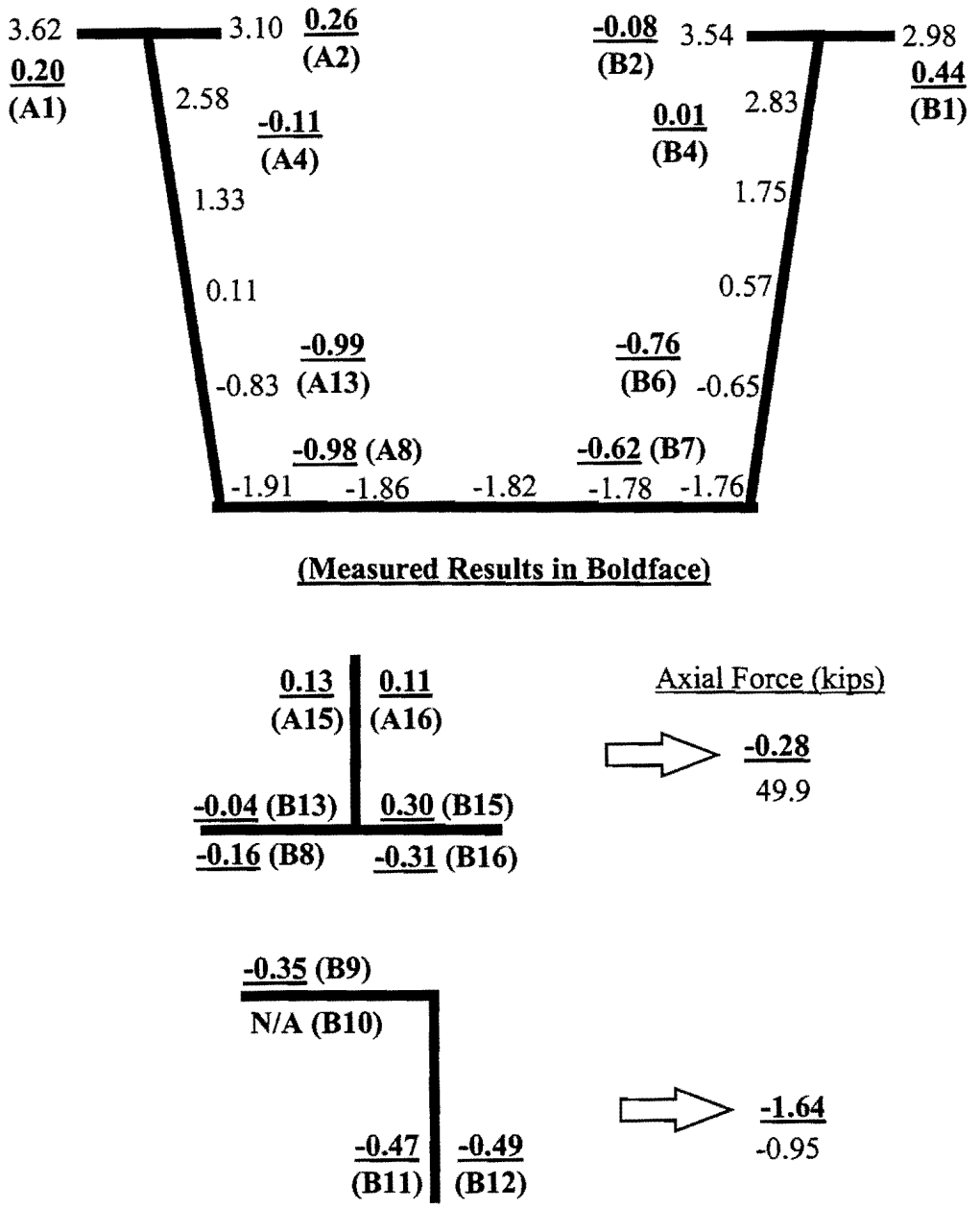

Figure 4.15. Field and FEA Results for Stage 2 Slab Construction, Section P

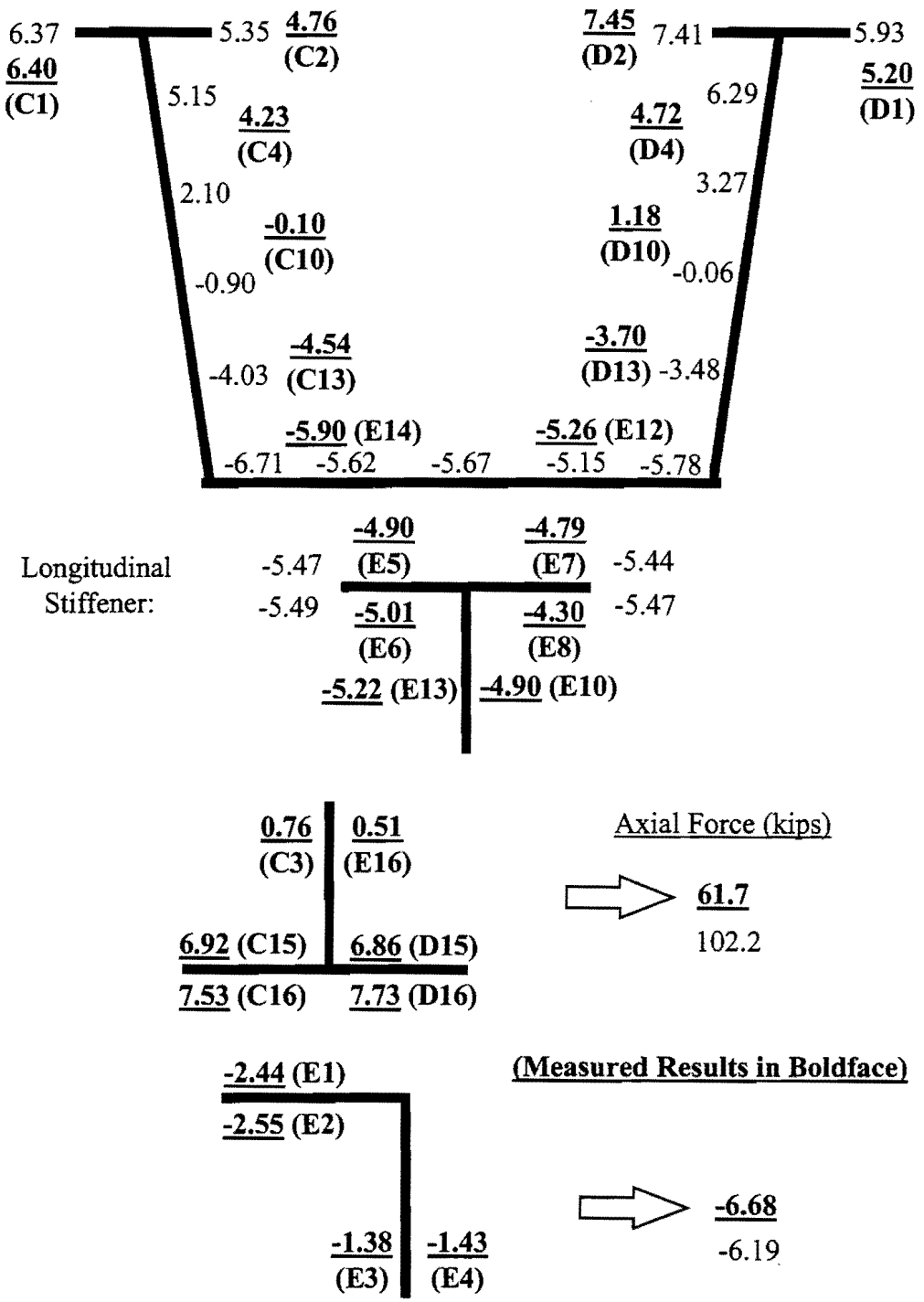

Figure 4.16. Field and FEA Results for Stage 2 Slab Construction, Section N

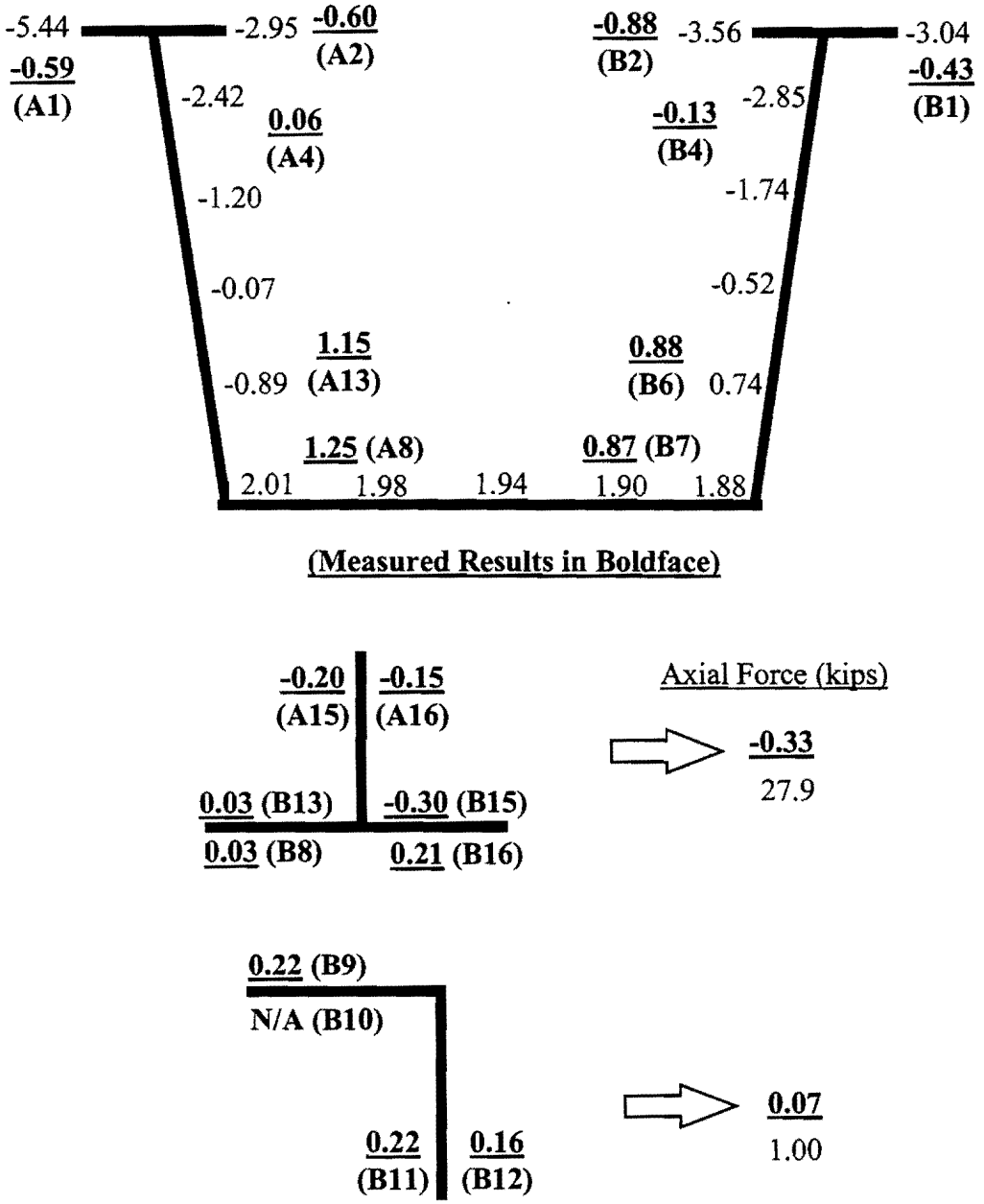

Figure 4.17. Field and FEA Results for Stage 3 Slab Construction, Section P

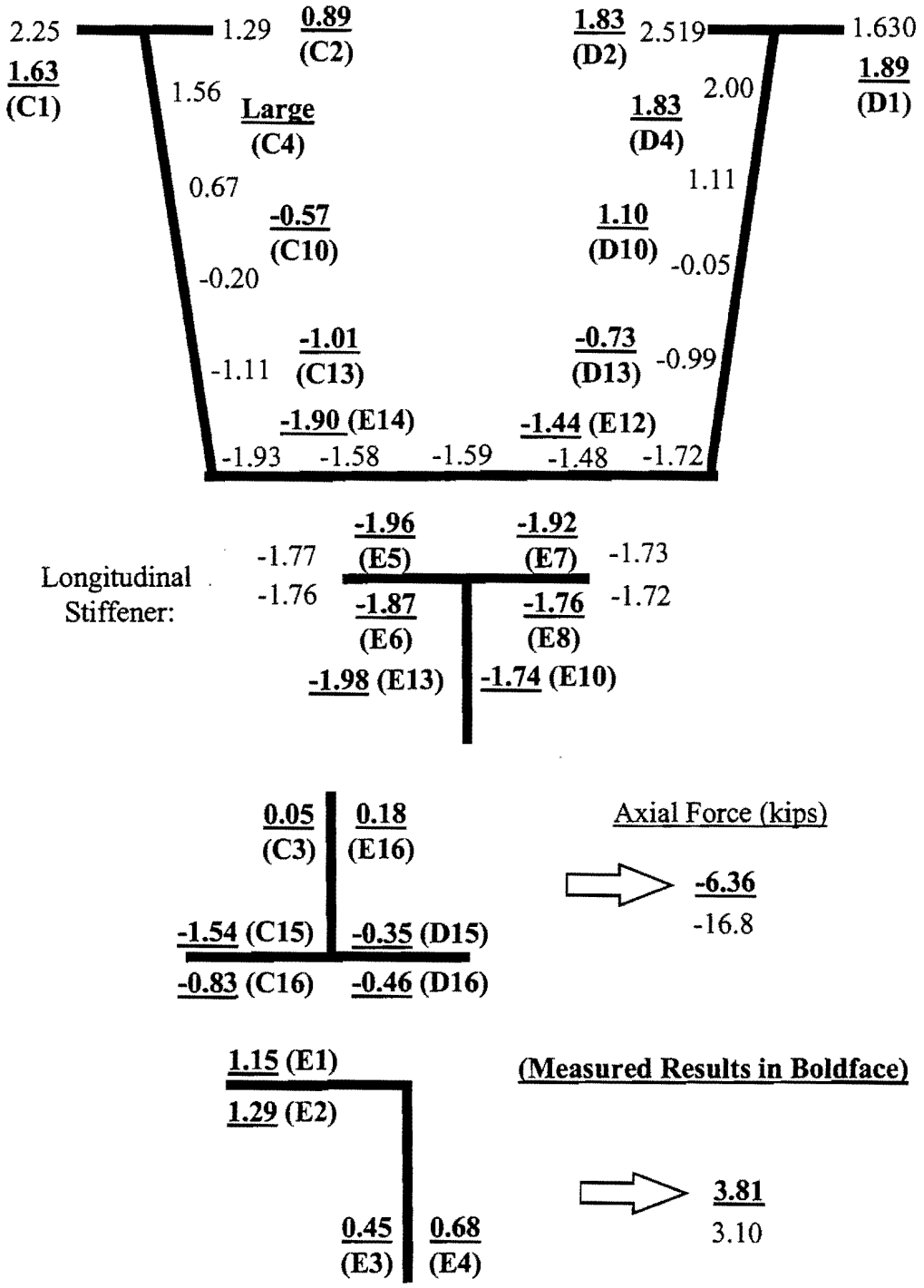

Figure 4.18. Field and FEA Results for Stage 3 Slab Construction, Section N

Measured brace forces at Section N (particularly the diagonal) had relatively poor agreement with FEA results during Stages 2 and 3 slab construction (Figs. 4.16 and 4.18). This differs from Stage 1 construction, when the measured brace forces agreed reasonably well with the FEA results at Section N (Fig. 4.14). The support detail for the deck forms in Section N was shown in Fig. 4.7. As indicated earlier, it is possible that in the early period of construction (Stage 1) the deck form system had some gaps in the connection to the girder at Section N, and thus the bracing effect of the deck form system was relatively small. If these connection gaps were closed during Stage 2 slab construction due to the deflection of the girder subjected to the concrete weight, the metal deck forms could provide significant bracing to the top flanges. Computing the percent difference of the FEA forces in diagonal with respect to the measured results yields the following results:

Stage 1: 6.8%
Stage 2: 65.8%
Stage 3: 163.7%

The metal deck form connection coming into contact in the middle of Stage 2 would explain why good agreement was achieved in Stage 1, poor agreement in Stage 2, and very poor agreement was observed in Stage 3. The measured and FEA results for the strut forces at Section N had reasonable agreement for all three stages of the slab construction. However, the strut does not significantly affect the torsional stiffness of the box girder and would not be significantly affected by the metal deck form. The poor agreement in the strut force at Section P in Stage 1 (Fig. 4.13) may be partly due to the missing data from one of the strain gages that was lost on the strut at Section P, resulting in less information to compensate the errors in the readings measured in the field.

4.4.3 Summary of FEA Modeling for Quasi-Closed Box Girder

The field results and the FEA solution for both the girder stresses and the brace forces were presented and compared. The agreement between the FEA solution and the field results varied depending on the stage of construction. Larger errors generally occurred with lower stress changes. The FEA model was able to reasonably predict the magnitude and distribution of the girder stresses and brace forces during girder erection. The FEA model during slab construction consisted of the quasi-closed box and did not include the effect of the metal deck forms or the partially hardened concrete. The FEA model of the quasi-closed box girder tended to overestimate the horizontal truss forces after the metal deck forms were added to the bridge. This would indicate that the metal deck forms help to resist the torsional loads applied to the girder. Although the metal deck forms reduced the forces in top flange truss, the top flange stresses were relatively unaffected. The FEA model often predicted not only the primary bending stresses relatively well, but also the distribution and magnitude of the lateral bending and warping stresses were in agreement with the field results.

The partially hardened concrete provided some composite action with the steel girder, which was not reflected in the FEA results. The FEA solutions were consistent with current design provisions that do not permit relying on bracing by the metal deck forms or the partially hardened concrete. Therefore, since the FEA model had good agreement with field results for the steel section alone, the computer model was used to conduct parametrical studies on the quasi-closed box girder. The top flange truss and internal K-frames of the box girder are studied in the next two chapters, using the FEA model developed in this chapter.

CHAPTER 5 ANALYSIS OF BOX GIRDERS WITH TOP FLANGE BRACING

5.1 Behavior of Box Girders with Top Flange Bracing

In Chapter 4, the three-dimensional FEA model for quasi-closed box girders was developed and verified by the field studies. In this chapter, the FEA model is used to study the behavior of quasi-closed box girders and the results will be presented focusing on the behavior of the top flange bracing system.

According to the current design method (Highway 1982, Four 1997), the horizontal truss fastened to the top flanges of the box girder is designed to carry brace forces resulting from the torsional moments and the lateral components of the vertical loads on the top flanges during the construction. Chapter 2 discussed methods used in estimating the axial forces in the diagonal members. The Equivalent Plate Method (EPM) method as shown previously in Fig. 2.12 is used to calculate the brace forces in the diagonals, while forces in the lateral struts was estimated using the formula previously shown in Fig. 2.14. To demonstrate the accuracy of the current design method, the FEA model discussed was used to perform a series of analyses to study the behavior of quasi-closed box girder.

As outlined in the last chapter, shell elements were used to model the box section, while truss and beam elements were used to model the top flange truss and internal K-frames. At internal K-frame locations, the struts of the top flange truss also act as the top laterals of the internal K-frame. The purpose of the internal K-frames is to control distortion of the box section and will be discussed in detail in Chapter 6. The distortional forces in the diagonals of a K-frame cause the two top laterals (L1 and L2 in Fig. 1.2a) to have equal magnitudes of compression and tension. If the strut from the top flange lateral truss was also part of the K-frame, the axial strut forces from the FEA results were the average of the forces in the two halves (L1 and L2 in Fig. 1.2a), thereby eliminating the K-frame component.

5.1.1 Torsional Loading

The straight girder shown in Fig. 5.1 was first analyzed with a three-dimensional FEA model. Twist of the simply-supported girder was prevented at the ends and a uniformly distributed torque of 5 k-ft/ft was applied. Forces in the truss members as determined using the EPM were based on the value of the torque at the middle of the corresponding truss panel. A SD-type and an X-type truss were considered. Figure 5.2 shows that the EPM has excellent agreement with the FEA results. The data points from the EPM and the FEA are nearly coincident. Negative values of the truss forces indicate compression. The torsional loading causes the diagonals within a panel of an X-type truss to have equal magnitude, however one diagonal is in compression while the other is in tension. The diagonals of adjacent panels in a SD-type truss typically alternate compression and tension.

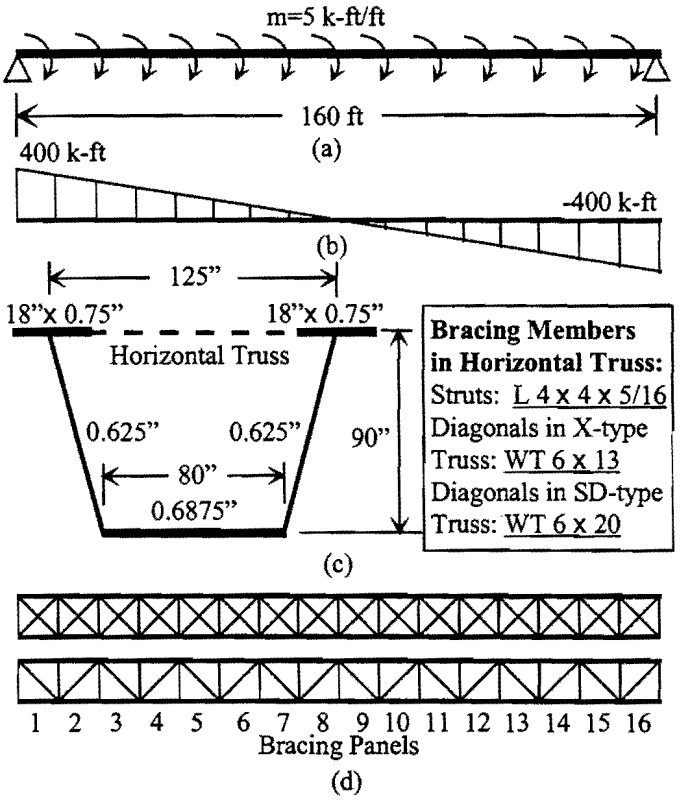

Figure 5.1. Pure Torsion on Simply Supported Straight Box Girder

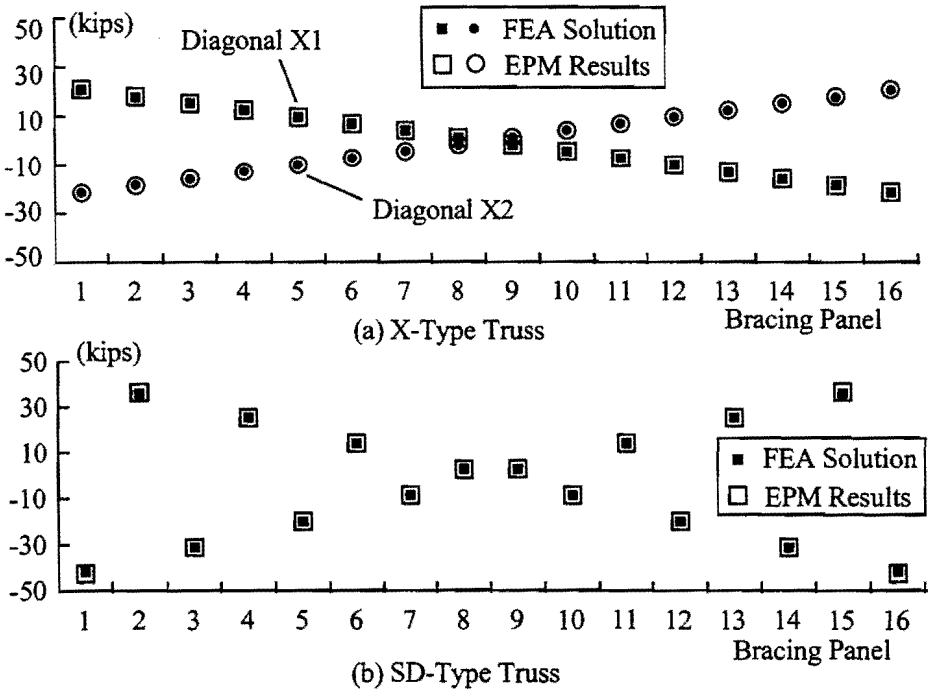

Figure 5.2. Brace Forces in Diagonals Due to Torsion

5.1.2 Combined Bending and Torsion on Quasi-Closed Box Girders

The straight girder in Fig. 5.1 was only subjected to torsional moment caused by the uniformly distributed torque. The torsional loading for most applications however is caused by gravity loading on curved girders. The EPM was also tested on the curved girder shown in Fig. 5.3. The radius of curvature of the girder is 955 ft, which results in a 6° subtended angle for every 100 ft. of girder length. The girder is non-prismatic, with two cross-sections, Sections P and N, used in the respective positive and negative moment regions as shown in Fig. 5.3. The distributed load of 1.65 kips/ft on each of the top flanges, simulates the gravity load from wet concrete as well as other construction loads. The horizontal top truss is an X-type system with 64 panels along the length of the bridge and a panel size of 10 ft. Torsional moments on the girder are caused by the horizontal curvature. The moment diagrams from bending and torsion are shown in Fig. 5.4. Since the girder is symmetrical about point C, the diagrams for only half the girder length are shown. The top flange truss consists of WT6x13 sections for the diagonals and L4x4x5/16 members for the struts. These members were selected using the EPM based on the maximum torque of 616 kip-ft that occurs to the left of the support at point B.

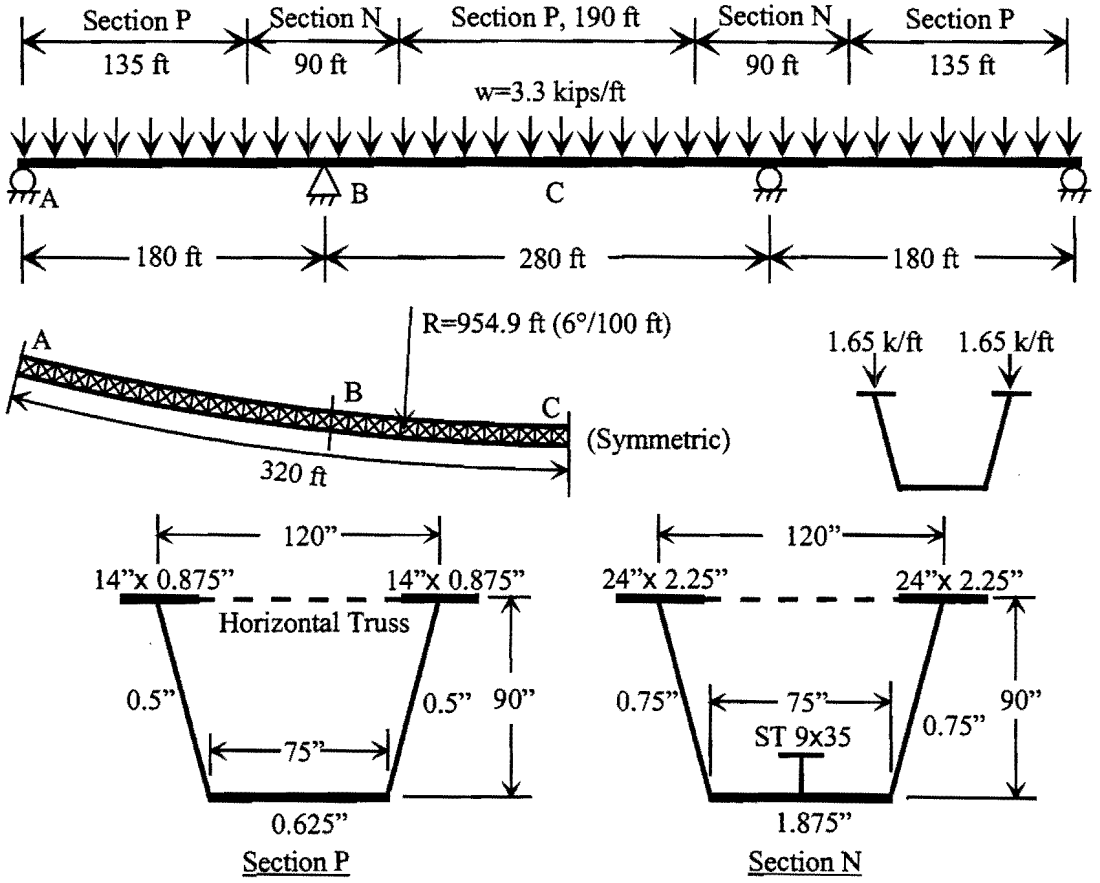

Figure 5.3. Curved Continuous Box Girder Bridge

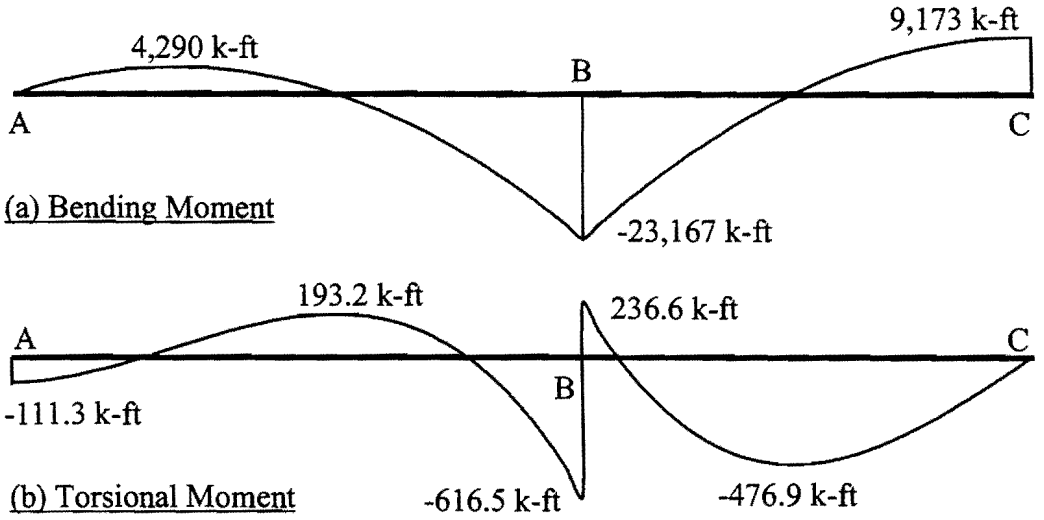

Figure 5.4. Bending and Torsional Moment Diagrams

The quasi-closed box girder was analyzed with a three-dimensional FEA model. Figure 5.5 shows graphs of the member forces along the girder length predicted by the EPM and the resulting values from the FEA results. Negative values of the forces indicate compression. The graphs of the diagonal forces show that the results predicted using the EPM have poor agreement with the FEA results. The EPM significantly underestimates the member forces at several locations along the length. There are a number of locations in which the EPM predicts tension in members that are actually in compression from the FEA results, which therefore may lead to potential problems with buckling of the brace. The graph in Fig. 5.5c shows that the forces in the struts from the FEA results are significantly larger than values predicted using the current design method. The main source for the difference between the FEA results and current design methods for the diagonals and the struts is due to vertical bending stresses in the box girder. In addition, part of the error in the strut forces is due to the erroneous assumption that the bottom flange resists half of the horizontal load component, p. With the exception of the girder self-weight, the entire lateral component from the applied load should be applied to the top flange.

Disagreement with the results by the current design method was also observed in the field studies that were discussed in Chapter 3. For example, during Stage 2 slab construction there was no direct loading on the top flanges at Section N as shown in Fig. 3.7b. The current design method will therefore yield zero brace force in the strut at Section N since $p = 0$. However, field results indicate that the strut at Section N was subjected to an axial force of -6.68 kips in compression (Fig. 3.46). A compressive force of similar level (-6.19 kips) was also predicted by the FEA solution, as presented in Fig. 4.16. Both the field and FEA results show that unconservative brace forces result from the current design method for lateral struts that was illustrated previously in Fig. 2.14.

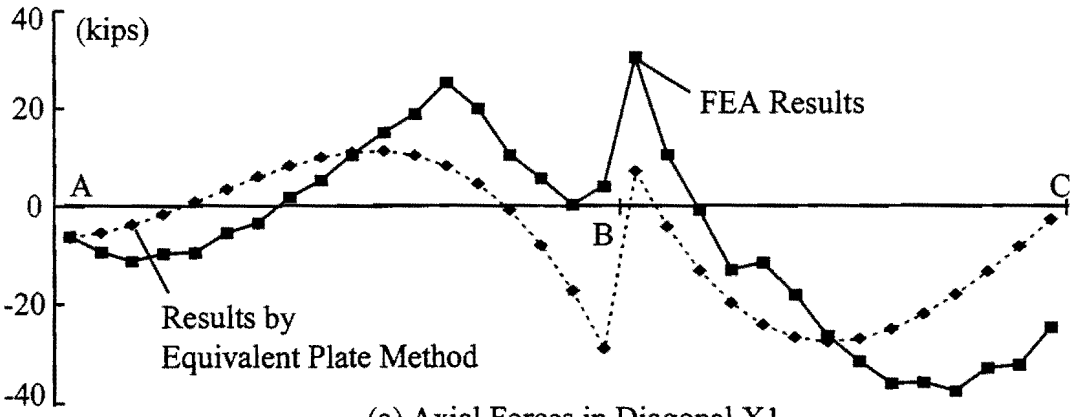

(a) Axial Forces in Diagonal X1

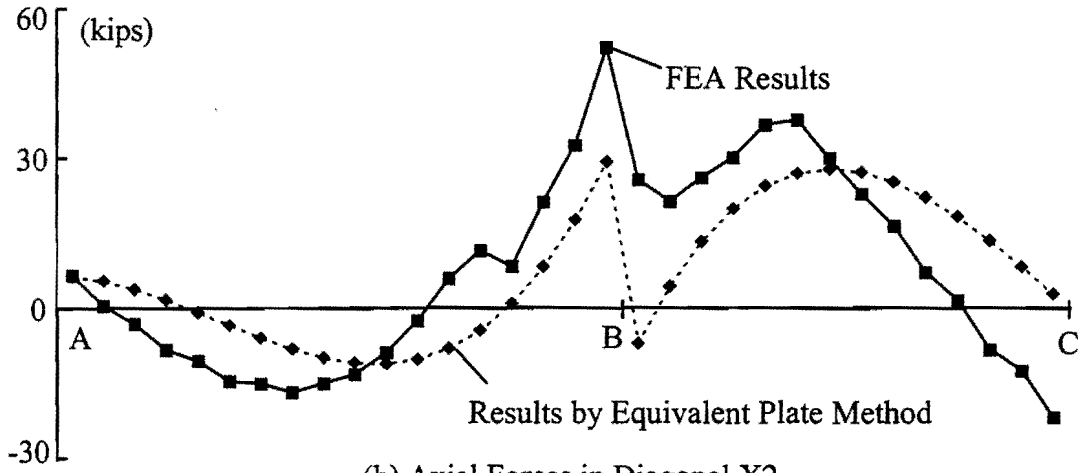

(b) Axial Forces in Diagonal X2

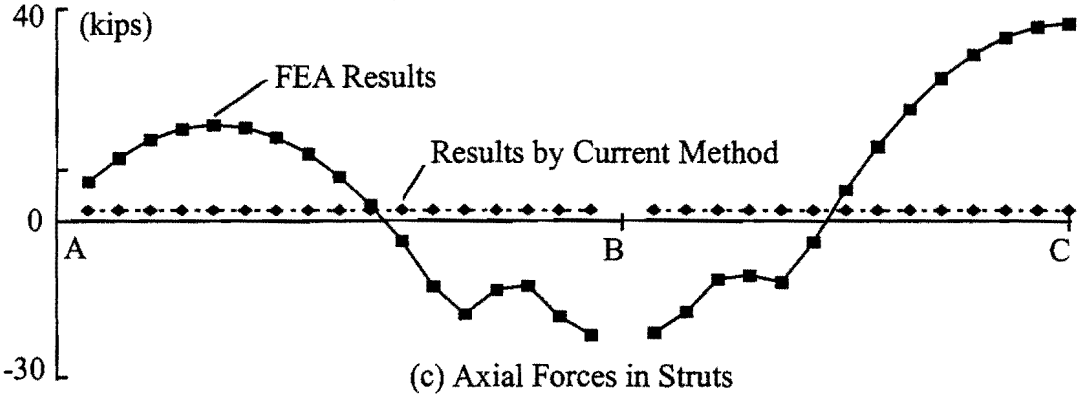

(c) Axial Forces in Struts

Figure 5.5. Brace Force Results for the Curved Girder

5.1.3 Vertical Bending of Quasi-Closed Box Girders

The straight girder shown previously in Fig. 5.1 was further studied to focus on the effect of box girder bending on the truss behavior. The 160-ft. long girder was simply supported with a uniformly distributed load of 1.65 k/ft on each top flange as shown in Fig. 5.6. A SD-

type and an X-type truss were considered in the analysis. The sizes of the diagonals were WT6x13 for the X-type system and WT6x20 for the SD-type system, while the struts were L4x4x5/16 for both systems.

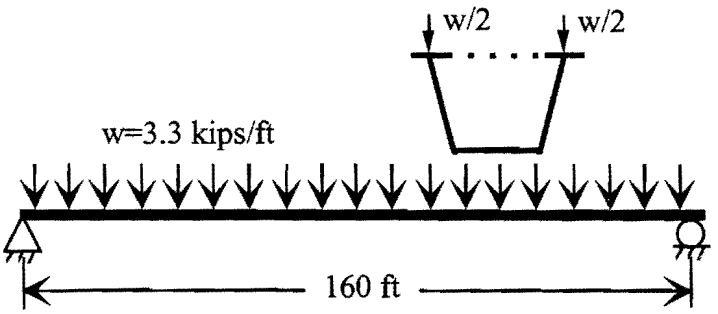

Figure 5.6. Simply Supported Girder Subjected to Transverse Load

Fig. 5.7 shows a graph of the FEA results for the forces in the diagonals and struts for both truss systems that were studied. Negative values indicate compression. The two diagonals in a given panel of the X-type truss have identical forces and are represented by a single data point in Fig. 5.7. The graphs show that large axial forces develop in the truss despite the absence of torsional moments. The distribution of the brace forces along the length has the same shape as the bending moment diagram implying vertical bending of the box girder causes these forces. The forces in the X-type truss system are larger than the corresponding forces in the SD-type truss. All of the forces are larger than values predicted using the current design method (Highway 1982) that was outlined earlier in Chapter 2. Since there is no applied torsion, the current design method would predict zero diagonal forces and a tensile force of 2.1 kips in all struts caused by the horizontal component of the applied load.

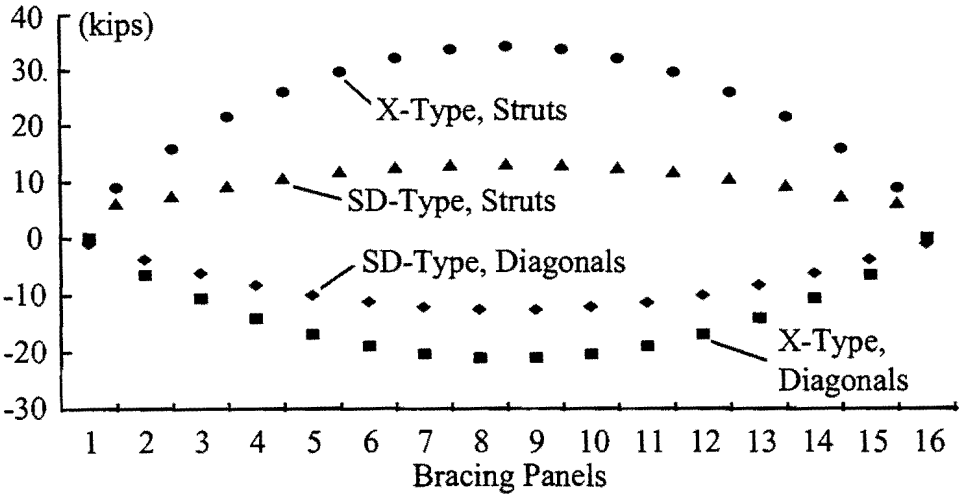

Figure 5.7. Brace Forces in Simply Supported Girder Due to Bending

The reason that forces develop in the truss with no torsional moment applied can be understood by considering the distribution of vertical bending stresses in a trapezoidal box girder. For quasi-closed box girders, the neutral axis of the steel section is usually near mid-depth of the girder as shown in Fig. 5.8. The horizontal truss system therefore connects to the girder in a region of high bending stress. Due to compatibility, the truss must experience the same strains as the box girder in the axial direction. This is why the diagonal forces shown in Fig. 5.7 are all in compression.

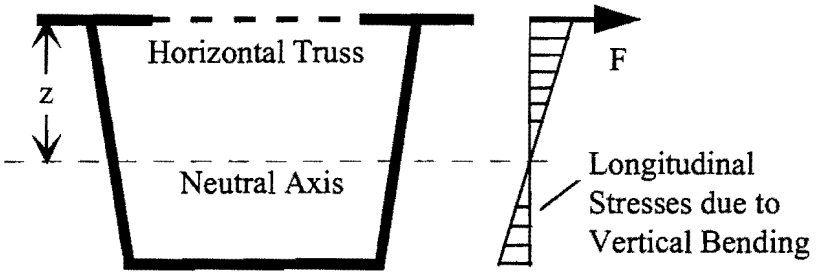

Figure 5.8. Brace Forces in Horizontal Truss Due to Vertical Bending Moment

5.1.4 Lateral Bending of Top Flanges

Before the effects of vertical bending of the box girder are addressed, it is important to discuss the bending behavior of the top flanges of the box girders. In addition to stresses caused by vertical bending of the box girder, the top flanges may also experience significant stresses due to lateral bending. Figure 5.9 shows the longitudinal stresses at the middle (point M) and the edges (points L and R) of one of the top flanges for the straight box girder shown in Fig. 5.6 with the X-type truss system. The differences between the stresses at the edge and those in the middle of the top flange represent the lateral bending stresses developed in the top flanges. The lateral load component acting between panel points of the top flange truss causes these lateral-bending stresses. As discussed earlier, the current method assumes that the top and bottom flanges each carry half of the lateral load component, p. The top flange is typically modeled as a continuous beam (between panel points) for which the maximum moment due to the lateral load component would be ($w_{LT}s^2/12$), in which s is the panel length and w_{LT} is the portion of the lateral load component applied to the top flange. The lateral load component for the beam in Fig. 5.6 is p = 0.41 k/ft. The current method would therefore use w_{LT} = 0.21kN/m, which results in a maximum lateral bending moment of 1.7 k-ft for a panel length of 10 ft. Converting the lateral bending moment to a stress gives a maximum value of 0.50 ksi. However, the FEA result for the maximum lateral bending stress is approximately 1.0 ksi, which is twice the predicted value by the current method. This indicates that the assumption in the current method that the top and bottom flanges each carry half of the horizontal component of the load is incorrect. The lateral stresses on the top flange are induced by the full component of the vertical load applied on the top of the web (p, as shown previously in Fig. 2.14). Therefore, the estimation of the lateral bending stress during the construction of the concrete deck must use the full horizontal components of the

gravity loads applied at the top flange. Although the girder self-weight may be divided between the top and bottom flange, this component is relatively small compared to the weight of the wet concrete and other construction loads and may be conservatively added to the total weight applied to the top flange.

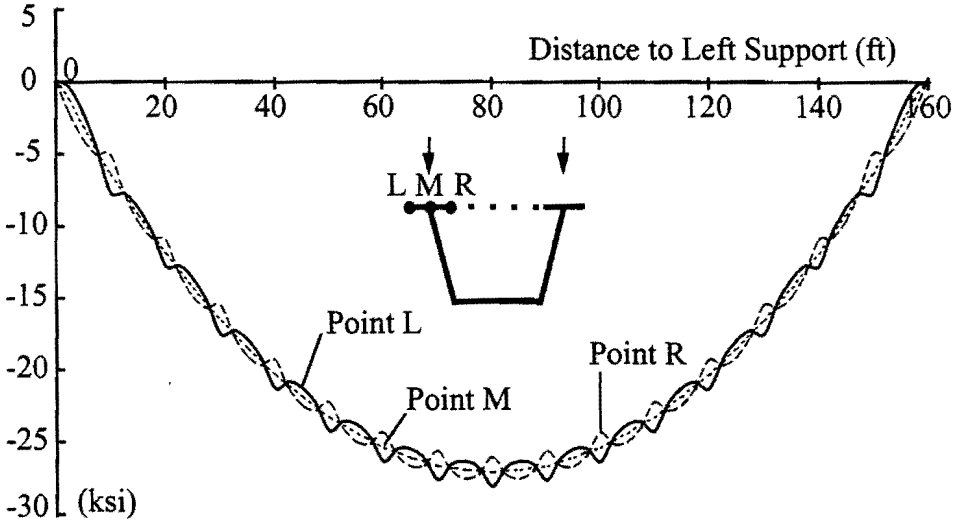

Figure 5.9. Distribution of Longitudinal Stresses in Top Flange of Box Girder with X-Type Truss

A more serious issue regarding lateral bending stresses occurs in girders with the SD-type truss system. The current design method predicts equal lateral bending stresses for both truss types (due to the sloping webs). As demonstrated by Fig. 5.10, however, the top flange lateral bending stresses with the SD-type truss are significantly larger than those in flanges with the X-type truss system. For the SD-type truss, the largest lateral bending stresses often range from 20 to 30% of the maximum vertical bending stress. The maximum lateral bending stress for the results shown in Fig. 5.10 is approximately 25% of the maximum axial bending stress.

In addition to having much larger magnitudes, the distribution of the lateral bending stress for the SD-type truss is quite different than that of the X-type truss. The wavelengths of the lateral bending stresses are twice as large for the SD-type as for the X-type truss. In a SD-type truss, the large strut force developed from vertical bending results in a large lateral force applied directly to the flange therefore causing lateral moments in the top flange as shown in Fig. 5.11. Although the horizontal component from the applied load does cause lateral bending, most of the lateral bending in a girder with a SD-type truss results from the large strut forces caused from vertical bending of the box girder. Although the internal K-frames were spaced at 20 ft. in the above analysis, Fig. 5.12 shows that providing additional K-frames has very little effect on the lateral bending stresses. The graph in Fig. 5.12 shows the lateral bending stresses when K-frames were spaced at 10 ft. The distribution of lateral bending stresses from Figs. 5.11 and 5.12 for the two K-frame spacings are nearly identical.

Using a closer spacing of internal K-frames provides better control over distortion of the box section, however the entire cross-section simply rotates and the top flanges still bend laterally with an effective span of two truss panels.

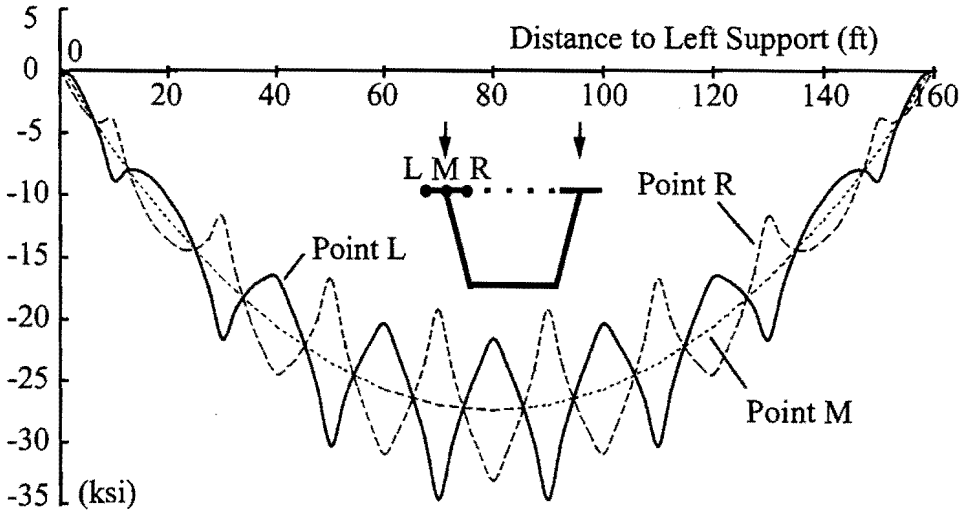

Figure 5.10. Distribution of Longitudinal Stresses in Top Flange of Box Girder with SD-Type Truss

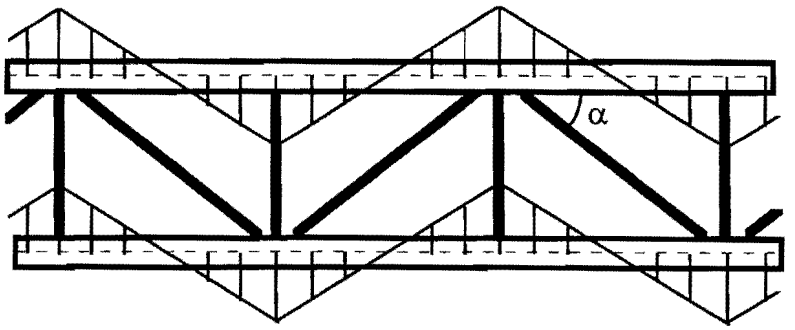

Figure 5.11. Lateral Bending Moments in Top Flanges with SD-Type Truss

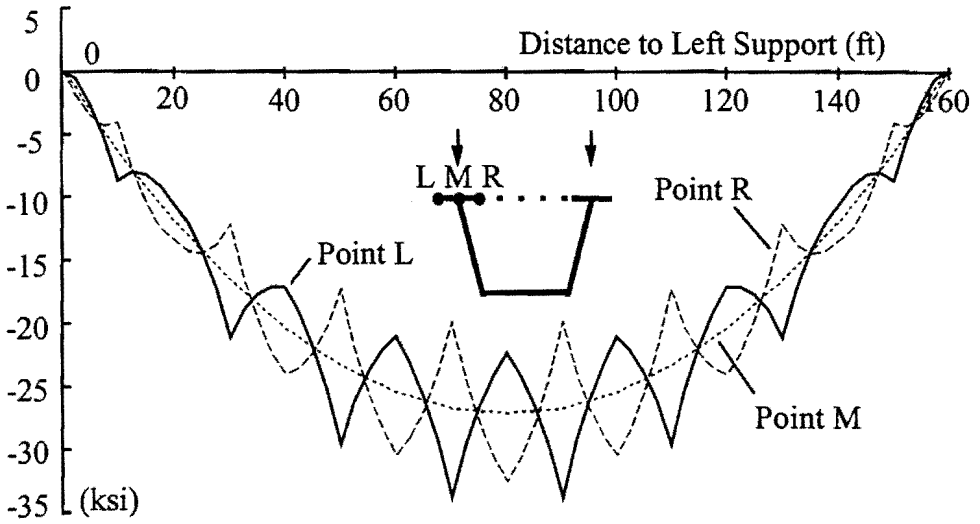

Figure 5.12. Distribution of Top Flange Stresses with SD-Type Truss, K-Frame Spaced at 10 ft

Since there are diagonals at both ends of a strut in the X-type truss, the strut forces do not cause lateral bending in the flanges. Top flange lateral bending in a girder with an X-type truss is caused by the horizontal component from the applied load as outlined above.

5.6 Vertical Bending Analysis of Box Girders

The FEA results provided in the preceding section clearly indicate that vertical bending will cause large brace forces in the top flange horizontal truss, as well as large lateral bending stresses in the top flanges if the truss is SD-type. These forces and stresses are not considered in the current design method. A thorough investigation on the effect of vertical bending of the quasi-closed box girder is therefore warranted.

An analytical study on the bending of box girders with a horizontal top flange truss system is carried out in this section. The following assumptions apply to the investigation:

1. The box girder is a prismatic section subjected to a state of uniform moment.
2. The web of the girder provides negligible lateral resistance to the top flange.
3. Effects of horizontal curvature on the bending behavior are neglected.

Figure 5.13 shows the interactive forces between the bracing members and the top flanges for (a) the X-type and (b) the SD-type truss systems. The force F is the resultant from the uniform vertical bending moment loading in the girder. The longitudinal strain in the box girder and the top flange horizontal truss are identical due to compatibility. Due to symmetry, for a given truss, all diagonals will therefore have the same force, D_{bend}, and the same sign (compression or tension). Similarly, for a given truss, all struts will have the same force, S_{bend} and the same sign.

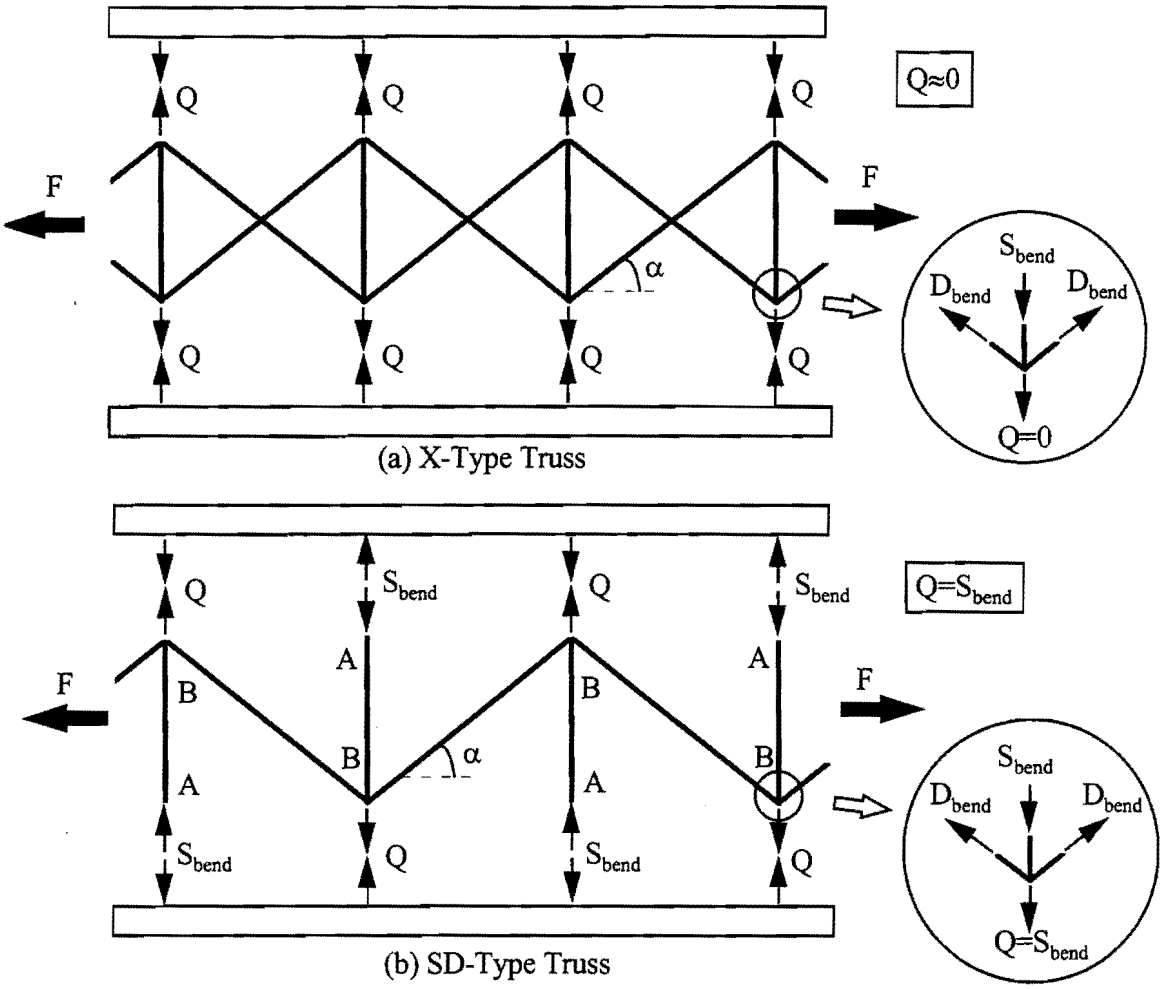

Figure 5.13. Interactive Forces between the Top Flanges and Horizontal Truss

5.2.1 X-Type Truss

The lateral interactive forces, Q, between the truss and the top flange, must be identical at all joints due to symmetry of the structure as shown in Fig. 5.13(a). Equilibrium of the top flange yields Q = 0, since the lateral stiffness of the web is assumed negligible as outlined above, however the flange may still experience some rigid body movement. Since Q = 0, the lateral bending stress due to the vertical bending will be equal to zero. Equilibrium of a joint gives the force in the strut as a function of the diagonal force

$$S_{bend} = -2D_{bend} \sin\alpha \ . \qquad (5.1)$$

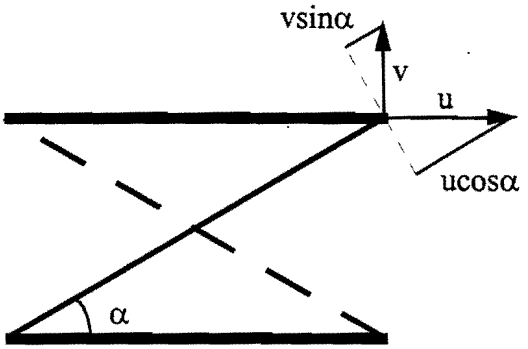

Figure 5.14. Elongation of the Diagonal of Horizontal Truss

To develop an expression for the force in the diagonal, consider a panel of the truss system between two struts as shown in Fig. 5.14. The axial elongation of all diagonals is the same due to symmetry and is defined as Δ_{diag}. The elongation, Δ_{diag}, can be expressed as (Fig. 5.14):

$$\Delta_{diag} = u\cos\alpha + v\sin\alpha \tag{5.2}$$

where, u and v are the relative displacements of a diagonal in the longitudinal and lateral directions (of the top flange), respectively. The relative displacement v, is the same as the elongation of the struts, for which basic engineering mechanics and Eq. 5.1 yield the following expression

$$v = \frac{S_{bend}}{EA_s} b = \frac{-2D_{bend}\sin\alpha}{EA_s} b \ , \tag{5.3}$$

where E is the elastic modulus, b is the panel width (strut length), and A_s is the strut area. The relative displacement u, is the same as the elongation of the girder at the truss. If the longitudinal stress in the girder at the truss connection is f_{xTop}, Hook's Law yields the following expression

$$u = \frac{f_{xTop}}{E} s \ , \tag{5.4}$$

where s is the panel length, $f_{x\,Top}$ is the longitudinal stress at the middle of the top flange due to vertical bending. The top flange stress, $f_{x\,Top} = M/S_{xTop}$ in which M is the bending moment on the cross-section of the box girder while S_{xTop} is the section modulus based on the extreme fiber distance to the top flange.

Similarly, the elongation of the diagonal is given by

$$\Delta = \frac{D_{bend}}{EA_d} d \ , \tag{5.5}$$

where d is the length of the diagonal, and A_d is the diagonal area.

Substituting Eqs. 5.3 to 5.5 into 5.2 and rearranging yields

$$D_{bend} = \frac{f_{xTop}\, s\cos\alpha}{K_2} \ , \tag{5.6}$$

in which

$$K_2 = \frac{d}{A_d} + \frac{2b\sin^2\alpha}{A_s} \ . \tag{5.7}$$

5.2.2 SD-Type Truss

The joints between the truss and the flanges can be divided into two types, A and B as shown in Fig. 5.13(b). At joint A only a strut is connected to the flange, while a strut and two diagonals frame into joint B. Since the lateral stiffness of the web is negligible, lateral equilibrium of a top flange gives that the interactive forces Q and S_{bend} are equal in magnitude and opposite in direction. Equilibrium of joint B in Fig. 5.13(b) gives

$$S_{bend} = -D_{bend} \sin\alpha \ . \tag{5.8}$$

The forces that develop in the diagonals are a function of the axial stiffness of the diagonals and struts as well as the lateral stiffness of the top flange of the box girders. When the truss is subjected to a strain in the axial direction of the box girder, the strut ties the two flanges of the box girder together. The top flanges of the box girder will bend due to the strut force, S_{bend}. The top flange will bend like a continuous beam between panel points as shown in Fig. 5.15 with a relative lateral deflection between two consecutive panel points, v_l given by

$$v_l = \frac{S_{bend}(2s)^3}{192EI_f} = \frac{-D_{bend}s^3\sin\alpha}{24EI_f} = -\frac{D_{bend}s^3\sin\alpha}{2Eb_f{}^3t_f} \ , \tag{5.9}$$

where I_f is the moment of inertia of the top flange in the lateral direction, and b_f and t_f are the respective width and thickness of the top flange. The elongation of the diagonal members can be expressed similar to Eq. 5.2 by

$$\Delta_{diag} = u\cos\alpha - (v_1 + v_2)\sin\alpha \ , \tag{5.10}$$

in which u is the elongation of the top flanges in a panel, defined by Eq. 5.4, and v_2 is the elongation of the struts defined by

$$v_2 = \frac{S_{bend}}{EA_s} b = \frac{-D_{bend}\sin\alpha}{EA_s} b \ . \tag{5.11}$$

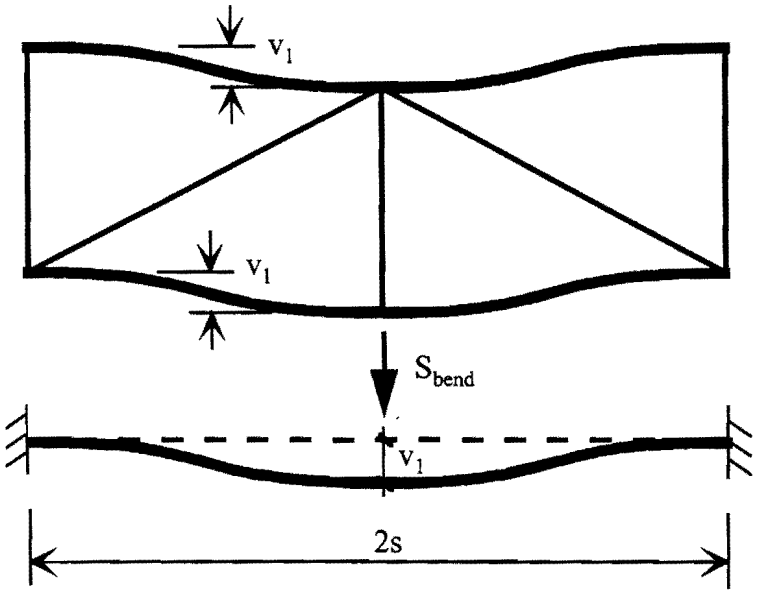

Figure 5.15. Lateral Displacement of Top Flanges Due to Strut Force

Equation 5.5 still applies to diagonals. Substituting Eqs. 5.4, 5.5, 5.9 and 5.11 into 5.10 and rearranging yields:

$$D = \frac{f_{xTop}\, s\cos\alpha}{K_1} \ , \tag{5.12}$$

$$K_1 = \frac{d}{A_d} + \frac{b}{A_s}\sin^2\alpha + \frac{s^3}{2b_f{}^3 t_f}\sin^2\alpha \ . \tag{5.13}$$

The lateral bending stress in the flange due to the force S_{bend} is given by

$$f_{L\,bend} = \frac{1.5s}{b_f{}^2 t_f} S_{bend} \ , \tag{5.14}$$

Equation (5.14) was found by dividing the maximum flange lateral moment of (S_{bend} (2s)/8)) by the flange section modulus (b_f^2 t_f)/6.

5.2.3 Modification of Top Flange Stresses

Since the top flange truss develops force due to the vertical bending of the box girder, it also contributes to the box girder bending stiffness. As a result, the actual top flange stress, f_{xTop}, is less than predicted by bending theory (M/S_{xTop}). Although it is conservative to neglect the contribution from the truss, a modification to the top flange stress can be made by considering the contribution of the diagonal bracing members to the bending capacity of box girders.

Consider first the box girders with an X-type horizontal truss system. The contribution of the top flanges and the truss system in resisting the overall bending moment on the cross-section of the girder is (Figs. 5.8 and 5.16)

$$M_t = Fz = 2f_{xTop}A_f z + 2D_{bend} z\cos\alpha \ , \tag{5.15}$$

in which A_f is the area of one top flange, and z is the distance from the neutral axis of the cross-section to the top flanges. Equations 5.15 and 5.6 result in

$$M_t = 2f_{xTop}(A_f + A_0^*)z \ , \tag{5.16}$$

in which

$$A_0^* = \frac{D_{bend}\cos\alpha}{f_{xTop}} = \frac{s\cos^2\alpha}{K_2} \ . \tag{5.17}$$

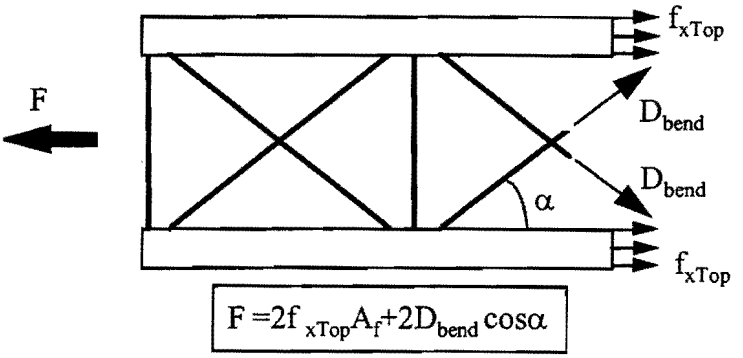

Figure 5.16. Resistance to the Bending Moment from Top Flanges and Horizontal Truss

Without bracing members, the stress in the top flanges satisfies $f_{xTop}=F/(2A_f)$. Therefore, A_0^* is the equivalent increase in area of a top flange due to the existence of the horizontal truss system. A similar expression can be derived for girders with the SD-type truss, resulting in the expression

$$A_0^* = \frac{s\cos^2\alpha}{2K_1} \quad . \tag{5.18}$$

A_0^* represents the equivalent area increment for *each* of the top flanges.

The above discussion provides a method to evaluate the improvement of the girder bending stiffness due to the existence of the top truss system, and to estimate the forces in the bracing members of the horizontal truss. The overall bending stiffness of a girder can be obtained simply by replacing the original top flange area A_f with the modified equivalent area, $A_f + A_0^*$, in which A_0^* is determined by Eq. 5.17 or 5.18. The cross-sectional moment of inertia of the box girder is then calculated based on the cross-section with this modified top flange area, and the stress in the top flanges, f_{xTop}, is determined using the modified cross-sectional modulus. Brace forces in the diagonals and struts are calculated based upon the top flange stress results using the equations for D_{bend} and S_{bend} as proposed earlier in this chapter.

A_0^* is usually small compared to the top flange areas in most cases unless relatively large bracing members are used in the horizontal truss with a relatively small α. Neglecting the effect results in conservative estimates of the truss forces and lateral bending stresses in the top flange.

5.3 Horizontal Components

Based upon the results shown in Section 5.1, the entire lateral load component, p (as shown in Fig. 2.14), should be applied to the top flange (instead of assuming that the bottom flange carries half). A force of ps results at each truss panel point due to the lateral load component, p.

The current design method (Highway 1982, Four 1997) assumes that under the lateral component p only the struts will develop axial forces. This is largely true in a SD-type truss, in which the forces in the diagonals are usually significantly smaller than those in struts due to the horizontal component. This was confirmed by both the FEA and analytical studies during this investigation. As a result, forces in the struts are assumed to be equal to ps while no axial forces is assumed in the diagonal members in the SD-type truss under the lateral load components.

In an X-type truss, however, the struts and the diagonals work together to carry the lateral load component, and the forces in the struts and in the diagonals are often at a similar level. Under a uniform lateral load component p, a force of ps results at each truss panel point. The diagonals and the struts in an X-type truss resist this force. The longitudinal deformation of the top flanges is assumed negligible. Therefore, if the elongation of the struts is v, the elongation of the diagonals, Δ_{diag}, is

$$\Delta_{diag} = v\sin\alpha \ . \tag{5.19}$$

The axial forces in the struts and diagonals are given by the following expressions:

$$S_{lat} = EA_s \frac{v}{b} \ , \tag{5.20}$$

$$D_{lat} = EA_d \frac{\Delta_{diag}}{d} = EA_d \frac{v}{d}\sin\alpha \ . \tag{5.21}$$

Equilibrium at the joints requires

$$S_{lat} + 2D_{lat}\sin\alpha = ps. \tag{5.22}$$

Substitution of Eqs. 5.20 and 5.21 into 5.22 results in the following expression for v,

$$v = \frac{ps}{\frac{EA_s}{b} + \frac{2EA_d}{d}\sin^2\alpha} \ . \tag{5.23}$$

Substituting Eq. 5.23 back into Eqs. 5.20 and 5.21 and rearranging results in the following expressions:

$$S_{lat} = \frac{d}{A_d K_2} ps \ , \tag{5.24}$$

$$D_{lat} = \frac{b\sin\alpha}{A_s K_2} ps \ , \tag{5.25}$$

where K_2 is given in Eq. 5.7.

The diagonal force due to the lateral load component in an X-type truss is relatively small compared to the bending and torsional components. The method presented in the next section designs only the struts for the force ps, as is recommended for the SD-type truss.

5.4 Proposed Design Method

In general, the forces that develop in the top flange horizontal truss can result from three components:

A. torsional moment on the girder,
B. vertical bending of the box girder,
C. lateral component of the applied load.

A complete design of the truss would therefore take all three of these potential components into consideration. Results have already been presented that demonstrate that the EPM provides good estimates of the truss forces that result from the applied torsion. Expressions will be presented in this section that can estimate the truss forces and top flange lateral bending stresses that result from vertical bending of the box girder and the lateral load component of the applied load. Using the principal of superposition, the force components from each of the above sources can be evaluated and the resultant forces summed.

5.4.1 Truss Forces Due to Vertical Bending of the Box Girder

The force that is induced in the truss due to vertical bending of the box girder is a function of the stiffness of the truss and the bending strain in the girder at the level of the connection to the horizontal truss. The equations derived in the last section for truss forces as well as the top flange lateral bending stresses, are summarized as follows:

For SD-Type Trusses:

$$D = \frac{f_{xTop}\, s \cos\alpha}{K_1}, \tag{5.26a}$$

$$S_{bend} = -D_{bend} \sin\alpha, \tag{5.26b}$$

$$f_{L\,bend} = \frac{1.5s}{b_f^{\,2} t_f} S_{bend}. \tag{5.26c}$$

For X-Type Trusses:

$$D_{bend} = \frac{f_{xTop}\, s \cos\alpha}{K_2}, \tag{5.27a}$$

$$S_{bend} = -2D_{bend} \sin\alpha, \tag{5.27b}$$

$$f_{L\,bend} = 0 \,, \tag{5.27c}$$

in which K_1 and K_2 are parameters defined by

$$K_1 = \frac{d}{A_d} + \frac{b}{A_s}\sin^2\alpha + \frac{s^3}{2b_f{}^3 t_f}\sin^2\alpha \,, \tag{5.28}$$

$$K_2 = \frac{d}{A_d} + \frac{2b\sin^2\alpha}{A_s} \,, \tag{5.29}$$

where f_{xTop} is the longitudinal stress at the middle of the top flange, s is the spacing of struts (panel length), α is the acute angle between the top flange and the diagonal, b_f and t_f are the respective values of the width and thickness of the top flange, d is length of a diagonal, b is the distance between the middle of the top flanges, and A_d and A_s are the respective cross-sectional areas of the diagonals and the struts. The diagonal forces, D_{bend}, will have the same state of stress (compression or tension) as the top flange at the point under consideration. Unlike the axial forces due to torsion, for X-type trusses both diagonals have the identical brace force (with the same sign). It is therefore important to maintain the sign convention for the forces when adding the bending component to the torsional component. For both truss types, the state of stress in the struts is opposite to that of the diagonals as given by the negative sign in Eqs. 5.26b and 5.27b.

The diagonal and strut forces given in the above expressions are a function of the member size (larger/stiffer members develop larger forces). It is therefore necessary to select a trial diagonal and strut size to compute these components. Depending upon the location along the girder length, trial sizes may be selected as a function of the torsional requirements given by the EPM. For regions of high bending moment and high torsional moments it is recommended to start the design process by doubling the force requirement for torsion (based on the EPM) to select trial member sizes, and then checking the bending behavior using the above equations.

The above expressions were derived assuming uniform moment and therefore a uniform stress within the panel length. For cases with variable moment, it is recommended to begin the procedure by calculating the values of D_{bend} using the stress at the middle of the panel, followed by calculating S_{bend} based on the average value of D_{bend} for two adjacent panels. For non-prismatic girders with a flange transition within the panel, [f_{xTop} s] in Eqs. 5.26a and 5.27a can be replaced with $\sum_{i=1}^{n} f_i s_i$ where f_i is the average top flange stress in the ith segment (within the panel) which has the length of s_i. It is also conservative to simply use the largest longitudinal girder stress within the panel. The bending forces in SD-type trusses are also a function of the size of the top flange. If a flange transition occurs within a panel it is

conservative to use the width and thickness of the larger flange in the above expressions. The width and thickness of the larger flange are used since this produces larger forces in the diagonal of a SD-type truss. The bending-induced forces in an X-type truss are not a function of the flange sizes. The numerical example in the next section demonstrates the use of the proposed equations.

5.4.2 Truss Forces Due to Lateral Components of Applied Loading

As was discussed earlier, the entire lateral load component, p, should be applied to the top flange (instead of assuming that the bottom flange carries half). In a SD-type truss, the struts carry the majority of the lateral load component. In an X-type truss, however, the struts and the diagonals work together to carry the lateral load component. Expressions for the strut and diagonal forces due to the lateral load component in an X-type truss were presented in Section 5.3. However, the diagonal force due to the lateral load component in an X-type truss is relatively small compared to the bending and torsional components. For simplicity, it is therefore recommended to design the strut to carry the entire lateral load component. This results in the following design expressions for both SD-type and X-type truss systems:

$$D_{lat} = 0 \ , \tag{5.30a}$$

$$S_{lat} = ps \ , \tag{5.30b}$$

$$f_{L\,lat} = \frac{ps^2}{2b_f{}^2 t_f} \ . \tag{5.30c}$$

D_{lat}, S_{lat} and $f_{L\,lat}$ in the above expressions are the diagonal force, strut force and lateral bending stress due to the lateral load component. All other terms in the above expressions have been previously defined. The expression for $f_{L\,lat}$ comes from modeling the top flange as a continuous beam supported at the truss panel points, for which the maximum moment is given by $ps^2/12$. Applying the flange section modulus of $b_f^2\ t_f/6$, results in the expression given in Eq. 5.30c.

5.4.3 Total Truss Forces and Top Flange Stresses

For design it is necessary to superimpose the forces and stresses due to vertical bending, the lateral load components, and the torsional moments. This therefore leads to the following expressions:

$$S_{Tot} = S_{bend} + S_{lat} \ , \tag{5.31a}$$

$$D_{Tot} = D_{EPM} + D_{bend} + D_{lat} \ , \tag{5.31b}$$

$$f_{L\,Tot} = f_{L\,bend} + f_{L\,lat} + f_{x\,Top} \quad . \tag{5.31c}$$

S_{Tot} and D_{Tot} above are the respective total forces in the strut and diagonals while $f_{L\,Tot}$ is the total top flange stress. D_{EPM} in Eq. 5.31b is the diagonal force from the torsional moment determined using the EPM. The stress given in Eq. 5.31c includes the top flange stress that results from both the lateral and vertical bending of the box girder. Additional lateral bending stresses result due to the curvature of the girder and can be calculated using Eq. 2.5 as recommended by the current design method. Some of the struts of the top flange lateral truss are also used as a top lateral for the internal K-frames that control distortion of the box. The distortional forces that result in the K-frames will be presented in Chapter 6.

It is important to maintain the proper sign convention while superimposing the forces. For example, torsional loading causes one of the diagonals of an X-type system to be in compression while the other one is in tension, however bending causes the same state of stress in both diagonals.

As discussed earlier, the top flange stresses due to vertical bending (f_{xTop}) are less than M/S_{xTop} because of the contribution from the horizontal truss to the bending stiffness of the box girder. A modification of the bending stiffness was proposed in Section 5.2.3. However, the increase of box girder bending stiffness due to the horizontal truss is generally small, and neglecting the effect results in conservative estimates of the truss forces and lateral bending stresses in the top flange.

In many details, the horizontal truss is not directly connected to the top flanges, but instead is fastened to the webs at a level lower than the top flanges. The box girders from the field studied has the lateral truss approximately 11 inches below the top flanges. The level of truss connection in this chapter was assumed to be at the junction between the web and the top flanges of the box girder. This is a conservative assumption (due to the larger bending stress as the top flange level) and results in reasonable estimate of the truss forces for most practical truss positions. A more general solution for cases in which the truss connection may be placed significantly below the top flange (> 10% of the girder depth) is provided in Appendix C.

5.5 Application of the Proposed Method

5.5.1 Comparison Between FEA Results and Proposed Equations

The proposed expressions presented in the previous section were compared with the FEA results on the straight girder previously shown in Fig. 5.7. Figure 5.17 shows a comparison between the proposed solutions and the FEA results for the truss forces along the girder length. The total forces in the struts and the diagonals were calculated using superposition as given in Eqs. 5.31a and 5.31b. The proposed equations have good agreement with the FEA results. Figure 5.18 shows a comparison of the bending stresses in the flange from the FEA

results and the value by adding the lateral bending stresses from Eqs. 5.26c and 5.30c to the vertical bending stress. The curves show that the proposed solutions provide a good envelope of the maximum and minimum stresses from the FEA results. In design, the value of interest would be the maximum lateral bending stress, which would be a function of the bending moment and the flange size. In a non-prismatic section, the engineer should be able to locate a few critical sections along the girder length that need to be checked.

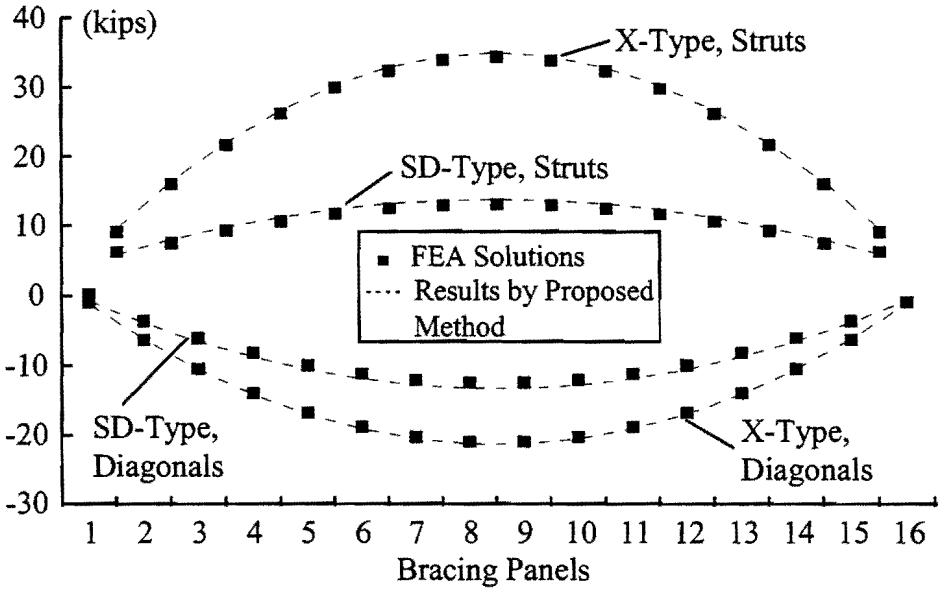

Figure 5.17. Proposed Equations and FEA for Truss Forces in the Straight Girder

The proposed expressions were also checked using the three-span curved girder previously shown in Fig. 5.3. Figure 5.5 had shown that only applying the EPM had poor agreement with the FEA results. Fig. 5.19 shows a graph of the FEA results and the proposed equations. The contribution of the diagonals in carrying the lateral load component (p), as expressed in Eqs. 5.24 and 5.25, has been considered, however the solution is not changed significantly if only the struts are designed to carry p. There are a few isolated points (around flange transitions and solid diaphragms) where there is a discernible difference between the proposed solutions and the FEA results, however even in these regions, the proposed expressions provide reasonable agreement with the FEA results. The proposed expressions generally have good agreement with the FEA results along the entire length of the girder.

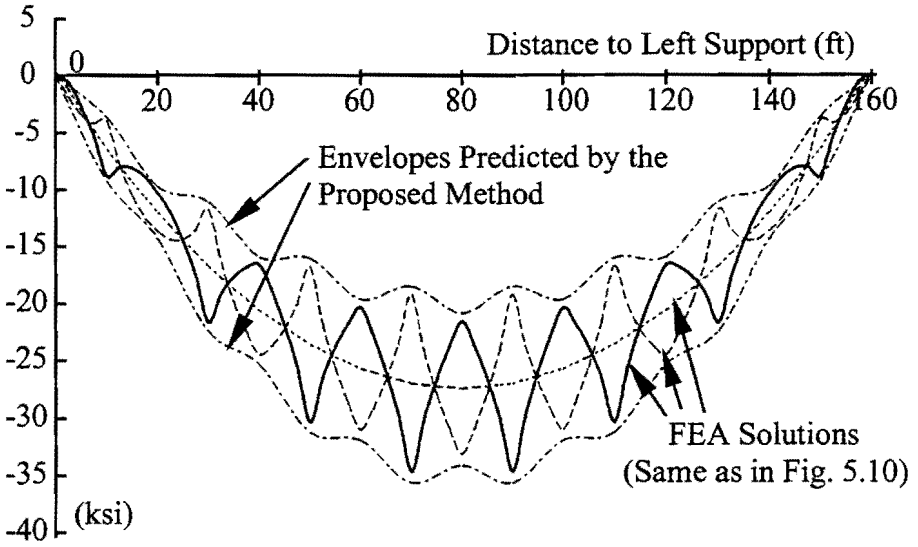

Figure 5.18. Proposed Equations and FEA for Top Flanges Stresses in the Straight Girder with SD-Type Truss

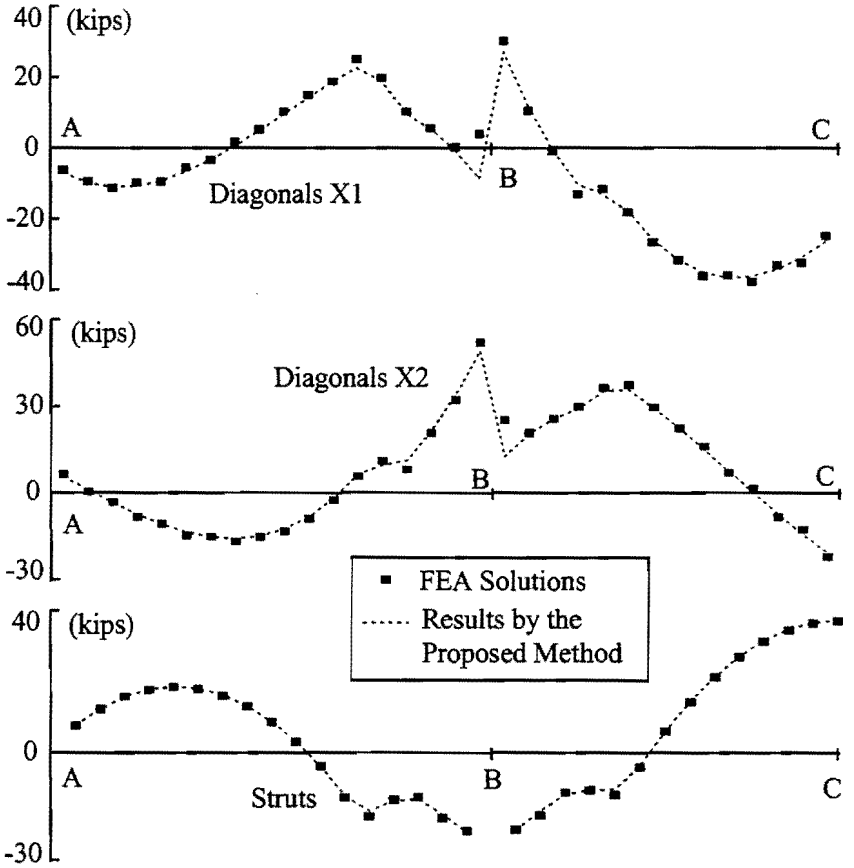

Figure 5.19. Proposed Equations and FEA for Truss Forces in Curved Girder

In design, the engineer would typically not have to apply the proposed equations along the entire girder length, but instead only in critical regions to size the top flange lateral truss members. Critical regions will generally occur around supports or other regions of high bending moment and torsion. It is important to note, however, that in some instances the maximum compression in the diagonal members may occur in a region of moderate moment and torsion. The maximum compression force in the diagonal of the top flange truss of the three span box girder previously shown in Fig. 5.3 occurs 95 ft to the right of Support B. The numerical example in the following sub-section shows the calculation of the diagonal and strut force in this region. The maximum compression in the struts usually occurs in the region with the highest top flange tensile stress.

Although the results presented in this paper have focused on the behavior of the top flange truss in box girders, the bending problems discussed may also arise in lateral bracing systems for I-shaped girders. A lateral truss is often provided near the bottom flange of I-girder bridges for bracing against wind loads. Since this truss connects to the girders near the bottom flange, the same bending-induced forces outlined earlier in this chapter will develop in these truss members. If the truss system used is either a SD-type or an X-type truss installed between two girders, the equations presented in this chapter are directly applicable.

5.5.2 Numerical Example

Consider the three-span box girder shown in Fig. 5.3. Determine the axial forces in the bracing panel in the interior span located 95.0 ft to the right of Support B (275 ft from Support A). The bending and torsional moment in the middle of the panel are 69,985 k-in and –4,554 k-in, respectively. Assume WT6x13 diagonals ($A_d = 3.8$ in^2) and an L4 x 4 x 5/16 strut ($A_s = 2.4$ in^2) for the X-type truss.

Torsion: Using the equations from the EPM as outlined in Fig. 2.12 the shear flow is given by $q = T/(2A_o)$. A_o is the area enclosed by the box. The average width of the box is $(120 + 75)/2 = 97.5$ in. and the depth is 90 in. from which $A_o = 97.5 \times 90 = 8775$ in^2. The shear flow is therefore, $q = 4554/(2(8775)) = 0.26$ kips/in. The width of the box at the top is 120 inches while $\alpha = 45°$, which therefore gives $D_{EPM} = qb/(2\sin\alpha) = 0.26 \times 120/(2 \sin(45°)) = \pm 22.0$ kips. Diagonal X2 will be in tension while X1 will be in compression.

Bending: The bending moment of 69,985 k-in causes a bending stress at the top flange equal to -17.81 ksi in compression. The length of the diagonal is 170 in. while the panel width is 120 in. from which

$$K_2 = \frac{d}{A_d} + \frac{2b\sin^2\alpha}{A_s} = \frac{170\text{ in}}{3.8\text{ in}^2} + \frac{2 \times (120\text{ in}) \times \sin^2(45°)}{2.4\text{ in}^2} = 94.7\text{ in}^{-1}.$$

With $K_2 = 94.7$ in^{-1}, the resulting diagonal force due to bending is given by

$$D_{bend} = \frac{f_{xTop} s \cos\alpha}{K_2} = \frac{-17.8 \text{ ksi} \times 120 \text{ in} \times \cos(45°)}{94.7 \text{ in}^{-1}} = -16.0 \text{ kips} .$$

The bending force in both diagonals X1 and X2 is -16.0 kips compression.

Total: Using Eq. 5.31b, the total axial forces are -22.0-716.0 = 38.0 kips for diagonal X1 (compression), and 22.0-16.0= 6.0 kips for diagonal X2 (tension). The FEA results are -35.8 kips for X1, and 7.1 kips for X2. NOTE: If the diagonal force due to the lateral load component is considered using Eqs. 5.24 and 5.25, the results are -36.5 kips for X1 and 7.5 kips for X2.

Strut Force: Using a bending moment of 50,173 k-in, the axial diagonal forces due to bending in the panel to the left of the above panel (265 ft to Support A) can be calculated as above to give D_{bend} = -11.5 kips. The axial force in the strut between these two panels due to bending is calculated by Eq. 5.26b using the average D_{bend} from the two adjacent panels

$$S_{bend} = -2D_{bend} \sin\alpha = -2\left[\frac{-11.5-16.0}{2}\right]\sin(45°) = 19.4 \text{ kips} .$$

The lateral component of the applied loading is p=1.65 × 0.25 = 0.41 kips/ft., which results in ps = 0.41×10 = 4.1 kips. The total strut force is therefore, S_{tot}=19.4 + 4.1=23.5 kips. FEA results is 21.2 kips. If Eq. 5.24 is used which accounts for the diagonals carrying a portion of the lateral load component, S_{lat} =1.9 kips which results in S_{Tot}=23.5+1.9 =21.3 kips.

CHAPTER 6 BRACE FORCES IN INTERNAL K-FRAMES OF QUASI-CLOSED BOX GIRDERS

6.1 Introduction

Chapter 5 focused on the brace forces in the horizontal top truss system during construction of box girder bridges. This chapter will focus on the brace forces in internal cross-frames of quasi-closed box girders.

The brace forces in internal K-frames are caused by the distortion of the box girder. Distortion of box girders was discussed briefly in Chapter 2, and will be further studied in this chapter. Some bridges employ intermediate external cross-frames between box girders, either permanently or temporarily for construction. Although intermediate external cross-frames are often unnecessary for strength, they are useful in controlling girder twist and deflections during construction. However, their presence may affect the brace forces in internal K-frames. All results presented in this chapter are forces with no intermediate external cross-frames. The only connection between the girders was the external solid diaphragms at the supports. Similar to the bridge models used in the previous chapter, the metal deck forms were neglected, and a single box girder was analyzed. Rigid diaphragms were simulated at the supports by preventing radial movement of two points on the web. The girder cross-section was free to warp at the supports.

6.2 Distortional Behavior of Box Girders

Box girder distortion was first studied by Vlasov (1961) while investigating the torsional behavior of thin-walled beams with a closed cross-section. A more rigorous theory was established by Dabrowski (1969), who developed the governing equation for box girder distortion and provided solutions for several simple cases. Nakai and Yoo (1988) presented the basic mechanics of box girder distortion as well as the results from parametric studies. Although these theoretical treatments are the basis for the development of design methods that will be presented in this chapter, the results from these studies are difficult to use due to the mathematical complexity. This section is therefore intended to provide a qualitative introduction of box girder distortion without using complex mathematical language.

As discussed in Chapter 2, a box girder is subjected to distortional loads if the external torsional loads do not result in a uniform Saint-Venant shear flow. The distortional behavior of box girders can be understood by examining how the transverse force components of the distortional loads are resisted in the girder. Consider a segment of a rectangular box subjected to a uniformly distributed distortional load q_f and q_w as shown in Fig. 6.1a, in which $q_f/q_w=b/h$. The cross-section of the box will distort under the distortional loads similar to the shape demonstrated in Fig. 6.1a. Taking sections as shown in Fig. 6.1b, the components of the distortional load, q_f and q_w, are balanced by the shear forces, f_w and f_f, in the plates in the through-thickness direction. From equilibrium, $q_f=2f_w$ and $q_w=2f_f$, and no in-

plane stress is induced on the cross-sections of the box girder. However, out-of-plane distortional bending stresses in all plates of the box girder are developed from the distortional moment illustrated in Fig. 6.1c. Therefore, this uniform distortional load is resisted by frame action of the box girder cross-section.

Distortion of box girder cross-section is measured by the Angular Distortion, Θ, which is proportional to the relative transverse deflections of opposite plates in the box girder as shown in Fig. 6.2. The amount of distortion developed due to q_f and q_w depends on the distortional stiffness of the cross-section. The distortional stiffness represents the ability of the box girder cross-section to resist the distortional loads and is a function of the cross-section dimensions, particularly the thickness of the plates.

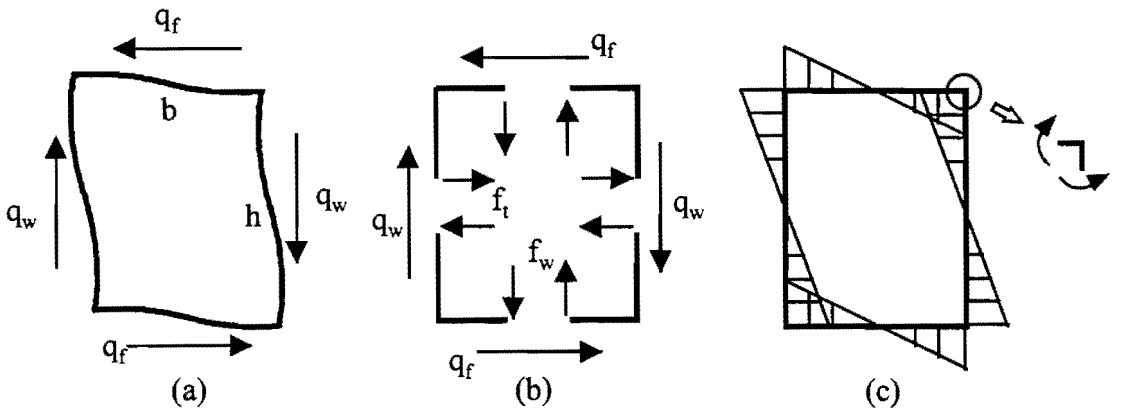

Figure 6.1. Out-of-Plane Bending Stresses in Box Girder Distortion

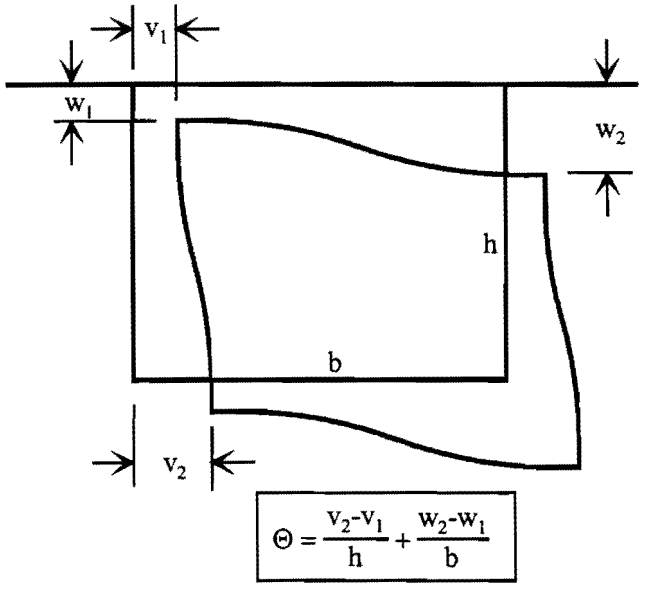

Figure 6.2. Angular Deformation of Box Girder Under Distortion

Internal cross-frames or diaphragms are usually provided every ten to twenty feet along the girder length to control distortion of the cross-section (Fig. 6.3a). The internal diaphragms and cross-frames provide resistance to distortional loads as shown in Fig. 6.3b. Internal cross-sectional bracing controls the distortional stresses since they provide supports for the plates to resist the components of the distortional loads in the form of concentrated reaction forces at the brace locations (Fig. 6.3c). Although the out-of-plane shears ($2f_w$ and $2f_f$ in Fig. 6.1b) in the plates still exist due to the angular distortion in the regions between the cross-frames, they are no longer the only resistance to the distortional loads and are usually less than the distortional load components, q_f and q_w. As shown Fig. 6.4, the remaining parts of the distortional loads, q_f-$2f_w$ and q_w-$2f_f$, are resisted by the in-plane shears at the cross-section of the plates, dV_f and dV_w, respectively. In-plane bending moments, M_f and M_w, are also developed on cross-sections of the plates, making the plates act like continuous beams supported at the cross-frame locations and subjected to loads of q_f-$2f_w$ and q_w-$2f_f$. These in-plane bending moments lead to the longitudinal warping stresses as demonstrated in Fig. 6.5 for general trapezoidal cross-sections. The distortional warping stresses are in the same direction of bending stresses and therefore must be examined in design to ensure that the total longitudinal stresses are within the design limits. The magnitude of the distortional stresses depends on the stiffness and spacing of the internal cross-frames, as will be discussed in the following section.

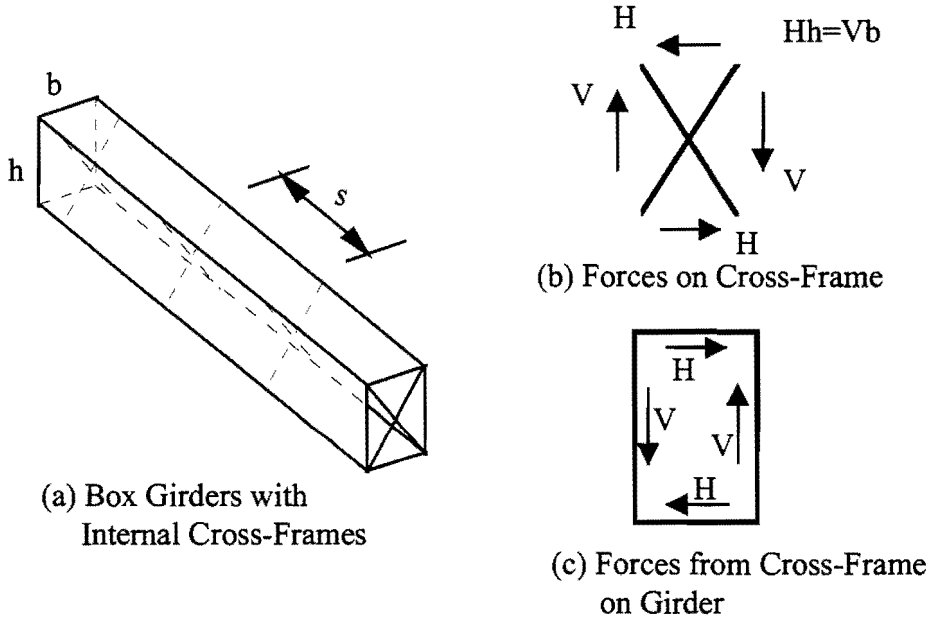

(a) Box Girders with Internal Cross-Frames

(b) Forces on Cross-Frame

(c) Forces from Cross-Frame on Girder

Figure 6.3. Internal Cross-Frames of Box Girder

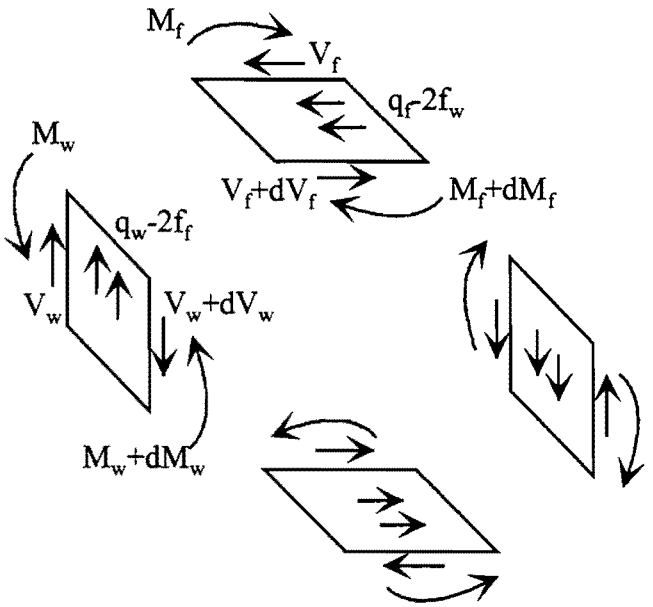

Figure 6.4. In-Plane Bending of Plates in Box Girder

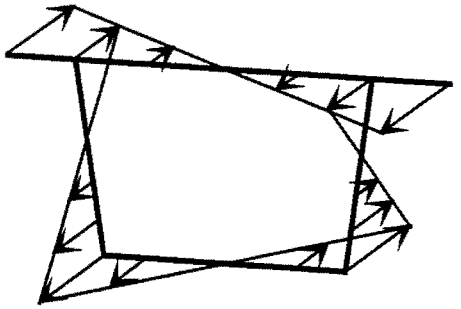

Figure 6.5. Distortional Warping Stresses on Box Girder Cross-Section

The out-of-plane shears in the plates, f_f and f_w, are linear functions of the distortion, i.e., f_f, $f_w \propto \Theta$. On the other hand, the in-plane resistance of the plates that is related to the warping deformation of the box girder, is proportional to the 4th order derivative of the angular distortion, Θ''''. The resulting equation that governs box girder distortion can be derived using energy methods as (Dabrowski 1969, Nakai and Yoo 1988)

$$EI_D \frac{d^4\Theta}{dx^4} + K_D\Theta = \frac{m_D}{2} , \qquad (6.1)$$

in which I_D is the warping constant of the box girder, and K_D is the distortional stiffness of the box girder cross-section. The expressions for I_D and K_D are complicated, as demonstrated in Fig. 6.6 for box girders with a rectangular cross-section (Nakai and Yoo 1988).

In Eq. 6.1, m_D is the load term representing the distortional load on the box girder. The distortional components on each plate can be expressed as a function of the torsional

moment, m_T, as previously demonstrated in Figs. 2.5c and 2.6c. It was found from the derivation that $m_D=m_T$. Thus in distortional analysis the torsional moment is used directly to represent the distortional loads applied on the box girder. This approach is only valid for girders with a rectangular cross-section. Trapezoidal cross-sections will be discussed later in the chapter, however, the distortional loads must be modified from the torsional moment and therefore $m_D \neq m_T$ in Eq. 6.1.

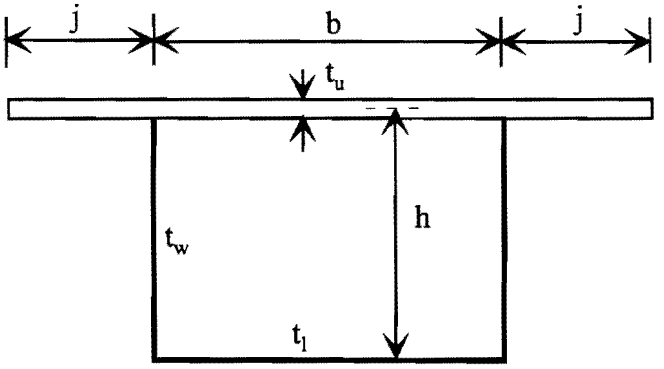

$$I_D=\frac{b^2h^2}{48(1+\beta)}[A_l\beta+A_w(2\beta-1)] \qquad K_D=\frac{24EI_w}{\alpha_0 h}$$

$$\alpha_0=1+\frac{2b/h+3(I_u+I_l)/I_w}{(I_u+I_l)/I_w+(6h/b)(I_uI_l/I_w^2)} \qquad \beta=\frac{A_u(1+2j/b)^2+3A_w}{A_l+A_w}$$

$$A_u=t_u(2j+b) \qquad A_w=t_wh \qquad A_l=t_lb$$

$$I_u=\frac{t_u^3}{12(1-\mu^2)} \qquad I_w=\frac{t_w^3}{12(1-\mu^2)} \qquad I_l=\frac{t_l^3}{12(1-\mu^2)}$$

(μ: Poisson's Ratio)

Figure 6.6. Stiffness Parameters for the Distortion of Rectangular Box Girder

Equation 6.1 is identical in form to the governing equation for a Beam-on-Elastic-Foundation (BEF). Therefore, a BEF analogy for the distortional analysis of box girders exists, as was discussed by Wright et al (1968). The distortional behavior of box girders can be effectively described by the BEF model. The resistance from the out-of-plane bending of the cross-section is simulated by continuous elastic support, while the stiffness of the internal cross-frames is simulated by discrete elastic supports at the cross-frame locations. The BEF analogy is demonstrated in Fig. 6.7, where the relationship between the terms in a traditional BEF and a box girder are compared.

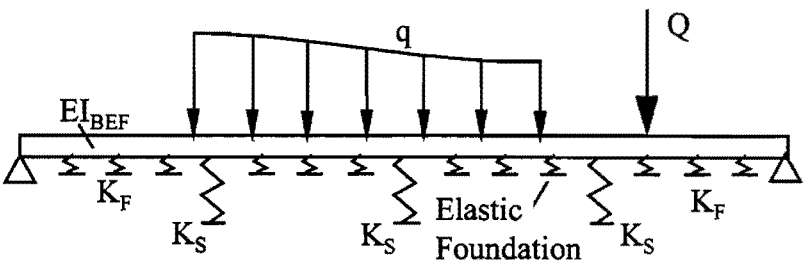

Beam-on-Elastic-Foundation		Box Girder
Bending Stiffness (EI_{BEF})	⇨	Warping Stiffness of Box Girder (EI_D)
Stiffness of the Elastic Foundation (K_F)	⇨	Distortional Stiffness of Cross-Section (K_D)
Stiffness of the Discrete Supports (K_S)	⇨	Stiffness of the Internal Diaphragms and Cross-Frames
Transverse Loads (Q, q)	⇨	Distortional Loads on Box Girder
Reactions on the Elastic Foundation	⇨	Distortional Stresses (Out-of-Plane Bending Stresses)
Reactions at the Discrete Supports	⇨	Forces in the Internal Diaphragms and Cross-Frames
Bending Stresses in the Beam	⇨	Warping Stresses in Box Girder
Deflection of the Beam	⇨	Angular Distortion of Box Girder (Θ)

Figure 6.7. Beam-on-Elastic-Foundation Analogy of Box Girder Distortion

6.3 Design Method for Distortion

The last section introduced the distortional analysis of box girders with intermediate internal cross-frames and discussed the BEF analogy. Although the BEF analogy is effective in predicting the distortional warping stresses, out-of-plane bending stresses, and even forces in the internal cross-frames, the analogy is rarely used in design due to the complexity of the method.

Solid diaphragms at supports as well as intermediate internal cross-frames are always provided in box girders to control the distortional stresses in the girder and to prevent lateral buckling of the top flanges during construction. Most previous research focused on the static response of the girder under distortional loads. The objective of distortional analysis was to

determine the spacing and stiffness of the internal cross-frames such that the distortional stresses are within a certain limit. In general, the out-of-plane distortional stresses are not the main concern in the distortional analysis. Most research efforts focused on the in-plane distortional warping stresses because these stresses are in the same direction of the bending stresses and therefore the total longitudinal stresses are the highest design stresses.

The current design recommendation (Guide 1993, Nakai and Heins 1977) is based on the criteria that the longitudinal distortional warping stresses are less than 10% of the bending stress. Using the finite difference method, Oleinik and Heins (1975) performed a parametric study on the governing equation for the distortion of curved box girders and concluded that in order to satisfy this requirement, the spacing of intermediate internal cross-frames, s, must not exceed

$$s = L\sqrt{\frac{R}{200L - 7500}} \leq 25 \text{ ft} \ , \tag{6.2}$$

in which R and L are the radius and span of the box girder bridge.

The above equation was derived by assuming that all the cross-frames and diaphragms are rigid. This assumption is not valid unless the cross-sectional areas of the cross-frame members are sufficiently large. For X-type cross-frames, the effect of cross-frame stiffness on distortional warping stresses was investigated (Williamson 1974, Guide 1993). It was proposed that for X-type cross-frames, the stiffness can be considered to be rigid if the cross-sectional area of the diagonals in the cross-frames is at least

$$A_b = 75\frac{sb}{h^2}\frac{t^3}{b+h} \ , \tag{6.3}$$

where b and d are the width and depth of the box girder cross-section, s is the spacing of the internal cross-frames, and t is the thickness, in., of the thickest plate of the box girder cross-section.

Equations 6.2 and 6.3 are the only design recommendation provided in the current specification (Guide 1993) for the design of curved box girder distortion. These results are based on studies carried out more than 20 years ago and have demonstrated several major deficiencies. Specifically, the following issues must be addressed before a complete and practical design method is developed.

1. The majority of the previous research focused on box girders with rectangular cross-section, however, modern box girder bridges generally use trapezoidal cross-sections. Although Eq. 6.1 is applicable to general trapezoidal box girders, several issues that are specifically associated to trapezoidal cross-sections must be clarified. For example, the

distortional load for trapezoidal box girders can not be represented simply by the torsional moments, as will be discussed in Section 6.5.

2. Equation 6.3 provides the stiffness requirement for internal cross-frames. The members in cross-frames are also subjected to axial forces and therefore, the criteria for the strength requirement for internal cross-frames must be established. The strength design relies on proper evaluation of the brace forces in the cross-frames. Although the BEF analogy can be used to calculate forces on the cross-frames, a simple and efficient method is not provided in the current design methods. The design example published by AISC (Highway 1982) does not consider the axial forces in the diagonals of the X-type cross-frames and simply treats the diagonals as secondary members on which only local buckling needs to be considered. The lateral struts are also erroneously designed by assuming the axial forces are only caused by the horizontal components of the bending loads on top flanges. The last chapter demonstrated that large strut forces can be induced by girder bending moments. This chapter will show that strut forces can also be induced by distortional loads. In addition, only X-type internal cross-frames are considered in the guide specification (Guide 1993) and in the design example (Highway 1982). K-shaped cross-frames as shown in Fig. 1.1 are increasingly used in modern box girder bridges. A major advantage of K-frames is the large space between the two diagonals that provide easy access for workers and inspectors. Design formulas for box girders with internal K-frames are therefore warranted.

3. Most of the previous work focused on the single, completely closed box girder model. During bridge construction, the cross-sections of box girders are quasi-closed with a horizontal top flange truss simulating the top plate. The distortional behavior of quasi-closed box girders have not been well studied. Similar to the torsional analysis, Oleinik and Heins (1975) treated the quasi-closed girder as a closed box girder for the distortional analysis by transforming the top flange truss system into a fictitious plate using the same formulation as for a torsional analysis (Kollbrunner and Basler 1969). This approach is questionable because the thickness of the equivalent plate was derived based on the torsional behavior the girder (Kollbrunner and Basler 1969), which is different from the distortional response of the quasi-closed box girders. In addition, little work has been conducted on the distortional analysis of the complete multi-box girder bridges with live loads.

4. As indicated earlier, internal cross-frames also serve as a bracing system to prevent buckling of the top flanges of the box girders. The spacing and stiffness of the internal cross-frames must be a function of the stability requirements during construction. Current design recommendations for internal cross-frames is based solely on the static analysis. No previous research has been conducted on the effect of internal cross-frames on the stability of box girders.

Because of deficiencies in the design method, a thorough investigation of the distortional analysis of box girders is necessary. In current practice, the spacing and stiffness of internal cross-frames are often based on typical details or following recommendations provided by Eqs. 6.2 and 6.3. The distortional warping stresses are usually believed to be small and are not considered in design if internal cross-frames with reasonable cross-sectional areas are provided at a ten to twenty feet spacing. This chapter will focus on the strength requirements for internal cross-frames in quasi-closed trapezoidal box girders, which is not considered in current specifications and design aids. Specifically, design equations to evaluate brace forces in internal cross-frames will be developed. Significant brace forces may be generated in internal cross-frames. Figure 6.8 presents the FEA results of the axial forces in the diagonals of the internal K-frames in the curved girder example that was studied in the last chapter (Fig. 5.3). An angle (L4×4×5/16, A=2.4 in^2) was used for both the strut and the diagonals of the K-frames. Equal amounts of tension and compression are developed in the two diagonals of the K-frames. These forces are caused due to the curvature of the girder; additional forces may also be induced by direct torsional loads such as those due to the eccentricity of the vertical loads.

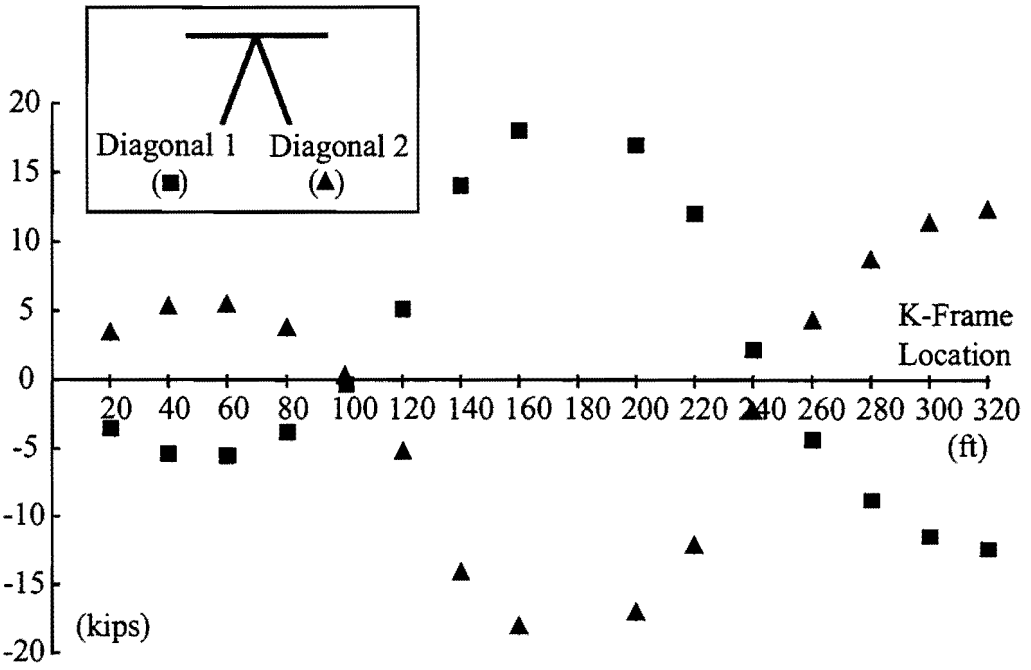

Figure 6.8. Brace Forces in the Diagonals of K-Frames in Curved Girder

A fundamental issue for the distortion of trapezoidal box girders is the determination of the distortional load. A review of the previous research work reveals that the distortional load was often improperly treated or even mistakenly evaluated, particularly for girders with trapezoidal cross-sections. A systematic method to separate the distortional components from

the external loads is developed in this chapter, and the resulting formulas are the basis for the estimation of the K-frames forces as well as all other aspects of a distortional analysis.

The three-dimensional FEA model that was used in the earlier chapters was used in the investigation. Girders with a trapezoidal cross-section were considered. Only K-frames were studied since this is the type of internal cross-frames that are generally used in modern box girder bridges.

6.4 FEA Results

6.4.1 FEA Models

The torsional behavior of quasi-closed box girders was discussed in the last chapter. The distributed torsional load applied on the girder previously shown in Fig. 5.1, was purely torsional. As shown in Fig. 6.9a, the 5 k-ft/ft distributed torsional load was realized by the uniform distributed forces, q_H and q_V, at the corners of the girder. The FEA results from the last chapter focused only on members in the horizontal truss systems. The FEA results for brace forces in the internal K-frames induced by the pure torsional loads are presented in Fig. 6.10. Only forces in one of the diagonals of each K-frames are presented. The other diagonal in a K-frame developed the same magnitude of force with an opposite sign. The results shown in Fig. 6.10 indicate that under the pure torsional loads the brace forces in internal K-frames were small, particularly compared with the brace forces in the top flange truss that were presented previously in Fig. 5.2. With the exception of the K-frames near the supports, brace forces in most K-frames were nearly zero regardless the type of horizontal bracing systems (X-type and SD-type) employed. Therefore, the force in the internal K-frames is only dependent upon the distortional loads.

To study the distortional behavior of quasi-closed box girders, the straight box girder with both the SD-type and X-type top flange bracing systems as shown in Fig. 5.1, was studied by the FEA model. The girders were subjected to the uniform distortional loads as shown in Fig. 6.9b. Unlike the loading in Fig. 6.9a, the distributed forces in Fig. 6.9b are purely distortional and generate no torsional moment on the girder.

With the force components (q_V and q_H) equal to those in the pure torsional load, the distortional load in Fig. 6.9b is the conjugate load to the pure torsional load shown in Fig.6.9a. As was discussed in Chapter 2, depending on the source of the torque, the torsional loads on box girders can be modeled as either vertical forces on the webs or horizontal forces on the top and bottom plates. The stresses and brace forces in girders subjected to the loads shown in Figs. 6.11a and 6.11b, which are similar to most torsional loads on box girder bridges, can be obtained by combination of the results from the loading cases shown in Figs. 6.9a and 6.9b. In particular, since purely torsional loads do not cause forces in the internal K-frames, the K-frame forces in girders shown in Fig. 6.11 are equal to the those from the girder under distortional load as shown Fig. 6.9b.

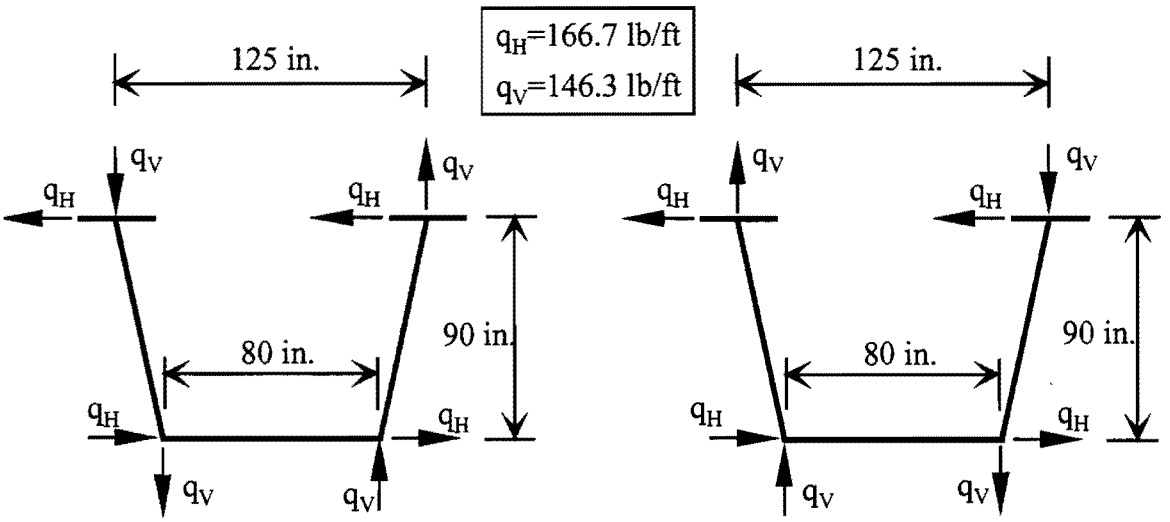

Figure 6.9. Torsional and Distortional Loads on the Quasi-Closed Box Girder

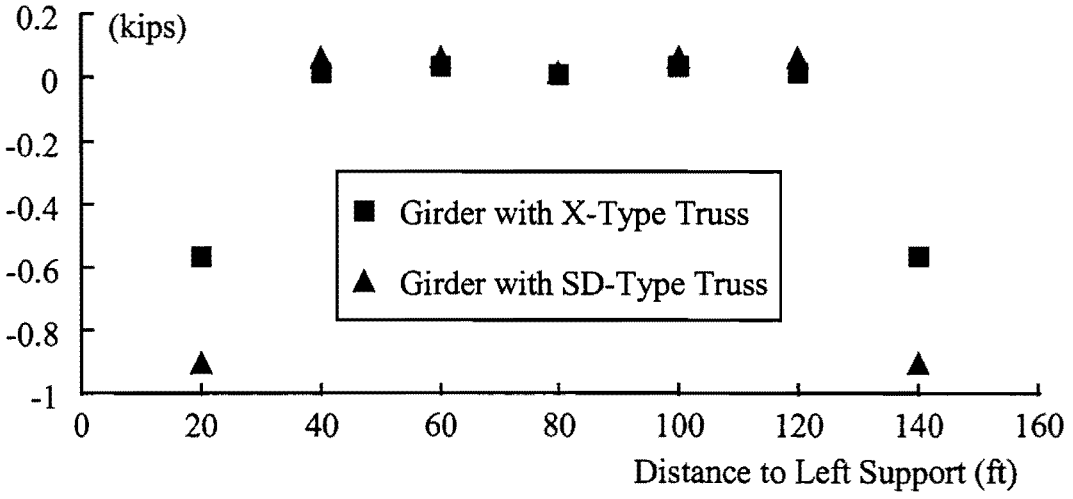

Figure 6.10. Brace Forces in Diagonals of K-Frames Under Pure Torsional Loads

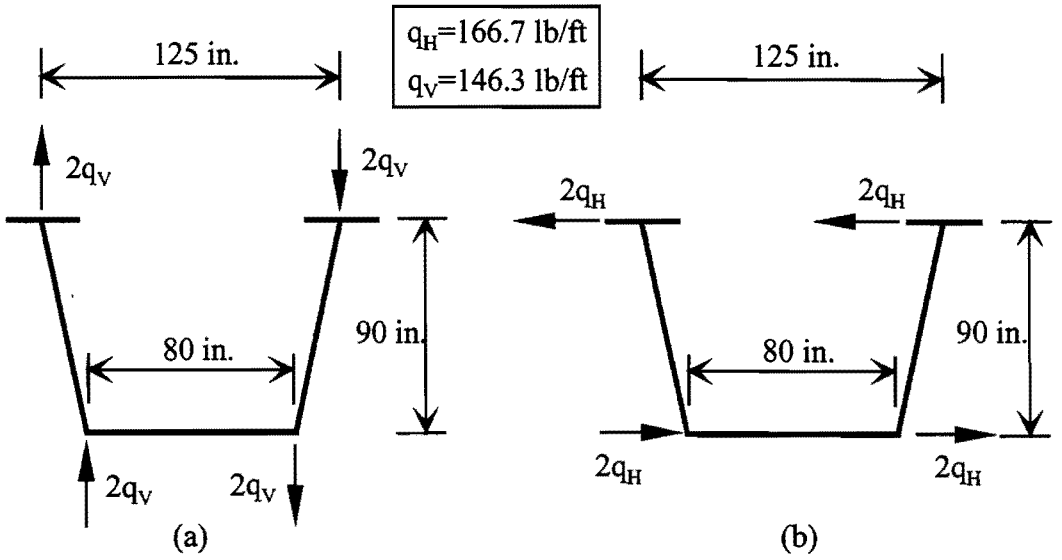

Figure 6.11. Torsional Loads by Vertical and Horizontal Forces

For each top flange truss system, the internal K-frames are spaced at either 10 or 20 feet, which results in four cases in the FEA analysis. The brace forces in both the horizontal top flange truss systems and in the internal K-frames under the distortional loads are presented and discussed in the next two sub-sections.

6.4.2 Girders with X-Type Horizontal Truss

Figure 6.12 shows the axial forces in all bracing members due to the distortional loads (Fig. 6.9b) on the girder with the X-type top flange bracing system. Only half of the girder length is shown due to symmetry. The two diagonals in each K-frame develop the same amount of axial force, however one is in tension and the other is in compression. Similar behavior is observed for the two sides of the strut in all K-frames. For a given brace spacing, the K-frame forces in the respective members are nearly uniform with the exception being the brace adjacent to the support. Comparing the two different spacings, the forces for the 20-ft K-frame spacing are essentially twice the values for the 10-ft spacing. The forces in the K-frames near the supports are smaller than in the other K-frames due to the large stiffness of the solid diaphragms provided at the supports. For the case of K-frames spaced at 20 ft, alternate struts are not part of a K-frame and therefore these struts experience zero force under the distortional loading.

Box girder distortion also causes axial forces in members of the horizontal top flange truss system. In the girder with 10 ft K-frame spacing (Fig. 6.12a), the axial forces in the majority of the diagonals of the top flange truss system are negligible. The forces in the diagonals near the supports are larger, due to the stiffness difference between K-frames and solid diaphragms. The brace forces in the horizontal truss are larger in the girder with the 20 ft spacing between K-frames (Fig. 6.12b). These forces are induced when the top flange truss

system transmits the lateral components of the distortional loads to the nearby K-frames and solid diaphragms. Brace forces in the horizontal truss increase if more bracing panels are enclosed between two consecutive internal K-frames. Compared to the truss forces induced by torsion and bending, however, the distortional loads generate relatively small axial forces in the top flange truss system. For example, the largest diagonal force in the X-type horizontal truss due to the conjugate pure torsional loads as shown in Fig. 6.9a was 21 kips (from Fig. 5.2), compared to 0.94 kips for the distortion (from Fig. 6.12). In general, if the spacing of the K-frames are controlled by Eq. 6.2, the brace forces in the top flange truss system due to the distortional loads are essentially negligible compared with those from torsional loads. The curved girder example in the last chapter also suggests that brace forces due to distortion can be neglected in the horizontal truss. Although distortional load components exist due to the curvature, the axial forces in the horizontal truss system were accurately predicted by considering only bending and torsion.

6.4.3 Girders with SD-Type Horizontal Truss

The brace forces in the girder with the SD-type horizontal top flange bracing system are presented in Fig. 6.13. Cases with the 10-ft and the 20-ft K-frame spacing were considered.

The brace forces for the 10-ft K-frame spacing (Fig. 6.13a) are similar to the case of the girder with the X-type top flange truss system (presented in Fig. 6.12a), particularly in the middle span region. The forces in the diagonals of the top flange truss are nearly zero except near the supports. Equal tensile and compressive forces have developed in the diagonals of the K-frames and in the two sides of the struts, respectively. The forces in the diagonals of the internal K-frames spaced at 20 ft are similar to those with the X-type horizontal truss system with the same K-frame spacing, and are approximately twice the magnitude of the values with a 10-ft K-frame spacing (Fig. 6.13b). The same amount of tension and compression is induced in the diagonals within a K-frame.

If the K-frames are spaced every two panels of the horizontal truss (20 ft), the axial forces in the diagonals of the horizontal truss increase (Fig. 6.13b). However, they are still considerably smaller than the forces induced by torsional loads previously shown in Fig. 5.2. Unlike the case shown in Fig. 6.12b, non-zero axial forces developed in struts that are not parts of the K-frames (Fig. 6.13b). Since there is only one diagonal in each panel of the top flange truss, the struts develop brace forces to counter-balance the diagonal forces induced by distortional loads. These global axial forces over the entire length of the struts also developed in those struts that are parts of the K-frames. As a result, the magnitudes of tensile and compressive forces in the two sides of the struts within a K-frame are different, as shown in Fig. 6.13b.

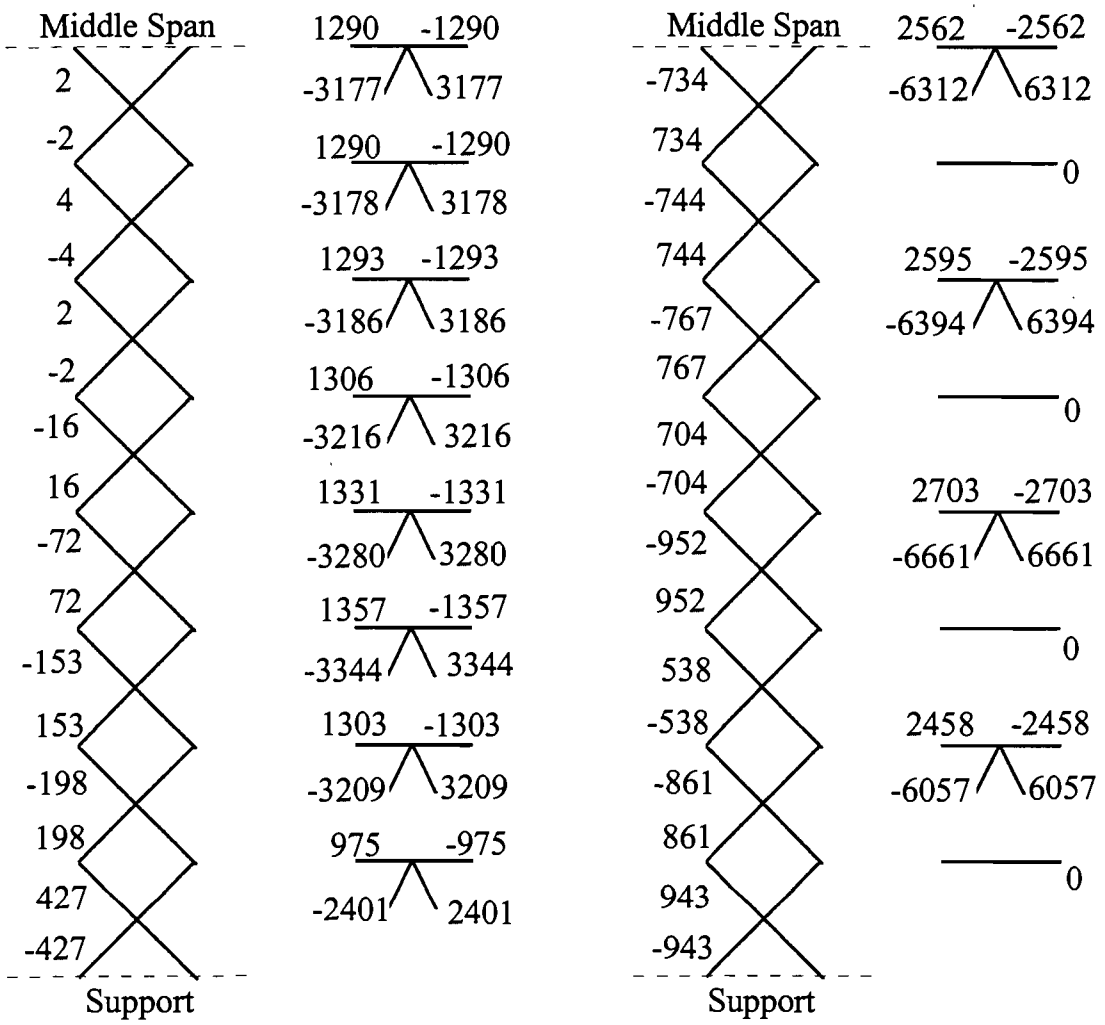

(a) K-Frames Spaced at 10 ft (b) K-Frames Spaced at 20 ft

Figure 6.12. Brace Forces Due to Distortional Loads in Box Girders with X-type Top Flange Truss System (lbs)

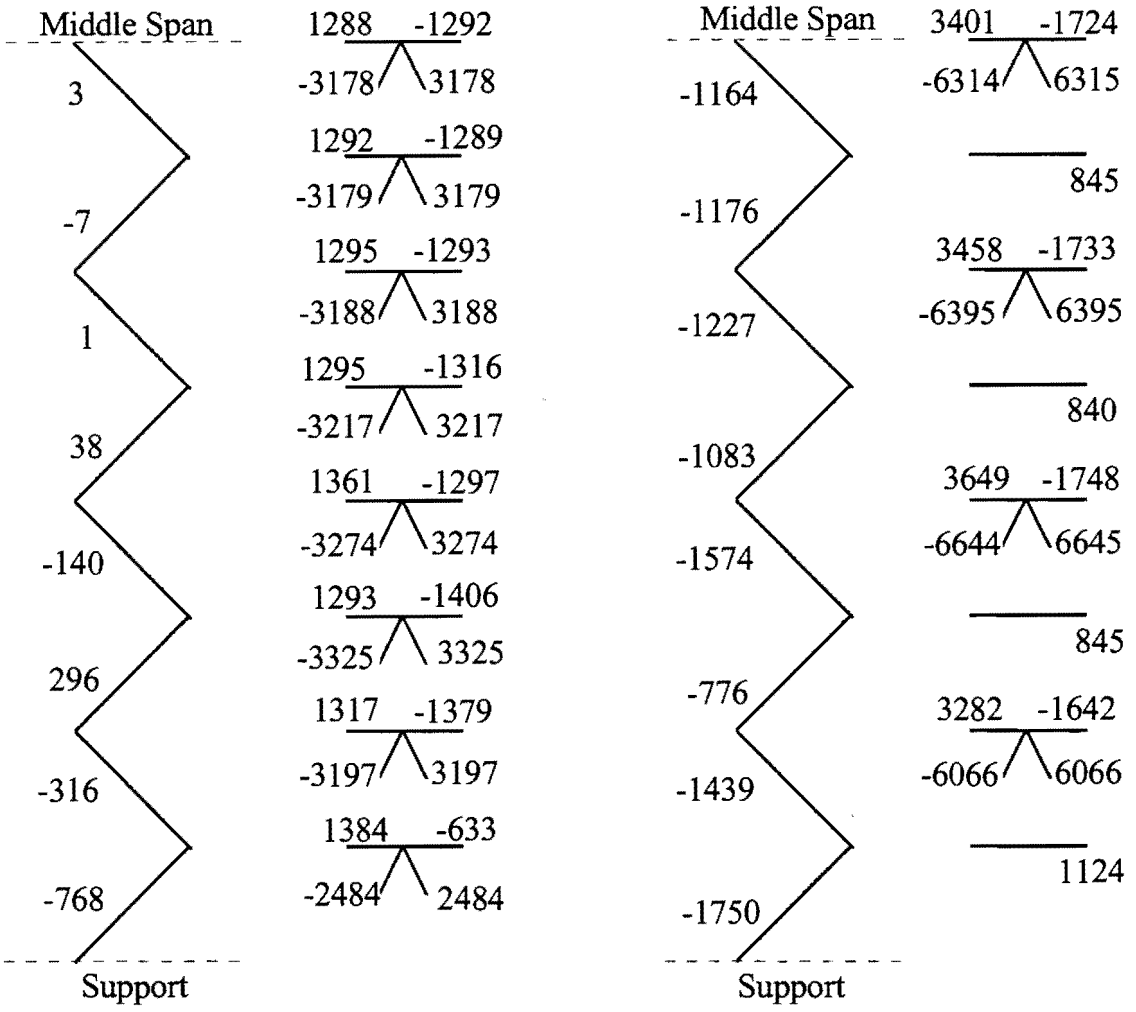

Figure 6.13. Brace Forces Due to Distortional Loads in Box Girders with SD-type Top Flange Truss System (lbs)

In the two sides of the struts, the force components induced by the distortional load are still equal in magnitude and opposite in direction. Therefore, averaging the forces (the algebraic values) in the two sides of the K-frame struts will eliminate the distortional components in the struts. The resulting values represent the global components from the horizontal truss, which are nearly equal to the brace forces in the alternate struts that are not parts of the K-frames. On the other hand, half of the difference of the two forces (also algebraic values) in a K-frame strut represents the axial forces induced by the distortional loads, and the results are essentially same as the K-frame forces in the girder with the X-type horizontal truss as presented in Fig. 6.12b.

If more than one bracing panel of the SD-type top flange truss is included between two consecutive K-frames, the global forces over the entire length of the struts always exist, resulting in unequal tension and compression in the two sides of the struts. However, these global forces are relatively small compared to the strut forces caused by bending, particularly if the spacing of the K-frames are within the limit provided by Eq. 6.2. For example, the largest strut force in the same girder subjected to 3.3 kips/ft bending load is 13.1 kips (from Fig. 5.7), while the largest (non-K-frame) strut force from distortional loading is 1.12 kips as shown in Fig. 6.13b. Since the bending induced strut forces are usually larger than the distortionally induced forces, the difference of the strut forces in two sides of the K-frames is not considered, and the behavior of K-frames in girders with both the X-type and SD-type horizontal truss systems is assumed the same.

In summary, it is assumed in this investigation that the spacing of the internal K-frames satisfy the limits of Eq. 6.2 in this report, and no more than three top flange bracing panels are included between two consecutive K-frames. The FEA results presented above indicate that distortional loads only cause a small amount of brace forces in the diagonals of the top flange truss system and therefore can be neglected. The top flange truss system is designed to carry forces caused by bending and torsional loads on the quasi-closed box girders, which has been discussed in the last chapter. Additional forces may be developed due to distortion in struts that are parts of the internal K-frames. Distortional loads may also induce brace forces in the diagonals of K-frames, and an approximate method is developed in the following sections to evaluate these forces.

6.5 Distortional Analysis of Quasi-Closed Box Girders

6.5.1 Static Equilibrium of K-Frames

Brace forces will develop in members of internal cross-frames subjected to distortional loads. Figure 6.14 shows an internal K-frame in a box girder subjected to a concentrated distortional load from forces V and H as shown in the figure. The depth of the box is h, while the widths of the bottom and top of the trapezoidal section are a and b, respectively. No torsional moment results from the components of the distortional load, hence V and H must satisfy

$$V(a+b) = 2Hh \ . \qquad (6.4)$$

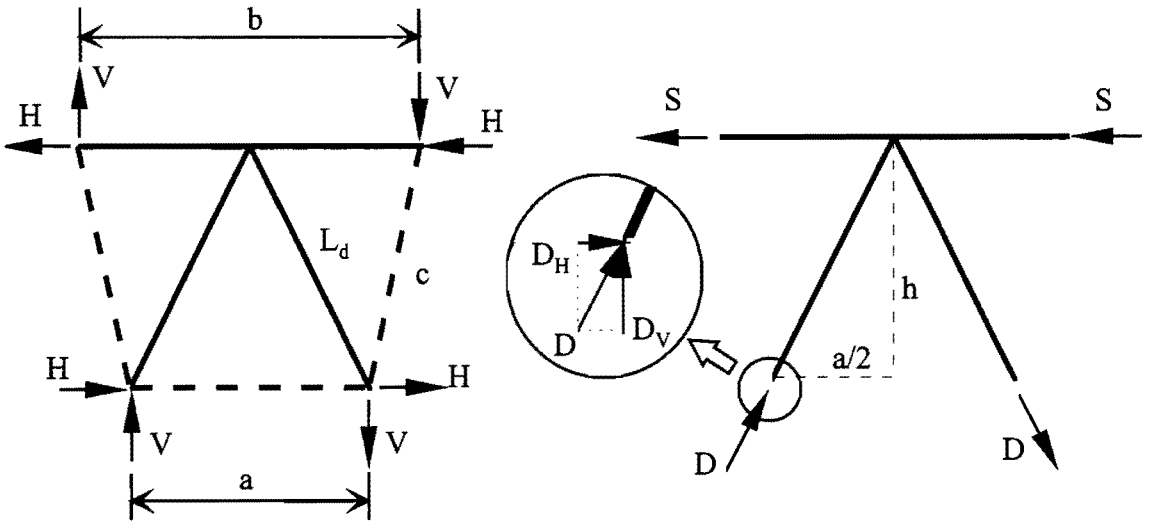

Figure 6.14. Static Equilibrium of Internal K-Frames in Box Girders with Distortional Load

The axial forces in the K-frame members due to the distortional loads can be derived using statics. Since the struts can only resist the horizontal loads, the vertical components (V) at the top is transmitted via the webs to the bottom corners, resulting in $D_V=2V$. Also, equilibrium of the K-frame in the horizontal direction leads to $D_h=S$. D_V and D_h are the components of the axial force D and have the relation of $D_h/(a/2)=D_V/h$, which results in the axial force in the strut to be

$$S=D_h=\frac{a}{2h}D_V=\frac{a}{h}V=\frac{2a}{a+b}H\ . \tag{6.5}$$

Thus, the axial force in a diagonal of the K-frame is

$$D=\sqrt{D_V{}^2+D_h{}^2}=\frac{2V}{h}\sqrt{h^2+(\frac{a}{2})^2}=\frac{2L_d}{h}V\ , \tag{6.6}$$

in which L_d is the length of the diagonals. Equal magnitudes of axial forces, D, are developed in the two diagonals, however one is in tension and the other is in compression as demonstrated in Fig. 6.14. Similarly, equal amounts of tension and compression, S, are developed in the two sides of the struts. Equations 6.5 and 6.6 imply that if the components of the distortional loads (H and V) that act on the K-frame are known, the axial forces in the K-frame can be determined.

6.5.2 Approximation of K-Frame Forces from Distortional Torsion

As discussed in Section 6.1, the distortional behavior of box girders can be modeled using the BEF model. The distortional forces on the internal K-frames, represented by H and V in Fig. 6.14, are the reaction forces at the discrete supports in the BEF analogy. Therefore, if the BEF analogy is used in a distortional analysis, the reaction at the supports can be used to calculate the axial forces in the internal K-frames, using Eqs. 6.5 and 6.6 as derived above.

Although the BEF analogy is rarely used in design due to the complexity of the method, the method can be used to formulate an approximate method to evaluate the brace forces in K-frames. If the elastic foundation under the beam is conservatively neglected, the reactions under the discrete elastic supports will generally increase, leading to a conservative estimate of the K-frame forces. The accuracy of the approximation depends on the spacing between the K-frames and the relative stiffness of the elastic foundation and the K-frames.

As indicated in Section 6.1, the elastic foundation represents the distortional stiffness of the box girder cross-section. This distortional stiffness depends mainly on the thickness of the plates, along with the shape and dimension of the cross-section. For a completed box girder, this stiffness is relatively large due to the large thickness of the top plate (the concrete slab). For a quasi-closed section, however, the top "plate" is only a horizontal truss. Between panel points of the top lateral truss, the box section is very weak in out-of-plane bending. The cross-section is open at the top for the majority of the girder length, which leads to a relatively small distortional stiffness of the cross-section. Therefore, neglecting the elastic foundation in the BEF model may be justified for quasi-closed box girders, resulting in a simplified Beam-on-Elastic-Supports model. The reactions can be obtained by solving the continuous beams, which still requires the calculation of the distortional properties of the box girder. A further simplification is made for distributed loads by assuming that the reaction forces are equal to the product of the K-frame spacing and the intensity of the distortional loads.

The proposed approximate method is verified by the FEA results for the straight girders presented in the last section. For K-frames spaced at 10 ft, neglecting the distortional stiffness results in

$$H=s(q_H)=10(166.7)=1667 \text{ lbs},$$

$$V=s(q_V)=10(146.3)=1463 \text{ lbs}.$$

The K-frame dimensions are a=80 in., b=125 in., h=90 in., and $L_d= (90^2+40^2)^{1/2}= 98.5$ in. Using Eqs. 6.5 and 6.6, the brace forces in the diagonals and struts of the K-frames are

$$D = \frac{2L_d}{h}V = \frac{2(98.5)}{90}(1463) = 3202 \text{ lbs},$$

$$S = \frac{a}{h}V = \frac{80}{90}(1463) = 1300 \text{ lbs.}$$

These values are within 5% of the FEA results shown in Figs. 6.12a and 6.13a for all K-frames except those near the supports. If the K-frames are spaced at 20 ft, the magnitudes of V and H double compared to the 10-ft spacing, and therefore D=6404 lbs and S=2601 lbs. These values have reasonable agreement with the FEA results presented in Figs. 6.12b and 6.13b. The only exception is for the K-frames nearest to the supports, in which the actual brace forces are always less than the values predicted by Eqs. 6.5 and 6.6 since the equations conservatively neglect the presence of the solid diaphragms at the support regions. For members in other K-frames, good agreement between the predicted values and the FEA results is achieved except the K-frame strut forces in girders with the SD-type horizontal truss. However, these differences are considered small as discussed in the preceding section, and Eqs. 6.5 and 6.6 will be used for girders with both types of top flange bracing systems.

6.6 Determination of Distortional Loads for Trapezoidal Box Girders

6.6.1 Introduction

In real bridges, distortional loads are not explicitly applied on girders as shown in Fig. 6.14, but instead are always combined with torsional loads. In order to use Eqs. 6.5 and 6.6 to calculate the K-frame forces, the distortional components from the external loads must first be determined.

Box girder distortion is caused by torsional loads that are not distributed in proportion to the Saint-Venant shear flow on the cross-section of the girder. A proof of this postulate is provided in Appendix D. As shown earlier in Figs. 2.5 and 2.6, torsional loads in bridges are usually applied to the girder either by a pair of vertical forces (resulting from the eccentricity of gravity loads to the centerline of the girder) or by a pair of horizontal forces (such as the equivalent forces resulting from the bending moment due to the curvature of the girder). The distortional components can be determined by subtracting the pure torsional load from the real load. The pure torsional load is the load that results in the same torsional moment of the acting load but is distributed along the cross-sectional profile in proportion to the Saint-Venant shear flow. Both the pure torsional load and the distortional load in the afore-mentioned two loading cases are derived in this section.

6.6.2 In-Plane Components of Pure Torsional and Distortional Loads

Both the pure torsional load and the distortional load consist of four forces acting in the planes of the plates of the box girder, as demonstrated previously in Figs. 2.5 and 2.6. These in-plane components that correspond to different external loads are determined in the first step. Consider first the case (Case 1) when the girder is subjected to two opposite vertical

forces at the top of the webs, resulting in a torsional moment of Nb (Fig. 6.15a). This is equivalent to the load case shown in Fig. 6.15b, in which N_t is the horizontal force in the plane of the top plate, and N_w is the force acting in the plane of the webs. N_t and N_w can be derived from N as

$$N_w = N / \cos\theta \ , \tag{6.7a}$$

$$N_t = 2N \tan\theta \ . \tag{6.7b}$$

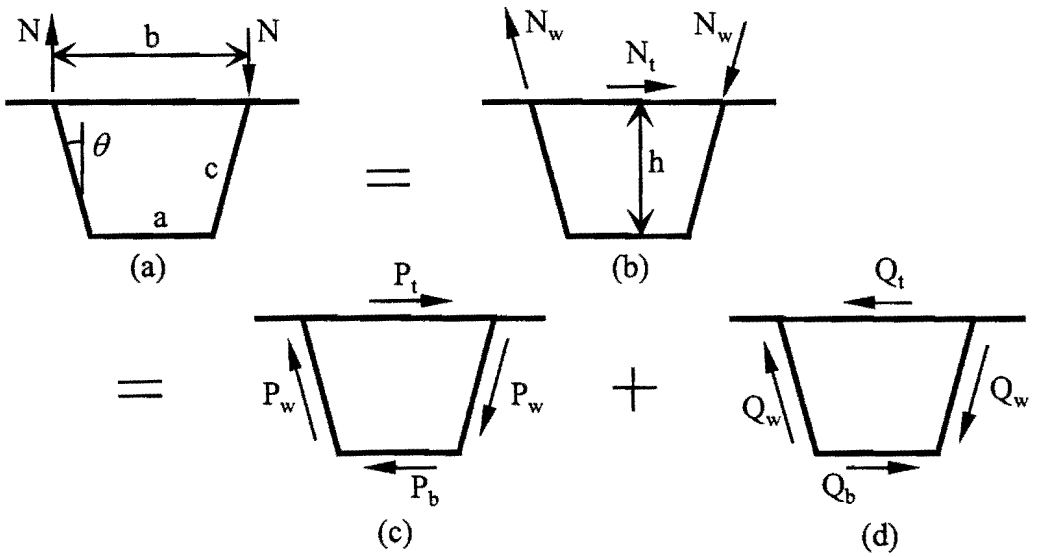

Figure 6.15. Torsional and Distortional Components Due to Vertical Loads

The Saint-Venant shear flow corresponding to the torque Nb is $Nb/(2A_0)$, in which A_0 is the enclosed area of the cross-section. This uniform "shear flow" along the circumference of the cross-section leads to the equivalent pure torsional components (Fig. 6.15c) to be proportional to the width of the corresponding plates, i.e.,

$$P_t = \frac{Nb}{2A_0} \times b = \frac{b^2}{2A_0} N \ , \tag{6.8a}$$

$$P_b = \frac{Nb}{2A_0} \times a = \frac{ab}{2A_0} N \ , \tag{6.8b}$$

$$P_w = \frac{Nb}{2A_0} \times c = \frac{bc}{2A_0} N \ . \tag{6.8c}$$

The distortional components on the plates of the box (Fig. 6.15d) are

$$Q_t = P_t - N_t = (\frac{b^2}{2A_0} - 2\tan\theta)N$$

$$= \frac{N}{2A_0}[b^2 - 2h(a+b)\tan\theta] = \frac{a^2}{2A_0}N \ , \qquad (6.9a)$$

in which the relations of A_0=h(a+b)/2 and h(tanθ)=c(sinθ)=(b-a)/2 have been applied. Similarly, the distortional components on the other plates of the box are derived by

$$Q_b = P_b = \frac{ab}{2A_0}N \ , \qquad (6.9b)$$

$$Q_w = N_w - P_w = (\frac{1}{\cos\theta} - \frac{bc}{2A_0})N = \frac{ac}{2A_0}N \ . \qquad (6.9c)$$

The assumed positive directions of all the forces are shown in Fig. 6.15.

Another case (Case 2) for torsional loading consists of two horizontal forces acting on the top and bottom plates of the box girder (Fig. 6.16a). The torsional moment is Nh, and the pure torsional load components in the plane of the individual plates can be derived similar to the previous case. Assuming the distribution of the torsional load is from Saint-Venant torsion yields the following expressions (Fig. 6.16b):

$$P_t = \frac{bh}{2A_0}N = \frac{b}{a+b}N \ , \qquad (6.10a)$$

$$P_b = \frac{ah}{2A_0}N = \frac{a}{a+b}N \ , \qquad (6.10b)$$

$$P_w = \frac{ch}{2A_0}N = \frac{c}{a+b}N \ . \qquad (6.10c)$$

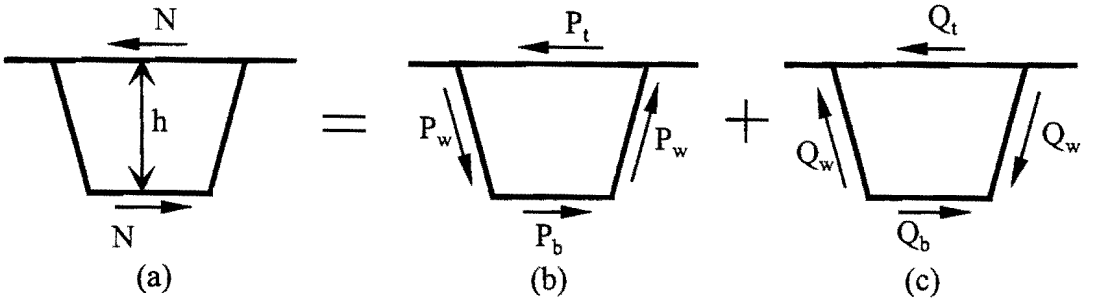

Figure 6.16. Torsional and Distortional Components Due to Horizontal Loads

The distortional components are shown in Fig. 6.16c and are derived similar to the previous case, which yields:

$$Q_t = N - P_t = N(1 - \frac{b}{a+b}) = \frac{a}{a+b}N \ , \tag{6.11a}$$

$$Q_b = N - P_b = N(1 - \frac{a}{a+b}) = \frac{b}{a+b}N \ , \tag{6.11b}$$

$$Q_w = P_w = \frac{c}{a+b}N \ . \tag{6.11c}$$

6.6.3 Distortional Components in Cartesian Coordinates

The calculation of the brace forces in the internal K-frames using Eqs. 6.5 and 6.6 requires the evaluation of the distortional loads. The distortional components must be transformed into vertical and horizontal directions and placed at the joints of the plates, which can be determined by static equilibrium. For instance, the distortional components due to the vertical loads (Case 1) are derived as:

$$V = \frac{1}{2}Q_w \cos\theta = \frac{Na}{4A_0}c\cos\theta = \frac{a}{a+b}\frac{N}{2} \ , \tag{6.12a}$$

$$H = \frac{Q_t}{2} + \frac{Q_w \sin\theta}{2} = \frac{Na}{4A_0}(a + c\sin\theta) = \frac{a}{h}\frac{N}{4} \ . \tag{6.12b}$$

H can also be derived by $\frac{Q_b}{2} - \frac{Q_w \sin\theta}{2}$ and the same result is obtained. Similarly, if the external loads result from horizontal forces (Case 2), the distortional components in the Cartesian coordinate system are:

$$V = \frac{h}{a+b}\frac{N}{2} \ , \tag{6.13a}$$

$$H = \frac{N}{4} \ . \tag{6.13b}$$

The results of these components for both the pure torsional and distortional loads are presented in Fig. 6.17 and 6.18.

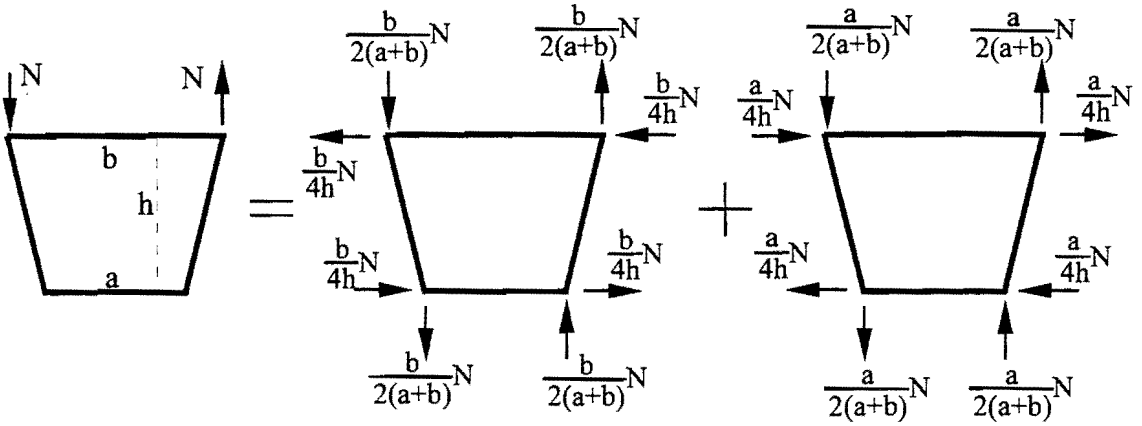

Figure 6.17. Torsional and Distortional Components at Joints Due to Vertical Loads

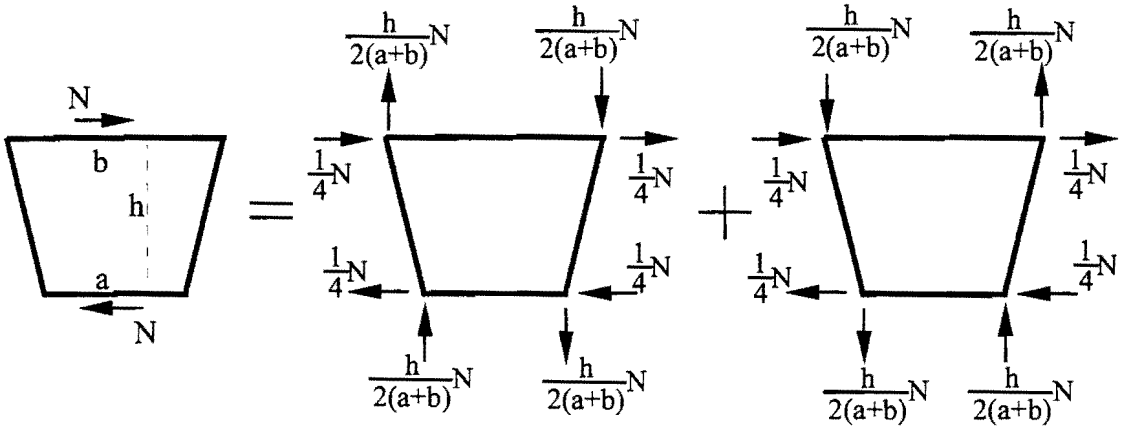

Figure 6.18. Torsional and Distortional Components at Joints Due to Horizontal Loads

Figure 6.17 reveals an important fact about the distortional components for box girders with trapezoidal cross-section. In the traditional theory of box girder distortion, the distortional load components on each plate are identical to the corresponding pure torsional components in magnitude, as demonstrated in Fig. 2.5 and 2.6 for rectangular cross-section ($m_T/(2h)$ for the top and bottom plates and $m_T/(2b)$ for the webs), as well as in Fig. 6.9 for trapezoidal cross-section (same q_V and q_H for both the torsional and distortional components). This leads to the direct use of m_T to represent the distortional load in the governing equation, i.e., $m_D=m_T$ in Eq. 6.1 as discussed in Section 6.1. This relation still holds for trapezoidal box girder subjected to two horizontal forces, as demonstrated in Fig. 6.18. However, when the torsional load on a trapezoidal box consists of two vertical forces at the top of the webs, as shown in Fig. 6.17, the distortional components are different from the torsional components by a factor of a/b. Therefore, instead of using m_T in equation Eq. 6.1 as

was used in previous studies (Dabrowski 1968, Nakai and Yoo 1988, Wright et al 1966), the distortional loads should be $m_D=m_T(a/b)$ if the torsional loads result from two vertical forces.

The use of m_T in the distortional analysis is also misleading when the box girder is subjected to torsional loads consisting of both horizontal and vertical forces. For example, when the actual load on a girder is purely distortional, which has zero torsional moment ($m_T=0$), the use of m_T to represent the distortional load will lead to zero distortion while in fact the girder is distorted in the same direction by the forces on the top and bottom plates and by those on the webs. In summary, torsional and distortional loads are not identical. If more than one couple is acting on the box girder, the distortional analysis must be performed on each couple separately rather than using the total torsional moments.

6.7 Design Formula for Brace Forces in Quasi-Closed Box Girders

As discussed earlier, torsional loads on box girders may be caused by vertical forces due to the eccentricity of the gravity center of the slab to the centerline of the girder, or by horizontal forces such as those induced by curvature of the girder. In each case, the applied loads can be treated as the superposition of the pure torsional loads and the distortional loads. The pure torsional loads, as shown in Fig. 6.15c and 6.16b, will not generate brace forces in the internal K-frames of the box girder. The design equations for the axial forces induced in the K-frames by distortional loads can be derived by applying Eqs. 6.5 and 6.6. The resulting expressions depend on how the torque is applied to the girders.

1. Torsion applied by Eccentric Vertical Force

The largest loading during the construction of box girder bridges is the distributed gravity load of the wet concrete. Figure 6.19 shows a girder that is subjected to a concrete gravity load with a resultant, w, that is offset from the girder centerline by an amount of e. The spacing of internal K-frames is denoted by s. The distortional loads on a K-frame can be obtained by replacing N with wse/b in Eq. 6.12, which results in

$$H = \frac{ae}{4bh} ws \ , \tag{6.14a}$$

$$V = \frac{ae}{2b(a+b)} ws \ . \tag{6.14b}$$

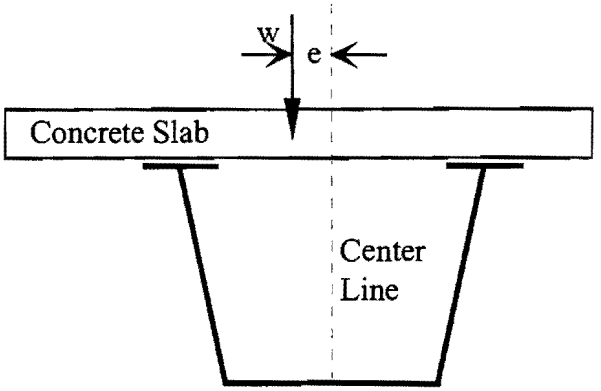

Figure 6.19. Eccentricity of Vertical Load

Substituting Eq. 6.14 into Eqs. 6.5 and 6.6, the brace forces in members of internal K-frames are derived by

$$D = \frac{L_d ae}{bh(a+b)} ws \ , \tag{6.15a}$$

$$S = \frac{a^2 e}{2bh(a+b)} ws \ . \tag{6.15b}$$

If a box girder is subjected to a concentrated load, Q, with eccentricity e to the centerline of the girder (such as the wheel loads from a screed), Eqs. 6.15a and 6.15b are still applicable for the calculation of the brace forces in K-frames except that the product of ws should be replaced with Q.

2. Torsion Applied Due to Girder Curvature

In curved box girder bridges, torsional moments may result from the curvature even when no direct torsional load is acting on the bridge. As discussed in Chapter 2, the effect of curvature can be approximated by a torsional load comprised of two horizontal forces, M/(Rh), on the top and bottom flanges of the girder, as demonstrated in Fig. 2.10. The distortional loads on an internal K-frame can be approximately determined by replacing N in Fig. 6.16 with Ms/(Rh), where M is the bending moment at the location of the K-frame, and R is the radius of the curved girder. The distortional components on the joints of the flanges and web can be derived from Eq. 6.13 as

$$H = \frac{s}{4Rh} M \ , \tag{6.16a}$$

$$V = \frac{s}{2R(a+b)}M \ . \qquad (6.16b)$$

From Eqs. 6.5 and 6.6, the resulting bracing forces in the K-frame are

$$D = \frac{L_d s}{Rh(a+b)}M \ , \qquad (6.17a)$$

$$S = \frac{as}{2Rh(a+b)}M \ . \qquad (6.17b)$$

For curved girders, brace forces due to both the load eccentricity and the girder curvature must be considered using Eqs. 6.15 and 6.17. The total forces are the superposition of these two results, and are dependent upon the respective distortional directions. Determination of the distortional direction may sometimes be confusing. It is suggested, conservatively, to simply add the absolute force values from different distortional loads together and the design force is compressive. For the lateral struts, however, additional forces over its entire length due to the bending loads as discussed in the last chapter must also be considered. The procedure is demonstrated in the following examples, which verify the effectiveness of Eqs. 6.15 and 6.17 by comparing the results based upon the proposed method to the FEA solution.

Example 1:

Consider the straight girder with the dimensions shown in Fig. 5.1, which was previously studied with bending, pure torsional as well as distortional loads. The same girder is considered in this example subjected to two different vertical forces on the top flanges, equivalent to an eccentric distributed vertical load w = 3.3 kips with an offset of 20.83 in. to the centerline of the girder (Fig. 6.20). K-frames are spaced at 20 feet. Other dimensions for the box girders are a = 80 in., b = 125 in., h = 90 in. and L_d = 98.5 in. Substituting these numbers into Eq. 6.15 yields D = 4.70 kips and S = 1.91 kips, respectively.
The FEA results as well as the above predicted force magnitudes in the K-frame members are presented in Fig. 6.21. Only one of the forces (the positive ones) for the diagonals and the struts in each K-frame is presented. The FEA strut force result in each of the K-frames is defined as half the difference between the forces in the two sides. Good agreement is achieved except for the K-frames near the supports. However, the actual forces in the K-frames adjacent to supports are always less than the predicted values under uniform distortional loads.

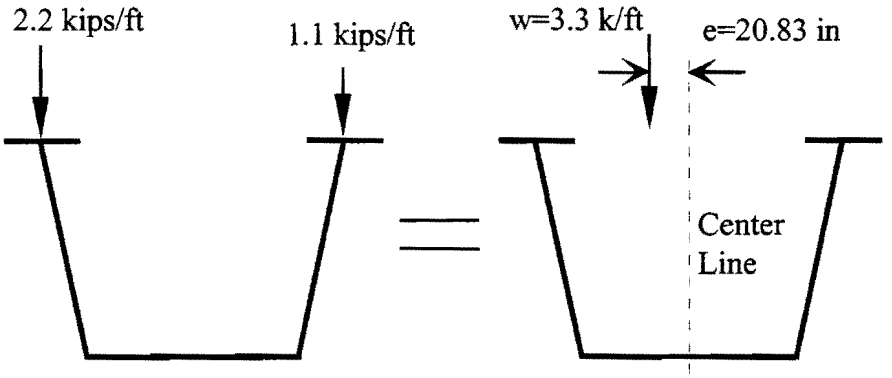

Figure 6.20. Eccentric Vertical Load on Box Girder

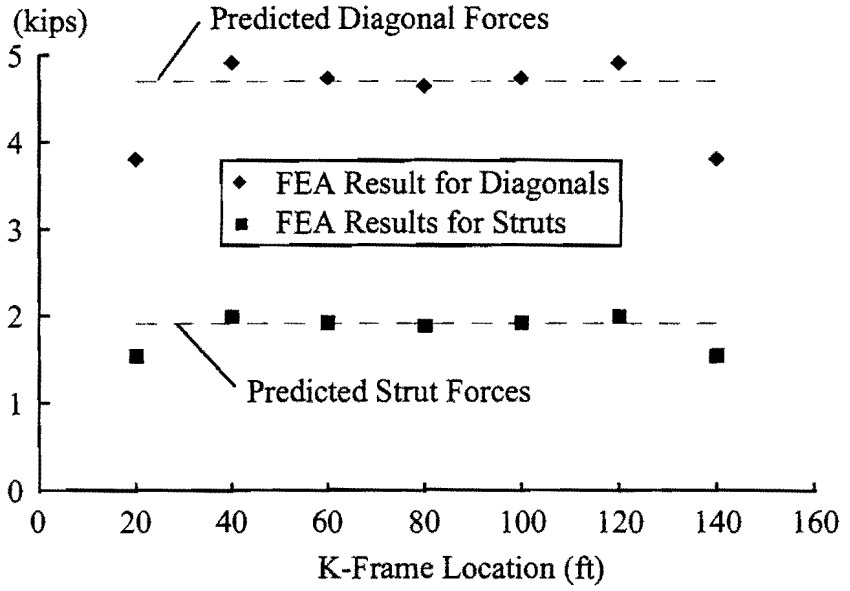

Figure 6.21. K-Frame Forces Due to Eccentric Vertical Loads

Additional forces develop in the struts due to the bending and lateral components of loads on the top flanges. These effects can be evaluated using the method developed in Chapter 5. It was derived (from Fig. 5.17) that throughout the entire length the strut at the mid-span developed the maximum forces of 34.9 kips for the X-type truss and 13.8 kips for SD-type horizontal truss. Therefore, by adding the distortional components of ±1.91kips the two sides of the struts are subjected to the axial forces of 36.8 kips/33.0 kips for the girder with X-type truss, and 15.7 kips/11.8 kips for the girder with SD-type truss, all in tension. The forces in the diagonals of the K-frames are ±4.70 kips, one diagonal is in tension and the other is in compression.

Example 2:

The brace forces in the curved girder previously shown in Fig. 5.3 were presented in Fig. 6.8 earlier in this chapter. Using the bending moments at the K-frame locations, the brace forces are calculated using Eq. 6.17. The geometrical dimensions are a = 75 in., b=20 in., h = 90 in., L_d = 97.5 in, R= 955 ft, and s =20 ft. The axial forces in the struts and diagonals at the left side of the K-frames are presented in Fig. 6.22. The strut forces from the FEA results were again derived by dividing the difference between the forces in the two sides of each K-frame by 2. Good agreement between the FEA results and forces obtained using Eq. 6.17 is achieved, as demonstrated in Fig. 6.22.

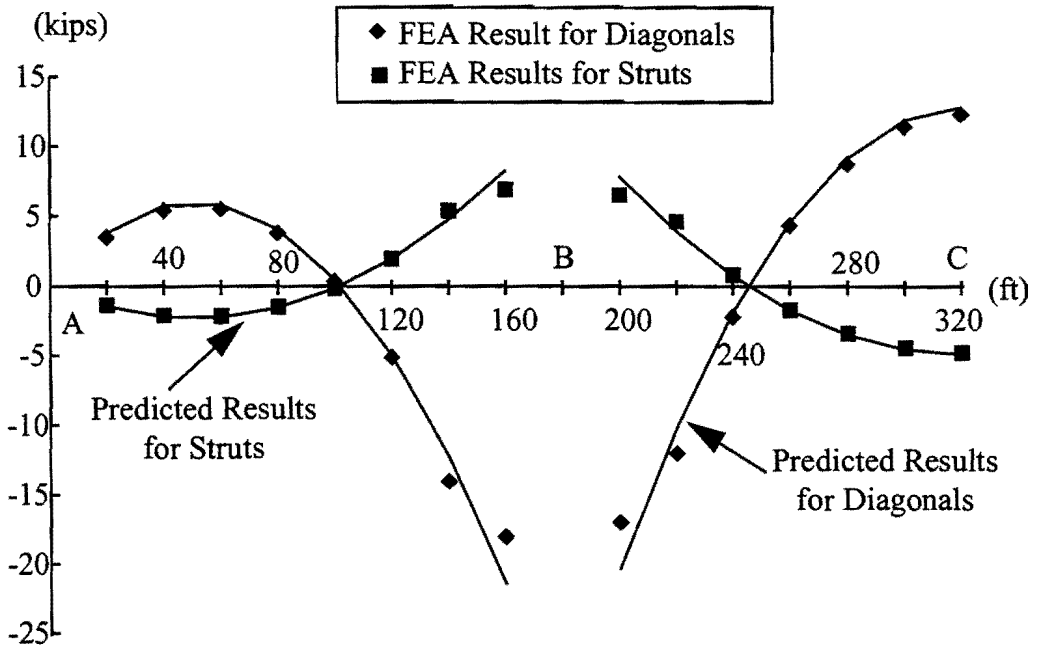

Figure 6.22. K-Frame Forces in Curved Continuous Box Girders

According to the proposed method, the largest diagonal brace force of the K-frames is ±21.4 kips (FEA result is ±18.0), which occurred in the K-frame 160 ft from Support A. Due to its location nearest to the interior support (Support B), the braces forces of this K-frame has the largest error between the FEA solution and the results based on the proposed method. However, conservative results were obtained using the proposed method.

The total brace forces in the struts can be estimated using the methods proposed in this chapter as well as in Chapter 5. The brace forces in the two sides of this K-frame is ±8.22 kips due to the distortional components. Through the entire length of the strut, a uniform axial force of -17.3 kips developed due to the bending of the box girder (from Fig. 5.19). The brace forces in all members in this K-frame can be obtained using superposition and the results are presented in Fig. 6.23a. FEA results are also included for comparison. The

agreement is reasonably well for this K-frame. Better agreement was achieved for other K-frames that are not adjacent to the supports, as demonstrated in Fig. 6.23b for the K-frame in the middle of the girder (320 ft to Support A). The current design method (Highway 1982) neglects the braces forces in the diagonals and predicts a uniform tensile force of 2.06 kips for all struts.

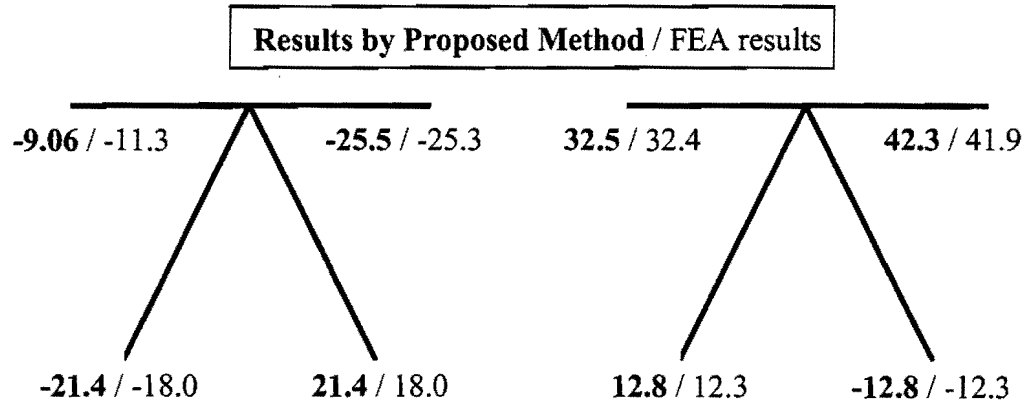

(a) K-frame at 160 ft to A (a) K-frame at 320 ft to A

Figure 6.23. Brace Forces in Two K-Frames of the Curved Girder

CHAPTER 7 FIELD AND COMPUTATIONAL STUDIES OF THE COMPOSITE BOX GIRDER BRIDGE UNDER LIVE LOADING

7.1 Introduction

The preceding chapters focused on the construction phase of box girder bridges, when the steel girders must support the wet concrete and the entire construction load. Once the concrete has hardened, the bridge becomes a composite structure so that the steel girders and the concrete slab act together to resist external loads. Therefore, the methodology used in the analysis for the completed bridge is significantly different from that used for the construction stage. In addition to the stresses produced by the dead load during construction, the live load will add additional stress in the steel girders. The determination of the stresses due to live loads is not only important for the design of the ultimate strength, but also essential for determining the fatigue rating of a bridge girder.

As introduced in Chapter 2, the live load lateral distribution method is the major design method in practice for the analysis of bridges subjected to live loads. The lateral distribution factor for steel box girder bridges in the current AASHTO specification as given by Eq. 2.7, is based on the research conducted by Mattock (1971). Although modifications have been proposed by Heins and Hall (1981) for curved bridges, no study was reported on continuous curved bridges, particularly for the behavior in the negative moment regions.

An effective design method must be based on a good understanding of the behavior of box girder bridges. Because of the limited past researches, there are a number of areas that are unclear on the live load box girder bridge behavior. For example, further study is required to address:

— Whether box girders act individually or interact with other adjacent other girders as a 3D structure;

— Whether the current distribution factor can be applied effectively to continuous curved box girder bridges;

— How torsional moments are distributed and resisted between box girders.

More investigations on box girder bridges are therefore warranted. This chapter presents the live load experiments conducted on the bridge that was studied during the construction phase in previous chapters. Girder stresses were measured with truck loads applied at different locations on the deck surface. The results from these field studies were compared to FEA models for the completed bridge. Two types of FEA models were employed in the study. A line element model was first developed by considering the interior box girder as an independent continuous beam with a composite cross-section. This relatively simple model is similar to the approach that is employed in most approximate methods or computer programs

currently used by bridge engineers. The other FEA model is a 3D model similar to those discussed in Chapter 4 for the study of the construction stages. The 3D model in the chapter includes the concrete slab as well as elements of the steel girder such as flanges, webs, bracing members, stiffeners, and diaphragms. Results from the field and computational studies are presented. Implication of the results are discussed, along with comparisons to the findings by previous research work.

7.2 Live Load Tests

The concrete deck of the bridge was constructed in late September of 1996. The parapets were completed in April of 1997. The live load tests were conducted on April 24th, 1997, soon after these curbs had been constructed. The bridge was open to public traffic in the Summer of 1997.

Live loads were applied by four trucks loaded with sand. Table 7.1 lists the axle weights of the individual trucks that were labeled A, B, C and D. Truck A, B and C have two axles in the back and a total of 10 wheels. Truck D had only one axle in the rear and a total of 6 wheels. The distances between the tires for all the trucks are illustrated in Fig. 7.1.

Table 7.1. Axle Loads and Total Weights of Testing Trucks (lbs)

	FRONT	BACK	TOTAL
TRUCK A	13,180	47,320	59,920
TRUCK B	12,960	42,800	55,520
TRUCK C	13,180	43,650	56,420
TRUCK D	8,700	24,300	32,680

The dimension of the slab plan was carefully measured and stations were painted on the slab surface prior to the tests so that the trucks could be properly positioned on the bridge. Stations were spaced at 25 ft. along the majority of the bridge length, however, in the negative moment regions near the two middle supports (Bents 18 and 19) the station interval was reduced to 5 ft. Each of the station locations consisted of a radial line over the width of the bridge. The centerline the bridge as well as the individual girder were marked on each station line so that the truck could be properly placed transversely on the bridge.

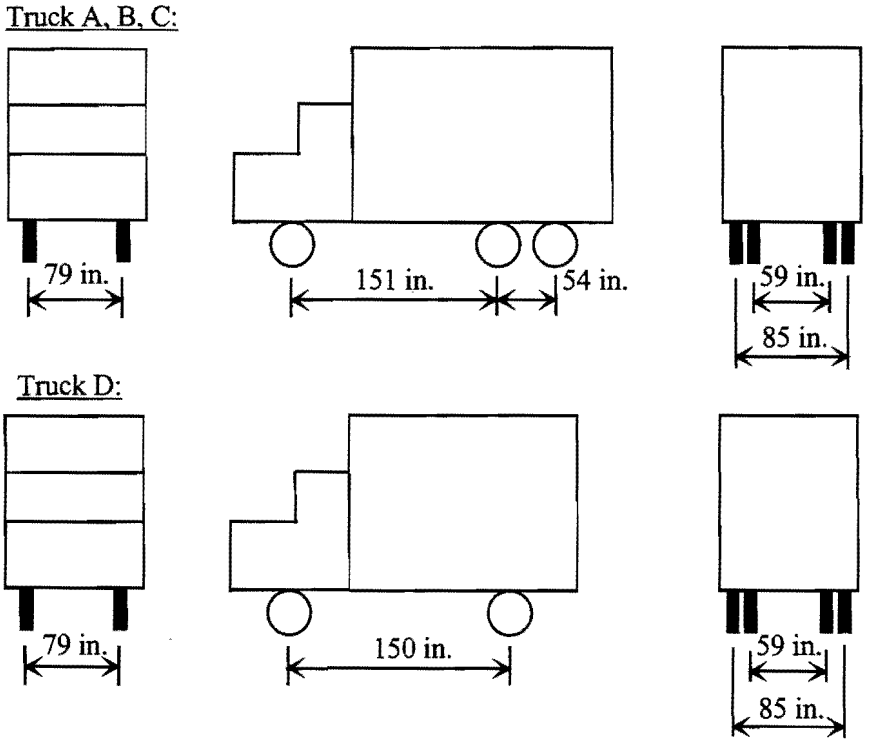

Figure 7.1. Tire Spacing of the Test Trucks

To obtain stress readings by different live loads, the trucks were positioned in different lateral formations and then paced across the bridge. A total of four tests were conducted using truck formations shown in Fig. 7.2. In each test, the trucks entered the bridge from the south end (Bent 17) and exited at the north (Bent 20). The trucks were stopped at every mark for approximately one minute. The exact time when the trucks were at a given station was recorded manually. Before the test, the 21X data acquisition system had been programmed to take a reading every 15 seconds. This ensured that during the tests approximately four stress readings were recorded for each truck location. The data was reduced after the tests to just one reading for each truck location by matching the time of each 21X scan to the corresponding truck location.

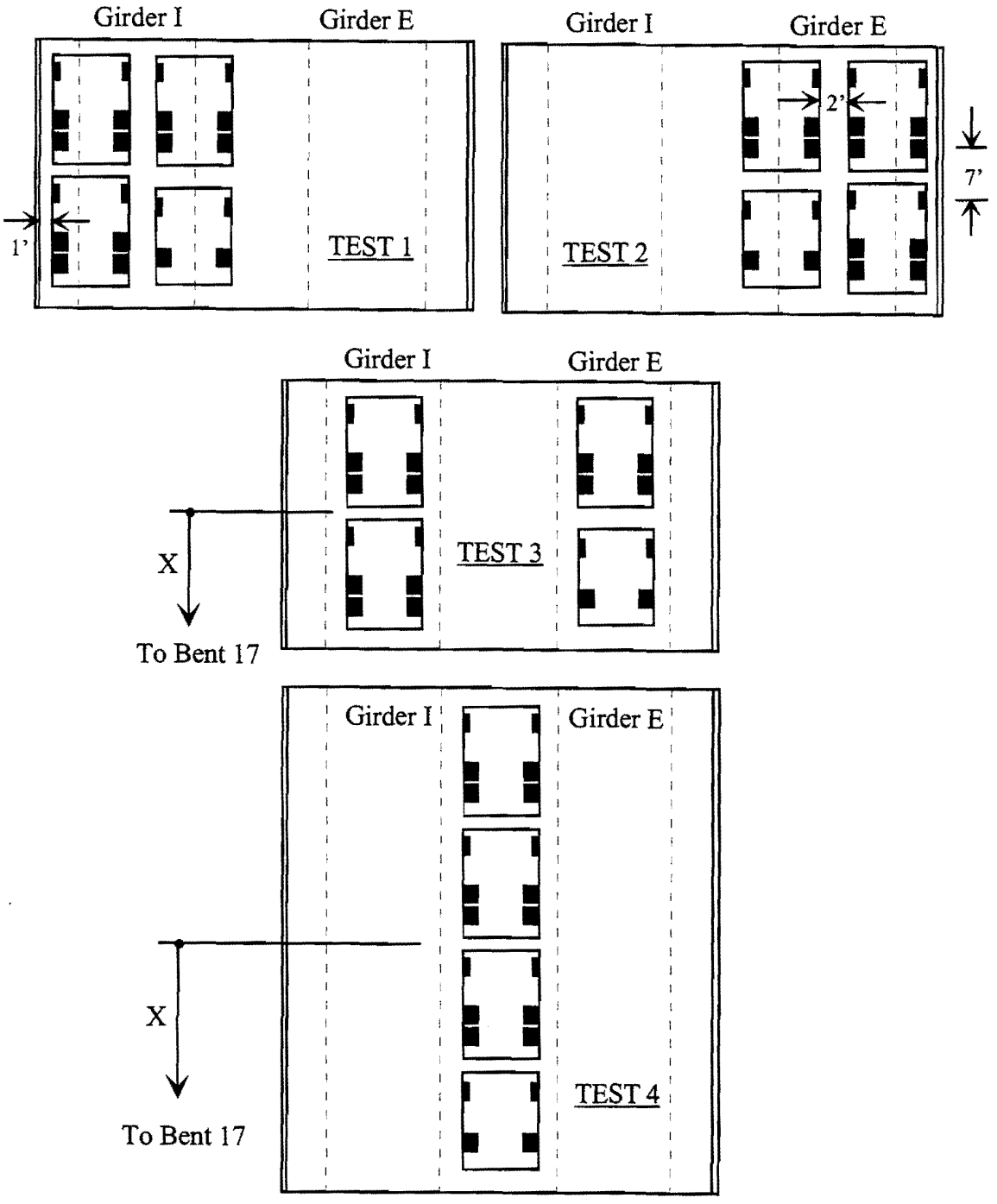

Figure 7.2. Truck Formations in Live Load Tests

7.3 Results from Live Load Tests

7.3.1 Composite Action

Test results indicate that for most of the truck locations, the stress readings from gages on the top flanges and on the bracing members of the horizontal truss were small at both Sections P and N. This is due to the composite action of the concrete slab. Therefore, an evaluation based on the test results on the composite action between the steel section and the concrete deck is first presented in this section.

The location of the test trucks is denoted by X, which is the distance from the center of gravity of the truck loads to Bent 17 measured along the centerline of the bridge. Figure 2.3a shows the largest top and bottom flange stresses at Section P during Test 1 with the trucks at X=50ft. Similarly, Fig. 7.3b shows the largest stresses on Section N during Test 1, which developed when the trucks were in the interior span at X=305 ft. Using the average stresses at the top and bottom flanges, the neutral axes for Sections P and N can be located at approximately 81.8 inches and 62.2 inches from the bottom flange, respectively.

The locations of the neutral axis for the composite section can also be determined from the dimensions of the cross-section. The effective width of the concrete deck in a composite cross-section is specified by AASHTO (1994). According to the specification, the effective width of the concrete deck for this bridge is equal to half the total width of the slab. Assuming the modular ratio of the steel to concrete is equal to 8, the equivalent area from the concrete deck for composite action is shown in Fig. 7.4. A uniform slab thickness of 9.5 inches was assumed. Figure 7.4 shows the neutral axis locations for Sections P and N, derived from effective concrete area as well as the cross-sectional dimensions presented previously in Table 3.2.

Figures 7.3 and 7.4 indicate that the locations of the neutral axes measured from the tests are close to those derived by considering composite action between the steel girder and the concrete deck, particularly at Section N. This implies that during the live load tests, composite action occurred not only in the positive moment region (Section P), but also in the negative moment regions (Section N) where the concrete was subjected to tensile stresses. Little cracking took place before and during the tests in the negative moment regions so that the concrete slab was involved with the steel sections in resisting the truck loads applied during the live load tests. The stresses in the concrete at the top flange level can be derived using the modular ratio between the steel and the concrete (assumed to be 8). The largest stress reading was 0.65 ksi at Gage C2, which resulted in 0.65/8=0.08 ksi concrete stress at the top flange level. The largest stresses in concrete occurred at the top surface of the deck. Using the neutral axis location shown in Fig. 7.3b, the largest tensile stress at the top of the deck (0.08)(27.84+10.75)/27.84 =0.11 ksi.

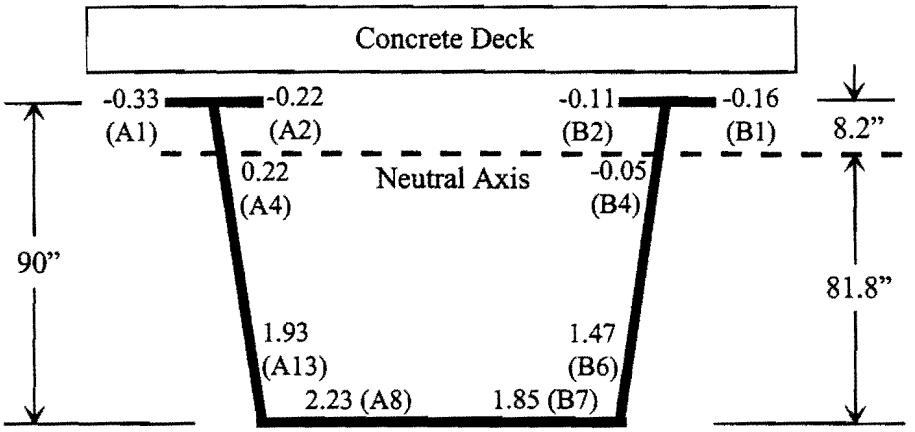

(a) Section P, X=30 ft

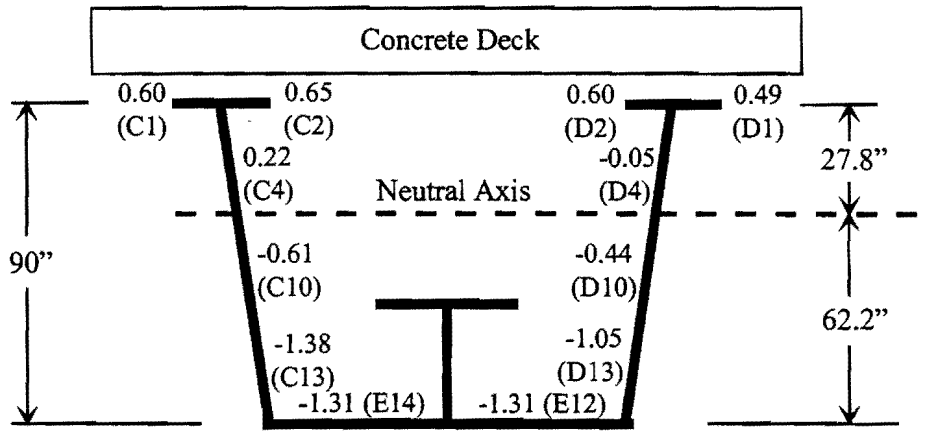

(b) Section N, X=305 ft

Figure 7.3. Girder Stresses and Neutral Axis from Field Test

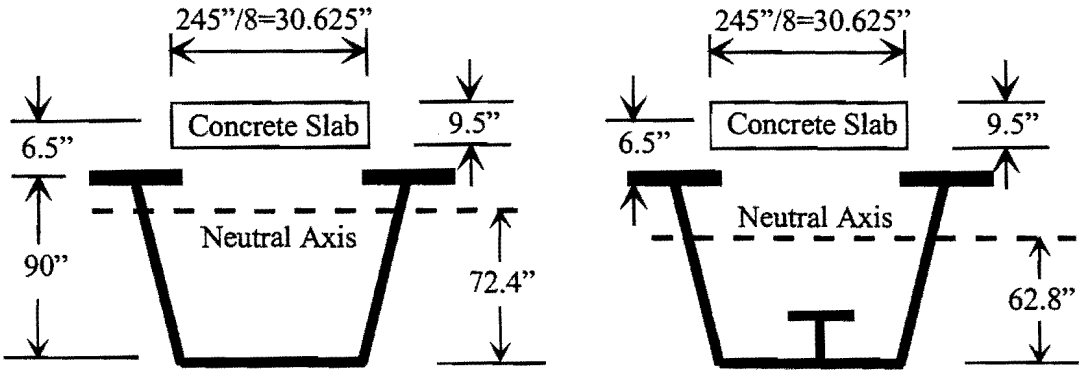

(a) Section P (b) Section N

Figure 7.4. Neutral Axes in Composite Cross-Sections

The composite action resulted in relatively small top flange stresses and brace forces in the horizontal truss near the top flanges. Therefore, discussions on the live load tests will focus mainly on the stresses in the bottom flange of the box girder, although test results on web stresses are also presented in Appendix E.

7.3.2 Stress Influence Lines from Live Load Tests

The increase in the stresses due to the truck loading will be graphed as functions of the truck location (X), thus the influence lines of the stresses at the measuring points were obtained from the live load tests. A negative X represents the case in which although the truck may have entered the bridge, the center of gravity has not yet passed Bent 17. The influence lines for the measured stresses at the bottom flange and the webs are presented in Appendix E, along with comments from the general observations on the behavior of the bridge.

The bottom flange stresses measured during the tests can further be processed to derive the bending and warping stresses in the bottom flange. The average stresses in the bottom flange are caused by bending, while the differences between the average stresses and the stresses at the edges of the bottom flanges are the warping stresses caused by torsion and distortion of the box girder. Warping stresses are usually distributed linearly over the width of the bottom flange. Since the bending stress in the bottom flange is uniform at a given location (the effect of shear lag is negligible), the resulting total stress in the bottom flange should also be linear over the width of the bottom flange, as illustrated in Fig. 7.5.

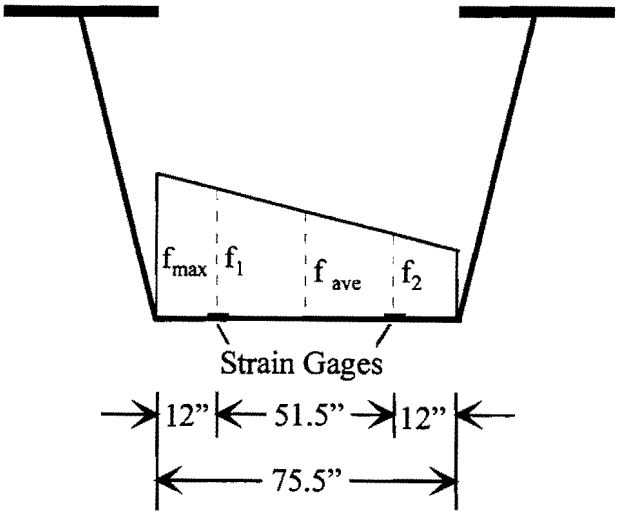

Figure 7.5. Distribution of Bottom Flange Stress

At both Section P and N, two gages were installed on the bottom flange with an equal distance to the center of the girder (Fig. 7.5). The bending stress (average stress at the center

of the bottom flange) and the maximum warping stress (at the junction between the bottom flange and the webs) can be derived from the test results using the following relations:

$$f_{bending} = \frac{f_1 + f_2}{2} , \tag{7.1}$$

$$f_{warping} = \frac{f_1 - f_2}{2}(\frac{75.5}{51.5}) = 1.466(\frac{f_1 - f_2}{2}) , \tag{7.2}$$

in which f_1 and f_2 are the readings from two gages at the same cross-section (Gages A8 and B7 for Section P, Gages E14 and E12 for Section N). The maximum total stress in the bottom flange occurs at the junction to the web and is given by

$$f_{total} = f_{bending} + f_{warping} . \tag{7.3}$$

Figures 7.6 to 7.9 present the influence lines of the bending stresses and the total stresses (at the junction) at Section P and N, derived from the stress readings using the above relations. For the total stress, the superimposed results with larger absolute values are presented.

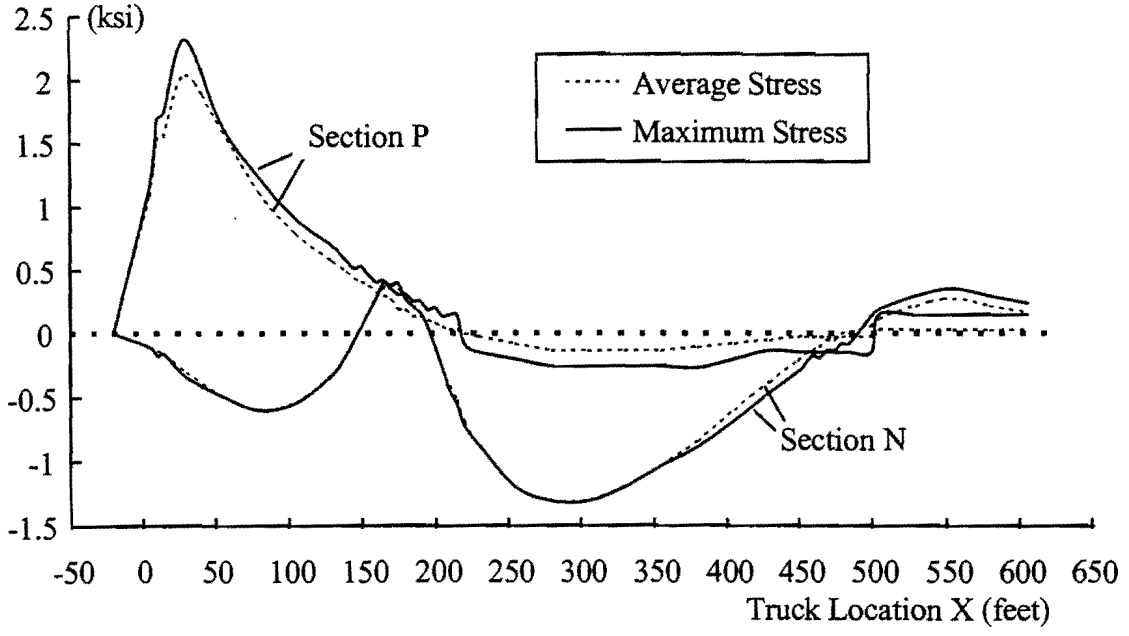

Figure 7.6. Average and Maximum Stresses for Live Load Test 1

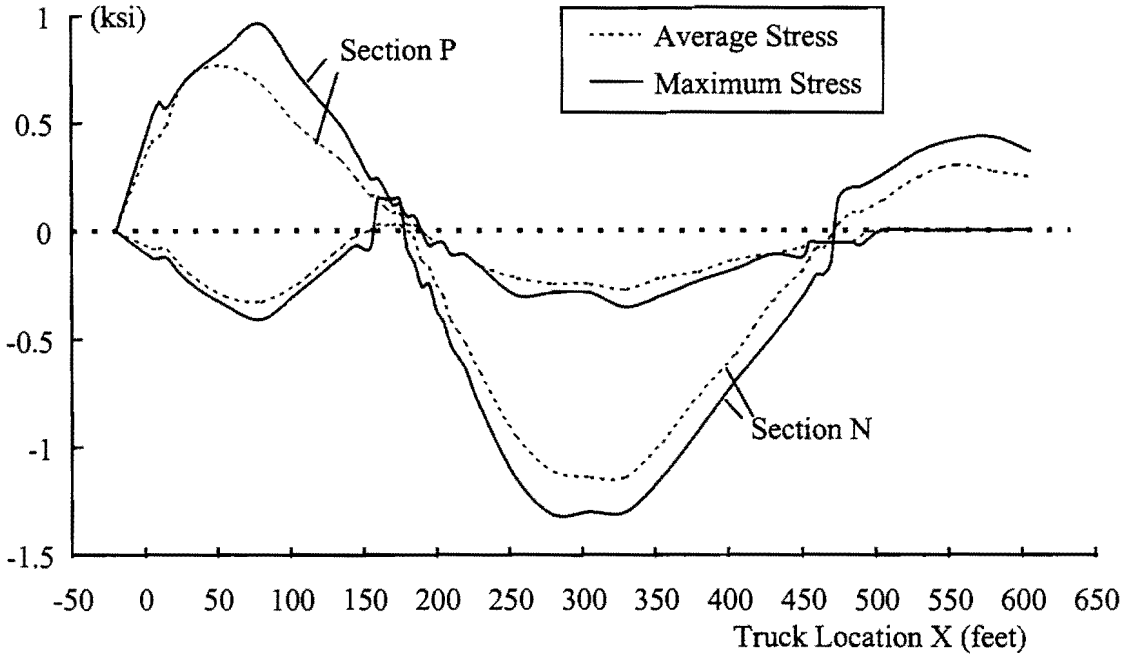

Figure 7.7. Average and Maximum Stresses for Live Load Test 2

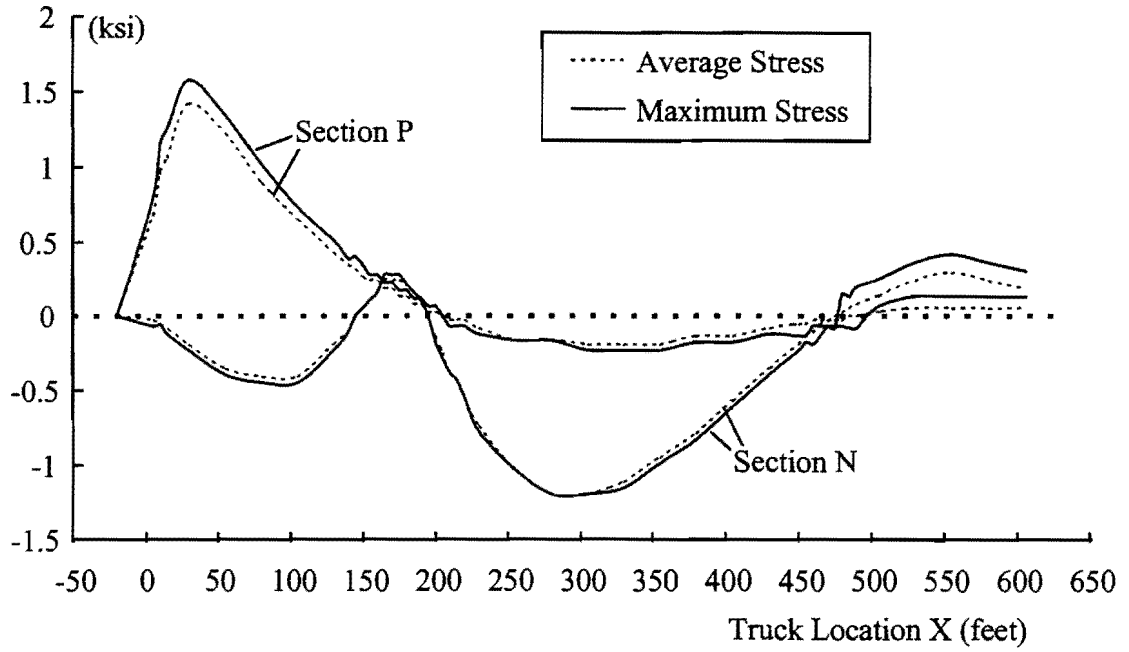

Figure 7.8. Average and Maximum Stresses for Live Load Test 3

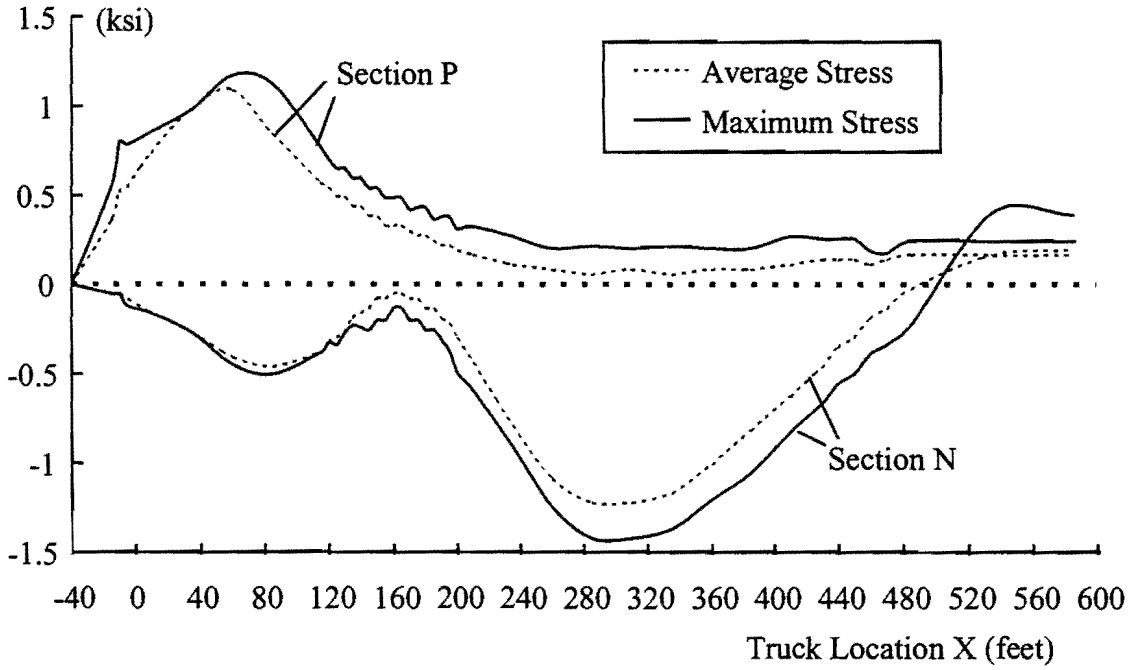

Figure 7.9. Average and Maximum Stresses for Live Load Test 4

7.3.3 Maximum Bending and Total Stresses

Tables 7.2 and 7.3 present the maximum bending and the total stresses that Section P and N experienced during the live load tests. The results show that the majority of the girder stresses were induced by bending. When the truck loads were at the longitudinal location that resulted in the maximum total stresses at the instrumented sections, it usually also generated the largest bending stresses on the cross-sections. The only exception occurred during Test 2, however, the locations corresponding to the maximum bending stresses (X=55 ft for Section P, 305 ft for Section N) and the maximum total stresses (X=80 ft for Section P, 280 ft for Section N) were relatively close. This implies that the cross-sections with maximum bending moment are also likely the cross-sections that would develop the maximum total stresses.

Mattock (1971) found from studies on straight box girder bridges that when a cross-section has the largest bending moment in a multiple-box bridge, the warping stresses in that cross-section are small, resulting in nearly uniform stress along the width of bottom flange. The design of the box girder is therefore controlled by bending. The test results presented in Table 7.2 and 7.3 show that the maximum warping stresses on Sections P and N were generally less than 15% of the respective maximum bending stresses. Although warping stresses were relatively large in Test 2 compared with the respective bending stresses (41.0% for Section P and 17.9% for Section N), a more reasonable comparison should be made between these warping stresses and the largest bending stresses the cross-sections would develop, which is 2.04 ksi for Section P and -1.31 ksi for Section N. As a result, the

percentage of the warping stresses were thus reduced to 13.7% at Section P and 15.3% at Section N, as shown in Tables 7.2 and 7.3.

Table 7.2. Maximum Bottom Flange Bending and Total Stresses at Section P

	$f_{max\ bending}$	$f_{max\ total}$
Test 1	2.04 ksi, when X=30 ft $f_{warping}/f_{bending}$=13.7% Corresponding f_{Total}=2.32 ksi	2.32 ksi Also when X=30 ft
Test 2	0.76 ksi, when X=55 ft $f_{warping}/f_{bending}$=10.5% Corresponding f_{total}=0.84 ksi	0.96 ksi, when X=80 ft $f_{warping}/f_{bending}$=41.0% $f_{warping}$/2.04=13.7%
Test 3	1.42 ksi, when X=30 ft $f_{warping}/f_{bending}$=11.3% Corresponding f_{total}=1.58 ksi	1.58 ksi Also when X=30 ft
Test 4	1.09 ksi, when X=60 ft $f_{warping}/f_{bending}$=7.33% Corresponding f_{total}=1.17 ksi	1.17 ksi Also when X=60 ft

Table 7.3. Maximum Bottom Flange Bending and Total Stresses at Section N

	$f_{max\ bending}$	$f_{max\ total}$
Test 1	-1.31 ksi, when X=305 ft $f_{warping}/f_{bending}$=0 Corresponding f_{total}=1.31 ksi	-1.31 ksi Also when X=305 ft
Test 2	-1.14 ksi, when X=305 ft $f_{warping}/f_{bending}$=14.0% Corresponding f_{total}=-1.30 ksi	-1.32 ksi, when X=280 ft $f_{warping}/f_{bending}$=17.9% $f_{warping}$/(-1.31)=15.3%
Test 3	-1.20 ksi, when X=305 ft $f_{warping}/f_{bending}$=0 Corresponding f_{total}=-1.20 ksi	-1.20 ksi Also when X=305 ft
Test 4	-1.23 ksi, when X=310 ft $f_{warping}/f_{bending}$=16.3% Corresponding f_{total}=-1.42 ksi	-1.42 ksi Also when X=310 ft

The instrumented cross-sections (Sections P and N) were not the critical sections on which the largest bending moment would develop. The level of warping stresses on critical cross-sections will be presented later in this chapter from the three-dimensional FEA solution. In general, the test results indicate the bending behavior of box girders should be the primary concern in design. An effective bending analysis is therefore essential in designing box girder bridges. The warping stresses are usually considered in the application of the lateral distribution factor. The line element FEA model discussed in the following section focuses on the bending analysis of box girder.

The test results will be further used to compare with the FEA results in the subsequent sections. Since Test 4 has the 1×4 truck formation while Tests 1, 2 and 3 all have the 2×2 formation (Fig. 7.2), further comparison will be made mainly on the first three tests in the discussion.

7.4 Finite Element Analysis of Box Girder Using Line Elements

As indicated earlier, box girders in completed bridges are usually analyzed during design using the line model such as the grid analysis. Live load moments on individual girders are evaluated with the application of lateral distribution factors. Therefore, a fundamental issue for the validity of this approach is whether the girders in a slab-girder system behave like an individual beam. This section presents the procedure and results of the simulation of the live load tests from a line element FEA model. The analysis was performed using simple straight beam elements. Improved elements that are able to account for torsional and even distortional deformation of box girders have been developed in recent years (Razaqpur and Li 1991, Zhang and Lyons 1984). However, the procedures of analyses based on different line elements are similar.

7.4.1 Line Element FEA Model

A line element model was used to model the interior girder (Girder I) that stresses were measured upon, as presented in the last section. Since the field studies indicated longitudinal bending stresses were dominant in the girder, curvature was neglected and the girders were modeled as straight girders. The line element solution therefore neglects the effects of torsion. The straight girder is assumed to have the span lengths equal to the developed lengths along the center line of the original curved girder. The continuous beam model for the line element analysis is illustrated in Fig. 7.10.

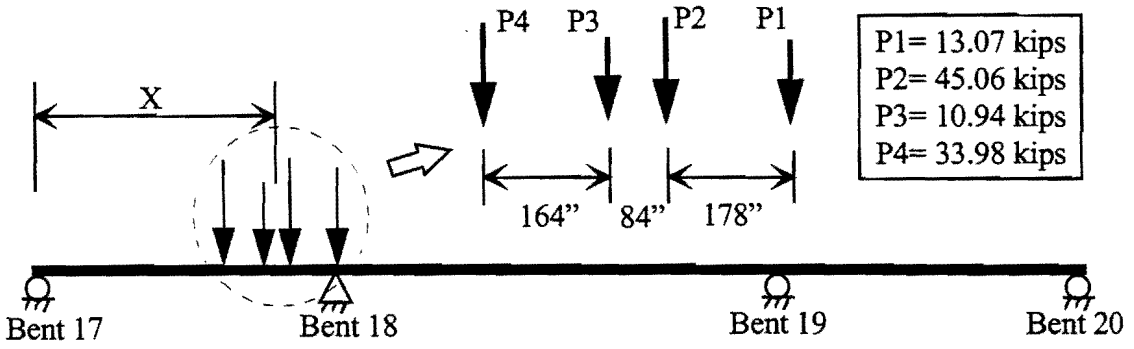

Figure 7.10. Continuous Beam Model in the Line Element Analysis

The analysis was performed using ANSYS with the use of a two-dimensional beam element. The element has two nodes, each with three degrees of freedom, namely, two linear displacements in the x and y directions and an in-plane rotation. The element requires the

input of the cross-sectional area and the moment of inertia. As demonstrated in the last section, composite action between the concrete deck and the steel girders existed during the live load tests. Therefore, the concrete slab was considered for both the positive and negative moment regions in calculating the cross-sectional properties of the girder. The size and location of the concrete slab used to calculated the cross-sectional properties were shown in Fig. 7.4.

Individual elements in the line element model consisted of prismatic sections. Flange transitions that affected cross-sectional properties were therefore realized between adjacent elements. The maximum length of an individual element was also confined to 3 ft. As a result, the total length of the three spans was divided by 221 elements (222 nodes) starting from Bent 17. Different elements were used at the two sides of the instrumented cross-sections such that Sections P and N were located at two FEA nodes (Nodes 6 and 60, respectively) rather than within the elements.

The wheel loads from the test trucks were treated as concentrated forces in the model. In particular, Tests 1, 2 and 3, each of which has the 2 by 2 truck formation (Fig. 7.2) were simulated. A total of four concentrated forces were therefore used to represent the axle loads in the line element model. The girder in the FEA model was subjected to a "standard" loading, and load distribution behavior will be studied later in comparing the line element solution to the test results. The concentrated loads in the line element model were assumed equal to the half of the total weight of the test trucks since there were two girders in the bridge. Therefore, Load P1 in Fig. 7.10 was equal to half the total axle load from the front wheels of Trucks A and C, and Load P2 was equal to half the total axle load from the rear wheels of these two trucks. Loads P3 and P4 in the figure were determined similarly from the weight of truck B and D. The spacing between two consecutive concentrated loads in the model was determined based on the wheel spacing and relative positions of the trucks as presented in Figs. 7.1 and 7.2. Similar to the field tests, the location of the trucks was specified by the distance, X, to Bent 17.

To simulate different truck locations, X in the program was defined as a variable that ranges from -10 ft to 660 ft in 10 ft increments. The fact that not all four wheel loads were on the girder for the first and last few steps of X was considered in the analysis. A concentrated force can be placed at any point between two nodes of a beam element. The moments and stresses were obtained at the FEA nodes.

7.4.2 Results from the Line Element Model

The line element FEA model was used to simulate the live load tests conducted on the bridge. The stress influence line was obtained by conducting several analysis with different truck locations, specified by X. For each X, the maximum bottom fiber stresses on Section P and N were recorded. The stresses were then graphed as functions of X, resulting in the stress influence lines for the bottom flange at both sections. These influence lines are graphed in

Fig. 7.11 together with the average bottom flange stresses from the live load tests at Section P and N. Results for Test 4 are excluded because of the different truck formation and larger temperature effects.

Figure 7.11a presents the stress influence lines at Section P from the tests and the line element analysis. The results indicate that the predicted stresses using the straight line element model matches reasonably well to the test results for most of the truck locations in all three tests. However, when the trucks were close to Section P, the measured stresses on the cross-section depended heavily on the lateral locations of the test trucks. As would be expected, the instrumented girder (Girder I) developed larger stresses when the load was applied closer to its centerline. In Test 1, the center of gravity of the trucks was almost coincident to the centerline of Girder I. The stresses of test 1 were therefore significantly larger than the stresses generated in the other tests when the center of gravity of the trucks were offset from the girder centerline. In particular, Test 2 in which the trucks were above Girder E produced smaller stresses than Test 3 when the center of gravity was near the centerline of the entire bridge (between the two girders). Since only half the total weight of the test trucks were used in the line element model, the predicted maximum stress is near the medium level of the maximum stresses of Tests 1 and 2, and is close to the stress results from Test 3. The difference between the line element solution to the stresses in Test 3 may be partially attributed to the small weight of Truck D that resulted in a fraction of the load greater than half the total on Girder I.

The influence lines of the average bottom flange stresses at Section N are presented in Fig. 7.11b. The largest stresses were generated when the trucks were in the interior span of the bridge, as shown by both the test results and the line element analysis. However, the differences between the maximum stresses from Tests 1, 2 and 3 were relative small. This implies that the maximum stress at Section N was relatively insensitive to the lateral locations of the live loads. The largest stress differences between the three tests occurred when the trucks were within the instrumented span with an X of approximately 80 ft. The largest stress at Section N occurred when the trucks were in the interior span. Test 1 generated the largest stresses while Test 3 corresponded to the smallest, however the difference between the maximum stress in the three tests is relatively small.

In general, the test results and the line element solution had reasonable agreement. The effect slab width specified by AASHTO provided good estimates of the properties of the composite cross-section. The girder closer to the truck loads generally developed larger stresses. The stresses in the exterior span were generally less dependent on the lateral locations of the trucks when the live loads were applied in the interior span of the three-span bridge.

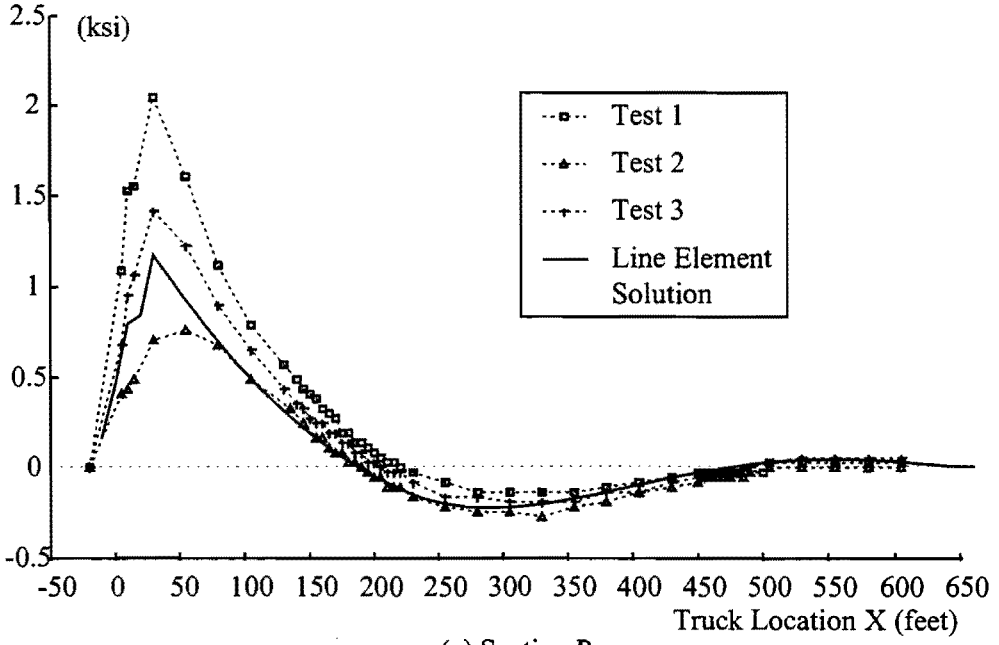

(a) Section P

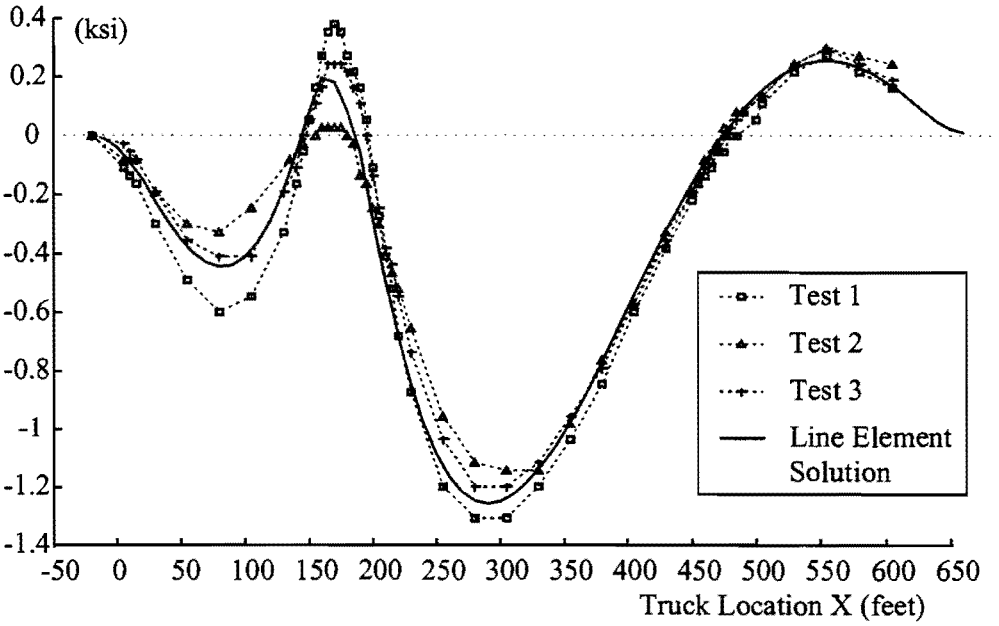

(b) Section N

Figure 7.11. Bending Stresses from Live Load Tests and Line Element Solution.

Figure 7.11 demonstrates that the line element FEA model is effective in modeling the bending behavior of box girders. However, the conclusions that can be drawn from the line element analysis are limited. Neither Section P nor Section N is the critical cross-section with the largest bending moments in the respective positive or negative moment regions. Although the largest stresses at the instrumented sections provide useful information on the behavior of girder interaction, the live load distribution factor used in design is usually for cross-sections with the largest bending moments. These critical cross-sections are typically located near the middle of each span (for positive bending moment) and right above the interior supports (for negative bending moment). In addition, the largest shear and torsional moment are also likely to develop at the supports, and the straight line element model is unable to give solutions on warping stresses. Investigation of lateral distribution factors for these critical cross-section requires a three-dimensional analysis that is able to couple the two girders and the concrete slab in one bridge model. The development of the 3D FEA model for completed bridges is discussed in the next section.

7.5 Three-Dimensional FEA Model for Completed Bridge

7.5.1 Modeling Concrete Slab in FEA Models

Many researchers have conducted three-dimensional numerical analyses of steel bridges subjected to live loads. Most of the early investigations made use of the semi-analytical methods, such as the Folded Plate Method (Meyer and Scordelis 1970) or the Finite Strip Method (Cheung 1982). The lateral distribution factor developed by Mattock (1971) for box girder bridges was based on results from a folded plate analysis in combination with the experimental studies. These methods, however, are often unable to incorporate different structural components, such as girder plates and bracing members, into a single model. The Finite Element Method is therefore widely used in modern bridge analysis. Three-dimensional FEA studies on I-girder bridges have been conducted by many researchers. However, nearly all three-dimensional numerical studies on box girder bridges conducted so far have been based on the folded plate method.

The finite element analysis of composite bridges requires proper modeling of the concrete deck in the model. The thickness of the concrete slab is usually much larger than the steel girder plates. Direct approaches for modeling the slab, therefore, made use of brick elements. For example, Tarhini and Frederick (1992) used the isotropic eight node brick element for the slab, and quadrilateral shell elements for the flanges and webs of I-girder bridges (Fig. 7.12a). The intensive use of the brick elements, however, generally leads to very large problems due to excessive degrees of freedom. Therefore, the model is difficult to be applied to large bridges, since it either results in too large of a problem or a course mesh that limits the proper modeling of the bridge detail and the accuracy of the analysis.

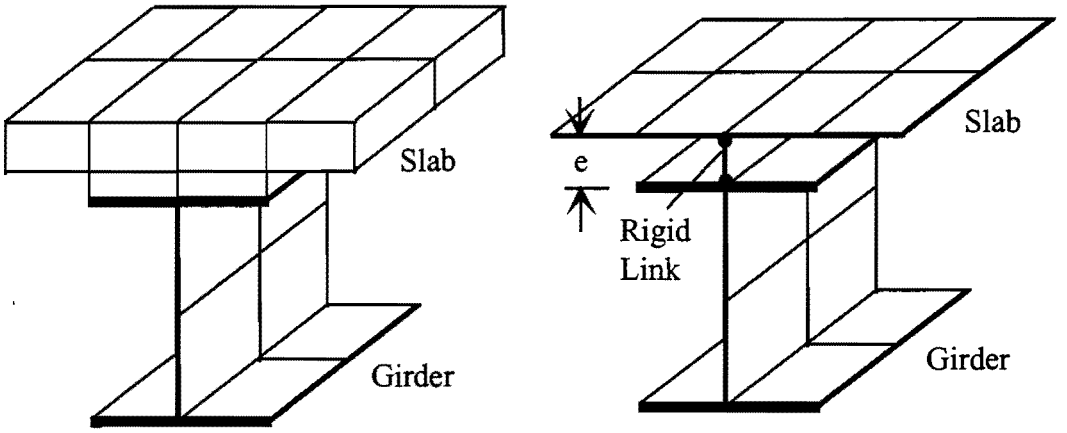

(a) Brick Elements for Slab (b) Shell Element for Slab

Figure 7.12. FEA Modeling of Concrete Slab

Most of the plate and shell elements developed in recent years are also able to model the shear deformation in the through-thickness direction. These elements are therefore not only applicable to thin plates and shells, but also for elements with intermediate thickness such a the concrete slab. Previous researchers have reported applications of shell elements in the modeling of bridge slabs. These models combined the shell element slab with the steel girders in the same FEA model. The girders were modeled either by line elements or shell elements, or the combination of both to represent different deformations of the girder webs and flanges (Fig. 7.12b).

A major difficulty, when the slab is idealized by shell elements, arises in dealing with the eccentricity between the deck and the top flanges (e in Fig. 7.12b). The shell elements for the concrete deck in a FEA model comprise a 2D surface that is located at the middle thickness of the slab. Since the concrete slab has a large cross-sectional area and thus a large contribution to the moment of inertia of the composite cross-section, the location of this surface relative to the steel girder must be accurately reflected in the FEA model. Although the thickness of the element is input prior to the analysis, it is not directly reflected in the geometry of the FEA model due to the 2D nature of shell elements. Therefore, the slab and the girders are separated structural components in the FEA model, and special techniques must be used to correlate the nodal degrees of freedom in slab and girders. In addition, contributions from the haunches between the slab and the top flanges of steel girders to the stiffness of the structure should also be considered.

Different methods have been employed by previous researchers to connect the girders and the slab in three-dimensional FEA models. The rigid link method has been a popular approach used in bridges with I-shaped girders (Brockenbrough 1987, Tabsh and Sahajwani 1997). The slab nodes directly above the top flange of the steel girders are connected to the girder by the rigid links, which are typically beam elements with a very large stiffness (Fig. 7.12b). This method is effective in modeling the bending deformation in the axial direction,

however, the shear capacity of the cross-section may be overestimated. If applied to box girders, the rigid links may also overestimate the distortional stiffness of the girder if the offset between the slab center and the top flanges is relatively large.

Many FEA programs also provide the capacity of coupling the degrees of freedom for separated nodes without using physical elements or constraints. For example, a linear variation in the strain distribution can be assumed for a line of nodes through the slab and along a girder web. However, this means that additional assumptions are introduced in the FEA model, and these pre-assumptions may be incorrect for complicated deformations such as torsional deformation or distortion of the box girder.

A proper modeling of the concrete slab is essential to the analysis of complete box-girder bridge. The analysis performed in this project employed a technique that combined the shell and brick elements for slab modeling, as will be discussed in the following sub-section.

7.5.2 FEA Model for the Complete Box Girder Bridge

The three-dimensional computational study for the complete bridge in this project is intended to simulate the live load tests performed on the bridge. Therefore, the concrete slab must be included in the FEA model. The girder geometry must be modeled as accurate as possible, and all structural components that may affect the behavior of the bridge under live loads should also be represented in the FEA model. However, coupling conditions between different nodes are difficult to predict due to the complicated deformation of the girders.

The three-dimensional FEA model for the twin box girder system was developed to study the construction stages, as was discussed in Chapter 4. The non-prismatic cross-sectional dimensions were modeled, along with the stiffeners, diaphragms, and the bracing members in the top flange truss systems and the internal K-frames. However, as discussed in Chapter 4, the quasi-closed box girder model had more than 40,000 nodes, and the analysis required substructuring. To avoid an excessively large problem size, the use of brick elements for the slab was abandoned.

A new method to model the slab system was proposed in the investigation. To limit the problem size, the slab was modeled by the 8-node quadrilateral shell elements that were also used to model the steel girders. The shell element is located at the mid-thickness of the slab. The 20-node brick elements as shown in Fig. 7.12 were used to model the haunches between the top flange of the steel section and the slab as demonstrated in Fig. 7.13. Therefore, no pre-assumed coupling condition was introduced in the analysis. The top and bottom surfaces of the brick elements overlap the shell elements for the slab and the top flanges and share the same nodes.

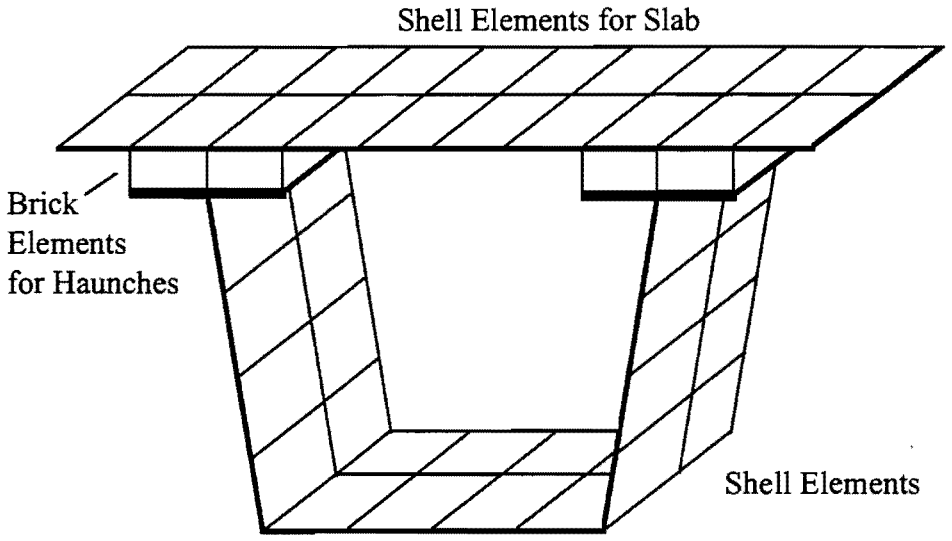

Figure 7.13. FEA Model Used in Simulating Live Load Tests

The composite action between steel girders and the concrete slab was therefore achieved in the FEA model through the connection of the haunches that were represented by the brick element. The brick element has three degrees of freedom at each node (translations in three direction). The shell elements have three additional degrees of freedom (rotations in three direction), however the rotations of the overlapped shell and brick elements were better described by the relative displacements of the different nodes.

Test and line element results presented earlier in this chapter showed that composite action existed in both the positive and negative moment regions. Therefore, the composite slab was modeled over the entire bridge length. A modular ratio of 8 was assumed between the steel and concrete. The thickness of the slab for the bridge was 9.5 inches over most of the bridge width, however the overhang of the slab actually had a tapered section with the thickness ranging from about 11 inches at the box girder flanges to 8 inches at the curbs. However, a uniform 9.5 inch thickness was also assigned for the overhang slab.

The three-dimensional model included both Girders I and E, as well as the concrete deck over the entire length of the bridge. All structural members, including the steel sections and the internal bracing members that were included in the FEA model for the construction phase, were also included in the complete bridge model. External K-frames were used between the girders at Bent 17 and 20, while solid diaphragms were placed at Bent 18 and 19. As a result of the completeness in modeling the structural components, the bridge model had approximately 60,000 nodes, and was divided into five substructures.

Wheel loads from the four test trucks were represented by 16 concentrated forces. The real magnitudes and spacing of the concentrated loads was determined based on the truck

information provided in Section 7.1. The concentrated forces were applied at the FEA nodes. A linear elastic analysis was conducted.

Despite the effort to model the complete bridge, there were a number of the uncertainties in the actual bridge that could affect the accuracy of the FEA results, including the actual slab thickness, the contribution of the stay-in-place deck form and the parapets to the stiffness of the bridge. Trial analyses were performed by varying the slab thickness, which indicated that a ±10% change in the slab thickness did not significantly affect the results. The FEA results presented in the next section were from a model with a uniform 9.5-inch thick slab over the entire bridge.

7.6 Results from Three-Dimensional FEA Model of Box Girder Bridge

7.6.1 Critical Loading Cases and Critical Cross-Sections

The 3D FEA model was used to study the maximum stresses at critical cross-sections with maximum bending moments. Therefore, only isolated loading cases that resulted in the largest moments on the critical cross-sections were analyzed. Three critical cross-sections were investigated with the model as shown in Fig. 7.14. The cross-section directly above Bent 18, labeled by Section N1, is a critical cross-section that has the largest negative bending moment. The other two critical sections with the largest positive bending moments were identified to be Section P1 in the exterior span and Section P2 in the interior span. The locations of the critical section and the truck loading that led to the largest bending moments were determined using the line element model discussed earlier.

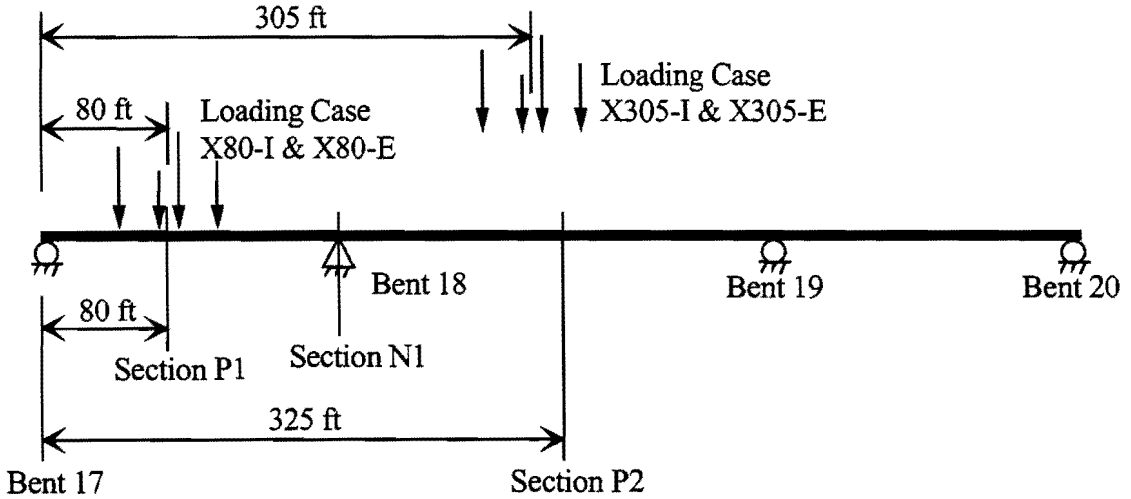

Figure 7.14. Locations of Critical Cross-Sections and Critical Loading

The line element results indicated that when the truck loads were in the middle regions of the exterior and interior spans, the largest positive bending moments developed in the middle

regions of the respective spans. On Section N1, the largest negative moment occurs when the trucks were placed in the interior span, close to the position that corresponded to the largest positive moment in Section P2. For simplicity, therefore, only two longitudinal load positions were studied, one in the interior span and the other in the exterior span. Specifically, the locations of the critical cross-sections, as well as the locations of the loads that produced the largest moments on these sections, were found as follows (Fig. 7.14):

- When the load is located at X = 80 ft. from Bent 17, the largest bending moment in the exterior span is 3,298 kip-ft at the cross-section (Section P1) located 80 ft. from Bent 17.

- When the load is located at X=305 ft. from Bent 17, the largest bending moment in the interior span is 4,084 kip-ft at the cross-section (Section P2) located 325 ft. from Bent 17.

- When the load is located at X=305 ft. from Bent 17, the cross-section located above Bent 18 (Section N1) develops the largest bending moment of -2,926 kip-ft.

For each of the longitudinal load locations, two lateral truck formations were studied, simulating live load Tests 1 and 2 in which the center of gravity of the trucks were placed near the centerlines of Girders I and E, respectively. Therefore, a total of four load cases were studied. These load cases were labeled by their locations as X80-I, X80-E, X305-I and X305-E, respectively. For example, X80-I indicates the trucks were placed above the interior girder, 80 ft. from Bent 17.

7.6.2 Comparison with Test Results

The results from the three-dimensional FEA model were first compared with the test results. Therefore, the bottom flange stresses at the instrumented sections, Sections P and N of Girder I, due to all four load cases as defined above were retrieved from the FEA model and are presented in Figs. 7.15 to 7.18. The test results for the corresponding load cases are also included in the graphs for comparison.

Figure 7.15 presents the bottom flange stresses from Test 1 and nodal FEA results with X80-I loading. Excellent agreement between the FEA solution and the test results was achieved at Section P as shown in the figure. The FEA solution and the measured values did not compared as well at Section N, however the agreement is still reasonable. The measured bottom flange stresses from the test results are approximately two third of the FEA solution. Results corresponding to X80-E truck loading are presented in Fig. 7.16. The bottom flange stresses at Section P had a good agreement, but poor agreement between the test and the FEA results was observed at Section N. The FEA model predicted a nearly zero bottom flange stresses at Section N, while test results show that approximately 0.3 ksi bending stress existed in the bottom flange. Section N was located near the inflection point of the bending

moments induced by the truck loads placed at X=80 ft, therefore the bending stresses were relatively small. Figures 7.17 and 7.18 show that when the trucks were placed in the interior span at X=305, reasonable agreement between the stresses from the live load tests and the FEA analysis were achieved at both Sections P and N. The directions of warping moments on the bottom flange were also generally consistent between the test and FEA results, particular on sections with larger stresses as shown in Figs. 7.15(a), 7.16(a), 7.17(b) and 7.18(b).

The stress results as presented in Figs. 7.15 to 7.18 corresponded to the load cases that led to the largest bending moments on the critical cross-sections. Several trial analyses were performed during the development of the three-dimensional FEA model for the composite bridge, including the truck load positions that produced the largest stresses at the instrumented cross-sections. The agreement was generally reasonable. Better agreement between the test results and FEA solution was usually achieved when the stress levels on the cross-sections were higher. This phenomenon agrees to the findings from the field and computational studies on the construction stages, as discussed in Chapter 4. The accuracy of the lower-level measured stresses were more likely to be eroded by various irregularities under the field conditions. The three-dimensional FEA model for the composite box girder bridge was therefore considered effective, particularly for stresses at the critical cross-sections where the stress levels are relatively large.

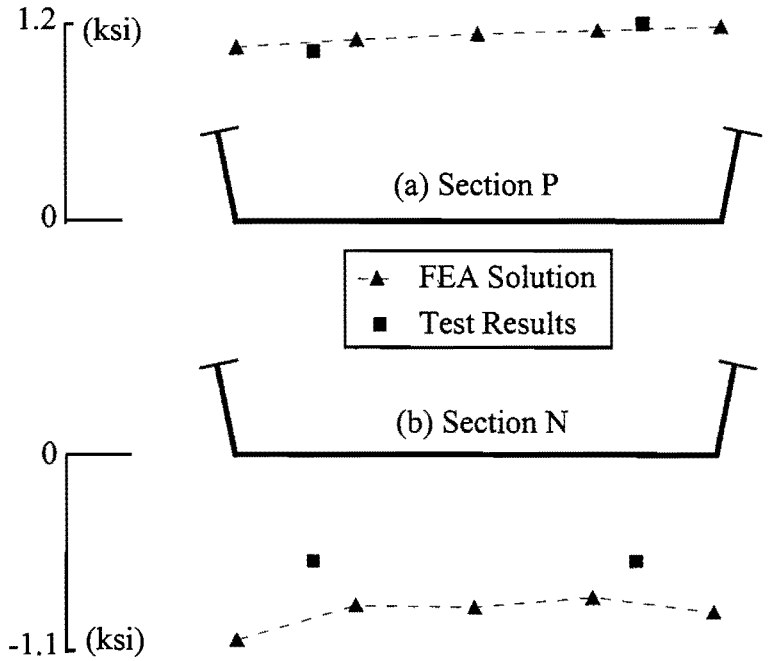

Figure 7.15. Bottom Flange Stresses on Sections P and N Under Live Load X80-I

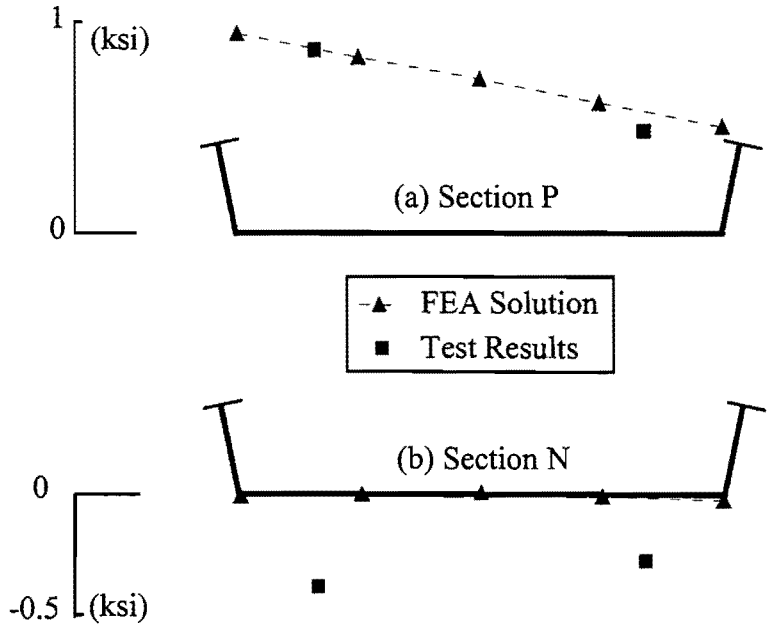

Figure 7.16. Bottom Flange Stresses on Sections P and N Under Live Load X80-E

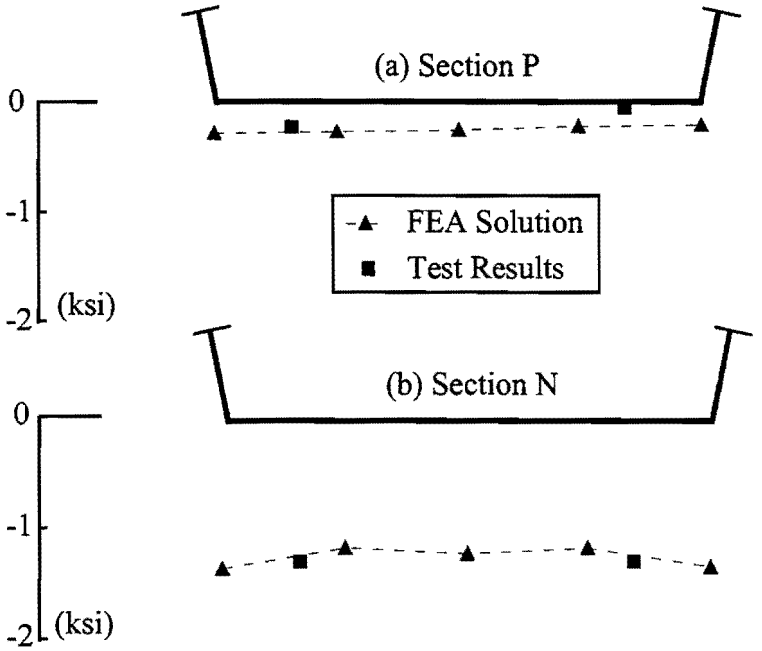

Figure 7.17. Bottom Flange Stresses on Sections P and N Under Live Load X305-I

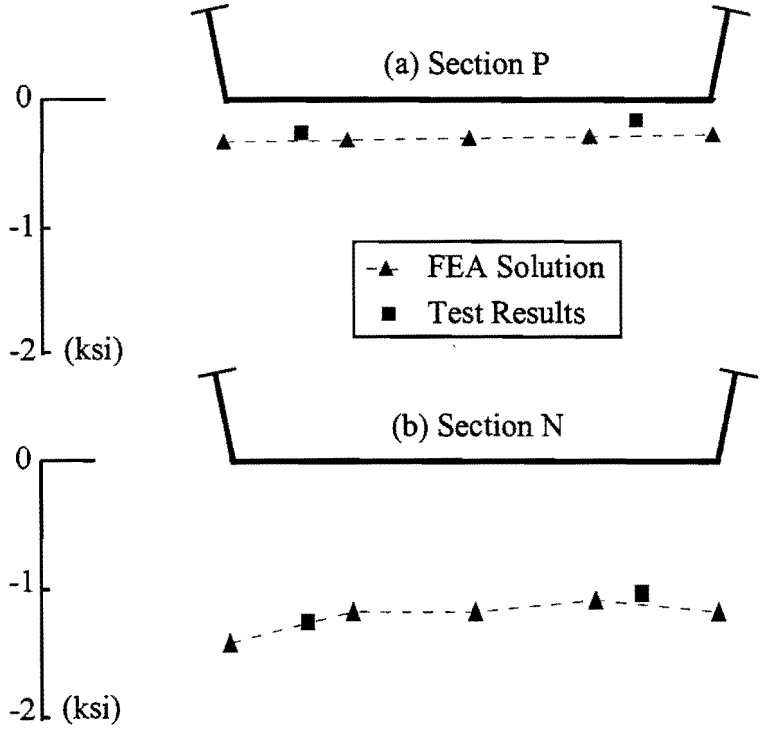

Figure 7.18. Bottom Flange Stresses on Sections P and N Under Live Load X305-E

7.6.3 Stresses at Critical Cross-Sections

The FEA results of the bottom flange stresses at the three critical cross-sections, defined in Fig. 7.14, in both Girders I and E are presented in Figs. 7.19 to 7.21. All four load cases were considered. There was no test result for these cross-sections, however, the average stresses predicted by the line element model for the corresponding longitudinal truck location are included in the graphs. The load in the line element model was equal to half the weights of the trucks.

Figure 7.19 shows the girder stresses at Section P1 when the trucks were positioned at X=80 ft. As would be expected, the results show that the girder directly below the truck loads always developed larger stress than the other girder. The line element solution due to half the total truck weight is at the intermediate level of the 3D FEA stress results of the two girders. Similar behavior was found in the other two critical cross-sections, Section N1 (Fig. 7.20) and Section P2 (Fig. 7.21), when the trucks were placed at X=305 ft.

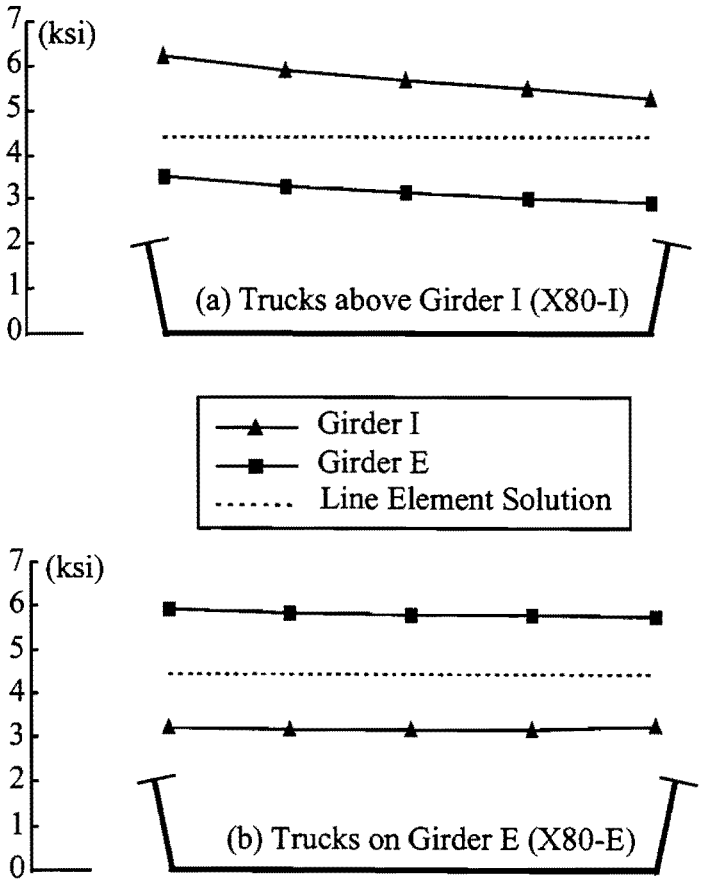

Figure 7.19. Bottom Flange Stresses on Section P1 by Truck Loads at X=80 ft

The distribution of the stresses over the width of the bottom flanges was nearly linear on Sections P1 and P2. However, stresses on Section N1 had more deviation from a linear distribution. Located directly above an interior support (Bent 18), the girder section at Section N1 connected to several other structural components, including the interior and exterior diaphragms, the bearing, and the longitudinal stiffener. A three-dimensional behavior could occurred, resulting in girder stresses different from those predicted by beam theory for bending and torsion, as demonstrated in Fig. 7.21. Further study is required to examine how severe the maximum girder stresses deviate from those predicted by beam theory, and the size of this localized region near the supports with nonlinear stress distribution.

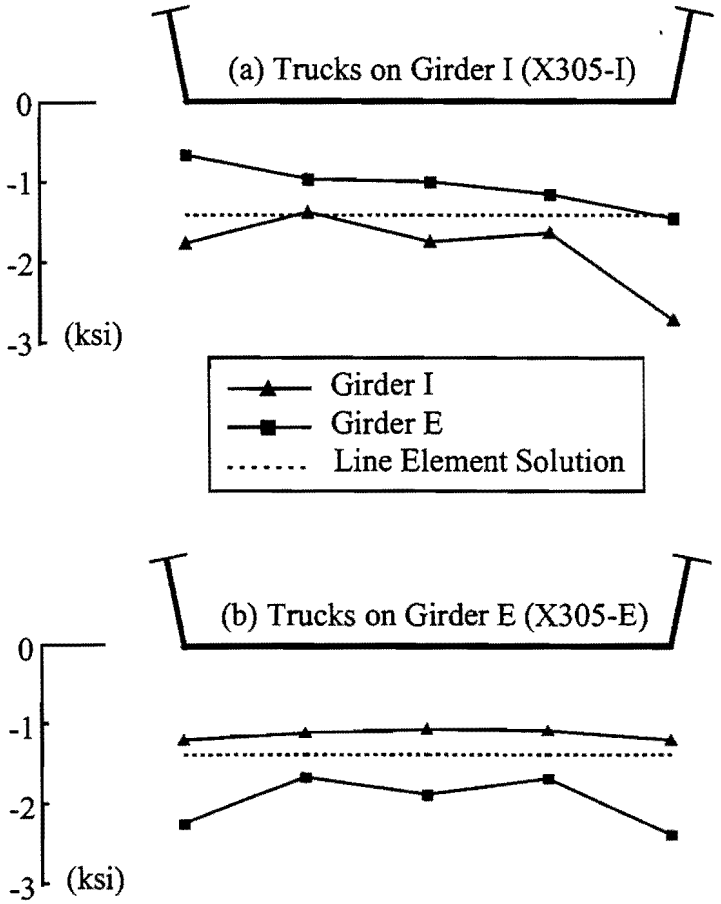

Figure 7.20. Bottom Flange Stresses on Section N1 by Truck Loads at X=305 ft

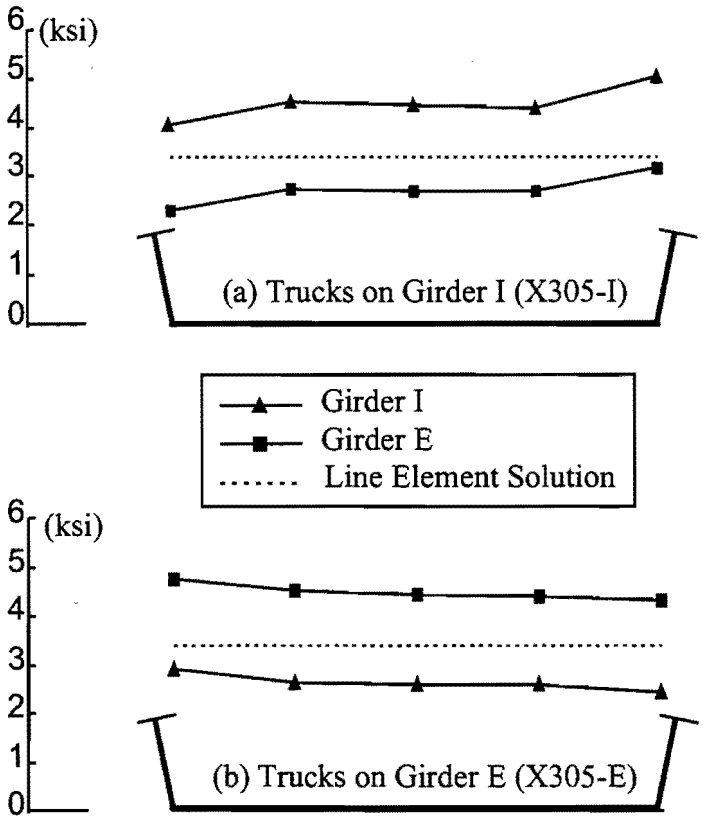

Figure 7.21. Bottom Flange Stresses on Section P2 by Truck Loads at X=305 ft

The results shown in Figs. 7.19 to 7.21 are further processed to derive the average stresses at the critical cross-section, as presented in Tables 7.4 to 7.6. The results show that at all three critical cross-sections, the stresses in Girder I due to the truck loads above Girder I (5.71 ksi in Table 7.4, for example) were relatively close to the stresses in Girder E due to the truck loads above Girder E (5.83 ksi in Table 7.4). Similarly, the stresses in Girders I and E when the trucks were directly over the adjacent girders were also relatively close. For example, this is demonstrated by the values of 3.20 ksi and 3.19 ksi in Table 7.4. This implies that the interior girder (Girder I) and the exterior girder (Girder E) reacted similarly to live loads. This kind of behavior is expected in a straight twin-box bridge due to symmetry in the lateral direction. Therefore, the curvature did not significantly change the bending behavior and the lateral load distribution in this twin-box girder bridge.

A parameter that characterizes the lateral distribution of live load is the ratio of the average stresses in adjacent girders at a radial cross-section. The values of this ratio of the stress in the girder directly underneath the truck load (the larger one) to that in the other girder (the smaller one) were computed and presented Tables 7.4 to 7.6. Because of the behavior as just stated in the last paragraph, the two ratios in each of the tables were relatively close. Furthermore, the results in Tables 7.4 to 7.6 shows that the ratios from the

different tables (for different cross-sections) are also in a similar level (ranging from 1.65 to 1.82, less than 6% difference from the average of 1.75). This implies that the behavior of the lateral distribution of truck loads on all three cross-sections were similar. A uniform lateral load distribution factor, therefore, may be applied to all three critical cross-sections of the bridges. This conclusion is consistent with the prediction by Mattock (1971), on which the current distribution factor (AASHTO 1994) is based.

Table 7.4. Average Bottom Flange Stresses (ksi) on Section P1 (X=80 ft)

	Girder I	Girder E	Ratio (larger/smaller)
Trucks above Girder I (X80-I)	5.71	3.19	5.71/3.19=1.79
Trucks above Girder E (X80-E)	3.20	5.83	5.83/3.20=1.82
Sum	8.91	9.02	
Line Element Results	8.91 (under full truck load)		

Table 7.5. Average Bottom Flange Stresses (ksi) on Section N1 (X=305 ft)

	Girder I	Girder E	Ratio (larger/smaller)
Trucks above Girder (X305-I)	-1.85	-1.04	(-1.85)/(-1.04)=1.78
Trucks above Girder E (X305-E)	-1.14	-1.98	(-1.98)/(-1.14)=1.74
Sum	-2.99	-3.02	
Line Element Results	-2.77 (under full truck load)		

Table 7.6. Average Bottom Flange Stresses (ksi) on Section P2 (X=305 ft)

	Girder I	Girder E	Ratio(larger/smaller)
Trucks above Girder I (X305-I)	4.49	2.72	4.49/2.72=1.65
Trucks above Girder E (X305-E)	2.62	4.48	4.48/2.62=1.71
Sum	7.11	7.20	
Line Element Results	6.85 (under full truck load)		

The stresses on all three critical cross-sections from the line element FEA solution were multiplied by a factor of 2 to represent the full truck loading and presented in Tables 7.4 to 7.6. The results are closed to the total stresses resulting from the sum of the stresses due to trucks above Girders I and E. This again confirms that the line element model is effective in predicting the average bending stresses in the box girders.

Since the stresses were not perfectly linear over the width of the bottom flange as shown in Figs. 7.19 to 7.21, the non-uniformity in the bottom flange stresses is represented by the differences between the largest stresses to the average stresses. The percentage of these differences over the average stresses is presented in Table 7.7. The results indicate that the

"warping" stresses in critical sections with positive bending moments (Section P1 and P2) were relatively small. Although sometimes the largest stresses was as much as 17% larger than the average bending stresses, the "warping" stresses were generally secondary. However, the largest girder stresses on the interior support (Section N1) may be significantly larger than the average stresses due to the 3D behavior in the region as discussed earlier. The bottom flange at the interior support is subjected to compressive stresses that may cause instability of the flange. Therefore, the negative moment regions of box girder near the interior support should be further studies to reveal the complex stress state in the bottom flange.

Table 7.7. Deviation of Maximum Stresses from the Average Stresses

Loading Case	Sec. P1 Girder I	Sec. P1 Girder E	Sec. N1 Girder I	Sec. N1 Girder E	Sec. P2 Girder I	Sec. P2 Girder E
X80-I	8.6%	10.7%				
X80-E	0.9%	1.8%				
X305-I			47.5%	7.0%	11.8%	16.7%
X305-E			39.6%	20.5%	9.9%	6.0%

7.6.4 Conclusions from 3D FEA Studies on Complete Box Girder Bridge

From the three-dimensional FEA model, the following conclusions can be drawn from the stress results on the critical cross-sections of the completed bridge subjected to the live loads:

1. The use of shell elements for the concrete slab and brick element for the haunches is effective in modeling the slab of box girder bridges. The composite action between the steel girders and the concrete deck was properly modeled by the method.

2. Bending stresses dominated the longitudinal stresses in the bottom flanges of the box girders. Warping stresses on cross-sections in the positive moment region were generally insignificant. On cross-sections directly above the interior supports, however, the stress distribution along the width of the bottom flange was sometimes severely nonlinear, and the largest stresses could be as nearly 50% higher than the average stresses.

3. The Line element model is effective in predicting the largest bending stresses. However, live load distribution factors must be applied. Composite action appears to be properly evaluated by the current specification.

4. Curvature did not significantly change the lateral distribution of live loads between the box girders in the bridge. The behavior of the individual girders were similar to each other.

5. A unique lateral distribution factor may be applied to all critical cross-sections of the continuous bridge, including the section in the negative moment region in predicting the bending stresses). The moments on the cross-section produced by live loads located in other spans was relatively insensitive to the lateral locations of the loads.

The results presented in this chapter show the behavior of the curved box girder bridge. Further studies are required to investigate the effect of the girder spacing and length, as well as the radius of curvature. The 3D FEA model developed can be used for additional studies to determine the lateral distribution factor. The study must the based on the standard truck loads specified by AASHTO, and the loads should be placed in the lateral positions that result in the largest stresses in the critical cross-sections of box girder bridges.

CHAPTER 8 CONCLUSIONS AND FUTURE WORK

8.1 Conclusions

The objective of this research was to study the behavior of trapezoidal box girder systems during construction and live loading to determine design requirements. Results were presented in this report from field and computational studies.

The field studies were conducted on a curved composite trapezoidal twin-box girder bridge. Girder stresses were measured during girder erection, construction of the concrete slab, and subsequent live loading. The construction of the box girder bridge was simulated with a three-dimensional FEA model of the quasi-closed steel section. The live load modeling of the bridge consisted of a line element model as well as a three-dimensional model of the composite section. Based on the field and computational studies, several observations and conclusions can be made.

The agreement between the FEA solution and the field results varied depending on the stage of construction. Larger errors generally occurred with relatively small changes in stress. The FEA model was able to reasonably predict the magnitude and distribution of the girder stresses and brace forces during girder erection. The FEA model during slab construction consisted of the quasi-closed box and did not include the effect of the metal deck forms or the partially hardened concrete. The FEA model of the quasi-closed box girder tended to overestimate the top flange truss forces after the metal deck forms were added to the bridge. Although the metal deck forms reduced the forces in the top flange truss, the top flange stresses were relatively unaffected. This would indicate that the metal deck forms help to resist the torsional loads applied to the girder, but do not accumulate significant forces due to box girder bending.

Partially hardened concrete provided some composite action with the steel girder, which was not reflected in the FEA results. Although the FEA model did not reflect the effect of the metal deck forms or the partially hardened concrete, these contributions are not permitted to be relied upon in design. Therefore, since the FEA model had good agreement with field results for the steel section alone, the computer model was used to conduct parametrical studies on the top flange truss and internal bracing. The following sub-sections summarize the findings from these computational studies.

8.1.1 Top Flange Horizontal Truss System

The purpose of the top flange horizontal truss is to form a quasi-closed cross-section, thereby increasing the torsional stiffness of the girder during construction. Current design methods for the truss system assume that the diagonals and the struts of the horizontal truss resist forces caused by torsion and the lateral load component from the sloping webs. Lateral

bending in the flanges is assumed to be caused only by the lateral load component and the curvature of the girder.

The field and FEA results indicated that the current design methods underestimate the magnitudes of the member forces in the top flange lateral truss in box girders. It was found in the investigation that the brace forces in the top flange truss system are also caused by the vertical bending of the box girder, which is not considered in the current design method. For trusses with a single diagonal, the forces induced by vertical bending produce large lateral bending stresses in the top flange. In addition, the top flange lateral bending stresses resulting from the horizontal component of the applied load are generally underestimated in the current design methods by approximately 50%. This error is due to the erroneous assumption that the top and bottom flange equally resist the horizontal load component. Although the lateral flange bending only produces a component of the total flange stress, in some instances the large error in the lateral flange bending stress may lead to localized flange yielding.

The brace forces and lateral bending stresses due to torsion are effectively predicted by the current design guides. Equations were developed in this report to estimate the top flange truss forces and the lateral bending stresses due to box girder bending, as presented in Eqs. 5.26 to 5.29. Brace forces and lateral bending stresses due to the lateral component of the applied load should be calculated using the full amount of the lateral load, and the resulting design equations are presented in Eq. 5.30. The design forces for members in the top flange truss should use the superposition of brace forces caused by vertical bending, torsion, and the horizontal load component. Lateral bending stresses in the top flange consist of those due to the curvature, the horizontal component, and the bending-induced forces from the struts in SD-type trusses. The results based on the proposed method have a good agreement with the FEA solution for straight and curved quasi-closed box girders.

8.1.2 Internal K-Frames

Internal K-frames of box girder are provided to resist distortion of the box girder. Traditional theory on box girder distortion was developed mainly for girders with rectangular cross-sections. For trapezoidal box girders, the distortional loads on the girders are incorrectly evaluated in the current theory if the distortion is induced by torsional loads comprised of vertical forces. A rigorous proof was provided to show that if no distortion occurs in a trapezoidal box girder, the distribution of torsional loads must be proportional to the Saint-Venant shear flow on the cross-section of the girder. The distortional components in external loads can thus be determined using this criteria.

Current design guides provide the spacing and stiffness requirements for internal K-frames. The issue of the strength requirement for internal K-frames was not addressed. Although analytical methods such as the Beam-on-Elastic-Foundation analogy were developed to calculate the stresses and K-frame forces due to distortion, these methods are

complex and developed for distortional analysis for single complete box girders. The K-frame forces are often considered secondary in design, and the resulting members may be inadequate or have a lower factor of safety than intended.

An approximate method to evaluate brace forces in internal K-frames in quasi-closed box girders is developed. FEA results show that large forces in K-frames may develop due to the distortion, while brace forces in the top flange horizontal truss system induced by box girder distortion are usually negligible. FEA results also indicate that the resistance to the distortional loads from the out-of-bending stiffness of the girder plates can be neglected in quasi-closed box girders. The forces can thus be approximated by a continuous beam analogy. Considerations were given to distortions induced by torsional loads comprised of either vertical forces (due to the eccentricity of the concrete slab) or horizontal forces (due to the bending moment in curved girders). Design formulas for the diagonals and struts of the internal K-frames corresponding to these loading cases were developed and given in Eqs. 6.15 and 6.17. The design equations had reasonable agreement with FEA results.

8.1.3 Behavior of Completed Box Girder Bridge Under Live Load

Field results were compared with FEA results consisting of a three-dimensional model and a line element model. The line-element solution had reasonable agreement with the three-dimensional model and the field results in predicting live load bending stresses in the box girders. However, larger stresses were induced in girders closer to the truck loads. Therefore, to predict the largest girder stress using the line element model, the lateral location of the applied loads must be considered by the application of the lateral distribution factor. Composite action appears to be properly evaluated by the current specification.

The three-dimensional composite FEA model consisted of shell elements for the concrete slab and the steel girders. The connection between the steel girder and the concrete slab was achieved with brick elements between the top flanges of the steel section at the slab centroid. The effectiveness of the model was verified by the live load test results. The composite action between the steel girders and the concrete deck was properly modeled by the method.

Test and FEA results indicated that the majority of the girder stresses due to live loads were caused by bending. Bending stresses dominated the longitudinal stresses on the critical cross-sections of the box girders, however, significant warping stresses (more than 10% of bending stresses) could develop in cross-sections in the positive moment regions. In the negative moment regions above the interior supports, a nonlinear stress distribution along the width of the bottom flange was observed for some loadings. The largest stresses for some cases were approximately 50% larger than the average stresses.

The lateral load distribution factor for steel box girder bridges in the current AASHTO specification is based on the research on simply-supported straight box girder bridges. The box girder that was used in the field and computational studies in this investigation was

curved and also continuous over three spans. Critical cross-sections with the largest positive and negative bending moments were studied using the FEA model. The largest live load bending stresses in a box girder were caused by the live loads placed directly above the girder in the transverse direction. The largest bending stresses in either girder were relatively close, implying that the behavior of the individual girders was similar to each other. A single live load distribution factor could therefore be applied on either girder despite their relative positions in the radial direction. In the longitudinal direction, it appears that a single lateral distribution factor could be applied to all critical cross-sections of the continuous bridge, including the sections in either positive or negative moment regions. The bending moments on box girder cross-sections produced by live loads located in other spans was relatively insensitive to the lateral load locations.

8.2 Future Work

The behavior and design requirements for trapezoidal box girders have a number of areas that require additional investigation. There is additional work that is being conducted on trapezoidal box girders at the University of Texas at Austin. This work includes studies on the stability requirements of the top flange lateral truss and also the behavior of the negative moment region of the bottom flange.

The details that are used on the top flange lateral truss can be relatively expensive and increase the overall cost of the box girder. In addition, as outlined in this report, current details can lead to large bending induced forces. Additional research should be conducted investigating improved details on the top flange bracing. One potential source of bracing that is currently not relied upon is the permanent metal deck forms. Results presented in Chapter 4 of this report showed that the metal deck forms did provide some bracing to the top flange. Additional research should be conducted investigating the bracing potential of these forms. The connection between the metal deck form and the box girder would have to be improved, however the forms may significantly reduce or even eliminate the top flange truss at a number of locations along the girder length. The metal deck forms would probably also not be significantly affected by box girder bending due to the accordion shape profile of the form in the longitudinal direction of the girder.

Although the bridge that was monitored in the field studies had external cross-frames and diaphragms only at the supports, most box girder bridges currently under construction in Texas employ external diaphragms approximately every 20 feet along the girder length. The use of these external bracing members increase the fabrication costs on the girders and are probably not necessary. Additional research should be conducted to investigate the bracing requirements for these external cross-frames and diaphragms.

Although lateral distribution of live load was discussed in Chapter 7, additional research is necessary to fully understand how the girders interact. Parametric studies should be conducted to investigate the effect of the girder spacing and length, as well as the radius of

curvature. Additional studies can be conducted employing FEA models similar to the models presented in Chapter 7.

APPENDIX A ELIMINATION OF TEMPERATURE EFFECT FROM FIELD DATA DURING CONSTRUCTION

A.1 Approach and Results

In Chapter 3, the strain gage readings during the bridge construction were presented. The time interval during which a construction activity took place was identified. The difference of the stress readings from an individual gage (Gage X) in this time interval, S_0, includes the combined results of the temperature effect and the stress change due to applied loads. To obtain the girder stresses caused by the applied construction loads, the temperature effect in S_0 should be eliminated. This was accomplished by analyzing the data in the days leading up to the construction activity, when there was no applied load and the change in gage readings was caused mainly by the variation of temperature.

The ratio of stress change to temperature change reflects the influence of temperature on girder stress. Theoretically, thermal stress in an elastic system is a linear function of temperature increment. The recorded data, however, shows that the ratios of stress change to temperature change were often not constant even in same field conditions. A number of irregularities in the field may affect the thermal behavior of the bridge, which need to be further studied.

A statistical method was used in this report to eliminate the temperature effect. The temperature effect on each gage was represented approximately by the average value of the ratios of the stress change to temperature changes in the previous two days prior to the construction activity. A linear interpolation or extrapolation scheme was applied to obtain the temperature effects for all the construction activities. The procedure for each construction activity is outlined as follows:

1. From the field data, read the temperature changes from both thermal couples in the time interval corresponding to the construction activity. Calculate the average of the two readings, which is denoted by ΔT_0.

2. Read the temperature changes in the same time interval on the previous two days. The averages of the temperature changes of the two thermal couples on each date are denoted by ΔT_{-2} and ΔT_{-1}. The corresponding changes in stress readings from Gage X in these two time intervals are denoted by S_{-2} and S_{-1}, respectively.

3. Determine the rates of stress increase on the previous two days by calculating the ratios $k_{-2}=S_{-2}/\Delta T_{-2}$ and $k_{-1}=S_{-1}/\Delta T_{-1}$. Average these ratios to obtain $k= (k_{-2} + k_{-1})/2$.

4. The temperature effect for the construction activity is assumed to be equal to $\Delta S=k\Delta T_0$. The stress at Gage X due to the applied loads is therefore $S=S_0-\Delta S$.

The temperature and stress readings, as well as the processing of these data to acquire the stresses due to applied loads, are presented in Table A.1 to A16. Further discussions are presented in Section A.2 following the results.

Table A.1. Temperature Change During the Erection of Segment 905 (°C)

	1/7/96	1/8/96	01/09/96
Temp. 1	-0.714	-0.764	-0.920
Temp. 2	-0.768	-0.514	-0.930
Average	-0.741 (ΔT_{-2})	-0.639 (ΔT_{-1})	-0.925 (ΔT_0)

Table A.2. Stress Change Due to the Erection of Segment 905

Strain Gage	Reading on 1/7/96 S_{-2} (ksi)	Rate on 1/7/96 $k_{-2}=S_{-2}/\Delta T_{-2}$ (ksi/°C)	Reading on 1/8/96 S_{-1} (ksi)	Rate on 1/8/96 $k_{-1}=S_{-1}/\Delta T_{-1}$ (ksi/°C)	Average Rate $k=(k_{-2}+k_{-1})/2$ (ksi/°C)	Temp. Effect $\Delta S=k(\Delta T_0)$ (ksi)	Reading on 1/9/96 S_0 (ksi)	**Stress by Appd. Ld. $S=S_0-\Delta S$ (ksi)**
A1	-0.109	0.147	-0.054	0.085	0.116	-0.107	0.654	**0.761**
A2	-0.109	0.147	-0.054	0.085	0.116	-0.107	0.599	**0.706**
B1	-0.109	0.147	-0.054	0.085	0.116	-0.107	0.490	**0.598**
B2	-0.109	0.147	-0.054	0.085	0.116	-0.107	0.980	**1.088**
C1	-0.054	0.073	-0.054	0.085	0.079	-0.073	1.579	**1.653**
C2	-0.109	0.147	-0.054	0.085	0.116	-0.107	1.579	**1.687**
C15	-0.109	0.147	-0.054	0.085	0.116	-0.107	4.248	**4.355**
C16	-0.109	0.147	-0.054	0.085	0.116	-0.107	5.065	**5.172**
D1	-0.054	0.073	-0.109	0.170	0.122	-0.113	1.470	**1.583**
D2	-0.109	0.147	-0.109	0.170	0.159	-0.147	1.688	**1.835**
D15	-0.381	0.514	-0.218	0.341	0.428	-0.396	2.505	**2.901**
D16	-0.109	0.147	-0.109	0.170	0.159	-0.147	5.174	**5.321**
E1	-0.109	0.147	0.000	0.000	0.073	-0.068	-0.980	**-0.912**
E2	-0.109	0.147	0.000	0.000	0.073	-0.068	-0.980	**-0.912**
E3	-0.109	0.147	0.000	0.000	0.073	-0.068	-0.490	**-0.422**
E4	-0.054	0.073	0.054	-0.085	-0.006	0.005	-0.436	**-0.441**
E5	-0.054	0.073	-0.109	0.170	0.122	-0.113	-1.525	**-1.412**
E6	-0.054	0.073	-0.109	0.170	0.122	-0.113	-1.579	**-1.467**
E7	-0.436	0.588	-0.599	0.937	0.763	-0.706	-1.089	**-0.384**
E8	-0.109	0.147	-0.054	0.085	0.116	-0.107	-1.307	**-1.200**
E9	-0.054	0.073	-0.054	0.085	0.079	-0.073	-1.579	**-1.506**
E10	-0.109	0.147	-0.109	0.170	0.159	-0.147	-1.579	**-1.433**
E15	-0.109	0.147	-0.054	0.085	0.116	-0.107	-1.089	**-0.982**
E16	-0.054	0.073	-0.054	0.085	0.079	-0.073	-1.198	**-1.125**

Table A.3. Temperature Change During the Splicing of Segment 907 (°C)

	2/9/96	2/10/96	2/11/96
Temp. 1	0.760	0.700	-0.980
Temp. 2	0.990	0.980	-1.100
Average	0.875 (ΔT_{-2})	0.840 (ΔT_{-1})	-1.040 (ΔT_0)

Table A.4. Temperature Change During the Crane Releasing of Segment 907 (°C)

	2/14/96	2/15/96	2/16/96
Temp. 1	-0.820	-0.74	-0.480
Temp. 2	-0.870	-0.640	-0.430
Average	-0.845 (ΔT_{-2})	-0.690 (ΔT_{-1})	-0.455 (ΔT_0)

Table A.5. Stress Change Due to the Splicing of Segment 907

Strain Gage	Reading on 2/9/96 S_{-2} (ksi)	Rate on 2/9/96 $k_{-2}=S_{-2}/\Delta T_{-2}$ (ksi/°C)	Reading on 2/10/96 S_{-1} (ksi)	Rate on 2/10/96 $k_{-1}=S_{-1}/\Delta T_{-1}$ (ksi/°C)	Average Rate $k=(k_{-2}+k_{-1})/2$ (ksi/°C)	Temp. Effect $\Delta S=k(\Delta T_0)$ (ksi)	Reading on 2/11/96 S_0 (ksi)	**Stress by Appd. Ld. $S=S_0-\Delta S$ (ksi)**
A1	0.054	0.062	0.000	0.000	0.031	-0.032	0.490	**0.523**
A2	0.000	0.000	0.000	0.000	0.000	0.000	0.381	**0.381**
A15	-0.054	-0.062	0.054	0.065	0.001	-0.001	0.708	**0.709**
A16	0.109	0.124	0.163	0.195	0.159	*-0.166*	*0.708*	**0.874**
B1	0.000	0.000	0.054	0.065	0.032	-0.034	0.327	**0.360**
B2	0.054	0.062	0.054	0.065	0.064	-0.066	0.545	**0.611**
B8	0.054	0.062	0.109	0.130	0.096	-0.100	-1.089	**-0.989**
B9	0.272	0.311	0.000	0.000	0.156	-0.162	-0.218	**-0.056**
B11	0.054	0.062	0.000	0.000	0.031	-0.032	0.054	**0.087**
B12	0.054	0.062	0.054	0.065	0.064	-0.066	0.109	**0.175**
B13	0.000	0.000	0.054	0.065	0.032	-0.034	-0.817	**-0.783**
B15	0.054	0.062	0.054	0.065	0.064	-0.066	-0.545	**-0.479**
B16	0.054	0.062	0.054	0.065	0.064	-0.066	-0.762	**-0.696**
C1	0.000	0.000	0.054	0.065	0.032	-0.034	0.762	**0.796**
C2	0.054	0.062	0.054	0.065	0.064	-0.066	0.762	**0.829**
C15	0.054	0.062	-0.054	-0.065	-0.001	0.001	2.178	**2.177**
C16	0.000	0.000	0.000	0.000	0.000	0.000	1.198	**1.198**
D1	0.054	0.062	0.054	0.065	0.064	-0.066	0.762	**0.829**
D2	0.054	0.062	0.000	0.000	0.031	-0.032	0.871	**0.904**
D15	0.436	0.498	0.490	0.584	0.541	-0.562	0.599	**1.161**
D16	0.000	0.000	-0.054	-0.065	-0.032	0.034	1.470	**1.437**
E1	0.000	0.000	0.054	0.065	0.032	-0.034	-0.381	**-0.348**
E2	-0.218	-0.249	0.109	0.130	-0.060	0.062	-0.218	**-0.280**
E3	0.054	0.062	0.109	0.130	0.096	-0.100	-0.163	**-0.064**
E4	0.054	0.062	0.054	0.065	0.064	-0.066	-0.163	**-0.097**
E5	-0.054	-0.062	-0.054	-0.065	-0.064	0.066	-0.654	**-0.720**
E6	0.000	0.000	0.000	0.000	0.000	0.000	-0.654	**-0.654**
E7	0.109	0.124	0.054	0.065	0.095	-0.098	-1.144	**-1.045**
E8	0.163	0.187	0.109	0.130	0.158	-0.165	-0.545	**-0.380**
E9	-0.054	-0.062	0.000	0.000	-0.031	0.032	-0.545	**-0.577**
E10	0.109	0.124	0.054	0.065	0.095	-0.098	-0.599	**-0.501**
E15	0.000	0.000	0.054	0.065	0.032	-0.034	0.054	**0.088**
E16	0.054	0.062	0.054	0.065	0.064	-0.066	-0.054	**0.012**

Table A.6. Stress Change Due to Crane Releasing of Segment 907

Strain Gage	Reading on 2/14/96 S_{-2} (ksi)	Rate on 2/14/96 $k_{-2}=S_{-2}/\Delta T_{-2}$ (ksi/°C)	Reading on 2/15/96 S_{-1} (ksi)	Rate on 2/15/96 $k_{-1}=S_{-1}/\Delta T_{-1}$ (ksi/°C)	Average Rate $k=(k_{-2}+k_{-1})/2$ (ksi/°C)	Temp. Effect $\Delta S=k(\Delta T_0)$ (ksi)	Reading on 2/16/96 S_0 (ksi)	**Stress by Appd. Ld. $S=S_0-\Delta S$ (ksi)**
A1	0.000	0.000	0.000	0.000	0.000	0.000	0.762	**0.762**
A2	-0.054	0.064	-0.054	0.079	0.072	-0.033	0.545	**0.577**
A15	-0.054	0.064	0.000	0.000	0.032	-0.015	0.708	**0.723**
A16	-0.054	0.064	-0.054	0.079	0.072	-0.033	0.762	**0.795**
B1	-0.054	0.064	0.000	0.000	0.032	-0.015	0.436	**0.450**
B2	0.000	0.000	-0.054	0.079	0.039	-0.018	0.817	**0.835**
B8	-0.054	0.064	-0.054	0.079	0.072	-0.033	-1.579	**-1.547**
B9	0.000	0.000	-0.054	0.079	0.039	-0.018	-0.327	**-0.309**
B11	0.000	0.000	0.000	0.000	0.000	0.000	0.000	**0.000**
B12	-0.054	0.064	-0.054	0.079	0.072	-0.033	0.054	**0.087**
B13	-0.054	0.064	0.000	0.000	0.032	-0.015	-1.362	**-1.347**
B15	0.000	0.000	-0.163	0.237	0.118	-0.054	-0.926	**-0.872**
B16	0.000	0.000	0.000	0.000	0.000	0.000	-1.198	**-1.198**
C1	-0.054	0.064	-0.054	0.079	0.072	-0.033	1.253	**1.285**
C2	-0.054	0.064	-0.054	0.079	0.072	-0.033	1.035	**1.067**
C15	-0.054	0.064	0.000	0.000	0.032	-0.015	1.961	**1.975**
C16	-0.054	0.064	-0.054	0.079	0.072	-0.033	2.287	**2.320**
D1	-0.054	0.064	-0.054	0.079	0.072	-0.033	1.089	**1.122**
D2	-0.054	0.064	-0.054	0.079	0.072	-0.033	1.307	**1.340**
D15	-0.436	0.516	-0.272	0.395	0.455	-0.207	1.198	**1.405**
D16	-0.054	0.064	-0.054	0.079	0.072	-0.033	2.342	**2.374**
E1	0.000	0.000	0.000	0.000	0.000	0.000	-0.490	**-0.490**
E2	-0.054	0.064	0.000	0.000	0.032	-0.015	-0.490	**-0.475**
E3	-0.054	0.064	0.000	0.000	0.032	-0.015	-0.272	**-0.258**
E4	-0.054	0.064	0.000	0.000	0.032	-0.015	-0.218	**-0.203**
E5	0.000	0.000	-0.054	0.079	0.039	-0.018	-1.089	**-1.071**
E6	0.000	0.000	-0.054	0.079	0.039	-0.018	-1.089	**-1.071**
E7	-0.871	1.031	-0.490	0.710	0.871	-0.396	-0.926	**-0.530**
E8	0.000	0.000	0.000	0.000	0.000	0.000	-0.926	**-0.926**
E9	0.000	0.000	0.000	0.000	0.000	0.000	-1.089	**-1.089**
E10	-0.109	0.129	-0.054	0.079	0.104	-0.047	-1.089	**-1.042**
E15	-0.054	0.064	-0.054	0.079	0.072	-0.033	0.000	**0.033**
E16	-0.054	0.064	0.000	0.000	0.032	-0.015	-0.054	**-0.040**

Table A.7. Total Stresses Due to the Erection of Segment 907

Strain Gage	Stress from Table A.5 (ksi)	Stress from Table A.6 (ksi)	**Total Stress (ksi)**
A1	0.523	0.762	**1.285**
A2	0.381	0.577	**0.958**
A15	0.709	0.723	**1.432**
A16	0.874	0.795	**1.669**
B1	0.360	0.450	**0.811**
B2	0.611	0.835	**1.446**
B8	-0.989	-1.547	**-2.536**
B9	-0.056	-0.309	**-0.365**
B11	0.087	0.000	**0.087**
B12	0.175	0.087	**0.262**
B13	-0.783	-1.347	**-2.130**
B15	-0.479	-0.872	**-1.350**
B16	-0.696	-1.198	**-1.894**
C1	0.796	1.285	**2.081**
C2	0.829	1.067	**1.896**
C15	2.177	1.975	**4.152**
C16	1.198	2.320	**3.518**
D1	0.829	1.122	**1.950**
D2	0.904	1.340	**2.243**
D15	1.161	1.405	**2.567**
D16	1.437	2.374	**3.811**
E1	-0.348	-0.490	**-0.838**
E2	-0.280	-0.475	**-0.755**
E3	-0.064	-0.258	**-0.321**
E4	-0.097	-0.203	**-0.300**
E5	-0.720	-1.071	**-1.791**
E6	-0.654	-1.071	**-1.725**
E7	-1.045	-0.530	**-1.575**
E8	-0.380	-0.926	**-1.306**
E9	-0.577	-1.089	**-1.666**
E10	-0.501	-1.042	**-1.543**
E15	0.088	0.033	**0.121**
E16	0.012	-0.040	**-0.028**

Table A.8. Temperature Change During Stage 1 Slab Construction (°C)

	9/12/96	9/13/96	9/14/96
Temp. 1	-2.51	-1.45	-1.62
Temp. 2	-2.36	-1.33	-1.32
Average	-2.435 (ΔT_{-2})	-1.390 (ΔT_{-1})	-1.47 (ΔT_0)

Table A.9. Stress Change During Stage 1 Slab Construction — Section P

Strain Gage	Reading on 9/12/96 S_{-2} (ksi)	Rate on 9/12/96 $k_{-2}=S_{-2}/\Delta T_{-2}$ (ksi/°C)	Reading on 9/13/96 S_{-1} (ksi)	Rate on 9/13/96 $k_{-1}=S_{-1}/\Delta T_{-1}$ (ksi/°C)	Average Rate $k=(k_{-2}+k_{-1})/2$ (ksi/°C)	Temp. Effect $\Delta S=k(\Delta T_0)$ (ksi)	Reading on 9/14/96 S_0 (ksi)	**Stress by Appd. Ld. $S=S_0-\Delta S$ (ksi)**
A1	-0.109	0.045	0.054	-0.039	0.003	-0.004	-4.030	**-4.026**
A2	-0.054	0.022	0.054	-0.039	-0.008	0.012	-6.100	**-6.112**
A4	0.054	-0.022	0.000	0.000	-0.011	0.016	-2.451	**-2.467**
A8	0.054	-0.022	0.000	0.000	-0.011	0.016	2.941	**2.924**
A13	0.055	-0.023	0.000	0.000	-0.011	0.017	2.430	**2.414**
A15	0.000	0.000	0.054	-0.039	-0.020	0.029	-2.451	**-2.479**
A16	0.109	-0.045	0.054	-0.039	-0.042	0.062	-2.396	**-2.458**
B1	-0.109	0.045	0.000	0.000	0.022	-0.033	-5.119	**-5.086**
B2	-0.054	0.022	0.163	-0.118	-0.048	0.070	-6.644	**-6.714**
B4	0.054	-0.022	0.000	0.000	-0.011	0.016	-2.560	**-2.576**
B6	0.000	0.000	0.000	0.000	0.000	0.000	1.852	**1.852**
B7	-0.163	0.067	-0.054	0.039	0.053	-0.078	2.396	**2.474**
B8	0.054	-0.022	0.000	0.000	-0.011	0.016	2.287	**2.271**
B9	-0.054	0.022	-0.054	0.039	0.031	-0.045	1.362	**1.407**
B11	0.054	-0.022	0.000	0.000	-0.011	0.016	-0.272	**-0.289**
B12	0.000	0.000	0.000	0.000	0.000	0.000	-0.436	**-0.436**
B13	0.000	0.000	-0.054	0.039	0.020	-0.029	1.743	**1.772**
B15	0.218	-0.089	0.000	0.000	-0.045	0.066	0.926	**0.860**
B16	0.054	-0.022	-0.054	0.039	0.008	-0.012	1.253	**1.265**

Table A.10. Stress Change During Stage 1 Slab Construction — Section N

Strain Gage	Reading on 9/12/96 S_{-2} (ksi)	Rate on 9/12/96 $k_{-2}=S_{-2}/\Delta T_{-2}$ (ksi/°C)	Reading on 9/13/96 S_{-1} (ksi)	Rate on 9/13/96 $k_{-1}=S_{-1}/\Delta T_{-1}$ (ksi/°C)	Average Rate $k=(k_{-2}+k_{-1})/2$ (ksi/°C)	Temp. Effect $\Delta S=k(\Delta T_0)$ (ksi)	Reading on 9/14/96 S_0 (ksi)	**Stress by Appd. Ld. $S=S_0-\Delta S$ (ksi)**
C1	0.054	-0.022	0.054	-0.039	-0.031	0.045	0.817	**0.772**
C2	0.054	-0.022	0.109	-0.078	-0.050	0.074	0.654	**0.579**
C3	0.054	-0.022	0.000	0.000	-0.011	0.016	0.054	**0.038**
C4	0.109	-0.045	0.000	0.000	-0.022	0.033	0.490	**0.457**
C10	0.110	-0.045	0.000	0.000	-0.023	0.033	0.000	**-0.033**
C13	0.110	-0.045	0.055	-0.040	-0.043	0.063	-0.552	**-0.615**
C15	0.163	-0.067	0.054	-0.039	-0.053	0.078	-0.980	**-1.058**
C16	0.054	-0.022	0.054	-0.039	-0.031	0.045	-1.198	**-1.243**
D1	0.000	0.000	0.000	0.000	0.000	0.000	0.708	**0.708**
D2	0.054	-0.022	0.054	-0.039	-0.031	0.045	0.980	**0.935**
D4	0.218	-0.089	0.054	-0.039	-0.064	0.095	0.708	**0.613**
D10	0.055	-0.023	-0.055	0.040	0.009	-0.013	0.166	**0.178**
D13	0.000	0.000	-0.055	0.040	0.020	-0.029	-0.497	**-0.468**
D15	0.109	-0.045	0.054	-0.039	-0.042	0.062	-0.980	**-1.042**
D16	0.109	-0.045	0.054	-0.039	-0.042	0.062	-1.198	**-1.260**
E1	0.054	-0.022	0.000	0.000	-0.011	0.016	-0.054	**-0.071**
E2	0.000	0.000	0.000	0.000	0.000	0.000	-0.109	**-0.109**
E3	0.000	0.000	0.000	0.000	0.000	0.000	-0.109	**-0.109**
E4	0.054	-0.022	0.054	-0.039	-0.031	0.045	-0.109	**-0.154**
E5	0.000	0.000	0.000	0.000	0.000	0.000	-0.545	**-0.545**
E6	-0.054	0.022	0.000	0.000	0.011	-0.016	-0.654	**-0.637**
E7	0.109	-0.045	0.000	0.000	-0.022	0.033	-0.436	**-0.469**
E8	-0.054	0.022	0.000	0.000	0.011	-0.016	-0.545	**-0.528**
E10	-0.054	0.022	-0.054	0.039	0.031	-0.045	-0.654	**-0.608**
E12	-0.054	0.022	-0.054	0.039	0.031	-0.045	-0.762	**-0.717**
E13	0.109	-0.045	0.054	-0.039	-0.042	0.062	-0.545	**-0.606**
E14	0.109	-0.045	0.000	0.000	-0.022	0.033	-0.599	**-0.632**
E16	0.054	-0.022	0.000	0.000	-0.011	0.016	0.054	**0.038**

Table A.11. Temperature Change During Stage 2 Slab Construction (°C)

	9/15/96	9/16/96	9/17/96
Temp. 1	-2.42	-3.24	-1.90
Temp. 2	-2.10	-2.92	-1.62
Average	-2.260 (ΔT_{-2})	-3.080 (ΔT_{-1})	-1.760 (ΔT_0)

Table A.12. Stress Change During Stage 2 Slab Construction — Section P

Strain Gage	Reading on 9/15/96 S_{-2} (ksi)	Rate on 9/15/96 $k_{-2}=S_{-2}/\Delta T_{-2}$ (ksi/°C)	Reading on 9/16/96 S_{-1} (ksi)	Rate on 9/16/96 $k_{-1}=S_{-1}/\Delta T_{-1}$ (ksi/°C)	Average Rate $k=(k_{-2}+k_{-1})/2$ (ksi/°C)	Temp. Effect $\Delta S=k(\Delta T_0)$ (ksi)	Reading on 9/17/96 S_0 (ksi)	**Stress by Appd. Ld. $S=S_0-\Delta S$ (ksi)**
A1	0.218	-0.096	0.327	-0.106	-0.101	0.178	0.381	**0.203**
A2	0.163	-0.072	0.381	-0.124	-0.098	0.173	0.436	**0.263**
A4	0.109	-0.048	0.218	-0.071	-0.059	0.105	0.000	**-0.105**
A8	0.000	0.000	0.000	0.000	0.000	0.000	-0.980	**-0.980**
A13	0.000	0.000	0.000	0.000	0.000	0.000	-0.994	**-0.994**
A15	0.163	-0.072	0.272	-0.088	-0.080	0.141	0.272	**0.131**
A16	0.218	-0.096	0.272	-0.088	-0.092	0.163	0.272	**0.110**
B1	0.000	0.000	0.381	-0.124	-0.062	0.109	0.545	**0.436**
B2	0.054	-0.024	0.381	-0.124	-0.074	0.130	0.054	**-0.076**
B4	0.000	0.000	0.163	-0.053	-0.027	0.047	0.054	**0.008**
B6	0.000	0.000	0.000	0.000	0.000	0.000	-0.762	**-0.762**
B7	-0.109	0.048	-0.163	0.053	0.051	-0.089	-0.708	**-0.619**
B8	0.163	-0.072	0.163	-0.053	-0.063	0.110	-0.054	**-0.165**
B9	0.054	-0.024	0.000	0.000	-0.012	0.021	-0.327	**-0.348**
B11	0.054	-0.024	0.054	-0.018	-0.021	0.037	-0.436	**-0.472**
B12	0.000	0.000	0.000	0.000	0.000	0.000	-0.490	**-0.490**
B13	0.109	-0.048	0.163	-0.053	-0.051	0.089	0.054	**-0.035**
B15	0.163	-0.072	0.436	-0.141	-0.107	0.188	0.490	**0.302**
B16	0.109	-0.048	0.163	-0.053	-0.051	0.089	-0.218	**-0.307**

Table A.13. Stress Change During Stage 2 Slab Construction — Section N

Strain Gage	Reading on 9/15/96 S_{-2} (ksi)	Rate on 9/15/96 $k_{-2}=S_{-2}/\Delta T_{-2}$ (ksi/°C)	Reading on 9/16/96 S_{-1} (ksi)	Rate on 9/16/96 $k_{-1}=S_{-1}/\Delta T_{-1}$ (ksi/°C)	Average Rate $k=(k_{-2}+k_{-1})/2$ (ksi/°C)	Temp. Effect $\Delta S=k(\Delta T_0)$ (ksi)	Reading on 9/17/96 S_0 (ksi)	**Stress by Appd. Ld. $S=S_0-\Delta S$ (ksi)**
C1	0.000	0.000	0.109	-0.035	-0.018	0.031	6.426	**6.395**
C2	0.054	-0.024	0.218	-0.071	-0.047	0.083	4.847	**4.763**
C3	0.000	0.000	0.000	0.000	0.000	0.000	0.762	**0.762**
C4	-0.054	0.024	-0.054	0.018	0.021	-0.037	4.193	**4.230**
C10	0.055	-0.024	-0.110	0.036	0.006	-0.010	-0.110	**-0.100**
C13	0.110	-0.049	-0.110	0.036	-0.007	0.011	-4.530	**-4.541**
C15	0.109	-0.048	0.218	-0.071	-0.059	0.105	7.025	**6.921**
C16	0.163	-0.072	0.109	-0.035	-0.054	0.095	7.624	**7.530**
D1	-0.054	0.024	0.000	0.000	0.012	-0.021	5.174	**5.195**
D2	0.054	-0.024	0.163	-0.053	-0.039	0.068	7.515	**7.448**
D4	0.218	-0.096	0.163	-0.053	-0.075	0.132	4.847	**4.715**
D10	0.000	0.000	-0.055	0.018	0.009	-0.016	1.160	**1.176**
D13	0.000	0.000	0.000	0.000	0.000	0.000	-3.701	**-3.701**
D15	0.163	-0.072	0.163	-0.053	-0.063	0.110	6.971	**6.861**
D16	0.163	-0.072	0.163	-0.053	-0.063	0.110	7.842	**7.732**
E1	-0.163	0.072	0.000	0.000	0.036	-0.064	-2.505	**-2.442**
E2	-0.272	0.120	-0.054	0.018	0.069	-0.122	-2.669	**-2.547**
E3	0.000	0.000	0.054	-0.018	-0.009	0.016	-1.362	**-1.377**
E4	0.054	-0.024	0.163	-0.053	-0.039	0.068	-1.362	**-1.429**
E5	0.054	-0.024	0.109	-0.035	-0.030	0.052	-4.847	**-4.899**
E6	0.000	0.000	0.000	0.000	0.000	0.000	-5.010	**-5.010**
E7	0.163	-0.072	0.163	-0.053	-0.063	0.110	-4.684	**-4.794**
E8	0.000	0.000	0.000	0.000	0.000	0.000	-4.302	**-4.302**
E10	-0.054	0.024	-0.109	0.035	0.030	-0.052	-4.956	**-4.904**
E12	-0.054	0.024	0.000	0.000	0.012	-0.021	-5.283	**-5.261**
E13	0.109	-0.048	0.218	-0.071	-0.059	0.105	-5.119	**-5.224**
E14	0.109	-0.048	0.109	-0.035	-0.042	0.074	-5.827	**-5.901**
E16	-0.054	0.024	0.000	0.000	0.012	-0.021	0.490	**0.511**

Table A.14. Temperature Change During Stage 3 Slab Construction (°C)

	9/19/96	9/20/96	9/21/96
Temp. 1	-3.63	-3.77	-8.01
Temp. 2	-3.08	-3.53	-7.24
Average	-3.355 (ΔT_{-2})	-3.650 (ΔT_{-1})	-7.625 (ΔT_0)

Table A.15. Stress Change During Stage 2 Slab Construction — Section P

Strain Gage	Reading on 9/19/96 S_{-2} (ksi)	Rate on 9/19/96 $k_{-2}=S_{-2}/\Delta T_{-2}$ (ksi/°C)	Reading on 9/20/96 S_{-1} (ksi)	Rate on 9/20/96 $k_{-1}=S_{-1}/\Delta T_{-1}$ (ksi/°C)	Average Rate $k=(k_{-2}+k_{-1})/2$ (ksi/°C)	Temp. Effect $\Delta S=k(\Delta T_0)$ (ksi)	Reading on 9/21/96 S_0 (ksi)	**Stress by Appd. Ld. $S=S_0-\Delta S$ (ksi)**
A1	0.272	-0.081	0.218	-0.060	-0.070	0.537	-0.054	**-0.591**
A2	0.327	-0.097	0.218	-0.060	-0.079	0.599	0.000	**-0.599**
A4	0.218	-0.065	0.381	-0.104	-0.085	0.646	0.708	**0.062**
A8	0.054	-0.016	0.000	0.000	-0.008	0.062	1.307	**1.245**
A13	0.055	-0.016	0.055	-0.015	-0.016	0.120	1.270	**1.150**
A15	0.218	-0.065	0.163	-0.045	-0.055	0.418	0.218	**-0.200**
A16	0.218	-0.065	0.163	-0.045	-0.055	0.418	0.272	**-0.146**
B1	0.272	-0.081	0.163	-0.045	-0.063	0.480	0.054	**-0.426**
B2	0.381	-0.114	0.163	-0.045	-0.079	0.604	-0.272	**-0.876**
B4	0.109	-0.032	0.218	-0.060	-0.046	0.351	0.218	**-0.133**
B6	-0.054	0.016	-0.054	0.015	0.016	-0.119	0.762	**0.881**
B7	-0.109	0.032	-0.218	0.060	0.046	-0.351	0.490	**0.841**
B8	0.163	-0.049	0.109	-0.030	-0.039	0.299	0.327	**0.027**
B9	0.000	0.000	0.054	-0.015	-0.007	0.057	0.272	**0.215**
B11	0.000	0.000	0.054	-0.015	-0.007	0.057	0.272	**0.215**
B12	0.000	0.000	0.054	-0.015	-0.007	0.057	0.218	**0.161**
B13	0.163	-0.049	0.109	-0.030	-0.039	0.299	0.327	**0.027**
B15	0.381	-0.114	-0.545	0.149	0.018	-0.136	-0.436	**-0.300**
B16	0.054	-0.016	0.054	-0.015	-0.016	0.119	0.327	**0.208**

Table A.16. Stress Change During Stage 3 Slab Construction — Section N

Strain Gage	Reading on 9/19/96 S_{-2} (ksi)	Rate on 9/19/96 $k_{-2}=S_{-2}/\Delta T_{-2}$ (ksi/°C)	Reading on 9/20/96 S_{-1} (ksi)	Rate on 9/20/96 $k_{-1}=S_{-1}/\Delta T_{-1}$ (ksi/°C)	Average Rate $k=(k_{-2}+k_{-1})/2$ (ksi/°C)	Temp. Effect $\Delta S=k(\Delta T_0)$ (ksi)	Reading on 9/21/96 S_0 (ksi)	**Stress by Appd. Ld. $S=S_0-\Delta S$ (ksi)**
C1	0.000	0.000	0.163	-0.045	-0.022	0.171	1.797	**1.627**
C2	0.218	-0.065	0.218	-0.060	-0.062	0.475	1.362	**0.886**
C3	0.054	-0.016	0.000	0.000	-0.008	0.062	0.109	**0.047**
C4	0.000	0.000	-0.163	0.045	0.022	-0.171	Large	**Large**
C10	0.110	-0.033	0.000	0.000	-0.016	0.126	-0.442	**-0.567**
C13	0.166	-0.049	-0.276	0.076	0.013	-0.100	-1.105	**-1.005**
C15	0.109	-0.032	-0.109	0.030	-0.001	0.010	-1.525	**-1.535**
C16	0.109	-0.032	-0.109	0.030	-0.001	0.010	-0.817	**-0.827**
D1	-0.218	0.065	-0.163	0.045	0.055	-0.418	1.470	**1.889**
D2	0.163	-0.049	0.054	-0.015	-0.032	0.243	2.069	**1.827**
D4	0.163	-0.049	0.054	-0.015	-0.032	0.243	2.069	**1.827**
D10	-0.276	0.082	-0.221	0.061	0.071	-0.545	0.552	**1.097**
D13	-0.276	0.082	-0.166	0.045	0.064	-0.487	-1.215	**-0.728**
D15	0.163	-0.049	0.054	-0.015	-0.032	0.243	-0.109	**-0.351**
D16	0.163	-0.049	0.000	0.000	-0.024	0.186	-0.272	**-0.458**
E1	-0.327	0.097	-0.436	0.119	0.108	-0.826	0.327	**1.153**
E2	-0.490	0.146	-0.654	0.179	0.163	-1.240	0.054	**1.294**
E3	-0.054	0.016	-0.109	0.030	0.023	-0.176	0.272	**0.448**
E4	-0.109	0.032	-0.163	0.045	0.039	-0.294	0.381	**0.676**
E5	0.327	-0.097	0.163	-0.045	-0.071	0.542	-1.416	**-1.958**
E6	0.163	-0.049	-0.054	0.015	-0.017	0.129	-1.743	**-1.871**
E7	0.381	-0.114	0.272	-0.075	-0.094	0.718	-1.198	**-1.916**
E8	0.163	-0.049	-0.054	0.015	-0.017	0.129	-1.634	**-1.763**
E10	0.000	0.000	-0.163	0.045	0.022	-0.171	-1.906	**-1.735**
E12	-0.163	0.049	-0.109	0.030	0.039	-0.299	-1.743	**-1.443**
E13	0.436	-0.130	0.327	-0.090	-0.110	0.836	-1.144	**-1.980**
E14	0.272	-0.081	0.218	-0.060	-0.070	0.537	-1.362	**-1.898**
E16	-0.109	0.032	-0.109	0.030	0.031	-0.238	-0.054	**0.183**

A.2 Discussion

The ratio of the temperature effect to the total change in stress readings, $\Delta S/S_0$, represents the relative amount of the temperature effect in stress changes. The numbers for ΔS and S_0 are underlined in Tables A.1 to A.16 if ΔS is larger than 10% of S_0. In most cases, temperature effects were much less than the stresses due to applied loads. However, there are a few exceptions in which temperature effects were the significant parts of the total changes in stress readings. One of these cases is the data from Gage E7 and G15 during the erection of girder. As discussed in Chapter 3, these two channels were probably wired to one-sided gages that had a poor temperature compensation capacity. Another circumstance of large temperature effect in stress reading is when the stresses due to applied loads were relatively small. For example, most of gages at Section P during Stages 2 and 3 slab construction had the ratios of $\Delta S/S_0$ larger than 10% (Tables A.12 and A.9). Stresses caused by the applied loads were small due to the composite action of the girder at Section P during these construction activities, which led to a larger percentage of temperature effect in the recorded data.

Section N during Stage 3 slab construction (Table A.16) is the only case that large temperature effects occurred on gages with appreciable stress increases (more than 1 ksi for several gages). Table A.14 shows that temperature dropped more severely during Stage 3 slab construction (-7.2°C) than during the same time intervals in the previous two days (-3.4°C and -3.7°C). The temperature effects presented in Tables A.16 were calculated from the algorithm discussed in Section A.1. Additional data are presented in Table A.17 to complement the information about the temperature effect for this construction activity. The table includes the increase of stress readings between 20:00, September 19 to 11:00, September 20, prior to Stage 3 slab construction. The amount of temperature changes in this period of time was close to the change during the construction, as shown in Table A.18. Therefore, the differences in stress readings in this period of time could be served as the temperature effects for Stage 3 slab construction.

Table A.17 shows that, for many strain gages, the stress changes between 20:00, September 19 and 11:00, September 20 were significantly different from the changes predicted by the algorithm discussed in Section A.1. More evidences are therefore needed to determine which group of data in Table A.17 better reflect the temperature effect for Stage 3 slab construction.

The data between 20:00 to 11:00 include some period of time during which part of the girder was exposed to the direct sunshine. A non-uniform temperature distribution may exist in the girder, causing the girder to deform in a way different from how it reacted to temperature changes at the night. For example, Table A.19 show the results at Gages C4, C10, C13 on the interior web, and Gages D4, D10 and D13 on the exterior webs, in two time intervals within the period of 20:00, 9/19 to 11:00, 9/20, both before the construction. Temperature dropped approximately 3° in both periods between 22:00 to 5:00 and between

2:00 to 11:00. However, the readings on the strain gages differ significantly as shown in Table A.19. In particular, Gages C4, C10 and C13 experienced tensile and compressive stresses in different periods, despite a nearly same temperature change. This behavior was believed to be caused by the non-uniform temperature gradient in different regions of the box girders. Therefore, the temperature effect presented in Table A.16, which was based on the reading between 22:00 to 6:00 when the temperature was nearly uniform over the girder, are more reliable. These results were therefore used in determining the stresses due to applied loads and the resulting stresses was presented in Table A.16 and Chapter 3.

Temperature effect is an important topic that will be further studied using the recorded data. Only the temperature effect during the construction was discussed in the report. The behavior of the completed bridge subjected to the temperature changes was studied by Lopez (1999).

Table A.17. Comparison of Different Potential Temperature Effects for Stage 3 Slab Construction

Strain Gage	Change in 20:00, 9/19 to 11:00,9/20 (ksi)	Temp. Effect from Table A.15 (ksi)	Strain Gage	Change in 20:00, 9/19 to 11:00,9/20 (ksi)	Temp. Effect from Table A.16 (ksi)
A1	0.381	0.537	C1	0.000	0.171
A2	0.436	0.599	C2	0.163	0.475
A4	0.817	0.646	C3	0.109	0.062
A8	0.054	0.062	C4	-0.054	-0.171
A13	0.276	0.120	C10	-0.166	0.126
A15	0.436	0.418	C13	-0.331	-0.100
A16	0.490	0.418	C15	-0.272	0.010
B1	0.654	0.480	C16	-0.109	0.010
B2	0.436	0.604	D1	-0.381	-0.418
B4	0.490	0.351	D2	0.109	0.243
B6	-0.109	-0.119	D4	0.545	0.243
B7	-0.545	-0.351	D10	-0.276	-0.545
B8	0.436	0.299	D13	-0.111	-0.487
B9	0.272	0.057	D15	0.327	0.243
B11	0.381	0.057	D16	0.218	0.186
B12	0.327	0.057	E1	-0.545	-0.826
B13	0.327	0.299	E2	-1.035	-1.240
B15	0.000	-0.136	E3	-0.163	-0.176
B16	0.381	0.119	E4	-0.272	-0.294
			E5	0.381	0.542
			E6	0.054	0.129
			E7	0.654	0.718
			E8	0.000	0.129
			E10	-0.272	-0.171
			E12	-0.109	-0.299
			E13	0.654	0.836
			E14	0.599	0.537
			E16	-0.381	-0.238

Table A.18. Temperature Change Before and During Stage 3 Slab Construction

Thermal Couple	From 20:00, 9/19/96 to 11:00, 9/20/96	From 22:00, 9/21/96 to 6:00, 9/22/96
Temp. 1	-8.19	-8.01
Temp. 2	-7.85	-7.24

Table A.19. Stress Change at the Webs at Section N Between 9/19/96 and 9/20/96

Thermal Couple or Strain Gage	Increase from 22:00 to 5:00 (ksi)	Increase from 1:00 to 11:00 (ksi)
Temp. 1	-3.52	-3.55
Temp. 2	-3.01	-3.28
C4	0.000	-0.109
C10	0.110	-0.773
C13	0.166	-1.381
D4	0.109	0.272
D10	-0.276	-0.055
D13	-0.221	-0.110

APPENDIX B DERIVATION OF AXIAL FORCES FROM STRESS READINGS ON BRACING MEMBERS

Longitudinal stresses in the instrumented bracing members of the box girder were measured at the isolated gage locations as illustrated previously in Figs. 3.8 and 3.27. These stresses should be converted into brace forces such as the axial forces and bending moments, which are the design parameters for bracing members. The conversion was also necessary in comparing the measured results with FEA solution. As discussed in Chapter 4, bracing members were modeled by truss or beam elements and thus the member forces were the direct outputs from the FEA model.

B.1 Stress Distribution on Cross-Sections of Bracing Members

The bracing members used in the box girders were the W-Tee and Angle sections. The shear centers of the cross-sections are located at the intersecting point of the two plates. According to the mechanics of the thin-walled structures, no warping stresses will be induced on these cross-sections when the members are subjected to torsional moments. Therefore, the longitudinal stresses in bracing members were caused only by the axial forces and the bending moments.

The longitudinal stresses induced by axial forces and bending moments are distributed linearly on the cross-section of the bracing members. The stress distribution on cross-sections of a bracing member can therefore be expressed by

$$f = a + bx + cy \ , \tag{B.1}$$

in which f is the longitudinal stress, a, b, c are constants, and x, y are the coordinate system on the cross-section of the member. Once a, b, c are determined, the member forces can be derived using the beam-column theory. For instance, if the origin of the x-y coordinate system passes through the centroid of the cross-section, the axial force in the member is (Nakai and Yoo 1988)

$$N = aA \ , \tag{B.2}$$

where A is the cross-sectional area of the bracing member.

Therefore, the brace forces can be obtained if Eq. B.1 is determined. Constants a, b, c are approximated from the measured results using the regression method as discussed in the followings.

B.2 Regression Method

To determine the distribution plane of the stresses (a, b, c in Eq. B.1), only three stress readings at three points that are not collinear are required. Most instrumented brace members had stress readings at more than three points. Because of the errors in the field measurement, these readings were not necessarily coplanar. To count-balance the field errors and better utilize the information from all gages, the three-dimensional linear regression algorithm was used to find an approximate plane to represent the stress distribution from the measured data. The regression method is based on the least square criteria such that the error between the data points and the representative plane is at the least (Weisberg 1985). The regression method is a statistical tool that does not rely on physical assumptions.

Assume gage i was located at point (x_i, y_i) and had the reading of f_i (i=1,2...n, $n \geq 3$). The equation of the approximate plane is still denoted by Eq. B.1. According to the method, constants b and c in the equation can be solved from the following equations:

$$\begin{cases} l_{11}b + l_{12}c = l_{10} \\ l_{21}b + l_{22}c = l_{20} \end{cases}, \tag{B.3}$$

in which

$$l_{11} = \sum_{i=1}^{n} (x_i - \bar{x})^2 , \tag{B.4a}$$

$$l_{22} = \sum_{i=1}^{n} (y_i - \bar{y})^2 , \tag{B.4b}$$

$$l_{12} = l_{21} = \sum_{i=1}^{n} (x_i - \bar{x})(y_i - \bar{y}) , \tag{B.4c}$$

$$l_{10} = \sum_{i=1}^{n} (x_i - \bar{x})(f_i - \bar{f}) , \tag{B.4d}$$

$$l_{10} = \sum_{i=1}^{n} (y_i - \bar{y})(f_i - \bar{f}) , \tag{B.4e}$$

$$\bar{x} = \frac{1}{n} \sum_{i=1}^{n} x_i , \tag{B.4f}$$

$$\bar{y} = \frac{1}{n} \sum_{i=1}^{n} y_i , \tag{B.4g}$$

$$\bar{f} = \frac{1}{n} \sum_{i=1}^{n} f_i . \tag{B.4h}$$

Once b and c are solved, constant a in Eq. B.1 is computed from the following relation

$$a = \bar{f} - b\bar{x} - c\bar{y} \ . \qquad \text{(B.5)}$$

B.3 Procedure and Results

The procedure to calculate the axial forces in the bracing members from the measured data was therefore to solve constants a, b, c from the data using the Eqs. B.3 to B.5, followed by the determination of the forces using Eq. B.2. The coordinates of the gages, (x_i, y_i), were determined from the member sizes and the actual locations of the gages (all 1 in. from the edges). The results were presented in Table B.1, and also in Chapter 3 along with the measured stress results as shown in Figs. 3.16, 3.25, 3.36, 3.46, and 3.57.

The correlation coefficient defined in the regression method, R, reflects how close the measured data to a linear distribution. The closer R to the value of one, the closer the test results to a linear distribution (R=1 if n=3). The results of R for all forces are also presented in Table B.1, which indicates that most of the axial forces derived from the measured stresses have a correlation coefficient close to 1. This implies that the assumption of linear stress distribution on the cross-sections of the bracing member is valid for most of the cases. Exceptions occurred when the forces were relatively small, which leads to the conclusion that larger axial forces measured in the tests are more reliable than those forces with less magnitudes.

Table B.1. Axial Forces / Correlation Coefficients from the Regression Method

	Section P Diagonal	Section P Strut	Section N Diagonal	Section N Strut
Erection of 905	N/A	N/A	38.8 k / 1.000	-2.55 k / 0.998
Erection of 907	-14.0 k / 0.999	0.20 / 1.0*	30.8 k / 0.982	-2.42 k / 0.998
Stage 1 Slab Constr.	8.81 k / 1.000	1.04 k / 1.0*	-9.55 k / 0.999	-0.45 k / 0.742
Stage 2 Slab Constr.	-0.28 k / 0.520	1.64 k / 1.0*	61.7 k / 0.999	-6.68 k / 0.993
Stage 3 Slab Constr.	-0.33 k / 0.549	0.07 k / 1.0*	-6.36 k / 0.909	3.81 k / 0.949

1.0*: Only three readings available and thus R always equal to 1.0

APPENDIX C BENDING ANALYSIS OF BOX GIRDER WITH HORIZONTAL TRUSS BELOW THE TOP FLANGE LEVEL

C.1 Vertical Bending Analysis with X-type Truss

In many details, the horizontal truss system is not fastened directly to the top flanges. Instead, the system is connected to the transverse stiffeners on the webs and is located below the top flange level as shown in Fig. C.1. The offset, e, typically ranges from 6 in. to more than 1 ft. The bending analysis of the these girders will be discussed in this appendix.

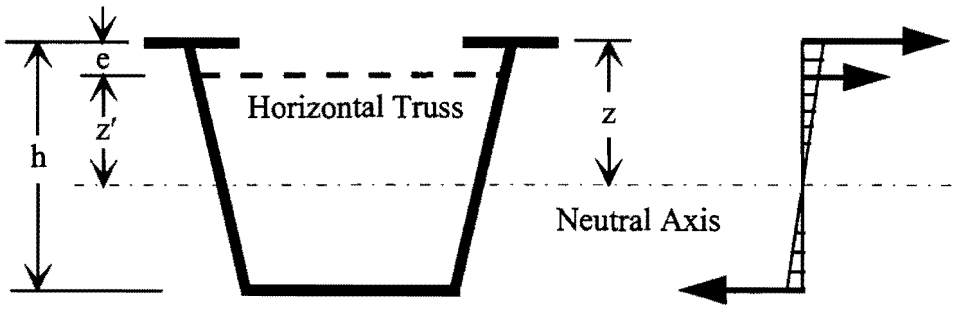

Figure C.1. Horizontal Truss Below the Top Flange Level

Assuming the stress distribution over the depth of the girder cross-sections is linear, the web stress at the level of the truss system, f', is

$$f' = \frac{z'}{z} f_{xTop} \ , \tag{C.1}$$

in which f_{xTop} is the longitudinal stress in the middle width of the top flange, z' is the distance from the neutral axis of the cross-section to the truss, z'=z-e (Fig. C.1). Using the same procedure as in Section 5.2.1, the following equation, which is similar to Eq. 5.6 except that f_{xTop} is replaced with f', can be derived for the brace force in the diagonals

$$D_{bend} = \frac{f' s \cos\alpha}{K_2} = \frac{f_{xTop} s \cos\alpha}{K_2} \cdot \frac{z'}{z} \ , \tag{C.2}$$

where K_2 is defined by Eq. 5.7. The axial force in the strut and the lateral bending stresses of the top flange can be derived from D_{bend} using Eqs. 5.27b and 5.27c, respectively.

To evaluate the contribution of the horizontal truss to the bending stiffness of the box girder, the following relation is derived from Eq. C.2,

$$\frac{D_{bend}\cos\alpha}{f_{xTop}} = A_0^* \frac{z'}{z}\ , \qquad (C.3)$$

in which A_0^* is given by Eq. 5.17. Similar to Eq. 5.15, the contribution from the top flanges and the horizontal truss to resist the vertical bending moment is (Fig. C.1)

$$M_t = 2f_{xTop}A_f z + 2D_{bend}\cos\alpha\, z' = 2f_{xTop}z(A_f + A_0^*(\frac{z'}{z})^2)$$

$$= 2f_{xTop}z(A_f + A^*)\ , \qquad (C.4)$$

in which

$$A^* = A_0^*(\frac{z'}{z})^2 \qquad (C.5)$$

is the equivalent increase in top flange area for each flange, representing the contribution of the truss system to the bending capacity of the girder.

However, the location of the neutral axis, z and z', for the modified girder cross-section is unknown before A^* is determined. This dilemma can be solved by a trial-and-error iteration procedure. In each step, a trial value of z is used, which is typically the result that was obtained in the last iteration. The procedure to calculate the brace forces in box girders with X-type bracing systems is, therefore, outlined as follows:

1. Calculate A_0^* using Eq. 5.17. Determine the location of neutral axis of the original cross-section (no bracing member considered). Assign the distance from the top flange to the neutral axis to z.
2. Let $z' = z - e$, and calculate $A^* = A_0^*(\frac{z'}{z})^2$.
3. Add A^* to the area of each of the top flanges. Determine the location of the neutral axis for this modified cross-section. Let z equal the distance from the new neutral axis to the top flange.
4. If the new z for the modified cross-section is different from the previous step, repeat step 2 and 3 until z converges.

5. Use the bending modulus of the modified cross-section (with the latest A^*) to determine the stresses in the top flange of the box girder, f_{xTop}.

6. Use Eqs. C.2 and 5.27b to determine the brace forces in the diagonals and struts.

In general, the shift of the neutral axis location due to the existence of the horizontal truss is small, as is the improvement of the cross-sectional modulus and thus the top flange stress. Neglecting the contribution of the horizontal truss to the bending stiffness will therefore result in a conservative solution of the brace forces in the horizontal truss system.

C.2 Vertical Bending Analysis with SD-type Truss

For girders with the SD-type truss located at a lever lower than the top flanges, FEA results show that the brace forces as well as the lateral bending stresses also depend upon the stiffness of the transverse stiffeners. Trial analyses on rectangular box girders (no horizontal load component) indicate that if the FEA results of the axial strut force (S_{bend}) is used to calculate the maximum lateral bending stresses by Eq. 5.26c, the stress values were larger than the actual FEA stress output. It has been found that the ratios of the direct FEA results of the lateral bending stress to the stress derived using Eq. 5.26c from FEA's S_{bend} values are approximately equal to the value of k, which is defined by

$$k = \frac{h - e}{h} . \qquad (C.6)$$

This suggests that the simple beam model illustrated in Fig. C.2 can be applied to simulate the behavior of the transverse stiffeners. The elastic support to the simple beam models the lateral bending stiffness of the top flanges.

The compatibility condition, Eq. 5.10, applies to all SD-type bracing systems regardless of the elevation of the truss. One of the parameters used in Eq. 5.10, v_1, is the relative horizontal deflection between consecutive truss joints (in addition to the elongation of the struts, v_2), and is determined by Eq. 5.9. If the truss is located at the top flange level, v_1 is identical to the relative lateral bending deflection of the top flange between two consecutive joints. If the truss is below the top flange, however, v_1 represents the same relative lateral displacement of the web between two consecutive joints at the level of the SD-truss. Deflection v_1 can be derived from the simple beam model as illustrated in Fig. C.2 as

$$v_1 = \frac{k^2 s^3 D_{bend} \sin\alpha}{2Eb_f^3 t_f} + \frac{2k^2(1-k)^2 h^3 D_{bend} \sin\alpha}{3EI_{st} \cos\phi} , \qquad (C.7)$$

in which I_{st} is the cross-sectional moment of inertia of the transverse stiffener in conjunction with a portion of the web plate. The deflection due to the elastic support is represented in the

first term. Equation 5.26b, which is still valid due to symmetry, has been applied in the derivation.

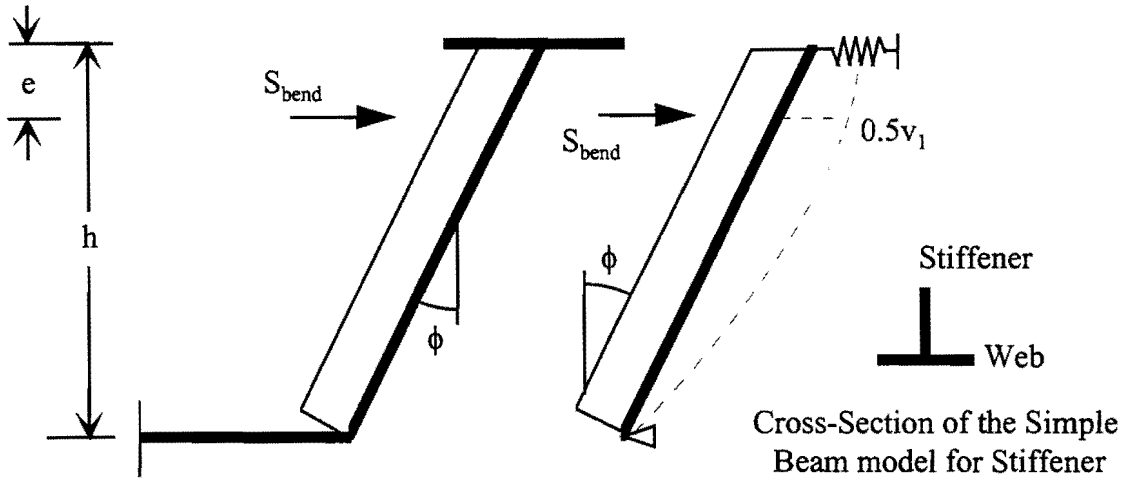

Figure C.2. Simple Beam Model for Stiffeners in Girders with SD-type Truss

Repeat the process of deriving Eq. 5.12 except using the new v_1 defined in Eq. C.7 and using f' from Eq. C.1 to replace f. The brace force in the diagonal of the SD-type truss can be derived as

$$D_{bend} = \frac{f_{xTop}\, s\cos\alpha}{K_1'} \cdot \frac{z'}{z}, \qquad \text{(C.8)}$$

where

$$K_1' = \frac{d}{A_d} + \frac{b}{A_s}\sin^2\alpha + \left(\frac{k^2 s^3}{2b_f^3 t_f} + \frac{2k^2(1-k)^2 h^3}{3I_{st}\cos\phi}\right)\sin^2\alpha\,. \qquad \text{(C.9)}$$

The brace forces in the lateral strut can still be determined using Eq. 6.26b, and the maximum lateral bending stress in the top flanges is

$$f_{L\,bend} = \frac{1.5kS_{bend}s}{b_f^2 t_f}\,. \qquad \text{(C.10)}$$

If k=1 (e=0), Eq. C.8 is identical to Eq. 5.26a. The formulation derived in this appendix is therefore a general expression that also applies to girders with truss system at the top flange level.

The axial brace forces and stresses are thus dependent on I_{st} in this modified formulation. The simply-supported beam that models the behavior of the stiffener, has a T-shaped cross-section as shown in Fig. C.2. The width of the Tee's flange, representing the portion of the

web acting with the stiffener, is unknown. The moment of inertia for the stiffener itself is $I_{st,0} = b_{st}^3 t_{st} / 12$, in which b_{st} and t_{st} are the depth and thickness of the stiffener, respectively. Introducing a new factor, η, such that

$$I_{st} = \eta I_{st,0} \ . \tag{C.11}$$

Numerical tests show that in most cases, a η between 2.5 to 4 led to results that are close to the FEA solution. Larger η always leads to more conservative solutions for brace forces and lateral bending stresses, but has little influence on the vertical bending stresses. Therefore, η = 3.5 is suggested for design purpose.

The contribution of the SD-type truss to the bending stiffness of the girder can be considered by introducing the increase in area for each of the top flange as

$$A^* = A_0^* (\frac{z'}{z})^2 \ , \tag{C.12}$$

in which A_0^* is defined by Eq. 5.18. Similar to the X-type truss, the location of the neutral axis can be determined by a trial-and-error iterative procedure using A^* defined in Eq. C.12. Again, the contribution from the horizontal truss to the bending stiffness of the box girder is marginal and the modification is usually unnecessary.

C.3 Lateral Load Components

When the horizontal truss system is below the top flange level, the axial forces in the truss due to the lateral load component (p) will increase. The explanation is provided in Fig. C.3 in which the stiffener is modeled as a simple beam supported at the bottom flange and the truss location while p acts on the top flange. The reaction at the joint between the truss and the stiffener, therefore, is approximately ps/k, in which k is defined by Eq. C.6.

The axial brace forces in the truss system due to the lateral component can be derived using the same procedure as in Chapter 5. For example, the brace forces in the X-type truss are

$$S_{lat} = \frac{d / A_d}{K_2} \cdot \frac{ps}{k} \ , \tag{C.13}$$

$$D_{lat} = \frac{b \sin\alpha / A_s}{K_2} \cdot \frac{ps}{k} \ . \tag{C.14}$$

However, since D_{lat} and S_{lat} are relatively small compared with the bending component, for simplicity p could be assumed to be resisted only by the struts. Therefore, the brace forces for both the X-type and the SD-type truss systems can be approximated by

$$D_{lat} = 0 \ , \tag{C.15}$$

$$S_{lat} = \frac{1}{k} ps \ . \qquad (C.16)$$

The lateral bending stresses are unaffected by the lower level of the truss location because p is acting directly on the top flanges. Therefore, the following equation identical to Eq. 5.30c is used to evaluate the lateral bending stresses due to the horizontal load component,

$$f_{L\,lat} = \frac{ps^2}{2b_f{}^2 t_f} \ , \qquad (C.17)$$

in which b_f and t_f are the width and thickness of the top flange.

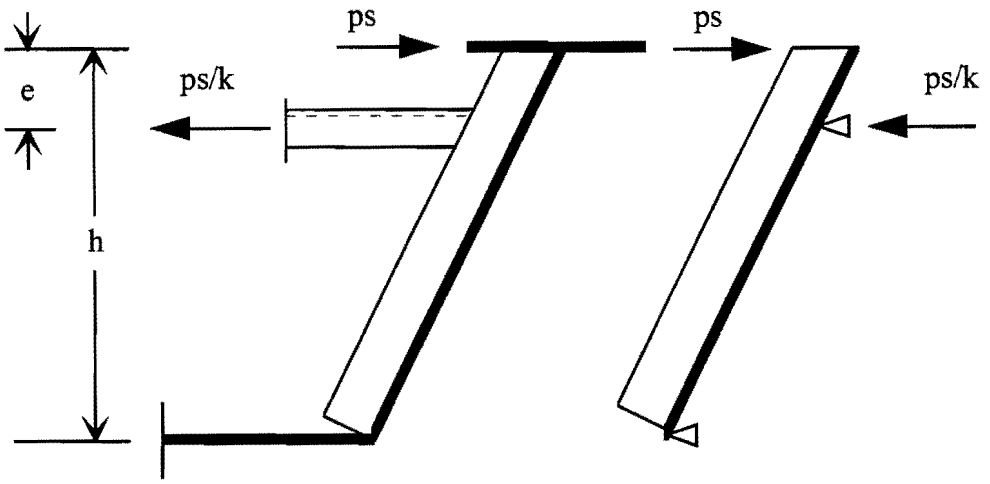

Figure C.3. Simple Beam Model for the Analysis of Horizontal Load Component

APPENDIX D DETERMINATION OF PURE TORSIONAL AND DISTORTIONAL LOADS ON BOX GIRDERS

D.1 Introduction

Torsional and distortional loads act on box girders in the form of transverse forces on the girder plates. These external forces result in zero bending moment on any cross-sections of the box girder. The longitudinal normal stresses on girder cross-sections, are generally caused by warping deformation. Torsional warping stresses are neglected in this discussion due to their relatively low level compared to those with distortional warping. Only distortional warping will be considered, and the term warping in this appendix always refers to distortional warping. A typical distribution of warping stresses for trapezoidal box girder is shown previously in Fig. 6.5.

The warping stresses shown in Fig. 6.5 may result from (a) the warping moments acting at the ends of the girder, and (b) the transverse loads on the plates. A box girder can be subjected to any warping moments at either ends while still keeping the equilibrium. If the out-of-plane bending stiffness of the girder plates is neglected, the distribution of the warping moment due to these external moments at the ends is linear along the girder length.

This appendix studies the warping property of box girders under general torsional loads. In particular, the torsional loads that will result in the box girder being in the state of pure torsion will be identified. Only when the transverse forces on girder plates contains no distortional components can a girder be in a state of pure torsion. The torsional loads without distortional components are defined as *pure torsional loads* as follows:

Definition 1: *Pure torsional loads consist of transverse forces on girder plates under which, except those by warping moments at the girder ends, no additional distortional warping stresses will be induced.*

Therefore, even when a girder is subjected to pure torsional loads, warping stresses may still exist, depending on the restraint conditions at the ends. However, the following lemma, which results from the above discussion, was used to find the pure torsional loads:

Lemma 1: *If a box girder is subjected to pure torsional loads, the distribution of the warping moment along the girder length is linear.*

Pure torsional loads only define the relative relations between transverse forces on girder plates, and are a function of the cross-section dimensions of box girders. The total moment resulting from a pure torsional load can be equal to any amount. An applied torsional load may contain the distortional components, which can be determined by subtracting the pure torsional load (with an equal magnitude of moment) from the applied transverse forces.

The objective of this appendix is to find the pure torsional loads which do not contain distortional components. The distortional loads can be determined afterwards. The cross-sections of the trapezoidal box girders being considered are assumed symmetrical about the central vertical axis. For simplicity, the double-symmetrical section is first studied.

D.2 Doubly Symmetric Rectangular Box Girder

Consider a doubly symmetric rectangular box girder subjected to general torsional loads. The thickness of the top and bottom plates is identical. The loads and stresses on the top plate and one of the webs are illustrated in Fig. D.1. Loads q_t and q_w are the transverse forces on the plates, and the out-of-plane resistance from the distortion of the cross-section is neglected.

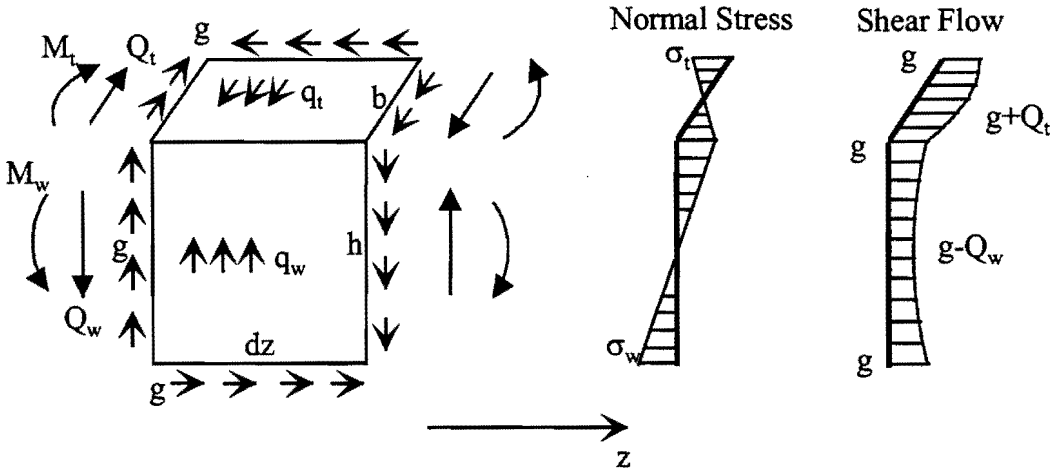

Figure D.1. Doubly Symmetric Cross-Section

Stresses that may develop on girder cross-sections include longitudinal warping stresses and shear stresses. The warping moment on the cross-section consists of in-plane bending moments of the plates, M_t and M_w, which cause the normal warping stresses, σ_t and σ_w, as shown in the figure. Assume each plate has a constant thickness; the warping stresses can be derived by assuming plane sections of plates remain plane during the warping deformation. Thus, the longitudinal normal stresses at the joint of the plates are

$$\sigma_t = \frac{6M_t}{b^2 t_t}, \tag{D.1}$$

$$\sigma_w = \frac{6M_w}{h^2 t_w}, \tag{D.2}$$

respectively. The normal stress at the joint must be equal, i.e., $\sigma_t = \sigma_w$. This results in

$$M_t = \lambda M_w \ , \tag{D.3}$$

in which $\lambda = b^2 t_t / h^2 t_w$.

Shear flows on the plates are generally nonlinear, as shown in Fig. D.1. Because of the symmetry in both directions, however, the shear flows at all four joints of the plates are equal and are denoted by g (lbs/ft). If the girder is in a state of pure torsion, a uniform shear flow, g, develops along the entire circumference of the cross-section.

In general, an in-plane shear force on the cross-section of each plate is a result of the superposition of two parts. The first is contributed from the pure shear, and the resulting shear forces from this part are gb and gh for the top plate and the web, respectively. Additional shear forces in the girder plates contribute to the non-uniform part of the shear flow. These shear forces, denoted by Q_t and Q_w for the top plate and the web, are corresponding to warping and are parabolic over the plate widths.

Figure D.2 shows the stresses and loads on the individual plates with an elementary length, dz. Equilibrium of the plate elements results in the following relations:
For the top plate (Fig. D.2a):

$$\frac{dQ_t}{dz} = -bg' - q_t, \quad \frac{dM_t}{dz} = Q_t \ , \tag{D.4}$$

$$\frac{d^2 M_t}{dz^2} = -bg' - q_t \ . \tag{D.5}$$

For the web (Fig. D.2b):

$$\frac{dQ_w}{dz} = hg' - q_w \ , \quad \frac{dM_w}{dz} = Q_w \ , \tag{D.6}$$

$$\frac{d^2 M_w}{dz^2} = hg' - q_w \ , \tag{D.7}$$

in which $g' = dg / dz$. The assumed positive directions for loads and stress resultants on each plate are shown in Fig. D.2.

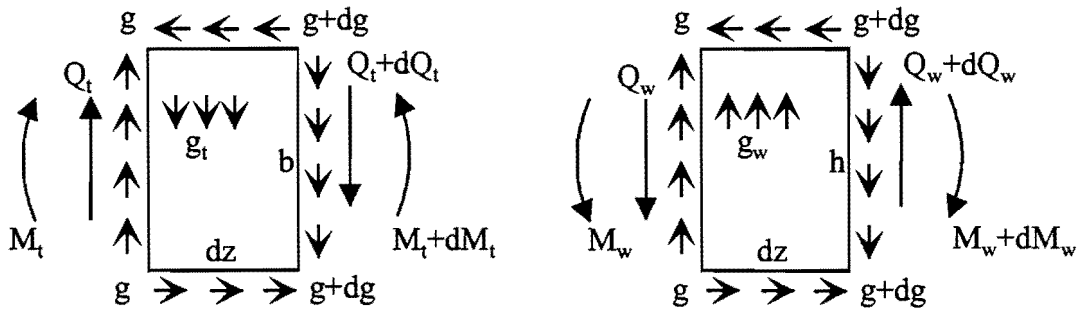

(a) Top Plate (b) Web

Figure D.2. Loads and Stress Resultants on Plate Element

According to Lemma 1, under the pure torsional loads the distribution of the warping moment over the girder length is linear. i.e.,

$$\frac{d^2M_t}{dz^2} = \frac{d^2M_w}{dz^2} = 0 \,. \tag{D.8}$$

Equations D.5, D.7 and D.8 result in

$$g' = \frac{q_w}{h} = -\frac{q_t}{b} \,. \tag{D.9}$$

Equation D.9 defines the distribution of a pure torsional loads on double symmetrical rectangular box girders. This relation was used in Chapter 2 to find the distortional components in applied torsional loads (Fig. 2.5).

Notice g′ can be determined by differentiating Eq. D.3 to yield

$$M_t'' = \lambda M_w'' \,. \tag{D.10}$$

Substituting Eqs. D.5 to D.7 into D.8, one can solve g′ as

$$hg' = \frac{\lambda q_w - q_t}{\lambda + \mu} \,, \tag{D.11}$$

$$bg' = \mu \cdot hg' \,, \tag{D.12}$$

in which $\mu = b/h$.

D.3 Trapezoidal Cross-Sections

To determine the pure torsional loads on trapezoidal box girder, the shear flows at the joints must first be solved. The transverse forces as well as the shear flows on the plates of the girder are shown in Fig. D.3, in which q_t, q_b and q_w are the respective transverse forces on the top plate, bottom plate and webs. An equal q_w is applied on both webs if no bending moment is induced in the girder.

Due to the non-symmetry in the vertical direction, the shear flows at the top and bottom joints of the web, denoted by g_t and g_b, respectively, are different. The symmetry in the horizontal direction, however, leads to same g_t and g_b for each of the webs. Therefore, the top and bottom plates are subjected to the loads and stresses similar to those shown in the Fig. D.2, with g being replaced with g_t for the top plate and with g_b for the bottom plate. The following relations similar to Eq. D.5 can be derived:

$$\frac{d^2M_t}{dx^2} = \frac{dQ_t}{dx} = -bg_t' - q_t \ , \tag{D.13}$$

$$\frac{d^2M_b}{dx^2} = \frac{dQ_b}{dx} = -ag_b' - q_b \ . \tag{D.14}$$

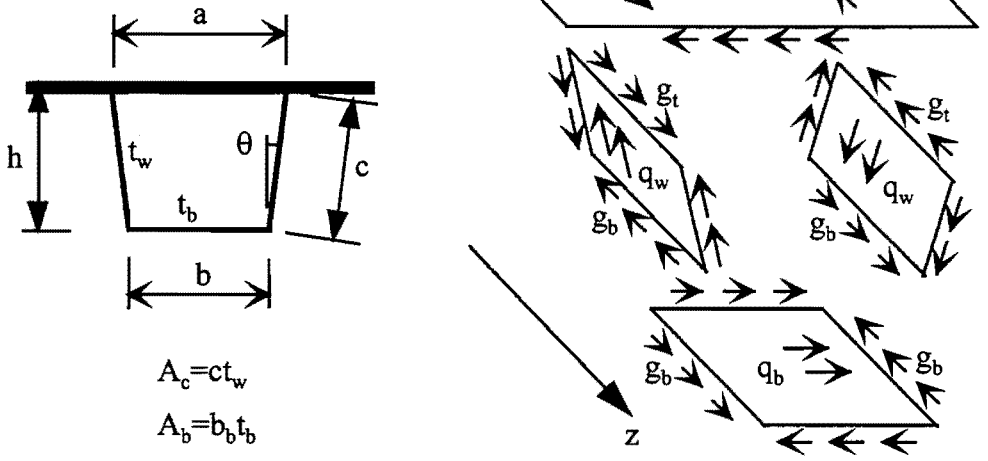

(a) Cross Section (b) Shear Flows

Figure D.3. Trapezoidal Cross-Section

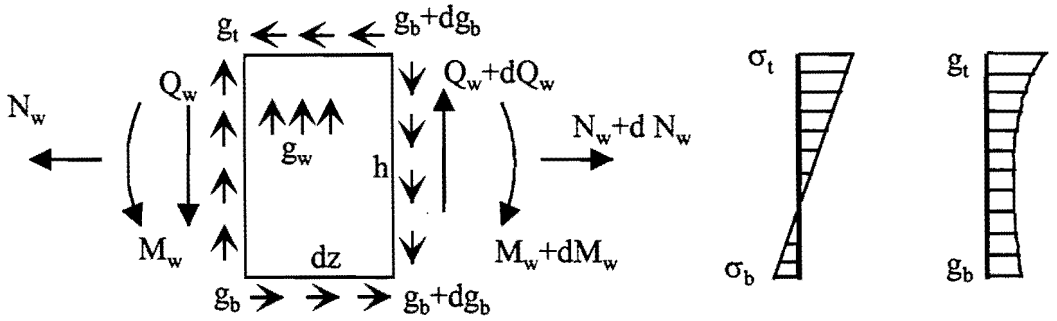

Figure D.4. Loads and Stresses on Web

Loads and stress resultants on webs are demonstrated in Fig. D.4, in which M_w is an in-plane bending moment and N_w is an axial force. Warping stresses are caused by M_w and N_w, which can be expressed using equilibrium as functions of web loads and shear flows as follows:

$$\frac{dN_w}{dz} = g_t - g_b \,, \tag{D.15}$$

$$\frac{d^2M_w}{dz^2} = \frac{dQ_w}{dz} = -q_w + \frac{c}{2}(g_t' + g_b') \,. \tag{D.16}$$

Assuming the longitudinal warping stresses are linearly distributed on the web cross-section, the warping stresses at the top and bottom joints of the webs can be derived as

$$\sigma_t = \frac{N_w}{A_w} + \frac{M_w}{W_w} \,, \tag{D.17}$$

$$\sigma_b = \frac{N_w}{A_w} - \frac{M_w}{W_w} \,. \tag{D.18}$$

in which A_w and W_w are the area and bending modulus of the web. The warping stresses at these joints can also be derived similar to Eq. (D.1) for the top and bottom plates by

$$\sigma_t = \frac{M_t}{I_t} \cdot \frac{b}{2} \,, \tag{D.19}$$

$$\sigma_b = \frac{M_b}{W_b} \,, \tag{D.20}$$

where W_b is the bending modulus of the bottom plate, and I_t is the in-plane moment of inertia of the top plate.

Equating D.17 with D.19 and D.18 with D.20 results in two linear equations in which the unknown variables are M_t, M_w, M_b and N_w. Substituting Eqs. D.13 to D.16 into these two equations, the gradient of the shear flows at the joints can be solved. The results are as follows:

$$g_t' = \frac{(1+3\alpha_b)\frac{q_w}{c} - \alpha_t(2+3\alpha_b)\frac{q_t}{b} + \alpha_b\frac{q_b}{a}}{1+2(\alpha_t+\alpha_b)+3\alpha_t\alpha_b}, \tag{D.21}$$

$$g_b' = \frac{(1+3\alpha_t)\frac{q_w}{c} - \alpha_b(2+3\alpha_t)\frac{q_b}{a} + \alpha_t\frac{q_t}{b}}{1+2(\alpha_t+\alpha_b)+3\alpha_t\alpha_b}, \tag{D.22}$$

where:

$$\alpha_b = \frac{A_c}{A_b},\ \alpha_t = \frac{A_c}{\tilde{A}_t},$$

A_c, A_b: Cross-sectional areas of the web and bottom flange,

$$\tilde{A}_t = \frac{12I_t}{b^2}.$$

According to Lemma 1, if the girder is subjected to pure torsional loads, M_t and M_b must satisfy

$$\frac{d^2M_t}{dz^2} = \frac{d^2M_b}{dz^2} = 0\ . \tag{D.23}$$

Equations (D.13), (D.14) and (D.23) yield

$$g_t' = \frac{q_t}{b}, \tag{D.24}$$

$$g_b' = -\frac{q_b}{a}\ . \tag{D.25}$$

Substituting Eqs. D.24 and D.25 into D.21 and D.22, the following relation between the transverse plate forces of a pure torsional loads can be derived

$$\frac{q_t}{b} = \frac{q_b}{a} = -\frac{q_w}{c}\ . \tag{D.26}$$

Equation (D.26) indicates that if the transverse forces on girder plates are proportional to the width of the corresponding girder plates (the width between the joints to the webs for the top plate), these forces form a pure torsional load. This distribution is identical to the shear flow in box girders under Saint-Venant torsion. Therefore, the following theorem is proved:

Theorem 1: *The transverse forces in a pure torsional load on box girders are distributed along the circumference of the box girder cross-section in proportion to the Saint-Venant shear flow.*

Let the transverse forces of a pure torsional load be denoted by $q_{t,pureT}$, $q_{b,pureT}$ and $q_{w,pureT}$, which satisfy Eq. (D.26). Assume

$$q_0 = \frac{q_{t,\,pureT}}{b} = \frac{q_{b,\,pureT}}{a} = -\frac{q_{w,\,pureT}}{c} \ . \tag{D.27}$$

If the moment of the pure torsional load is T, it can be derived that

$$q_0 = \frac{T}{2A_0} \ , \tag{D.28}$$

in which A_0 is the enclosed area of the box. Therefore, if the transverse forces on girder plates, q_t, q_b and q_w, result in a total torsional moment of T, the transverse forces corresponding to the equivalent pure torsional loads are:

$$q_{t,pureT} = \frac{T}{2A_0} b \ , \tag{D.29a}$$

$$q_{b,pureT} = \frac{T}{2A_0} a \ , \tag{D.29b}$$

$$q_{w,pureT} = \frac{T}{2A_0} c \ . \tag{D.29c}$$

The distortional load is the difference between the applied load and the equivalent pure torsional load, i.e.,

$$q_{t,\,distortion} = q_t - \frac{T}{2A_0} b \ , \tag{D.30a}$$

$$q_{b,\,distortion} = q_b - \frac{T}{2A_0} a \ , \tag{D.30b}$$

$$q_{w,\,distortion} = q_w - \frac{T}{2A_0} c \ . \tag{D.30c}$$

Equation D.30 was used in Chapter 6 to find the distortional loads on trapezoidal box girders.

APPENDIX E LIVE LOAD TEST RESULTS

Live load tests on the box girder bridge were conducted on April 24, 1997. The results from the live load tests are presented in this appendix. The stresses measured during the tests were graphed as functions of the truck location, therefore the stress influence lines are presented. The location of the test trucks are specified by X, the distance from the center of gravity of the trucks to Bent 17. X is always measured along the centerline of the bridge.

Only the stresses in the bottom flange and the webs are included. The stresses in the top flanges as well as in the top flange horizontal truss were relatively small due to the composite action of the concrete slab, as was discussed in Chapter 7. Temperature effect was not eliminated from the stress results. Temperature effect was relatively small in Tests 1 and 2 because the steel section were fully covered by the slab from direct sunshine. Tests 3 and 4 were conducted after 3:30pm, and part of the interior web of the girder (towards the west) was exposed to the direct sunshine. Temperature effects can be observed from the influence lines of Test 3 and 4.

The truck formation for each test is presented before the results. Comments for each test are presented to give a brief explanation and general observation on the test.

Truck Formation: The center of gravity of the trucks was nearly coincident to the centerline of the interior girder. The distance between the inside surface of the curb to the nearest tire was approximately 1 ft, and the distance between the back tires of Truck A, B and the front tires of Truck C, D was approximately 7 feet.

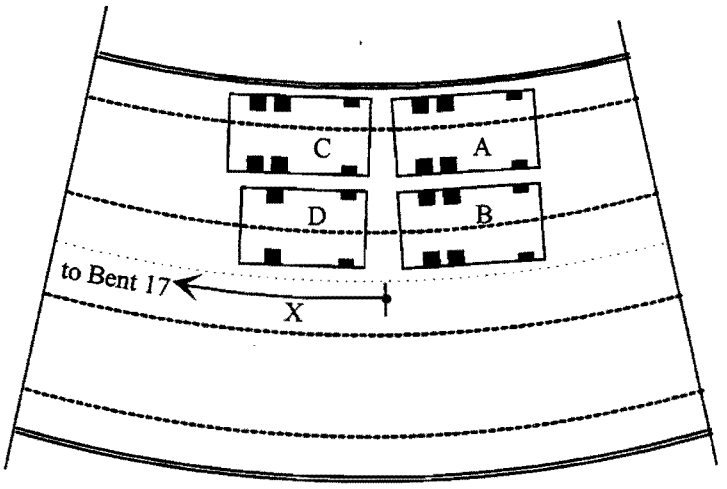

Figure E.1. Live Load Test 1

Time: 11:00 am to 12:40 pm.

Comments: The measured stresses on Sections P and N are graphed in Figs. E.2 and E.3, respectively. The maximum stress at Section P occurred at interior side of bottom flange. The maximum stresses at both sides of Section N were nearly identical. Influence lines converged to values nearly zero when the truck exited the bridge, implying that the temperature effects were relatively small.

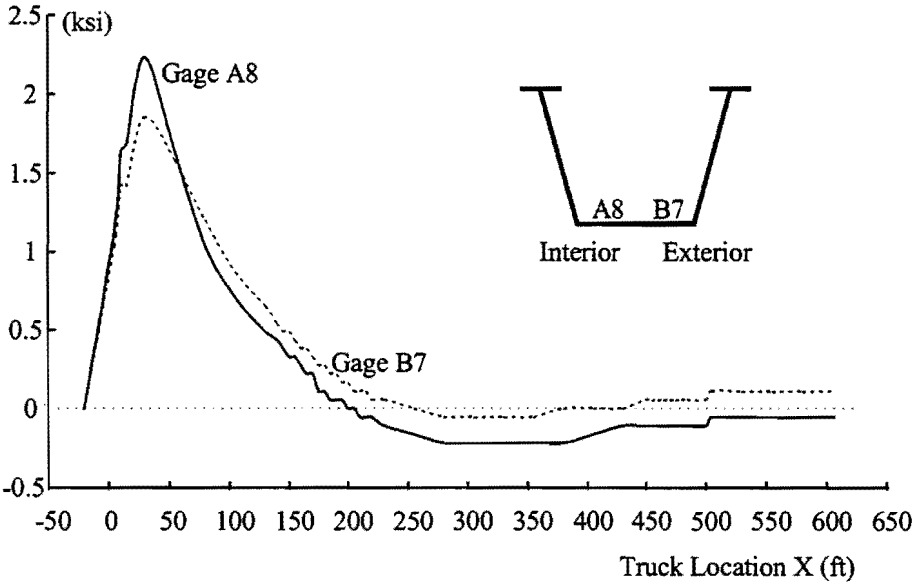

(a) Bottom FLange

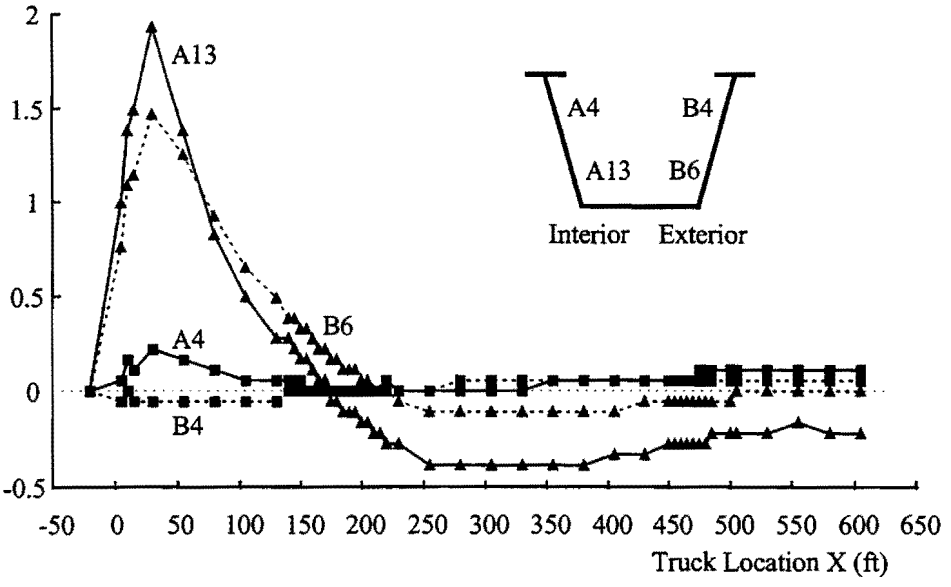

(b) Webs

Figure E.2. Stresses on Section P in Live Load Test 1

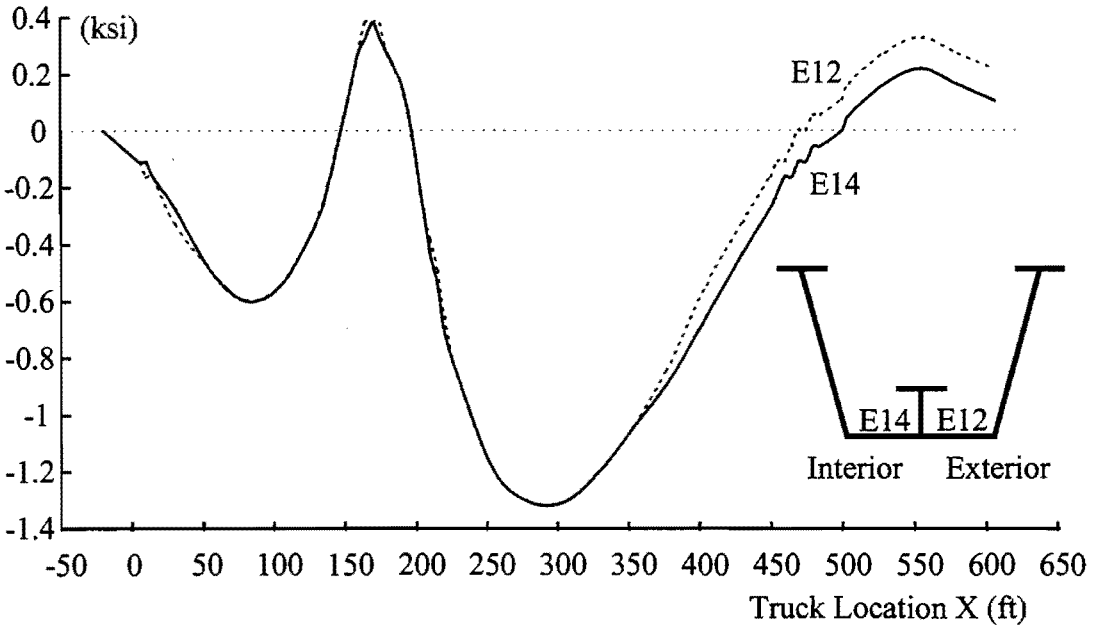

(a) Bottom Flange

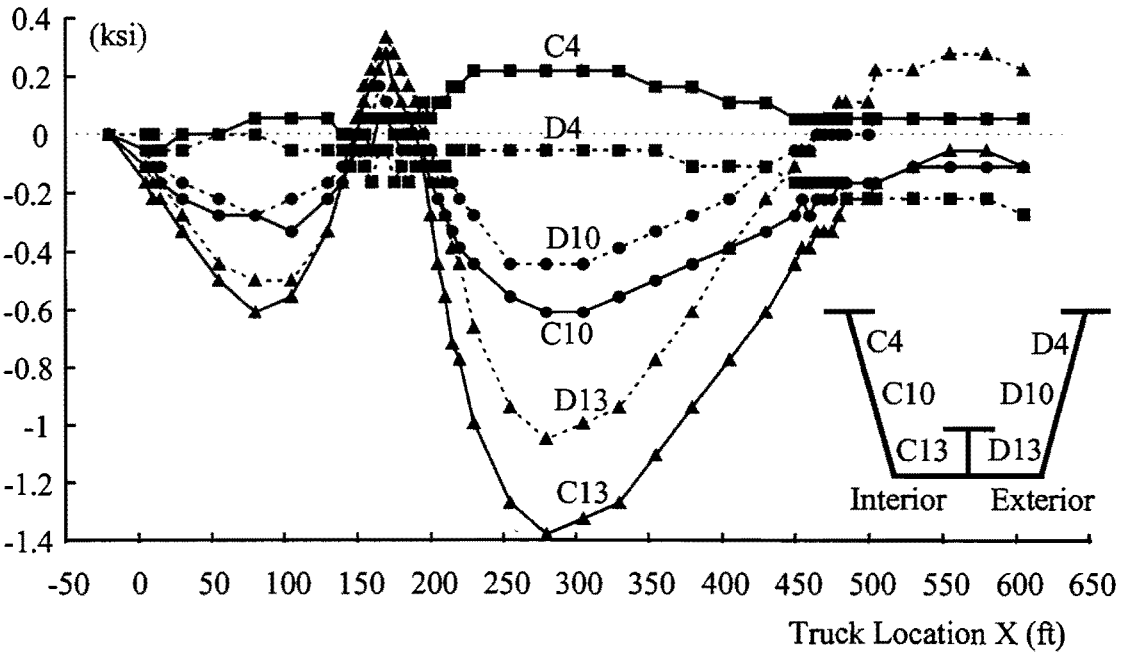

(b) Webs

Figure E.3. Stresses on Section N in Live Load Test 1

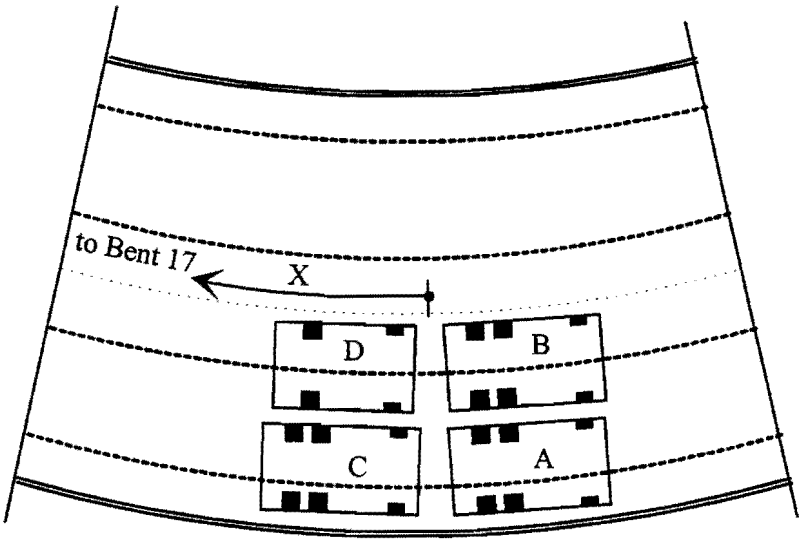

Figure E.4. Live Load Test 2

Time: 1:50 pm to 3:05 pm.

Truck Formation: The center of gravity of the trucks was nearly coincident to the centerline of the exterior girder. The distance between the inside surface of the exterior curb to the nearest tire was approximately 1 ft, and the distance between the back tires of Truck A, B and the front tires of Truck C, D was approximately 7 feet.

Comments: The measured stresses on Sections P and N are graphed in Figs. E.5 and E.6, respectively. The maximum stress at Section P occurred at interior side of bottom flange. The two sides of the cross-sections generally had larger stress differences than Test 1. The largest stress at Section P was significantly smaller than that occurred in Test 1. However, the largest stress at Section N was close to the level of Test 1. Temperature effects were relatively small compared with the largest stresses induced by the truck loads.

(a) Bottom Flange

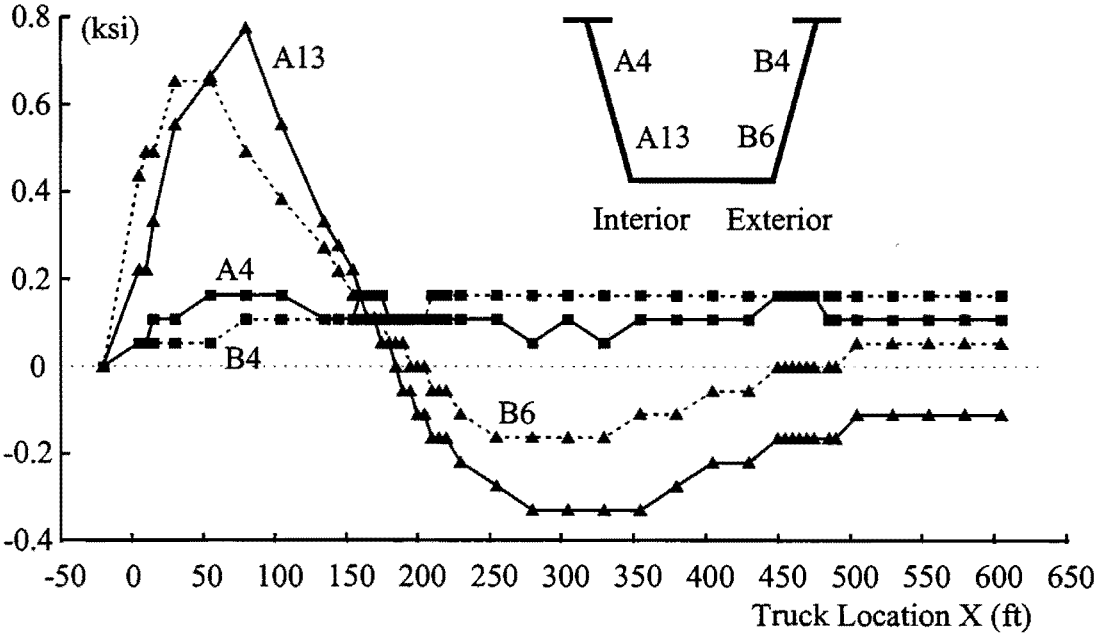

(b) Webs

Figure E.5. Stresses on Section P in Live Load Test 2

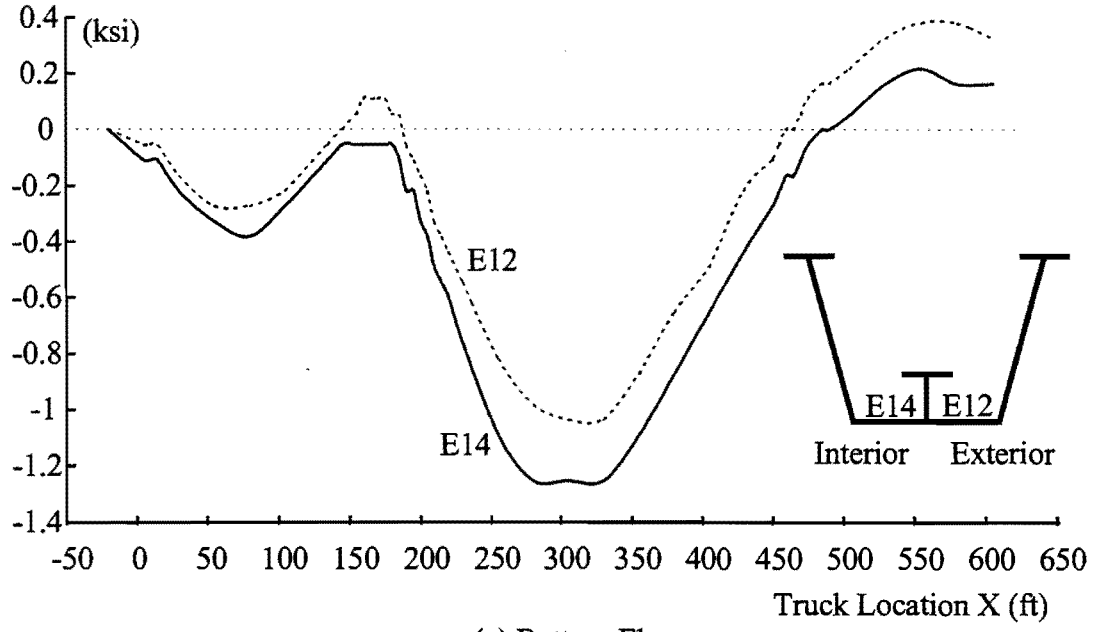

(a) Bottom Flange

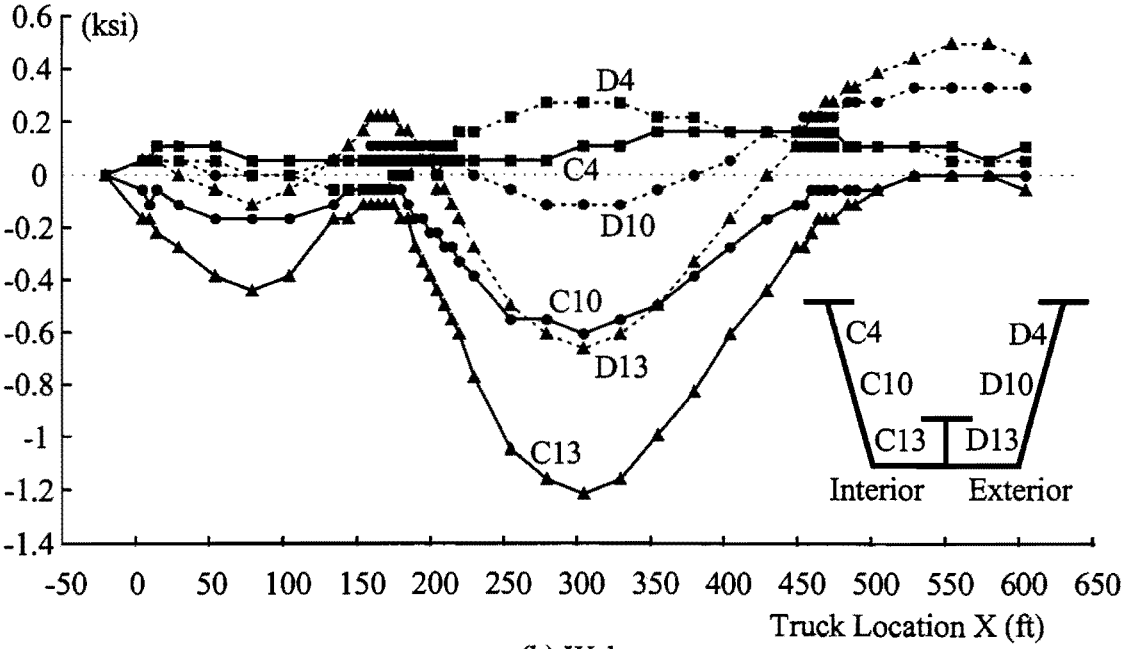

(b) Webs

Figure E.6. Stresses on Section N in Live Load Test 2

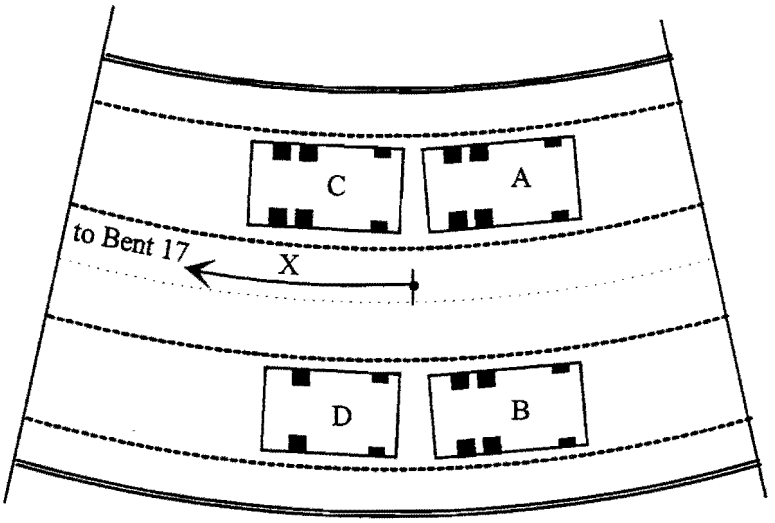

Figure E.7. Live Load Test 3

Time: 3:40 pm to 5:20 pm.

Truck Formation: Trucks A and C were placed above the interior girder while trucks C and D were on the exterior girder. The distance from the back tires of Truck A, B to the front tires of Truck C, D was approximately 7 ft.

Comments: The measured stresses on Sections P and N are graphed in Figs. E.8 and E.9, respectively. The largest stress at Section P was smaller than that in Test 1, but larger than in Test 2. The maximum stress at Section N was at the similar level to Tests 1 and 3. The stress difference at two sides of the bottom flange was smaller than that in Test 2. The interior side of the bottom flange at Section P developed larger stresses than the exterior side when the truck loads were in the same span of the section. Significant temperature effect was observed on Gage C3, which was located in the region exposed to the direct sunshine in the late afternoon.

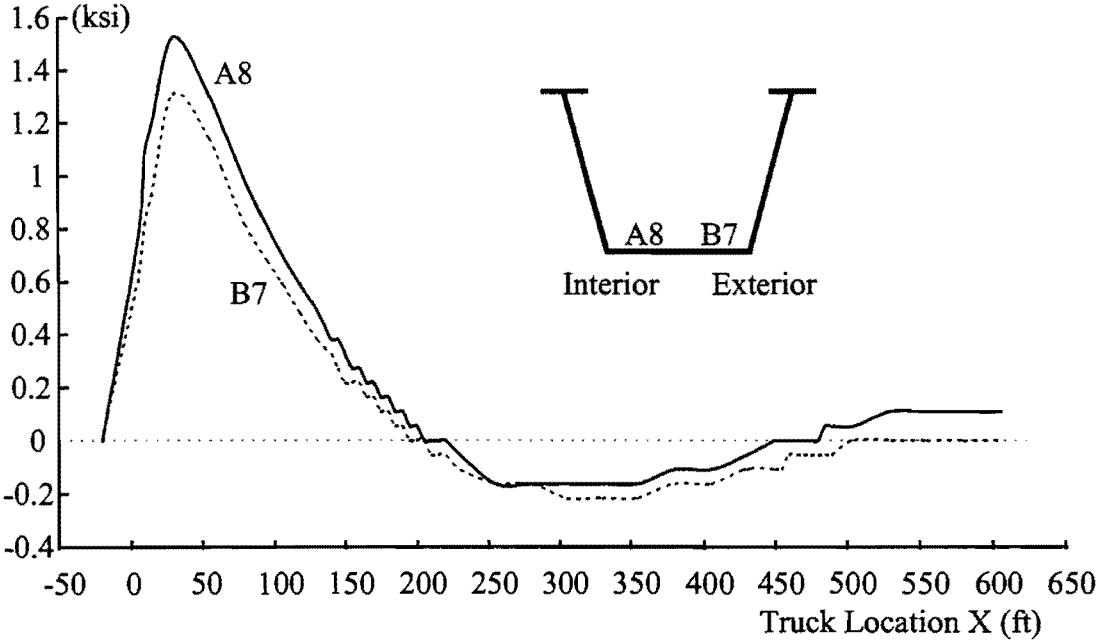

(a) Bottom Flange

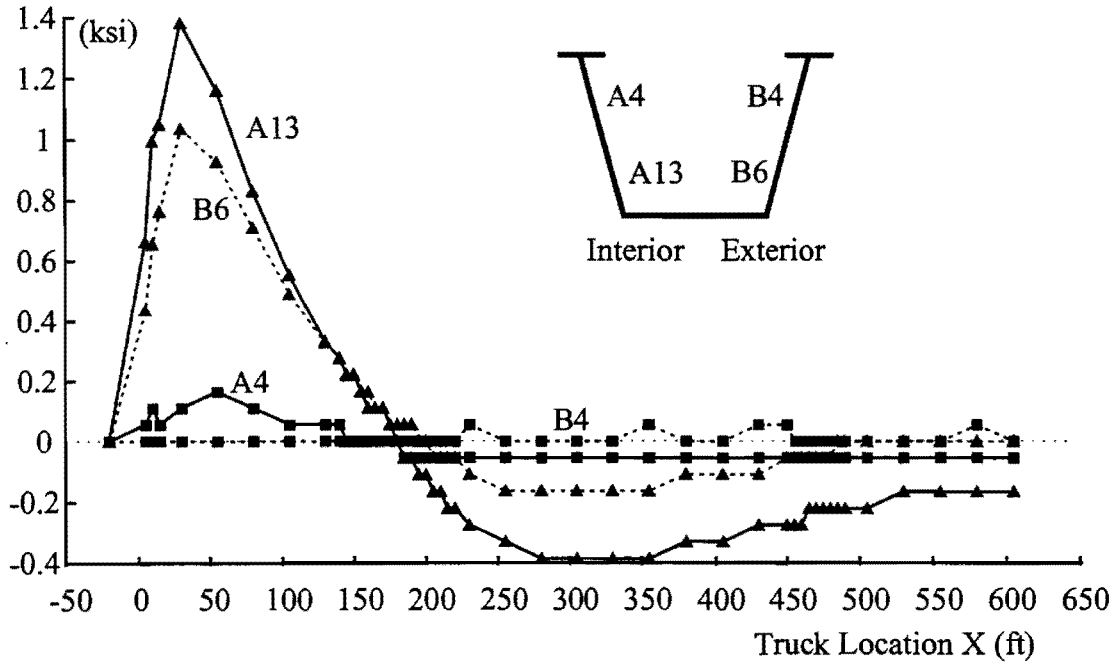

(b) Webs

Figure E.8. Stresses on Section P in Live Load Test 3

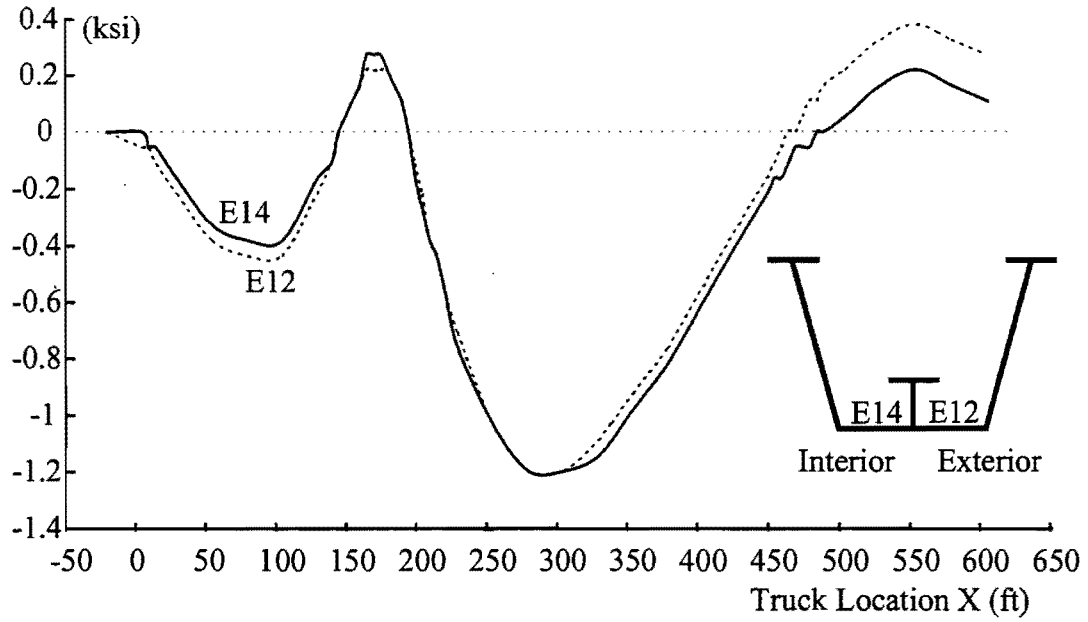

(a) Bottom Flange

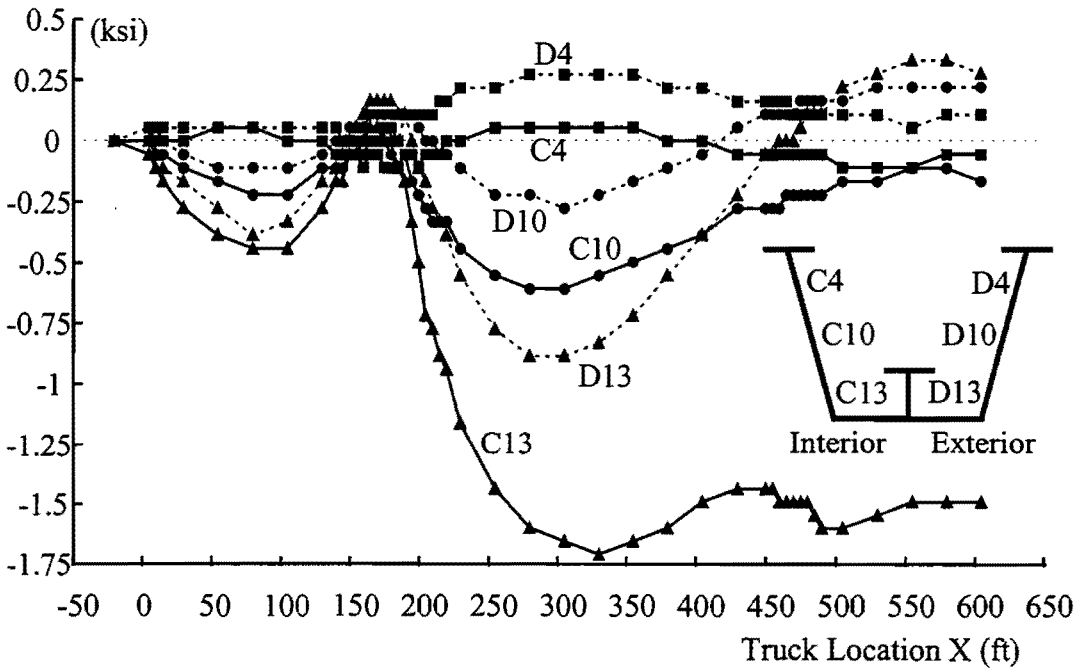

(b) Webs

Figure E.9. Stresses on Section N in Live Load Test 3

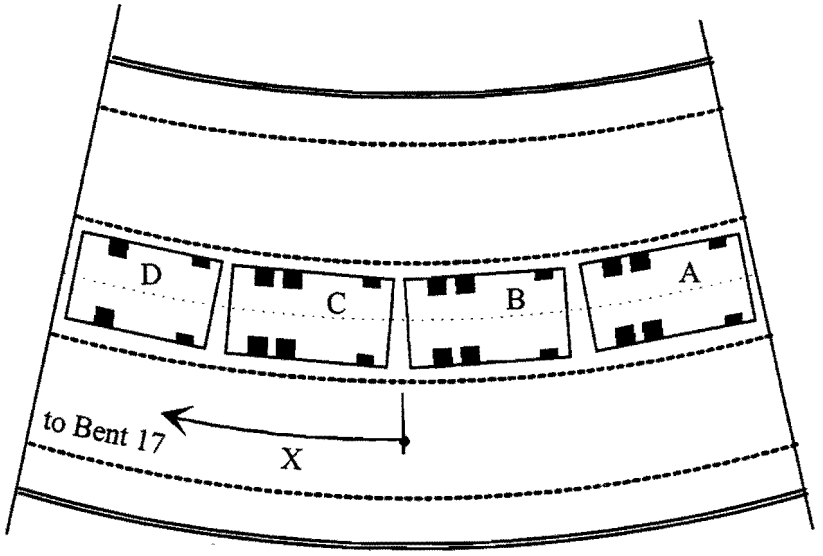

Figure E.10. Live Load Test 4

Time: 5:30 pm to 6:30 pm.

Truck Formation: The trucks were aligned to be coincident to the centerline of the bridge. The distances between the back tires of a truck to the front tires of the following truck were approximately 7 ft.

Comments: The measured stresses on Sections P and N are graphed in Figs. E.11 and E.12, respectively. The stress differences at the two sides of bottom flange were larger than Tests 1 ad 3 on both Sections P and N. The maximum stress at Section P was smaller than Tests 1 and 3, but larger than Test 2. The largest stress at Section N was still close to those in previous three tests. Temperature effects on the interior web at both Sections P and N were observed.

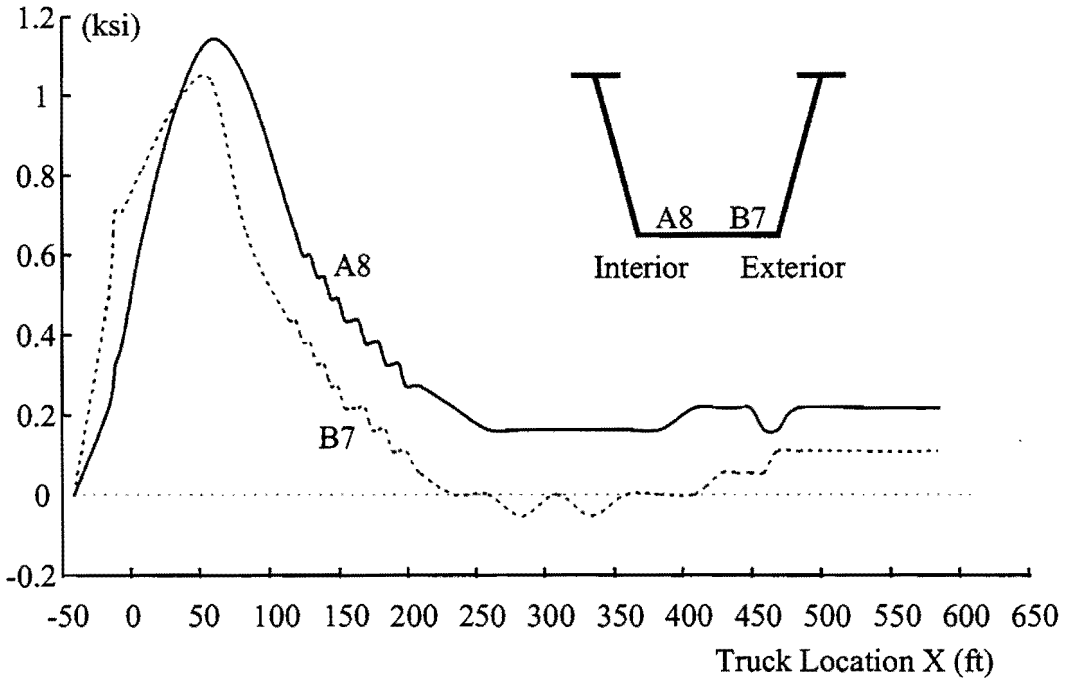

(a) Bottom Flange

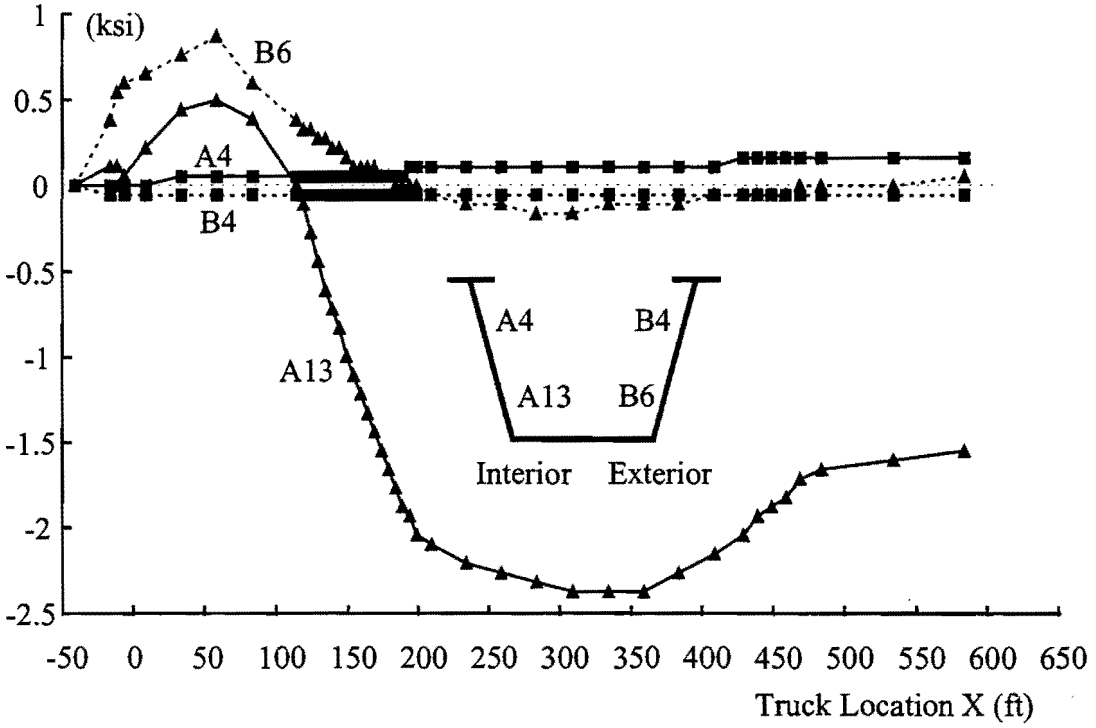

(b) Webs

Figure E.11. Stresses on Section P in Live Load Test 4

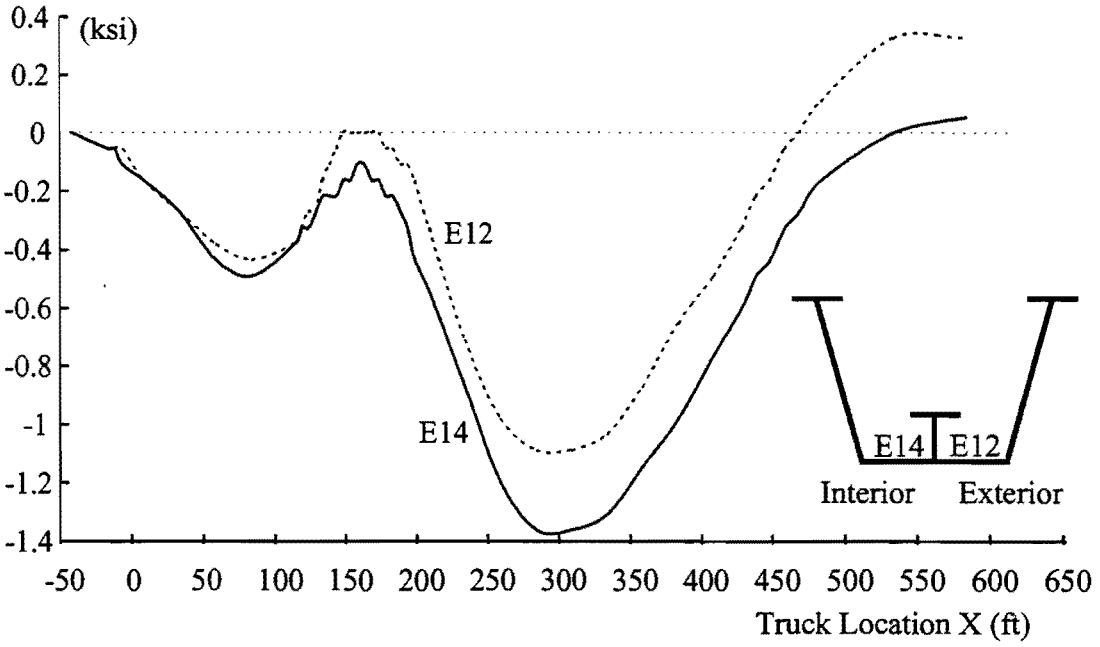

(a) Bottom Flange

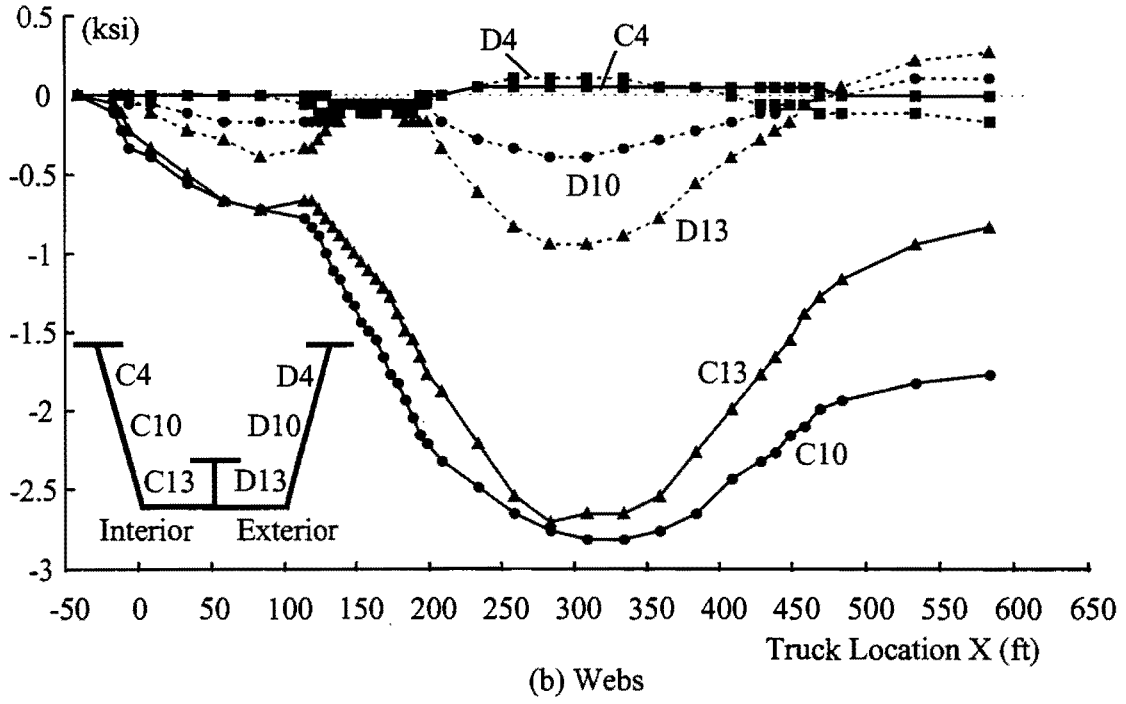

(b) Webs

Figure E.12. Stresses on Section N in Live Load Test 4

REFERENCES

"AASHTO LRFD Bridge Design Specification" (1994), Interim Specification - 1996, American Association of State Highway Officials, Washington, D.C.

ANSYS (1996), "Finite Element Program Users Manual, Version 5.0," ANSYS, Inc.

Brockenbrough, R. L. (1986), Distribution Factors for Curved I-Girder Bridges," *Journal Structural Engineering,* ASCE, Vol. 112, No. 10, pp. 2200-2215.

Cheung, Y. K. (1976), "Finite Strip Method in Structural Analysis," Pergamon Press.

Dabrowski, R. (1968), "Curved Thin-Walled Girders," Cement and Concrete Association, London.

"Four LRFD Design Examples of Steel Highway Bridges" (1997), Highway Structures Design Handbook, Vol. II, American Iron and Steel Institute and National Steel Bridge Alliance, Chicago.

Galambos, T. V., Hajjar, J. F., Leon, R. T., Huang, W. H., Pulver, B. E., and Rudie, B. J. (1996). "Stresses in Steel Curved Girder Bridges," University of Minnesota, Department of Civil Engineering, Report No. 96-28. Minneapolis, Minnesota.

"Guide Specifications of Horizontally Curved Highway Bridges" (1993), American Association of State Highway Officials, Washington, D.C.

Hall, D. H. (1997), "Why Steel Box Girders?", *Modern Steel Construction*, Vol. 37, No. 4, pp. 13-16, AISC.

Hall, D. H. and Yoo, C. H. (1998), "Recommended Specifications for Steel Curved-Girder Bridges," NCHRP Project 12-38.

Heins, C. P. (1975), "Bending and Torsional Design in Structural Members," Lexington Books, Lexington, Mass.

Heins, C. P. (1978), "Box Girder Design – State of the Art," *Engineering Journal*, AISC, Vol. pp. 126-142.

Heins, C. P. and Hall, D. H. (1981), "Designer's Guide to Steel Box Girder Bridges," Bethlehem Steel Corporation, Booklet No. 3500, Bethlehem, Pennsylvania.

Helwig, T. A. (1994), "Lateral Bracing of Bridge Girders by Metal Deck Forms," Ph.D. Dissertation, Department of Civil Engineering, University of Texas at Austin.

"Highway Structural Design Handbook," (1982), Vol. 2, AISC Marketing, Inc.

Kollbrunner, C. F. and Basler, K. (1969), "Torsion in Structures – An Engineering Approach," Springer-Verlag, New York.

Lopez, M. G. (1999), "Thermally-Induced Deformations and Stresses in a Steel Trapezoidal Twin-Box Girder Bridge," M.S. Thesis, Department of Civil Engineering, University of Texas at Austin.

McManus, P. F., Nasir, G. A., and Culver, C. G. (1969), Horizontally Curved Girders — State of the Art," *Journal of the Structural Engineering Division*, ASCE, Vol. 95, No. ST5, pp.

Mattock, A. H. (1971), "Development of Design Criteria for Composite Box Girder Bridges," Development in Bridge Design and Construction, Crosby Lockwood & Sons, London, England.

Mattock, A. H. and Kaar, P. H. (1961), "Precast-Prestressed Concrete Bridges – 6. Test of Half-Scale Highway Bridge Continuous Over Two Spans," *J. Res. Dev. Labs Portld Cem. Ass.*, Vol. 3, No. 3, pp. 30-70.

Meyer, C. and Scordelis, A. C. (1970), "Analysis of Curved Folded Plate Structures," Report No. UC SESM 70-8, University of California at Berkeley, California.

Nakai, H. and Heins, C. P. (1977), "Analysis Criteria for Curved Bridges," *Journal of Structural Engineering,* ASCE, Vol. 103, No. ST7, pp. 1419-1427.

Nakai, H. and Yoo, C. H. (1988), "Analysis and Design of Curved Steel Bridges," McGraw-Hill Book Co.

NCHRP (1998), "Improved Design Specification for Horizontally Curved Steel Girder Highway Bridges," Project 12-38. http://www2.nas.edu/trbcrp/6826.html

Olenik, J. C. and Heins, C. P. (1975), "Diaphragms for Curved Box Girder Bridges," *Journal of the Structural Division*, ASCE, Vol. 101, No. ST10.

Razaqpur, A. G. and Li, H. (1991), "Thin-Walled Multicell Box-Girder Finite Element," *Journal of Structural Engineering,* ASCE, Vol. 117, No. 10, pp. 2953-2971.

Richardson, Gordon & Associates, Consulting Engineers (1963), "Analysis and Design of Horizontal Curved Steel Bridge Girders," United States Steel Structural Report, ADUSS 88-6003-01.

Tabsh, S. W. and Sahajwani, K. (1997), "Approximate Analysis of Irregular Slab-on-Girder Bridges," *Journal of Bridge Engineering*, ASCE, Vol. 2, No. 1, pp. 11 - 17.

Task Committee on Curved Box Girders of the ASCE-AASHTO Committee on Flexural Members of the Committee on Metals of the ASCE Structural Division (1978), "Curved Steel Box-Girder Bridges: State-of-the-Art," *Journal of the Structural Division*, ASCE, Vol. 104, No. ST11, pp. 1719-1739.

Tarhini, K. M. and Frederick G. R. (1992), "Wheel Load Distribution in I-Girder Highway Bridges," *Journal Structural Engineering,* ASCE, Vol. 118, No. 5, pp. 1285-1294.

Till, W. T., Poellot, W. N., Jr. and Hedgren, A. W., Jr, (1976), "Curved Girder Workshop," Federal Highway Administration, Washington, D. C.

Timoshenko, S. P. and Gere, J. M. (1961), "Theory of Elastic Stability," 2nd edition, McGrow-Hill, New York.

Tung, D. H. and Fountain, R. S., (1970), "Approximate Torsional Analysis of Curved Box Girders by the M/R Method," *Engineering Journal*, AISC, Vol. 7, No. 3, pp. 65 - 74.

United States Steel Corporation (1984), "V-Load Analysis," USS Highway Structures Design Handbook, ADUSS 88-8535-01, Vol. 1, Chapter 12.

"DESCUS-II, Analysis of Curved Box Girder Bridges, Version 3.1," (1997) Opti-Mate, Inc., Bethlehem, PA, 1996

Vlasov, V. Z. (1961), "Thin-Walled Elastic Beams," 2nd edition, National Science Foundation, Washington D.C.

Weisberg, S. (1985), "Applied Linear Regression," 2nd edition, John Wiley & Sons, New York.

Williamson, D. M. (1974), "BEF Analogy for Cross-Sectional Deformation of Curved Box Girders with Internal Diaphragms," M.S. Thesis, Civil Engineering Department, Carnegie-Mellon University, Pittsburg, PA.

Wright, R. N., Abdel-Samad, S. R. and Robinson, A. R. (1968), "BEF Analogy for Analysis of Box Girders," *Journal of Structural Engineering*, ASCE, Vol. 94, No.ST7, pp. 1719 - 1743.

Zhang, S. H. and Lyons, L. P. R. (1984), "A Thin-Walled Box Beam Finite Element for Curved Bridge Analysis," *Journal of Computers & Structures*, Vol. 16, No. 6, pp. 1035-1046.

Zienkiewicz, O. C. (1977), "The Finite Element Method," 3rd edition, McGraw-Hill.